PROCESS CHARACTERIZATION AND OPTIMIZATION OF ROLL-TO-ROLL PLASMA CHEMICAL VAPOR DEPOSITION FOR GRAPHENE GROWTH

by

Majed A. Alrefae

A Dissertation

Submitted to the Faculty of Purdue University

In Partial Fulfillment of the Requirements for the degree of

Doctor of Philosophy

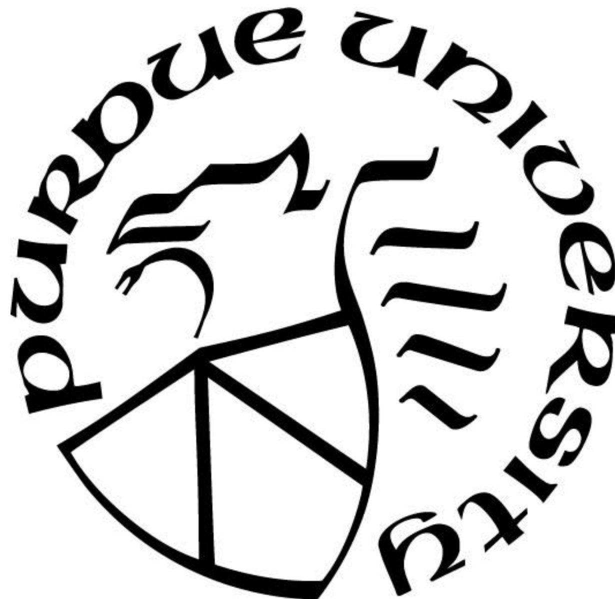

School of Mechanical Engineering

West Lafayette, Indiana

May 2018

THE PURDUE UNIVERSITY GRADUATE SCHOOL
STATEMENT OF COMMITTEE APPROVAL

Prof. Timothy S. Fisher, Co-chair

School of Mechanical Engineering

Prof. Ilias Bilionis, Co-chair

School of Mechanical Engineering

Prof. Robert P. Lucht

School of Mechanical Engineering

Prof. Alina A. Alexeenko

School of Aeronautics and Astronautics

Approved by:

Prof. Jay P. Gore

Head of the Graduate Program

Dedicated to my wife Banan, our kids: Taleen, Tamim and Rayan, and my mom Saeedah.

ACKNOWLEDGMENTS

I would like to thank my advisor, Professor Timothy S. Fisher, for his support, guidance and encouragement during my Ph.D. work under his supervision. Prof. Fisher is a great mentor who has always extended the boundaries of my scientific research and professional life. His availability and openness for questions, advice, and discussion have streamlined my doctoral work. Prof. Fisher is also a great entrepreneur who has built great opportunities for research extending beyond the laboratory into commercialization.

I would also like to thank my co-advisor, Professor Ilias Bilionis, who has greatly helped in optimizing the roll-to-roll process. Prof. Bilionis has provided substantial knowledge in developing design of experiment methods to understand and control plasma processes with data-driven models.

I would like to thank Professor Robert P. Lucht, from whom I learned a lot in both research and teaching. Prof. Lucht's classes in statistical thermodynamics, thermodynamics, and laser diagnostics have been great resources in learning how best to utilize *in situ* optical spectroscopy and characterize the plasma environment.

Professor Alina A. Alexeenko has provided great expertise in modeling plasma and has provided delightful insights and advice during our update meetings throughout my doctoral study.

I appreciate Prof. Sergey O. Macheret for his great expertise in explaining plasma physics and learning from his plasma physics course.

I would like to thank Prof. Andrey A Voevodin for the initial electrical characterization of the plasma and the great discussions during the preparation of the CVD book chapter.

Also, I appreciate Prof. Xianfan Xu for the generous use of the Raman spectroscopy setup in his laboratory. Special thanks to Dr. Dmitry Zemlyanov for XPS measurements, Dr. Rosa Diaz for performing TEM measurements, and Xingtao Liu for TEM sample preparation of the graphite film using focused ion beam.

My work at Birck Nanotechnology Center has been a great experience, and I would like to thank every individual within the Birck family for his/her help during my Ph.D. work. Special thanks to Guy Telesnicki, who has made the operation of the R2R system so easy and smooth. Also, I would like to thank Prof. Ali Shakouri, Ron Reger, Tim Miller, Dan Hosler, Dr. Nithin

Raghunathan, Mary Jo Totten, and Kyle Corwin. Special thanks to the business office in Birck Nanotechnology Center, especially Tracy Hudson and Cindy Sanders.

Also, I would like to thank my colleagues: Anurag Kumar, Kim Saviers, Arpan Kundu, Nick Glavin, Stephen Hodson, Galen Jackson, Aman Sajita, Alfredo Tuesta, Aaditya Candadai, Yuan Hu, Gayathri Shivkumar, and Piyush Pandita for sharing knowledge in advancing science and technology without borders.

I would like to thank Cathy Elwell, Julayne Moser and Prof. Jay P. Gore from the School of Mechanical Engineering for their great help and support during my graduate studies. I would like to thank Magdalene Jackson for reviewing this dissertation and providing useful comments.

Special thanks to my sponsor, Royal Commission of Jubail and Yanbu, Saudi Arabia for funding my doctoral study. Also, I would like to thank the US National Science Foundation through its Scalable Nanomanufacturing Program for the roll-to-roll plasma CVD experiment.

I am extremely thankful for the love and support from my wife, Banan, and the joy of our children: Taleen, Tamim, and Rayan. My mom, Saeedah, has also provided great encouragement during my life and studies.

TABLE OF CONTENTS

LIST OF TABLES ix
LIST OF FIGURES x
LIST OF ABBREVIATIONS xvii
LIST OF SYMBOLS xix
ABSTRACT xxii
1. INTRODUCTION 1
2. LITERATURE REVIEW 4
2.1 Graphene Properties and Production 4
2.2 Synthesis of Graphene by Plasma CVD 6
2.2.1 Growth of Single-layer Graphene by Plasma CVD 9
2.2.2 Growth of Few- and Many-layer Graphene by Plasma CVD 11
2.2.3 Growth of Graphene Nanopetals by Plasma CVD 12
2.3 Optical Emission Spectroscopy (OES) 12
2.3.1 Temperature Measurements using OES 13
2.3.2 OES as an in situ Growth Characterization Tool 14
2.4 Roll-to-Roll CVD Processes for Large Production of Graphene 15
3. PROCESS OPTIMIZATION OF GRAPHENE GROWTH IN A ROLL-TO-ROLL PLASMA CVD 18
3.1 Motivation and Background 18
3.2 Experimental Setup 19
3.2.1 Roll-to-Roll Plasma CVD System 19
3.2.2 Graphene Characterization 20
3.2.3 Multi-objective Optimization Method 22
3.3 Results and Discussion 23
3.3.1 Graphene Quality Optimization and Characterization 23
3.3.2 The Effects of the Plasma Parameters on Graphene Quality 26
3.3.3 Correlating Results from OES with Graphene Quality and Process Parameters 30
3.3.4 Graphene Deposition at Higher Web Speeds 36

3.3.5 Conclusion 39

4. THERMAL AND SPECTROSCOPIC ANALYSIS OF PLASMA ROLL-TO-ROLL DEPOSITION OF GRAPHENE 40

4.1 Motivation and Background 40

4.2 Experimental Setup 41

4.3 Heat Transfer Model 43

4.3.1 Analytical Model Derivation 44

4.3.2 Numerical Model Derivation 46

4.4 Results and Discussion 47

4.4.1 Determination of Heat Transfer Parameters from Temperatures Measurements 47

4.4.2 Effects of Web Speed and Plasma Power on Cu Foil Temperature Profile 51

4.4.3 Effects of Web Speed and Plasma Power on Graphene Growth 54

4.4.4 Effects of Plasma Length on Cu Foil Temperature Profile and Graphene Growth 56

4.4.5 The Optimized Condition for Continuous Graphene Growth on Cu Foil 59

4.5 Conclusion 61

5. THE ROLE OF HEAT TRANSFER IN ROLL-TO-ROLL DEPOSITION OF GRAPHENE ON NICKEL FOIL 62

5.1 Motivation and Background 62

5.2 Results and Discussion 64

5.2.1 Roll-to-Roll Deposition of Graphene on Ni Foil 64

5.2.2 Ni Foil Temperature Distribution during Roll-to-Roll Graphene Growth 66

5.2.3 Correlation between Graphene Growth and Ni Foil Temperature Distribution 71

5.3 Conclusion 75

6. THERMAL CHARACTERIZATION OF A CAPACITIVELY COUPLED RADIO-FREQUENCY HYDROGEN PLASMA 76

6.1 Motivation and Background 76

6.2 Experimental System 76

6.3 Results and Discussion 80

6.3.1 Effects of Set Power and Gas Pressure on Power Dissipation and Rotational Temperatures 80

6.3.2 Effects of Nitrogen, Oxygen, and Methane Addition on Power Dissipation and Rotational Temperatures 83
6.3.3 Differences among H_2, N_2^+ and CN Rotational Temperatures 86
6.4 Conclusion 88
7. EXPERIMENTAL ANALYSIS OF AN 80 KHZ CAPACITIVELY COUPLED ARGON PLASMA 90
7.1 Motivation and Background 90
7.2 Experimental Setup 91
7.3 Results and Discussion 93
7.3.1 Electrical and Spectroscopy Characterizations 93
7.3.2 Comparison between Species Emission from OES 97
7.3.3 Plasma Hysteresis during the Transition from Gamma to Hybrid Mode 99
7.4 Conclusion 100
8. DIRECT LARGE-SCALE DEPOSITION OF THIN GRAPHITE FILM ON CU FOIL ... 101
8.1 Results and Discussion 102
8.2 Conclusion 106
9. CONCLUSIONS 107
REFERENCES 112
APPENDIX A. PROCESS OPTIMIZATION OF GRAPHENE GROWTH IN A ROLL-TO-ROLL PLASMA CVD SYSTEM 136
APPENDIX B. FIN MODEL DERIVATION 145
VITA 148
PUBLICATIONS 149

LIST OF TABLES

Table 2.1: Overview of the plasma CVD systems used to grow graphene. SLG: single-layer graphene, FLG: few-layer graphene, MLG: multilayer graphene, petals: graphene nanopetals, DC: direct current plasma, r-rf: remote radio frequency plasma, rf: radio frequency plasma, MW: microwave plasma, CH_4: methane, C_2H_2: acetylene, H_2: hydrogen, Ar: argon, O_2: oxygen Cu: copper, Ni: nickel, Si: silicon, SiO_2: silicon dioxide, Co: cobalt, Gr: graphite anode, Al: aluminum, “oil”: oil extracted from a tea tree... 6

Table 2.2: Commonly used species with their transitions to measure rotational temperature in plasma systems.. 14

Table 2.3: Summary of available CVD process for large area graphene production. 16

Table 3.1: Plasma operating conditions and constraints implemented in this work. 20

Table 4.1: Comparison between the I_D/I_G and I_{2D}/I_G ratios of graphene grown by the vertical and horizontal configurations at various plasma powers and web speeds.. 58

Table 5.1: Comparison of process parameters during graphene growth on Ni substrate. CVD: chemical vapor deposition, MPCVD: microwave plasma CVD, PECVD: plasma-enhanced CVD, PLD: pulsed laser deposition, rf CVD: radio-frequency plasma CVD.. 63

Table 5.2: Comparison between Raman peak intensity ratios for graphene on Ni foil and Cu foil at various plasma powers and web speeds. 75

Table A.1: The species emission lines used in this work. 142

LIST OF FIGURES

Figure 3.1: (a) Setup of the roll-to-roll plasma CVD system. (b) The plasma region where the copper foil is processed for graphene growth. (c) Top view of the chamber with the optical emission spectroscopy setup. 20

Figure 3.2: Raman spectra of graphene that show more defects with increased plasma residence time. Other conditions are kept constant at 60% H_2, 25% CH_4, and 15% Ar at 15 mbar. 21

Figure 3.3: Summary of the optimization process methodology used in this chapter. 23

Figure 3.4: Sequential optimization of graphene on both sides of Cu foil. SEM images are shown for representative low and high qualities of graphene. 24

Figure 3.5: (a) Raman spectrum of the optimized condition. (b) Spatial dependence of I_D/I_G representing uniform growth of graphene for the optimized condition, whereas the quality is not uniform for graphene growth at 50% H_2, 21% CH_4, 0% N_2, 0% O_2, 29% Ar at 18.8 mbar and 1250 W. SEM images of graphene on copper obtained from (c) secondary electrons (SE) and (d) backscattering electrons (BSE) of a uniform deposition whereas (e) shows a non-uniform deposition from backscattering electrons (BSE) taken from a non-optimized condition. 25

Figure 3.6: Sequential batch runs during the exploration and optimization process. The model results in (b) Validation 6 agree better with the experimental results than the results in (a) Validation 4 due to the increased number of experiments. 27

Figure 3.7: The sensitivity analysis of the process inputs that affect the I_D/I_G extracted from the statistical surrogate models. 27

Figure 3.8: I_D/I_G response surfaces as a function of (a) pressure, (b) nitrogen, (c) oxygen and (d) plasma power. The line shows the mean values of the response surface for the predictive model. The shaded uncertainties represent the lack of knowledge (blue) and noise from the experiment (pink). The response surfaces are obtained for fixed conditions of the optimized condition 31% H_2, 25% CH_4, 4% N_2, 1% O_2, and 39% Ar at 9.2 mbar and 750 W, as indicated by the red and yellow arrows. 29

Figure 3.9: A plasma emission spectrum sample measured during the growth process. Important species in the plasma are indicated in the spectrum. 30

Figure 3.10: (a) The importance of species emission from OES affecting I_D/I_G ratio. The box plots show the median in red between the first and third quartiles. The emission intensities variations of (b) Ar^+ and (c) C_2 with plasma power. (d) The increase of Ar^+ emission intensity with increased gas pressure. 31

Figure 3.11: The effects of oxygen mole fraction on the emission intensities of (a) O and (b) C_2. (c) The variation of CN emission intensity with N_2 mole fraction. 33

Figure 3.12: (a) The emission intensity ratio effects of (a) CH/O, (b) CH/C_2 and (c) H_2/H on the I_D/I_G ratio........ 34

Figure 3.13: The importance of species emission from OES affecting: (a) D-peak position, (b) D-peak FWHM and (c) G-peak FWHM. 35

Figure 3.14: (a) The D-peak position decreases when the intensity ratio of CH/O increases. (b) The effects of the Ar^+/O ratio on the FWHM of the D-peak. (c) The exponential decay of the G-peak FWHM with increased CH/O ratio. 35

Figure 3.15: Proposed deposition mechanism of graphene on copper substrate during the roll-to-roll plasma CVD process. 36

Figure 3.16: (a) The variation of I_D/I_G ratio with web speed. (b) Raman spectra of Case 2 samples at different speeds. (c) Optical transmittance of graphene of Case 2 as a function of web speed, inferring a deposition rate of 7 (±1) layers/min as plotted in the inset. 37

Figure 3.17: SEM images of graphene on copper foil substrate as a function of web speed. 38

Figure 4.1: (a) Schematic of the roll-to-roll plasma CVD system showing the pre-plasma, plasma, and post-plasma regions during graphene growth. The plasma region starts at y = 438 mm (y' = 0 mm). (b) The modeling domain of the Cu foil starts from the top spool and ends at the bottom spool after graphene deposition in the plasma region. The positions of the temperature measurements of Cu foil in the plasma region are also indicated........ 42

Figure 4.2: (a) Emission spectra from the plasma with and without the Cu substrate, showing the broad baseline with the inclusion of Cu substrate. (b) The variations of Cu substrate emission with vertical positions in the plasma region at a fixed plasma power of 1250 W and a web speed of 0 mm/min. (c) The effects of web speed on Cu foil emission from the same region (500 mm) and at constant plasma power (1250 W). (d) The gas and electrodes measurements as a function of plasma power........ 48

Figure 4.3: (a) Cu foil temperature distributions from the analytical and numerical models with and without the radiation term. The effects of (b) h_1 and h_3, and (c) h_2 on the Cu foil temperature profiles from the numerical model. 51

Figure 4.4: The Cu foil temperature distribution from the numerical model compared to the measured Cu foil temperatures in the plasma region at (a) 1250 W and (b) 1050 W at various web speeds. (c) Heat transfer coefficient in the plasma (h_2) as a function of plasma power and web speed. 53

Figure 4.5: (a) A Raman spectrum of graphene at 1250 W and 0 mm/min showing the prominent peaks of graphene. (b) The I_D/I_G peak ratio and (c) The I_{2D}/I_G peak ratio as a function of the web speed at different plasma powers. 55

Figure 4.6: (a) Comparison between Cu foil temperature measurements from the vertical and horizontal configurations at various positions in the plasma region. The conditions are 850 and 1250 W at 0 mm/min. (b) Cu foil temperature at 1050 W and various web speeds for the horizontal setup. (c) The heat transfer coefficient in the plasma region (h_2) as a function of web speed and plasma power for the two configurations.. 57

Figure 4.7: (a) Temperature distribution of the Cu foil at the optimized throughput deposition of graphene at 1450 W and 30 mm/min. (b) The emission spectrum of $Ar/H_2/CH_4$ near the foil region in the middle of the plasma (i.e., y=500 mm) as a function of plasma power............................ 59

Figure 4.8: (a) Raman spectrum of graphene grown at the optimized condition showing a high peak of the 2D peak. (b) SEM image of graphene on Cu presenting a uniform deposition of graphene of the optimized condition.. 60

Figure 5.1: Raman spectra of graphene on Ni foil as a function of web speed at (a) 1050 W and (b) 850 W plasma powers.. 65

Figure 5.2: SEM images of graphene on Ni foil at a fixed plasma power of 850 W and various web speeds of (a) and (b) 0 mm/min, (c) and (d) 50 mm/min, and (e) and (f) 150 mm/min. 66

Figure 5.3: (a) Ni emission spectra at 490 mm as a function of plasma power. (b) The variation of Ni emission as a function of position in the plasma region and web speed at 850 W................. 67

Figure 5.4: (a) Comparison between Ni foil temperature distributions from the model and experimental measurements at 850 W and various web speeds. (b) The heat transfer coefficient in the plasma region (h_2) for Ni foil at different plasma powers and web speeds. The spatial resolution of emission measurements is about 2 mm. 68

Figure 5.5: Comparison between Ni and Cu foil temperature distributions at 1050 W and web speeds of (a) 0 mm/min, (b) 50 mm/min, and (c) 150 mm/min... 69

Figure 5.6: The effects of web speed on β_1 and β_3 for Cu and Ni foils....................................... 71

Figure 5.7: Diffusion length of carbon atoms in Ni foil at a plasma power of 850 W and various web speeds. Optical images of graphene on Ni foil at 0 and 150 mm/min are included to demonstrate the deposition of a thick graphite film at 0 mm/min in contrast to a uniform growth of few-layer graphene at 150 mm/min. The scale bars in these optical images are 20 μm. 72

Figure 5.8: (a) Cooling rates of Ni foil during the R2R process at plasma powers of 850 and 1050 W with 50 and 150 mm/min web speeds. (b) Comparison between the cooling rate from the fin model (web speeds of 50 and 150 mm/min) and the lumped capacitance model for the stationary case (i.e., 0 mm/min) at a fixed plasma power of 850 W. 74

Figure 6.1: The experimental setup showing the capacitively coupled plasma system generated between the two rectangular electrodes. The current and voltage waveforms are measured using Amp and voltage probes, respectively. The optical emission spectroscopy (OES) setup consists of lenses that collect and direct the light to a fiber optic which is connected to the entrance of the spectrometer. The light is finally detected by a CCD camera. 77

Figure 6.2: The current and the voltage waveforms of 95%/5% H_2/N_2 plasma as a function of pressure and set power. (a) and (b) represent the voltage and current traces, respectively, at 9 mbar as a function of set power. (c) and (d) show the voltage and current traces, respectively, at 500 W set power as a function of pressure. 78

Figure 6.3: The emission spectrum of H_2 at 2.25 mm from the left electrode. The Q-branch lines used to determine the rotational temperature are indicated by arrows in the plot of the spectrum. The Boltzmann plot used to determine the rotational temperature is shown as an inset. The plasma condition is 95% H_2/5% N_2 at 9 mbar and 1100 W set power. 79

Figure 6.4: (a) The measured emission spectra of CN and its fit using LIFbase. (b) The residual of the difference the experimental and theoretical spectra of CN divided by the corresponding peak intensity. (c) Comparison between the measured and the synthetic emission spectra of N_2^+. (d) The residual of the difference the experimental and theoretical spectra of N_2^+ divided by the corresponding peak intensity. The plasma condition is 95% H_2/5% N_2 at 9 mbar and 1100 W set power.. 79

Figure 6.5: (a) The rotational temperatures of N_2^+, CN and H_2 as a function of plasma power. The plasma composition is 95%/5% H_2/N_2. These temperatures are measured at a position of 4 cm from the left electrode. (b) Spatial measurements of the rotational temperature at set powers of 500 and 1100 W. 81

Figure 6.6: (a) Spatial emission of the plasma and (b) The root-mean-square (RMS) of the voltage and current as a function of plasma power. The plasma condition is 95% H_2/5% N_2 at 9 mbar.. 81

Figure 6.7: (a) The rotational temperatures of N_2^+, CN and H_2 as a function of pressure. These temperatures are measured at a position of 4 cm from the left electrode. (b) Spatial measurements of the rotational temperature at 4 and 9 mbar. The plasma condition is 95% H_2/5% N_2 at 9 mbar and a set power of 500 W. 82

Figure 6.8: (a) Spatial emission of the plasma as a function of pressure. (b) The root-mean-square (RMS) of the voltage and current as a function of pressure. The plasma condition is 95% H_2/5% N_2 at 9 mbar and a set power of 500 W. 83

Figure 6.9: The variations of spatial plasma emission with (a) N_2 mole fraction, (a) O_2 mole fraction, and (a) CH_4 mole fraction at a set power of 1000 W and 9 mbar. 84

Figure 6.10: (a) The rotational temperatures of N_2^+, CN and H_2 as a function of nitrogen mole fraction at 9 mbar and a set power of 1000 W. Temperatures are measured at a position of 4 cm from the left electrode. (b) The spatial dependence of the rotational temperatures at 97%/3% H_2/N_2 (3%N_2) and 91%/9% H_2/N_2 (3%N_2). 85

Figure 6.11: (a) The rotational temperatures of N_2^+, CN and H_2 as a function of oxygen mole fraction at a set power of 1000 W and 9 mbar. The temperatures are measured at a position of 4 cm from the left electrode. (b) The spatial dependence of the rotational temperatures at 92%/5%/ 3% $H_2/N_2/O_2$ (3% O_2) and 86%/5%/9% $H_2/N_2/O_2$ (9% O_2).. 85

Figure 6.12: The rotational temperatures of N_2^+, CN and H_2 as a function of methane mole fraction. The plasma set power and pressure are kept constant at 1000 W and 9 mbar, respectively. The temperatures are measured at a position of 4 cm from the left electrode. (b) The spatial dependence of the rotational temperatures at 90%/5%/5% $H_2/N_2/CH_4$ (5% CH_4) and 80%/5%/15% $H_2/N_2/CH_4$ (15% CH_4).. 86

Figure 7.1: The experimental setup of the capacitively coupled plasma at 80 kHz. The current and the voltage probes are placed on the ignitor connected to the graphite electrode. Emission of the plasma in the range of 300-800 nm is measured using an iCCD camera. Also, optical emission spectroscopy (OES) is used to detect the emission spectrum between the electrodes................. 92

Figure 7.2: (a) Voltage and (b) current waveforms of Ar plasma measured at 13.8 mbar with plasma set powers of 300 and 900 W... 93

Figure 7.3: (a) The RMS values of voltage and current at 9.5 and 13.8 mbar as a function of plasma set power. (b) The dissipated power in the plasma as a function of measured current at 5.5, 9.5 and 13.8 mbar. (c) The current and voltage characteristics at 5.5, 9.5 and 13.8 mbar. 94

Figure 7.4: Spatial profiles of plasma emission showing the differences between plasma luminosity in alpha and gamma modes at (a) 5.5 mbar, (b) 9.5 mbar and (c) 13.8 mbar as a function of plasma set power. Plasma images from the iCCD camera are shown at 9.5, and 13.8 mbar are shown in the inset of (b) and (c) respectively, at plasma set powers of 300 and 1100 W. The intensity scale for these images is 0 to 25,000 counts. 96

Figure 7.5: (a) Fourier transform coefficients of the voltage waveform at 13.8 mbar and different plasma powers. (b) The time-derivative of the voltage square waveform compared to sinusoidal waveforms at 80 kHz and 720 kHz with identical RMS and offset voltages at 13.8 mbar pressure and 300 W set power.. 96

Figure 7.6: Plasma emission spectra measured near the discharge gap center (around 2.6 cm from the left electrode) at (a) 9.5 mbar and (b) 13.8 mbar as a function of plasma set power.............. 97

Figure 7.7: Spatial emission intensity profiles of (a) Ar at 866.8 nm, (b) Ar^+ at 476.5 nm, (c) C_2 at 516.2 nm and (d) H_β at 486.1 nm.. 98

Figure 7.8: (a) The RMS current and voltage curve at 9.5 and 13.8 mbar as a function of increasing/decreasing plasma set power. (b) The emission intensity at the middle of the discharge at 9.5 and 13.8 mbar as a function of increasing/decreasing plasma set power. 99

Figure 8.1: (a) SEM image of the uniform graphite film on Cu foil. (b) TEM image of the thin graphite film between Cu foil and Pt protective layer. The thickness of the graphite film is about 26 nm. (c) The graphite film remains uniform except for some regions (toward the right of the sample) where large voids are observed between the graphite film and Cu foil. 103

Figure 8.2: (a) Raman and (b) XPS spectra of the deposited carbon film at different plasma conditions of Ar-H_2-CH_4, Ar-H_2-CH_4-N_2, and Ar-H_2-CH_4-N_2-O_2. The plasma set power and gas pressure remain constant at 1250 W and 15 mbar, respectively. 104

Figure 8.3: (a) Optical emission spectra of Ar-H_2-CH_4, Ar-H_2-CH_4-N_2 and Ar-H_2-CH_4-N_2-O_2 plasmas. (b) Comparison between the species emission intensities as a function of plasma compositions at 1250 W and 15 mbar. The emission intensity is normalized by Ar emission line at 703 nm. The inset shows a zoom-in to the spectra near 516 nm which shows strong C_2 band emission from Ar-H_2-CH_4-N_2-O_2 plasma. 105

Figure A.1: Images of the plasma emission at different plasma conditions showing: a) stable alpha plasma at 30% H_2, 20% CH_4, 10% N_2, 10% O_2, 30% Ar, 7 mbar and 800 W, b) unstable alpha plasma at 0% H_2, 20% CH_4, 0% N_2, 10% O_2, 70% Ar, 15 mbar and 850 W, c) stable gamma plasma at 40% H_2, 20% CH_4, 0% N_2, 0% O_2, 40% Ar, 16 mbar and 1250 W, and d) unstable gamma plasma at 0% H_2, 0% CH_4, 10% N_2, 0% O_2, 90% Ar, 14 mbar and 750 W. 136

Figure A.2: (a) Raman spectra of the copper-only background without graphene growth. The average baseline of the copper background signal is subtracted from the Raman spectrum of graphene on copper foil as shown in (b). The condition of graphene growth is 20% H_2, 27% CH_4, 10% N_2, 3% O_2, 40% Ar, 9.3 mbar and 850 W. 137

Figure A.3: Raman spectra of graphene after transfer to a Si/SiO_2 substrate. The condition of graphene growth is similar to Figure A.2: 20% H_2, 27% CH_4, 10% N_2, 3% O_2, 40% Ar, 9.3 mbar and 850 W. 137

Figure A.4: (a) The I_D/I_G ratio of graphene on the left and right sides of the copper foil for experiment numbers 76 and 87. (b) The thermocouple and the pyrometer temperatures of both experiments. The conditions were the same: 31% H_2, 25% CH_4, 4% N_2, 1% O_2, 39% Ar, 9.2 mbar and 750 W. 140

Figure A.5: Optical images of (a) bare copper foil before oxidation test, (b) bare copper foil after oxidation test, (c) and (d) graphene on copper foil after oxidation. The growth condition for graphene on copper foil in (c) and (d) is similar to Case 2 in the main paper (33% H_2, 30% CH_4, 10% N_2, 8% O_2, 19% Ar, 15 mbar, and 1250 W) at web speeds of 45 and 959 mm/min, respectively. The scale bar is 10 μm. 141

Figure A.6: The effects of decreasing plasma length using small and large electrodes with plasma lengths of 5 and 20 cm, respectively. The length of the plasma has minimum influence of graphene quality due to large impact of ion bombardment in the plasma. The conditions for the experiments are: 1) 39% H_2, 20% CH_4, 10% N_2, 7% O_2, and 24% Ar at 10.5 mbar and 750 W, 2) 31% H_2, 25% CH_4, 4% N_2, 1% O_2, and 39% Ar at 9.2 mbar and 750 W, 3) 33% H_2, 30% CH_4, 10% N_2, 8% O_2, and 19% Ar at 15.0 mbar and 1,250 W, 4) 10% H_2, 19% CH_4, 10% N_2, 6% O_2, and 55% Ar at 10.6 mbar and 700 W. 141

Figure A.7: Plasma emission images showing the effect of pressure on the plasma type. The transition occurs near 15.4 mbar. The other plasma conditions are the same: 70% H_2, 25% CH_4, 5% O_2 at 1000 W. The scale of the emission is from 10 to 5,535 counts...................................142

Figure A.8: (a) I_D/I_G ratio of graphene on copper foil as a function of the projected variables, *z*. The line describes the model, while the shaded area shows the uncertainty of the model. (b) The coefficients of the variable *z* which are chosen based on a hierarchical Bayes model assuming Gaussian noise. 143

Figure A.9: The optimized condition (31% H_2, 25% CH_4, 4% N_2, 1% O_2, and 39% Ar at 9.2 mbar and 750 W) produces higher values of CH/O, CH/C_2 and H_2/H. The effects of pressure on (a) CH/C_2, and (b) H_2/H. (c) CH/C_2 decreases linearly with plasma power. The variations of CH/O as a function of (d) O_2 mole fraction and (e) N_2 mole fraction. 144

LIST OF ABBREVIATIONS

1D	One dimensional
2D	Two dimensional
BSE	Backscattering electrons
CARS	Coherent anti-stokes Raman spectroscopy
CCD	Charge-coupled device
CCP	Capacitively coupled plasma
CRDS	Cavity ring down spectroscopy
CVD	Chemical vapor deposition
DC	Direct current
DOE	Design of experiment
FET	Field-effect transistor
FLG	Few-layer graphene
FWHM	Full width at half maximum
GPR	Gaussian process regression
HOPG	Highly-oriented pyrolytic graphite
iCCD	Intensified charge-coupled device
IAF	Information acquisition function
LIF	Laser induced fluorescence
max	Maximum
MLG	Multi-layer graphene
MPCVD	Microwave plasma chemical vapor deposition
MW	Microwave
near-IR	Near-infrared
OES	Optical emission spectroscopy
PECVD	Plasma-enhanced chemical vapor deposition
PEF	Pareto efficient frontier
PET	Polyethylene terephthalate
R2R	Roll-to-roll

RMS	Root mean square
rf	Radio frequency
sccm	Standard cubic centimeters per minute
SE	Secondary electrons emission
SEM	Scanning electron microscopy
SLG	Single layer graphene
TEM	Transmission electron microscopy
XPS	X-ray photoelectron spectroscopy

LIST OF SYMBOLS

α	Alpha mode
α	Thermal diffusivity of the foil, m^2/s
a	Fin model constant
A	Linear offset of the spectrum from Cu or Ni foils
A_c	Cross-sectional area, m^2
A_{ul}	Einstein coefficient for spontaneous emission, s^{-1}
A_s	Surface area, m^2
B	Pre-exponent constant
β	The exponent in the analytical solution of the fin model
c	Speed of light, m/s
C	Constant in the analytical solution of the fin model
C_P	Specific heat, J/kgK
C_s	Sheath capacitance, F
D_T	Carbon diffusivity, m^2/s
D_0	Entropic pre-factor, m^2/s
δ	Substrate thickness, m
Δy	Control volume length, m
E	Emission intensity, a.u.
$\mathbf{E}$	Expectation over the measurement noise
$\vec{E}$	Electrical field, V/m
E_D	Diffusion activation energy, eV
E_u	Upper state energy, eV
ε	Emissivity
F	View factor
g_u	Degeneracy of the upper state
γ	Gamma mode
h	Planck's constant, J.s
h_∞	Convective heat transfer coefficient, W/m^2K

h_{rad}	Radiative heat transfer coefficient, W/m^2K
I	Plasma current, Amp
I_{dis}	Displacement current, Amp
I_{2D}	2D-peak intensity of graphene from Raman spectroscopy, a.u.
I_D	D-peak intensity of graphene from Raman spectroscopy, a.u.
I_G	G-peak intensity of graphene from Raman spectroscopy, a.u.
j	Cell position
J^*	Radiosity from the Cu foil to the surrounding, W/m^2
k	Thermal conductivity, W/mK
k_B	Boltzmann's constant, J/K
L	Length, m
l	Length scale
L_a	Crystalline size, μm
L_D	Diffusion length, μm
λ	Wavelength, nm
m	Fin model constant
M	Lumped capacitance model constant
N_u	Number density in the upper electronic level, m^{-3}
N_o	Population at the ground level, m^{-3}
v_{ul}	Transition frequency, Hz
$\boldsymbol{O_i}$	Experimentally measured I_D/I_G ratio
ω	Frequency, Hz
P	Power, W
p	perimeter, m
Pe	Peclet number
q	Conductive heat transfer rate, W
q_{conv}	Convective heat transfer rate, W
$q_{rad,R}$	Radiation heat transfer rate, W
ρ	Density, kg/m^3
σ	Stefan Boltzmann constant, W/m^2K^4

t	Time, s
T	Temperature, K
T_{surr}	Chamber wall temperature, K
T_e	Electron temperature, eV
T_{vib}	Vibrational temperature, K
T_{rot}	Rotational temperature, K
T_{gas}	Translational temperature, K
T_∞	Ambient gas temperature, K
θ	Transformed temperature, K
U	Web speed, m/s
V	Plasma voltage, V
$\forall$	Volume, m^3
V_o	Plasma voltage amplitude, V
w	Substrate width, m
W	Electrode width, m
w_i	Importance factor
$\mathbf{x}$	Process control parameter
y	Position, m
y'	Transformed position, m
z	Variable that maps the I_D/I_G in the emission mapping analysis
Z	Partition function
Z	Atomic number

ABSTRACT

Author: Alrefae, Majed, A. PhD
Institution: Purdue University
Degree Received: May 2018
Title: Process Characterization and Optimization of Roll-to-Roll Plasma Chemical Vapor Deposition for Graphene Growth
Major Professor: Timothy S. Fisher

Large-scale production of graphene and other nanostructures remains a hindrance to their adoption in the semiconductor and materials manufacturing industries. The main purpose of this thesis is to develop an efficient and scalable technique for depositing graphene on various flexible substrates. Hence, a custom-built roll-to-roll capacitively coupled plasma chemical vapor system for deposition of graphene on flexible substrates is thoroughly described in this work. Graphene quality on Cu foil has been optimized for a roll-to-roll process using statistical optimization methods. Since graphene quality and uniformity depend on plasma input parameters, such as plasma power, gas pressure, and the gas mixture used, effects of input parameters have been explored to maximize graphene quality, as quantified by Raman spectroscopy using the I_D/I_G intensity ratio. Furthermore, *in situ* optical emission spectroscopy (OES) has been developed and utilized to determine the effects of several plasma species on graphene growth and quality. OES results demonstrate that graphene quality on Cu foil increases with CH radical emission; however, O and H atoms, C_2 and CN radicals, and Ar^+ ion all negatively correlate to graphene quality. Results aid in developing a conceptual model for a graphene growth mechanism that indicates the adverse impact of ion bombardment on graphene quality in the low-frequency capacitively coupled plasma. However, the existence of active carbon species in the plasma, such as CH radical, accelerates the growth process and leads to moderate-quality graphene deposition on Cu foil at web speeds reaching as high as 1 m/min.

Nevertheless, graphene quality measured from Raman spectroscopy declines significantly with increased Cu foil velocity (web speed) in the roll-to-roll process, inducing a critical limitation in current production rates for roll-to-roll CVD nonmanufacturing techniques. With the aid of heat transfer modeling of the moving foil, we show that the graphene quality decrease is primarily due to Cu foil temperature decline with increased web speed. The Cu foil temperature distribution is

determined both experimentally and numerically during roll-to-roll graphene growth as a function of web speed, plasma power and plasma length. The maximum Cu foil temperature in the plasma rises with increased plasma power due to increased heating from the plasma. However, the maximum Cu foil temperature decreases with increased web speed caused by higher heat advection by the moving foil. In addition, shortening the plasma slit (by decreasing the electrodes length) cools the Cu foil temperature and diminishes its temperature uniformity in the plasma region. Consequently, graphene crystallization, identified using Raman spectroscopy, improves with higher Cu foil temperatures. As a result, an optimum condition is defined by raising the plasma power, lowering the web speed and increasing the plasma region length, which consistently produces high-quality graphene on Cu foil.

The throughput of graphene production can be increased by utilizing Ni foil as a substrate since carbon solubility in Ni is higher than in Cu. Thus, the effects of web speed and plasma power on Ni foil temperature distribution are evaluated during graphene deposition in the roll-to-roll process. Furthermore, the Ni foil cooling rate, which strongly affects carbon atom segregation from Ni after the growth process, is derived from the heat transfer model. Plasma power has negligible effects on the cooling rate, whereas the web speed has a significant impact on the cooling rate. Consequently, graphene has comparable quality at different plasma powers, whereas web speed controls graphene quality, particularly with regards to uniformity and thickness. Our work highlights the benefits of using Ni foil in a roll-to-roll process for graphene deposition at higher web speeds and lower substrate temperatures, rather than using Cu foil, which requires significantly more substrate heating.

Plasma plays a crucial role in heating the foil for graphene deposition in the roll-to-roll process, without the need of a supplemental heating source. Thus, accurate measurement of the translational gas temperature in the plasma is vital, since gas temperature strongly influences the foil temperature distribution, which, in turn, affects graphene growth kinetics. Optical emission spectroscopy (OES) is used to measure the rotational temperatures of N_2^+ (B-X), CN (B-X) and H_2 ($d^3\Pi_u \rightarrow a^3\Sigma_g^+$), and to determine accurate translational gas temperatures. Power dissipation in the plasma is also measured to understand gas temperature variation for the experimental input conditions. Thus, the effects of plasma power, gas pressure and the addition of nitrogen (N_2), oxygen (O_2) and methane (CH_4) gases on power dissipation and gas temperature in a hydrogen (H_2) plasma are assessed. The rotational temperatures measured from the gas species have different

values due to the non-equilibrium nature of the plasma. Of the gases measured, the rotational temperature of N_2^+ is most accurate in representing the translational gas temperature. These results improve the understanding and control of the thermochemical environment for carbon nanostructure growth in the plasma chemical vapor deposition processes.

Graphene quality significantly depends on gas pressure since our plasma roll-to-roll system is sustained by a capacitively coupled plasma that operates in two modes, depending on the gas pressure and discharge gap. The modes are identified as alpha and gamma modes, and are sustained by volume ionization and secondary electron emission processes, respectively. Up to our knowledge, the presence of both modes at 80 kHz plasma frequency has not previously been reported. Thus, a detailed characterization of argon plasma is attempted to determine the underlying plasma physics of the low-frequency plasma. Due to strong ion bombardment on the electrodes, the gamma mode coexists with the alpha mode, resulting in a hybrid mode. The voltage square waveform is found to play an important role in sustaining this hybrid mode. The hybrid mode exists at low gas pressures of 5.5 and 9.5 mbar in the plasma set power ranges from 300 to 1100 W. However, the plasma at 13.8 mbar gas pressure transforms from hybrid to gamma mode when the plasma set power is beyond 750 W due to increased secondary electron emission processes. The emission spectra measured from optical emission spectroscopy reveal the presence of non-Ar species in the gamma mode, such as H, CH, and C_2. These species are sputtered from the graphite electrodes by ion bombardment to produce secondary electrons that sustain the gamma discharge. Results show the possibility of sustaining the hybrid mode at a low plasma frequency using a tailored waveform.

As a results of these plasma characterization tools, we report a continuous and rapid roll-to-roll deposition of thin graphite film on Cu foil. The composition of the $Ar/H_2/CH_4/N_2/O_2$ plasma plays significant role in the successful direct growth of the thin graphite film on copper foil. Optical emission spectroscopy is used to characterize the plasma during graphite synthesis and show that the addition of N_2 enhances the plasma reactivity, and O_2 was found to increase the deposition rate of the graphite film. The film was characterized by Raman spectroscopy, scanning electron microscopy (SEM), transmission electron microscopy (TEM) and X-ray photoelectron spectroscopy (XPS). The described large-scale graphite production can produce a graphite-Cu-graphite structure or uniform thin graphite films for thermal management applications in electronics devices.

Graphene growth optimization, substrate thermal analysis, and plasma characterizations are used to control graphene mass-production in a custom-built roll-to-roll plasma CVD system. These techniques are addressed to provide a route for nanomanufacturing of graphene and graphite on Cu and Ni foils. These methods aid in understanding the correlations between process conditions and graphene quality, as well as the interactions between the plasma and the substrate, to yield high-throughput production of high-quality graphene. The procedure outlined here can be applied to efficiently scale-up the production of other micro- and nanomaterials.

1. INTRODUCTION

Graphene, which was first isolated unambiguously in 2004, is a 2D nanostructure material made of carbon atoms arranged in a hexagonal lattice [1], [2]. Graphene possesses outstanding properties such as high electrical [3] and thermal [4] conductivities, mechanical strength [5], and absolute gas impermeability [6]. A tremendous numbers of graphene applications have been demonstrated, such as transparent electrodes [7], photodetectors [8], corrosion protection [9], energy storage [10], and biosensors [11], among many others. However, in order to incorporate graphene into commercial and industrial products, graphene production needs to be efficiently expanded [12].

Chemical vapor deposition (CVD) of graphene on metallic substrates, such as Ni and Cu, has emerged as a feasible technique to mass-produce graphene and meet existing and future graphene demand [12]. The CVD method is a single-step process utilizing inexpensive catalytic substrates to decompose the carbon source (mostly methane) and deposit high-quality and large-area graphene, which then can be transferred to an arbitrary substrate, such as PET or Si [13], [14]. Therefore, roll-to-roll CVD processes have been demonstrated for large quantity production of graphene on Cu foil [7], [15]–[17].

The roll-to-roll CVD process needs to deposit high-quality graphene at faster production rates and reduced energy input to be feasible for semiconductor and materials manufacturing industries [18]. In contrast to batch systems where the substrate remains stationary on a substrate holder for a definite amount of deposition time, the synthesis of graphene in roll-to-roll processes is limited by the Cu foil temperature drop at higher web speeds. Therefore, a detailed heat transfer analysis is needed to define the Cu foil temperature distribution as a function of web speed to increase the production rate of graphene on Cu foil. Alternatively, graphene production rate can be improved when using Ni foil as a substrate which has high carbon solubility with superior hydrocarbon decomposition reactivity and a greater lattice match with graphene [19].

Low-temperature plasmas can be utilized as activation sources for large-scale deposition of graphene due to the strong coupling between the plasma and the substrate that eliminates the need for supplemental heating [20]. Hence, the determination of the plasma gas temperature is crucial to control the deposition process and scale-up plasma CVD systems since low-temperature

plasmas exist in non-equilibrium states [21]. In addition, the system inputs, such as plasma power, gas pressure, and gas mixture, affect the plasma properties and eventually graphene growth. Due to the complexity of plasma sources, previous graphene synthesis studies considered the plasma as a "black-box" with more focus on the deposited film characterizations. Nevertheless, the understanding of plasma properties and their interactions with the gas mixture and the substrate increase the potential applications of plasma sources for graphene and other nanostructure mass production in similar ways to the semiconductor industry that depends heavily on plasma etching and deposition systems.

The purpose of the dissertation is to scale up graphene production by characterizing and optimizing a custom-built roll-to-roll plasma chemical vapor deposition system. A literature review about graphene properties, its growth in plasma CVD, plasma diagnostics, and current roll-to-roll processes are covered in Chapter 2. Graphene properties are first reviewed, as motivations behind the need of graphene large-scale production are a direct result of the usefulness of graphene due to its properties. Then, a thorough description of the graphene growth mechanism in plasma CVD is presented, followed by a review of recent optical diagnostics to show their feasibility for understanding and controlling graphene synthesis in plasma CVD systems. Finally, the current roll-to-roll CVD processes for graphene growth are summarized.

Chapter 3 demonstrates the results of optimizing graphene deposition on Cu foil in the roll-to-roll process. Applying a multi-objective optimization statistical technique, the quality of graphene grown on both sides of the Cu foil is improved within various plasma input parameters. *In situ* optical emission spectroscopy (OES) is applied during the optimization process to define plasma species that affect graphene growth and quality, and to develop a conceptual model for graphene growth mechanism in our system.

In Chapter 4, a 1D heat transfer model is derived to determine the Cu foil temperature distribution during graphene growth in the roll-to-roll process. The model is validated with *in situ* temperature measurements from the Cu foil's near-infrared emission, as detected by a broadband spectrometer. Graphene quality, measured by Raman spectroscopy, is correlated to Cu foil temperatures produced by different process conditions to reach optimum graphene quality at a higher web speed.

Next, in Chapter 5, the role of heat transfer in graphene deposition on Ni foil is studied using the heat transfer model derived in Chapter 4. Ni foil is examined with the intent to scale up

graphene deposition on substrates with high carbon solubility beyond Cu. The modeled Ni temperature distribution is also validated with *in situ* temperature measurements from the near-infrared emission of Ni foil during graphene growth.

Chapter 6 presents the gas temperature measurements of H_2 plasma to thermally characterize the plasma at experimental conditions used for graphene growth in Chapter 3. The temperature distribution from the rotational temperatures of N_2^+, CN and H_2 were measured using optical emission spectroscopy. Furthermore, the power supplied to the plasma was measured, showing that less than 50% of the set plasma power is dissipated in the plasma.

The existence of a hybrid alpha and gamma mode in the roll-to-roll plasma system is reported in Chapter 7. Electrical and spectroscopic measurements are carried out at different gas pressures and plasma set powers to map the operation conditions for each mode. Plasma characterizations aid in understanding the plasma physics needed to control graphene mass production in roll-to-roll plasma CVD systems.

Chapter 8 shows the successful deposition of a thin graphite film on Cu foil in a roll-to-roll process. The deposited graphite film on Cu foil, which has high potential as a heat spreader interfacial material, is characterized by Raman spectroscopy, SEM, TEM, and XPS to determine the film's quality, uniformity, composition, and thickness. In addition, the effects of the plasma gas mixture are studied to understand the control the synthesis of thin graphite on Cu foil than can be adopted for efficient thermal management in electronic devices.

Chapter 9 summarizes the findings from this dissertation and proposes future research work to scale up the production of graphene and other nanostructures.

2. LITERATURE REVIEW

Chapter 2 originates mainly from the preprint of a book chapter "Plasma Chemical and Physical Vapour Deposition Methods and Diagnostics for 2D Materials," published in 2D Inorganic Materials beyond Graphene, R. CNR and W. UV, Eds. 2017, pp. 275–315. doi.org/10.1142/9781786342706_0007, © copyright World Scientific Publishing Company, https://www.worldscientific.com/worldscibooks/10.1142/q0078#t=toc, which is reused with permission [22]. Copyright @ 2017 World Scientific Publishing Company.
[22] M. A. Alrefae, N. R. Glavin, A. A. Voevodin, and T. S. Fisher, "Plasma Chemical and Physical Vapour Deposition Methods and Diagnostics for 2D Materials," in 2D Inorganic Materials beyond Graphene, R. CNR and W. UV, Eds. 2017, pp. 275–315.

Section 2.4 originates mainly from the published manuscript [23] which is reused with permission form AIP Advances, Vol. #7, Article ID #11, (2017); used in accordance with the Creative Commons Attribution (CC BY) license.
[23] M. A. Alrefae, A. Kumar, P. Pandita, A. Candadai, I. Bilionis, and T. S. Fisher, "Process optimization of graphene growth in a roll-to-roll plasma CVD system," *AIP Adv.*, vol. 7, no. 11, p. 115102, Nov. 2017.

2.1 Graphene Properties and Production

Graphene consists of a single layer of carbon atoms arranged in a hexagonal lattice structure. Thus, graphene is considered to be the main structure of other carbon nanostructures such as fullerenes, carbon nanotubes, graphene nanoperals, and graphite [24]. Free-standing graphene was studied theoretically in 1947 [25], and was successfully isolated experimentally in 2004 [1], [26], triggering tremendous research in most science and technology disciplines. Graphene layers can be formed in single-layer, bi-layer, and few-layer (3-9 layers) while ten layers or more of graphene turn into a thin graphite film [24]. Single-layer graphene has a zero bandgap, but the electronic structure becomes more complicated with increasing graphene layers, due to the overlap of conduction and valence band [26].

Graphene's unique combination of mechanical and electrical properties makes it useful for a variety of applications. Because there is a significant ambipolar electric field in graphene, the charge can be altered between holes and electrons with concentrations up to 10^{13} cm^{-2}, leading to a strong mobility of $2.5x10^5$ cm^2/Vs at 300 K [3], [26]. Furthermore, graphene shows excellent electrical properties, including quantum Hall effect with massless electrons acting as Dirac fermions with a Fermi velocity of 10^6 m/s [24], and its dispersion relation has a linear correlation

at the first Brillouin zone corners [27]. Also, graphene has excellent properties, with intrinsic strength of 130 GPa and Young's modulas of 1 TPa [3], thermal conductivity of 3000 W/mK [28] with large gas impermeability [6], and high optical transparency with light absorption of only 2.3% [29]. Because of these exceptional properties, graphene is an exceptional material with demonstrated applications that are expected to disrupt major industries and that promise to advance solutions for current and future challenges, as reviewed extensively in Refs. [12], [30], [31].

The exceptional properties of graphene and potential applications have motivated research groups to develop a number of methods to produce graphene. The initial small-scale method was mechanical exfoliation from highly-oriented pyrolytic graphite (HOPG), by Novoselov et al. [1]. Even though the quality of graphene using mechanical exfoliation is high, large scale production is extremely limited due to the production of small flakes of less than 1000 μm^2 [13]. Hence, several large-scale methods have been developed to scale up graphene production. The first large-scale method is liquid exfoliation of graphene from graphite or graphite oxide, which are placed in solvent to promote surface tension and to produce graphene platelets, albeit with some structural defects at lower yield and high energy cost [32], [33]. The second large-scale method is graphene growth on silicon carbide (SiC) at high temperatures of around 1473 K to allow Si to sublimate the surface and produce a few layers of graphene [34]. However, graphene growth on SiC is limited due to the high-temperature requirement combined with the high-cost of the SiC substrates and smaller domain sizes of produced graphene [12].

The third, and most feasible, large-scale method of mass-producing graphene is chemical vapor deposition (CVD) on metallic substrates, such as Cu and Ni [7], [13], [35], [36]. Large-area and high-quality graphene can be deposited on a given substrate, which is typically heated to approximately 1173-1273 K in vacuum tube furnaces within a mixture of CH_4 and H_2 gases. Graphene samples can then be directly transferred to arbitrary substrates by etching the metallic substrate [13], [14]. Thermal CVD methods have been reviewed extensively and more information can be found in references [37]–[40]. Alternatively, plasma CVD can be used to deposit graphene with faster growth times and lower energy input, although with moderate rarther than high quality results [20], [41]. The next sections review the deposition process of graphene in plasma CVD.

2.2 Synthesis of Graphene by Plasma CVD

Plasma CVD can lead to mass production of high quality graphene that can require lower substrate temperatures compared to thermal CVD. Furthermore, the deposition time in plasma CVD decreases sharply to a few minutes (or even seconds) for single or few-layer graphene growth. Table 2.1 provides a summary of plasma CVD systems and deposition parameters that have been used to grow single-layer, few-layer and many-layer graphene (SLG, FLG and MLG, respectively) as well as graphene nanopetals. Different plasma sources have been used to generate the energy required to decompose the feed gas into different radicals. These include direct current (DC), radio frequency (rf) (common frequency of 13.56 MHz) and microwave (MW) (common frequency of 2.45 GHz) plasmas. Further details of common plasma sources used for materials deposition can be found in [42], [43] and [44]. These plasma sources used for material deposition have typical ionization fractions of order 10^{-7} - 10^{-4} and electron number densities of 10^{9} - 10^{11} cm^{-3} [45]. These non-equilibrium plasmas operate at low gas temperatures and over a range of pressures from 0.01 to 100 Torr.

Table 2.1: Overview of the plasma CVD systems used to grow graphene. SLG: single-layer graphene, FLG: few-layer graphene, MLG: multilayer graphene, petals: graphene nanopetals, DC: direct current plasma, r-rf: remote radio frequency plasma, rf: radio frequency plasma, MW: microwave plasma, CH_4: methane, C_2H_2: acetylene, H_2: hydrogen, Ar: argon, O_2: oxygen Cu: copper, Ni: nickel, Si: silicon, SiO_2: silicon dioxide, Co: cobalt, Gr: graphite anode, Al: aluminum, "oil": oil extracted from a tea tree.

Layer	Plasma	Power (W)	Pressure (Torr)	Gases	Substrate	Substrate Temperature (˚C)	Deposition Time (min)	Ref.
SLG	rf	10 - 200	0.01	CH_4- H_2 -Ar	Cu	700 - 830	0.2 - 4	[46]
SLG	r-rf	80	0.05 - 0.3	CH_4 - H_2 (or C_2H_4 - H_2)	Sapphire, SiO_2	400 - 700	20 - 80	[47]
SLG	MW	1400	20	CH_4 - H_2	Ni	450 - 750	1	[41]
SLG	MW	1000	15 - 60	CH_4 - H_2	Cu	No heating	10	[48]
SLG	MW	10-40	0.5	CH_4-H_2 - N_2	Cu	No heating	5 - 20	[49]
SLG - FLG	DC	170	1.5	CH_4 and H_2	Ni	450	1 - 12	[50]
SLG - FLG	rf	200	7.5	CH_4 - H_2 - Ar	Ni	650	0.5	[51]
SLG - FLG	rf	50-600	1	CH_4 - H_2 - Ar	Cu	950	0.1 - 60	[52]
SLG - FLG	rf	100-300	0.01-0.02	CH_4 - H_2	Cu	500 – 950	5	[53]
FLG	DC	-	80	CH_4 - H_2	Si, Ni	950	5 - 10	[54]
FLG	DC	500 - 800	1	C_2H_2 - H_2	Ni Glass	1000 450	10 – 20 6 and 12	[55] [56]
FLG	r-rf	100	0.2	CH_4	many substrates	550	120 - 240	[57]

Table 2.1: Continued.

FLG	rf	200	1.65	CH_4 - H_2 - Ar	Co	800	0.25 - 20	[58]
FLG	rf	0-600	1	CH_4 - H_2 - Ar	Si, Sapphire	700 - 1000	1	[59]
FLG	rf	100	0.3	CH_4 - Ar	Ni	475	1.7 - 10	[60]
FLG	MW	1,600 - 4,500	0.03 0.23	CH_4 - H_2 – Ar	Cu, Al	No heating	0.5 – 3 1.7	[61] [62]
FLG	MW	400	10	CH_4 - H_2	Cu	No heating	0.5 - 2	[20]
FLG-MLG	rf	50-150	0.01-0.05	CH_4 - H_2 - Ar	Ni	200 - 800	0.2 - 120	[63]
FLG-MLG	r-rf	550	0.3	CH_4 - Ar	quartz, Cu	650	5 - 15	[64]
MLG	rf	150-250	0.38-0.75	CH_4 - Ar	Si	300 - 380	60 - 240	[65]
Petals	DC	-	10 - 200	H_2	Gr anode	No heating	2 - 3	[66]
Petals	DC	-	3.75	C_2H_2	Cu, Si	750	4	[67]
Petals	DC	400 - 600	60 - 150	CH_4 - H_2	Si	No heating	25	[68]
Petals	rf	100-500 900	0.1	CH_4 (or C_2F_6, CF_4) - H_2	many substrates	500 600 – 900	10 – 4800 5 - 40	[69] [70]
Petals	rf	900	0.001 - 760	CH_4 - H_2	Si Cu, Si	600 – 1100 750	20	[71] [72]
Petals	rf	1000	0.02	C_2H_2 - H_2	Ni	620 – 850	10	[73]
Petals	rf	500	0.15	H_2 –"oil"	Si	800	1 - 4	[74]
Petals	rf	900	1	CH_4 - H_2	Cu, Si	680	20 and 60	[75]
Petals	MW	500	1	CH_4 - H_2	Si, sapphire	650	5 and 10	[76]
Petals	MW	2,000	40	CH_4 - H_2	many substrates	No heating	0.02 – 50 0.2 - 1.3	[77] [78]
Petals	MW	700 - 1000	30 30-40	CH_4 - O2 - H_2 CH_4 - H_2	graphite fibers	No heating 900	30 15	[79] [80]
Petals	MW	300 - 700	30	CH_4 - H_2	SiO_2 Carbon cloth	No heating	0.5 – 30 25	[81] [10]

Energetic electrons in the plasma are able to provide collisional dissociation of the feed gases, which are methane and hydrogen in most cases. For example, the products of electron impact reactions of CH_4 (Reactions R1, R2 and R3 below) can enhance the kinetics of the gas phase and the generations of CH_3, CH, C_2 radicals, H atom and different ions [82]. These active radicals and ions, among others, reach the substrate surface with high energy, diffuse and provide active nucleation sites for graphene deposition [58], [68]. The area of plasma modeling, its kinetics and correlation to films deposition is an active research to understand and optimize growth processes [83] [84] [85].

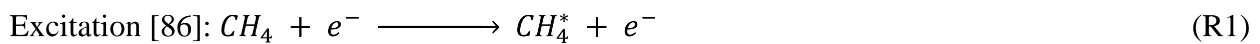

Excitation [86]: $CH_4 + e^- \longrightarrow CH_4^* + e^-$ (R1)

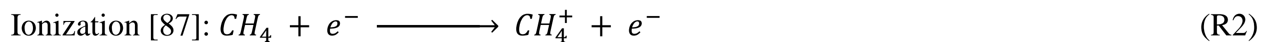

Ionization [87]: $CH_4 + e^- \longrightarrow CH_4^+ + e^-$ (R2)

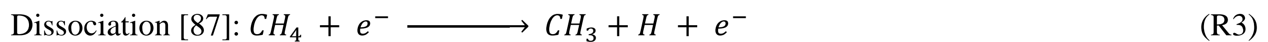

Dissociation [87]: $CH_4 + e^- \longrightarrow CH_3 + H + e^-$ (R3)

Denysenko et al. [85] reported the simulated fluxes of ions and radicals in inductively coupled $Ar/CH_4/H_2$ plasmas for carbon nanostructure deposition [85]. The plasma frequency was 0.46 MHz with power and pressure ranges of 1.8 - 3 kW and 20 - 70 mTorr, respectively. The deposited fluxes were defined as the number of radicals and ions deposited on the surface per area per time, represented by the product of the number density, the velocity and either the sticking coefficient factor for radicals or the ratio between the densities at the wall to the bulk for ions. The deposited flux densities of H, CH, CH_2 and CH_3 radicals at a plasma power near 2 kW were found to be about $2x10^{15}$, $2x10^{14}$, $2x10^{13}$ and $1.5x10^{13}$ cm^{-2} sec^{-1}, respectively. However, the deposited ion fluxes at the same power were higher, with values of approximately $1x10^{17}$, $8x10^{15}$, $5x10^{14}$, $2x10^{14}$, $2x10^{14}$ cm^{-2} sec^{-1} for Ar^+, H^+, H_2^+, CH_3^+ and CH_4^+, respectively. These results suggest that ions have more influence on the film depositions than neutral species. Furthermore, CH has higher deposition flux than other hydrocarbon radicals, and H (including H^+) has the highest flux among radicals (and ions). The control of these fluxes by optimizing the plasma power and the flow rates of CH_4 and Ar can lead to higher quality of 2D films with lower defects and higher deposition rates.

The process parameters for graphene growth by plasma CVD affect the quality and structure of the deposited films [46], [68]. As the plasma power increases, more carbon and hydrogen radicals are produced, directly influencing the quality of the films [68]. More ions with high energy are available to damage the films or create defects [48], [49]. Depending on the plasma source and conditions, the power generally varies from 50 to 5000 W, as presented in Table 2.1. However, most plasma discharges used for graphene (and other materials) occur at low pressures to satisfy the breakdown condition, which depends on the product of pressure and the distance between the electrode known as Paschen's law [88]. This low pressure has the effect of decreasing the density of the plasma, while increasing the kinetic energy of arriving ions, which affects growth rate, morphology and structure of the graphene films [44]. Less dense and higher energy radicals in low-pressure plasmas produce longer surface diffusion times before carbon atoms are locked in the structure, and this process helps to provide a more ordered structure but requires longer deposition times [49].

One recent development in plasma CVD involves atmospheric pressure systems to reduce the use of high-vacuum mechanical equipment and to increase the growth rate by a higher concentration of the carbon-source feed gas [89]. The most common carbon source feed gas used

in graphene synthesis is CH_4, but other gases such as C_2H_2, C_2H_4, C_2F_6 and CF_4 may be used, as shown in Table 2.1. These are typically used in low concentrations while H_2 or Ar are added as bath gases to increase the pressure of the system. Furthermore, H_2 is commonly used due to its etching role as well as to enhance hydrocarbon gas-phase reactions [39].

The growth of graphene by plasma CVD occurs at lower substrate temperatures compared to thermal CVD, and hence a wider range of substrate materials can be used. These substrates range from metals and glasses to carbon fiber. The substrates can be supplementally heated to higher temperatures to enhance surface reactions and diffusion processes, or their heating may solely come from the plasma. For example, it was reported that thin foils of copper and nickel introduced at room temperature to a MW plasma CVD reactor are heated to 700-900°C in a few seconds [20]. Thus, the deposition time in plasma CVD processes may lead to a non-linear growth rate and influence the resulting film structure and morphology.

Unlike thermal CVD in which self-limiting graphene growth has been reported [13], [38], the time of deposition in plasma CVD determines the number of layers (or thickness) of graphene films and their morphology [90]. The self-limiting growth mechanism of graphene in thermal CVD processes is due to the highly inert surface of the well-ordered hexagonal structure, preventing nucleation of the subsequent layers. In plasma CVD growth, the surface of graphene has multiple grain boundary and point defects from the higher initial nucleation density and ion bombardment, which promote new nucleation sites on otherwise inert surface. For films with reduced surface energy and hence wettability to the surface, a Volmer-Weber growth mechanism [91], [92] leads to film branching and bending away from the initial substrate surface. Thus, the graphene film thickness in plasma CVD processes continues to increase until the few-layer graphene sheets curl to form vertical graphene or graphene nanopetals.

2.2.1 Growth of Single-layer Graphene by Plasma CVD

The growth of a single-layer graphene with relatively few defects on a copper substrate has been demonstrated using microwave plasma [48] [49]. The process begins with H_2 plasma and a small concentration of cyano radicals, methane and nitrogen to etch the copper oxide and smooth the substrate surface. Nucleation and growth of graphene occurs on both the top and the bottom sides of the Cu foil. Single-layer graphene grows on the bottom surface only, whereas the top side of the copper substrate was directly exposed to plasma and thus has more defects. However, the

plasma environment is important to etch copper oxide and the amorphous carbon and to supply the active radicals for graphene deposition. Also, results from Raman spectroscopy showed a decrease of defects with time due to merging graphene domains to form a single layer. In this recent study, the measured electron mobility at 300 K was as high as $6.0x10^4$ $cm^2V^{-1}s^{-1}$, compared to $3x10^4$ $cm^2V^{-1}s^{-1}$ for graphene grown using thermal CVD from [93].

Kim et al. [46] used CH_4/Ar and H_2/CH_4 mixtures in an inductively coupled rf plasma to grow single-layer graphene on copper foil. With the absence of H_2 in the feed gas, the plasma was used to decompose CH_4 to create radicals such as H_2 and H atom. With increasing power, more hydrogen is produced from methane, resulting in increased grain size due to the higher H density. As H increased with power from 10 to 50 W, the grain size increased and the nucleation density decreased due to the active role of H as a catalyst for graphene deposition. However, when power increased above 50 W, more H was produced causing an apparent saturation effect and providing more etching. Thus, a competition exists between deposition and etching of graphene due to the roles of H in graphene deposition. For instance, the reaction of H with carbon radicals (CH_x) to produce H_2 and more active radicals such as CH_{x-1}, e.g., $(CH_x + H \to CH_{x-1} + H_2)$, enhances the deposition process. As the amount of H increases at higher power, etching by H results in decreased graphene grain size through the reaction: $H + graphene \to CH_x + (graphene - C)$. On the other hand, no variation in grain size and nucleation density was observed for H_2/CH_4 plasma due to the presence of hydrogen in the feed gas. Finally, the measured electron mobility was 3200 $cm^2V^{-1}s^{-1}$ at 300 K with a carrier density of $1x10^{12}$ cm^{-2}.

The effect of hydrogen on the grain size of single-layer graphene was investigated by Vlassiouk et al. [39] in a thermal CVD process. They found that the grain size increases with the H_2 (a surrogate of H) up to a critical pressure of H_2, after which the grain size decreases. The shape of the grains become more regular with increased H_2 and reaches a hexagonal structure at high H_2 pressure that eliminates further increases in grain size.

Microwave plasma was used to grow a high quality single layer graphene on nickel foil by setting H_2:CH_4 ratio to 80:1 [41]. They found that the defects of the graphene increases with decreasing the substrate temperature. This affects the graphene sheet resistance which has the lowest value of 590 Ω/□ for a graphene grown using a substrate temperature of 750 ^oC.

Wei et al. [47] used remote rf H_2 plasma to grow single layer graphene on dielectric substrates (sapphire and SiO_2) and found mobility of the fabricated field-effect transistors (FETs)

in the range of 550 to 1600 $cm^2V^{-1}s^{-1}$. This study demonstrated the use of plasma CVD (with CH_4 or C_2H_4 as a carbon source) to grow high-quality, single-layer, micrometer-scale graphene crystals for direct integration into electronic devices without the need for graphene transfer.

With plasma CVD, the growth of single-layer graphene requires lower time depending on the operation conditions [46], [53]. As time increases, more graphene layers are deposited due the presence of active radicals such as CH, C_2, and CH_3. Also, as the CH_4 concentration increases, more carbon radicals exist, resulting in more layers of graphene [94]. Terasawa and Saiki [53] observed that the number of layers of graphene is higher at lower substrate temperature. For example, they were able to grow single-layer graphene at 900 ^oC but few graphene layers were synthesized at 500 ^oC. Furthermore, as the thickness of the graphene increases or as the CH radical emission intensity increases, the Raman I_D/I_G ratio increases, indicative of a decrease in grain size. At lower substrate temperature, the carbon radicals in the plasma (C_2 in this case) start depositing on the Cu substrate to form graphene with small grains. Copper has been shown to decompose hydrocarbons to yield C atoms that can penetrate into the copper and then precipitate to form single-layer graphene, as in the case in thermal CVD [38]. Once the substrate temperature is increased to about 900 ^oC, carbon radicals reach the catalytically active copper surface to grow single-layer graphene with larger grain size. For longer deposition time, a second layer of graphene is deposited due to the presence of active radicals such as C_2. Thus, the rate of this deposition is much faster than thermal CVD, which depends solely on the Cu to catalyze the deposition. The grain size typically decreases with the successive graphene layers until reaching about 10 nm depending on the concentrations of C_2 and CH [38].

2.2.2 Growth of Few- and Many-layer Graphene by Plasma CVD

The few-layer graphene growth mechanism on nickel substrates using plasma CVD is explained in [54],[60]. Carbon radicals originating in the plasma reach the Ni surface where the C atoms dissolve to form NiC, if the temperature of the substrate is higher than about 475 ^oC. This low substrate temperature is enabled in the plasma due to the existence of rich density of carbon radicals. During cooling, the dissolved carbon atoms desorb and precipitate on the Ni surface. Therefore, unlike copper, there is no catalyst effect for graphene growth on Ni substrates as for both Ni and Cu substrates with thermal CVD. However, for substrate temperature less than 450 ^oC, the solubility of carbon on nickel decreases to 0%; consequently, Cheng et al. [63] proposed

another growth mechanism for this case where nucleation and growth of carbon radicals occurs at defects with no influence of dissolution in the Ni substrate.

The number of graphene layers increases with deposition time [46], [53], [20] and methane concentration in the feed gas [94], [20] and depends on the plasma power [46] as well as the substrate temperature [53], [59]. Furthermore, the substrate material plays a major role in determining the growth time of graphene as well as its crystal size [57]. This may be related to the rate of adsorption of carbon radicals from the plasma based on substrate roughness and lattice orientation [57].

2.2.3 Growth of Graphene Nanopetals by Plasma CVD

Graphene nanopetals were first produced in a hydrogen arc discharge [66] and then microwave plasma [76] CVD during the synthesis of carbon nanotubes. The direction of these nanopetals is predominantly vertical on substrates (thus the pseudonym 'vertical graphene', VG) due to the presence of a vertical electric field. A recent review by Bo et al. [44] summarizes the synthesis of nanopetals by plasma CVD in which the effects of plasma sources, feedstock gas, temperature, pressure and substrates are discussed. The growth of graphene nanopetals requires no catalyst and starts with a base of graphene layers that grow parallel to the substrate [71], [95]. Due to the weak interaction between the graphene mono-layers and the forces at the grain boundaries which increase with time, the edges of the top layers are curled upward. These localized vertical edges act as electrical field concentrators, attracting carbon radicals to further increase the height of the nanopetals rather than their width [69]. Such localized electrical field concentration, $\vec{E}$, and its impact on the nanostructure growth is an important characteristic of plasma assisted deposition and was reviewed recently for carbon nanotube and 2D material growth [82]. In the addition to the electrical filed effect, the presence of atomic hydrogen provides an important role to etch amorphous carbon and to prevent the nucleation and secondary growth on the growing protrusion to yield thin nanopetals. Moreover, the height of these nanopetals increases with time, while the thickness remain relatively constant with time [69].

2.3 Optical Emission Spectroscopy (OES)

Different diagnostics techniques have been used to monitor plasma characteristics and their correlation to film growth. Optical emission spectroscopy (OES) can access the upper states of

atoms/molecules and measure their relative intensities and temperatures. OES does not require light sources such as lasers and thus simplify experimental setup. On the other hand, laser absorption techniques can be used to measure the ground state populations of species and molecules. More sophisticated techniques, such as CARS (Coherent Anti-Stokes Raman Spectroscopy) are powerful in accurately measuring species temperatures and concentrations [96], [97]. Other plasma diagnostics technique such as Langmuir probe [98], mass spectroscopy [46], [99], and Laser Induced Fluorescence (LIF) [100] also provide useful insights of the plasma and its effects on the grown films.

Optical emission Spectroscopy (OES) has been recognized as a simple technique to characterize plasma systems [101], [102], [103] and is commonly used to characterize plasma systems for nanomaterials growth. OES is a sensitive and a nonintrusive technique to infer gas temperatures and relative densities of emitting species in plasmas. Plasmas typically have plenty of molecules in electronically excited states that emit photons at different wavelengths. The emission intensity can be expressed as:

$$E = N_u A_{ul} h v_{ul} \tag{1}$$

where E is the intensity of the emission intensity corresponding to a transition from an upper energy level (u) to a lower energy level (l), N_u is the number density in the upper level, A_{ul} is the Einstein coefficient for spontaneous emission, h the Planck's constant, and v_{ul} is the frequency of the transition. The population N_u can be expressed assuming Boltzmann distribution:

$$N_u = N_o \frac{g_u}{Z} \exp\left[-\frac{E_u}{k_B T}\right] \tag{2}$$

where N_o is the population at the ground level, g_u is the degeneracy of the upper state, Z is the partition function, E_u is the energy of the upper state, k_B is Boltzmann's constant, and T is the temperature. Knowledge of the molecule spectroscopic model aids in determining the temperature and the relative densities from the emission spectrum [104].

2.3.1 Temperature Measurements using OES

The system temperatures (rotational, vibrational and excitation, or 'electronic') can be found either by fitting the above equation to the measured intensity or using the Boltzmann plot of the specified transitions. For non-equilibrium plasma, the electron temperature is higher than the translational (gas) temperature, and in general the following inequality holds: $T_e \geq T_{vib} \geq$

$T_{rot} \geq T_{gas}$. OES can be used to access all of these modes to estimate, using simple experimental setup, the temperature of each level [102], [105], [106], [107]. In general, a Boltzmann plot is used to determine the corresponding temperature. Alternatively, fitting the measured spectrum allows the estimation of the rotational and/or vibrational temperatures.

A recent review by Brüggeman et al. [21] surveyed different methods of finding gas temperatures from rotational lines of non-equilibrium plasmas using OES. The measured rotational temperature can be used to represent the translational (gas) temperature if both translation and rotational levels are in thermal equilibrium. In such cases, the rotational energy transfer must be fast so that the rotational level becomes thermally distributed. In most cases of plasmas for CVD processes, the production mechanisms of the excited states are dominant by the electron excitation. Consequently, the rotational distribution of the excited state is a projection of that of the ground state, and their temperatures are related. The gas temperature can be determined from the rotational temperature from several species, such as N_2, OH, N_2^+, H_2, O_2, CN, C_2 and CH. Table 2.2 lists the species that have been used to measure the gas temperature in non-equilibrium plasmas that have similar behavior as in the plasma CVD systems.

Table 2.2: Commonly used species with their transitions to measure rotational temperature in plasma systems.

Species	Transition	Wavelength (nm)	Method	Ref.
N_2	C-B (2nd positive system)	360 - 382	Spectrum Fit	[108] - [109] - [110]
N_2^+	B-X (1st negative system)	380 - 395	Spectrum Fit	[110]
H_2	$d^3\Pi - a^3\Sigma$ (Fulcher α band)	590 – 620	Boltzmann plot Spectrum Fit	[109] - [111]
C_2	$d^3\Pi_g - a^3\Pi_u$	510 – 520 520 – 570	Spectrum Fit Boltzmann plot	[112] - [113]
CN	$B - a$	382 – 389	Spectrum Fit	[112]
CH	$A\,^2\Delta - X\,^2\Pi$	420 – 440	Spectrum Fit	[114] - [115]
OH	A-X	306 - 314	Spectrum Fit	[108] - [110] - [116]
O_2	B - X	758–772	Spectrum Fit	[116]
NO	A-X	240 - 248	Spectrum Fit	[108]

2.3.2 OES as an *in situ* Growth Characterization Tool

The emission intensities of H, CH and C_2 from OES, in a $CH_4/H_2/Ar$ plasma for diamond growth in a microwave plasma CVD reactor was compared to the results from cavity ring down spectroscopy (CRDS) [117]. Using a scaling factor, the results from OES showed similar trends as a function of input parameters when compared to CRDS. Hence, OES is commonly used as an

in-situ diagnostic tool to correlate the quality of deposited films during plasma CVD. The growth of diamond has been extensively studied using OES in microwave plasma assisted CVD systems [118], [119], [120], [121], [122], [123], [124]. It has also been used to characterize the growth of graphene nanopetals in plasma CVD systems [125], [126], [127], [128], [129] and [89]. For example, Ma et al. [130] applied OES to characterize graphene growth as a function of plasma parameters (power, flow rates of C_2H_2 and H_2) with Cu substrates. C_2 and H emission intensities were used as signatures for the quality of graphene growth through correlation to sheet resistance and the I_D/I_G ratio from Raman scattering spectroscopy, respectively. Similarly, the emission intensity of CH was correlated with I_D/I_G during the growth of graphene on Cu foil [53]. This linear relationship between CH and I_D/I_G confirms the decrease in the grain size for multilayer graphene with increasing CH radical concentration.

2.4 Roll-to-Roll CVD Processes for Large Production of Graphene

A roll-to-roll manufacturing technique (R2R) is commonly implemented to process various flexible substrates [131]. The R2R technique has several advantages over other batch production methods, such as higher production rate, higher efficiency with lower cost. Thus, the R2R has been successfully applied for micro- and nanometer-scale manufacturing of solar cells [132], [133], thin organic films [134], plastic optical films [135], lithography on plastics [136] among others. However, high throughput is the bottleneck for integrating these R2R processes into existing or future manufacturing facilities, especially for products at nanoscale sizes [131].

Implementing a roll-to-roll approach in CVD systems is a feasible method for mass production of graphene. Table 2.3 summarizes the available roll-to-roll CVD processes that have been used to grow graphene on Cu foil. Bae et al. [7] was the first to report the production of high-quality graphene on Cu substrate using a larger furnace with 8” inner diameter. A roll-to-roll transfer process to a PET substrate was implemented with a feed rate of 200 mm/min. The transferred graphene was used as a transparent electrode with optical transmittance of 97%, and sheet resistance of 150 Ω/□. Similarly, Vlassiouk et al. [137] grew graphene on a large-area Cu substrate with a stationary atmospheric pressure CVD setup.

The above two studies used a static configuration for graphene growth and then applied a roll-to-roll transfer process. However, Hesjedal [15] developed a roll-to-roll atmospheric pressure

CVD setup to grow graphene with a speed of 10-400 mm/min. The heating and cooling rates, which were identical, had no effect on the growth quality, since the solubility of carbon atoms in copper is small [13]. In order to produce high quality graphene, H_2 and Ar were supplied from the main inlet, with CH_4 being introduced through a diffuser at the middle of the furnace.

Another study by Polsen et al. [16] reported the development of a roll-to-roll concentric tube furnace to grow graphene on a copper substrate with a speed variation range of 25-500 mm/min. Two sequential zones were utilized to control the annealing and growth processes separately. The copper foil was wrapped around the smaller tube, while H_2 and He flowed into the annular region between the two tubes to heat the substrate before the growth process. A separate flow containing C_2H_4 flowed through the inner tube and entered the annular region through holes, at which point it mixed with H_2 and He. Ultimately, the quality of graphene (measured by I_G/I_D ratio from Raman spectroscopy) decreased with increased speed because of the shorter residence time for the Cu foil in the furnace.

Table 2.3: Summary of available CVD process for large area graphene production.

Heating method	**Cu foil dimensions**	**P (mbar)**	**Gas**	**Substrate Temperature**	**Speed (mm/min)**	**Residence time (min)**	**I_D/I_G**	**Ref.**
Thermal furnace	76 cm diagonal	0.6	H_2, CH_4	1000 ºC	Stationary	60	Small	[7]
Thermal furnace	25 and 125 µm, 43X91 cm^2	1013	H_2, CH_4, Ar	1000 ºC	Stationary	300	Small	[137]
Thermal furnace	25 µm, 100 cm long	1013	H_2, CH_4, Ar	1000 ºC	10-400	0.75 – 30	0.2	[15]
Thermal furnace	50.8 µm, 0.6X60 cm^2	5	H_2, C_2H_4, He	1010 ºC	25-500	0.6 – 12	0.1-1	[16]
Thermal furnace	40 µm, 12X60 cm^2	1013	H_2, CH_4, N_2	1010–1070 ºC	5	60	Small	[17]
Joule heating	36 µm, 23X1000 cm^2	10	H_2, CH_4	1000 ºC	100	4	Small	[138]
Remote MW plasma	33 µm, 29X48 cm^2	0.3	H_2, CH_4, Ar	400 ºC	300	1.6	0.5	[62]

An atmospheric roll-to-roll thermal CVD system for graphene growth with a speed of 5 mm/min was reported by Zhong et al. [17]. High-quality graphene of greater uniformity was grown

in the middle portion of the Cu foil (about 15 cm in length) because the temperature in the center was higher than the temperature at the outer regions. The edges along the length of the copper foil had lower temperatures because of heat loss to the atmosphere. Even though there was no pre-annealing zone, the quality of the deposited graphene was high because of the high temperature (1070 ^{o}C) environment in the system.

The furnaces used in the aforementioned studies are not efficient because of high power inputs and long processing times. For example, the typical power consumption of furnaces used in the studies ranged from 800 to 3500 W since most of the power was consumed maintaining a high temperature furnace. Therefore, the speed of the discussed thermal roll-to-roll processes was low to allow for sufficient heating of the substrate. A high temperature is necessary because of the catalytic nature of the substrate, which is activated at higher temperatures, and because of the need to decompose the precursor gas for graphene growth. To increase the efficiency of roll-to-roll processes, several approaches have been suggested for supplying the required energy to the CVD system. For instance, a direct Joule heating source was applied to a Cu substrate by Kobayashi et al. [138] to produce 100 m of graphene in a roll-to-roll CVD process with a speed of 100 mm/min. Electric currents passed through two rollers where Cu foil was suspended to increase foil temperature to about 1000 ^{o}C. Kobayashi et al. used a high concentration of CH_4 (90%) with only 10% H_2 to increase the deposition rate. Graphene micro-cracks on the copper substrate were found under tension because of the difference between the thermal expansion coefficients of graphene and copper.

Another way to increase the efficiency of roll-to-roll CVD processes is to use a microwave plasma at 2.45 GHz, as reported by Yamada et al. [62]. Eight antennae equipped in quartz tubes were used to generate the plasma, increasing the processing speed to 300 mm/min and lowering the direct heating of the copper substrate to 400 ^{o}C. The deposited graphene had moderate quality and large sheet resistance, two qualities that were attributed to the absence of the annealing step and/or the defects originating in the plasma or during the transfer process to a PET substrate. Therefore, a statistical optimization method is discussed in the following chapter to increase the quality of graphene on Cu foil in a roll-to-roll plasma CVD.

3. PROCESS OPTIMIZATION OF GRAPHENE GROWTH IN A ROLL-TO-ROLL PLASMA CVD

Chapter 3 originates mainly from the published manuscript [23] which is reused with permission form AIP Advances, Vol. #7, Article ID #11, (2017); used in accordance with the Creative Commons Attribution (CC BY) license.
[23] M. A. Alrefae, A. Kumar, P. Pandita, A. Candadai, I. Bilionis, and T. S. Fisher, "Process optimization of graphene growth in a roll-to-roll plasma CVD system," *AIP Adv.*, vol. 7, no. 11, p. 115102, Nov. 2017.

3.1 Motivation and Background

In the past, statistical techniques such as Taguchi's method [139], [140] and factorial designs [141] have been used to find optimum conditions for graphene and carbon nanotube synthesis, respectively. However, basic factorial designs become less effective for large and complex systems. Thus, a holistic framework encompassing design, control and quantification of uncertainty is required. Such an approach based on statistical methods can be further strengthened by data obtained from an *in situ* monitoring system of the growth process.

The intensity of the emission lines from OES can be used to understand species concentrations in the plasma qualitatively [117]. Previous experimental results indicate that the I_D/I_G ratio, which is an inverse measure of graphene quality and grain size, improves with increased CH emission intensity from OES [53]. In contrast, previous numerical studies have found that the CH species is more favorable than other carbon species for graphene growth on Cu [142], [143]. Because of the dearth of prior experimental work to determine the roles of different plasma species in graphene growth, this work utilize OES to reveal the effects of different species on graphene quality and to understand and control the deposition at a relatively large scale.

A design of experiments (DOE) technique is implemented in this chapter to optimize the deposition of graphene on copper foil in a roll-to-roll plasma CVD system. Plasma power, pressure and gas constituents of hydrogen (H_2), methane (CH_4), nitrogen (N_2), oxygen (O_2), and argon (Ar) are varied to optimize the growth of graphene. Statistical data-driven models have been built to study the effects of these process parameters on the graphene quality, which is defined by the intensity ratio of the D and G peaks (I_D/I_G) from Raman spectroscopy. Also, quantitative monitoring of the plasma species during graphene growth is demonstrated using OES. A

deposition model of graphene on copper foil in the present system is developed based on the results from OES and Raman correlations. Finally, the effects of the processing speed on graphene deposition are studied and show that plasma CVD is suitable for large-scale production of graphene.

3.2 Experimental Setup

3.2.1 Roll-to-Roll Plasma CVD System

Figure 3.1 shows the roll-to-roll plasma CVD system in which a sample is placed in the top free-moving winder, passes through the plasma region, and finally collects in the bottom driving winder. The plasma power is supplied from an rf power generator at a frequency of 80 kHz with a maximum power of 5000 W (Diener Electronics Co.). The power is supplied through igniter rods connected to two parallel rectangular electrodes. A capacitively coupled plasma (CCP) is generated between the two electrodes, which are separated by a 4.5 cm gap. The copper sample (76 μm thick and 2.54 cm wide annealed copper 110) is placed 1.5 cm from the right electrode, and the frontal areas of the left and right electrodes are 136.0 and 62.5 cm^2, respectively. The asymmetry of the electrodes ensures that the substrate is placed in a higher temperature region. Graphene grows on both sides of the copper foil with different qualities and deposition rates depending on process conditions.

Gas mixtures of hydrogen (H_2), methane (CH_4), nitrogen (N_2), oxygen (O_2) and argon (Ar) flow in the chamber with maximum flow rates of 1000, 1000, 100, 100 and 5000 standard cubic centimeters per minute (sccm), respectively. The pressure in the chamber is monitored by 10 and 100 mbar pressure gauges. The process parameters (i.e., plasma power, pressure, and mole fractions of H_2, CH_4, N_2, O_2, and Ar) vary between lower and upper limits to explore the parametric space during the optimization process, as listed in Table 3.1. Limits and the plasma/power constraint are selected to sustain a stable plasma during the growth process (see Figure A.1 in Appendix A).

In situ emission of the plasma in the range of 300-933 nm was detected by a spectrometer during the optimization process experiments (Fig. 3.1(c)). The optical emission spectroscopy consists of lenses to focus the plasma emission to a fiber optic which is connected to a spectrometer (Princeton Instruments, Acton SP-2756). The spectrometer has a focal length of 750 mm and a

grating of 1800 G/mm. The diffracted light is detected by a CCD camera (Princeton Instruments, PIXIS 256E). The wavelength of the spectrometer was calibrated using a Mercury light source. Emission intensity was also calibrated using an intensity calibration light source to account for grating and CCD camera efficiencies.

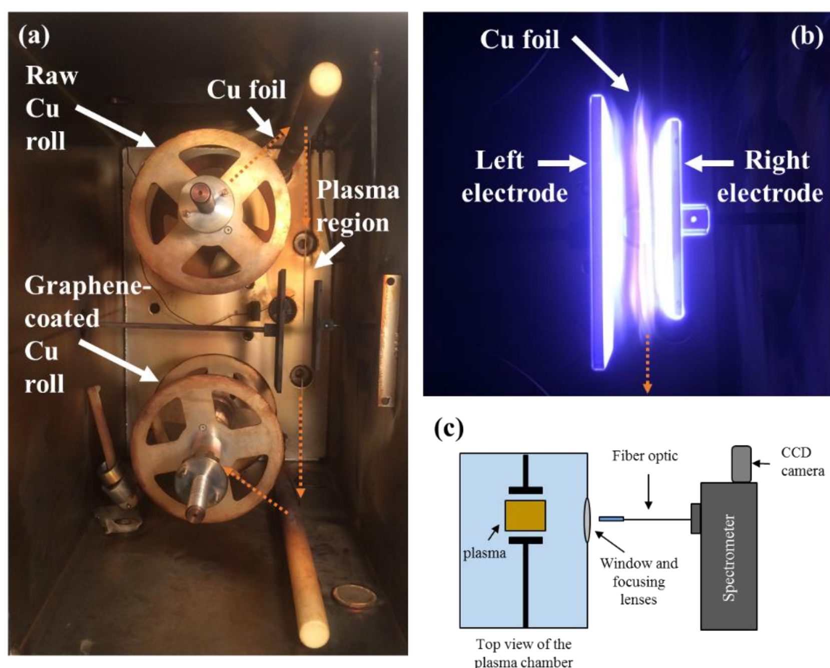

Figure 3.1: (a) Setup of the roll-to-roll plasma CVD system. (b) The plasma region where the copper foil is processed for graphene growth. (c) Top view of the chamber with the optical emission spectroscopy setup.

Table 3.1: Plasma operating conditions and constraints implemented in this work.

Parameter	Lower Limit	Upper Limit	Constraint
Hydrogen (H_2)	20%	60%	$H_2(\%) + CH_4(\%) + N_2(\%) + O_2(\%) + Ar(\%) = 100\%$
Methane (CH_4)	10 %	30 %	
Nitrogen (N_2)	0 %	10 %	
Oxygen (O_2)	0 %	10 %	
Argon (Ar)	20 %	50 %	
Pressure	7 mbar	18 mbar	$0 < \text{Pressure (mbar)} + \frac{\text{Power (Watt)}}{50} < 10$
Power	500 Watt	1400 Watt	

3.2.2 Graphene Characterization

Graphene films were analyzed using a scanning electron microscopy (SEM) (Hitachi Corp., s-4800) by measuring secondary electrons (SE) and backscattering electrons (BSE) [144]. Optical transmission measurements of graphene transferred to a glass slide were performed in the visible

wavelength range (PerkinElmer, Lambda 950) to estimate graphene thickness. Also, Raman spectroscopy (Horiba Ltd.) was used to study the quality of graphene on both sides of the copper foil. The wavelength of the laser excitation is 532 nm with a magnification of 100x. The Raman spectrum is obtained directly on the Cu substrate to eliminate effects induced by the transfer of graphene from the copper substrate to background-free substrates (i.e., SiO_2/Si). Several graphene samples were transferred to SiO_2/Si substrates and show similar results to the direct measurements from the Cu substrate after background subtraction (see Figures A.2 and A.3 in Appendix A).

In the optimization process, the speed of the moving copper foil in the plasma (web speed) is set to about 45 (± 3) mm/min to minimize the effects of ion bombardment. Figure 3.2 presents Raman spectra of graphene showing D, G, D′ and 2D peaks at 1350, 1580, 1620 and 2700 cm^{-1}, respectively [145]. The G peak represents the sp^2 carbon structure due to C-C in-plane vibrations, whereas the D and D′ peaks appear because of defects in the graphene lattice. The 2D (or G′) peak is an overtone of the D peak and occurs because of a double-resonance process. The peak intensity ratio of the 2D and G peaks (I_{2D}/I_G) and the lineshape of the 2D peak can be related to the number of layers of graphene [146]. Nevertheless, graphene samples produced from CVD processes have been reported to have weak coupling between layers resulting in disordered layer stacking [145]. Therefore, interpretation of (I_{2D}/I_G) and the lineshape of the 2D peak from Raman results of these samples should be made with care.

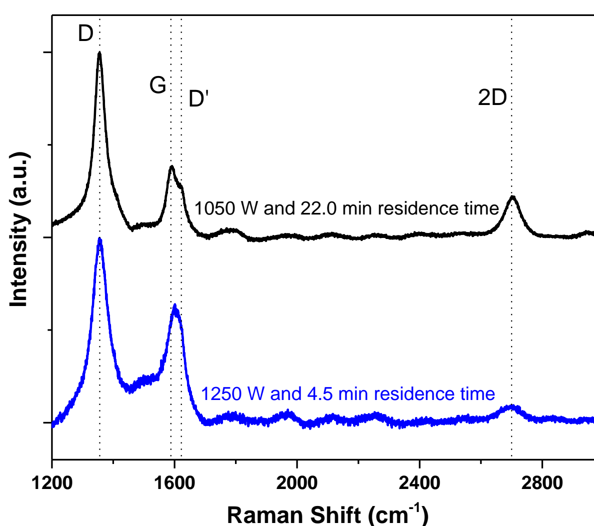

Figure 3.2: Raman spectra of graphene that show more defects with increased plasma residence time. Other conditions are kept constant at 60% H_2, 25% CH_4, and 15% Ar at 15 mbar.

Alternatively, the D and G peak ratio (I_D/I_G) has stronger correlation to the defect density level and the crystalline size (L_a) [147]–[149]. For instance, the I_D/I_G ratio decreased from 2.6 to

1.6 upon lowering the residence time from 22.0 minutes (which was placed stationary in the plasma) to approximately 4.5 minutes (using a web speed of 45 mm/min and assuming that the plasma has a length of about 20 cm near the Cu foil region) as shown in Fig. 3.2. The defect density increases with residence time due to increased ion bombardment that initiate defects in the lattice. Therefore, I_D/I_G is preferred to I_{2D}/I_G for representing the quality of graphene, and the I_D/I_G ratio is used in this chapter as an objective function in our statistical optimization process as explained next.

3.2.3 Multi-objective Optimization Method

A statistical design methodology [150] is applied to minimize the I_D/I_G ratio from Raman spectroscopy for the right and left sides of the foil. We minimize both objectives by casting the problem as a two-objective stochastic optimization problem:

$$\hat{x} = \arg\max \mathbf{E}[\mathbf{O_i}(\mathbf{x})], \quad i=1,2 \tag{3}$$

where $\mathbf{x}$ is the process control parameter (plasma power, gas pressure and gas constituents), $\mathbf{O_i}(\mathbf{x})$, is the experimentally measured I_D/I_G ratio of the graphene deposited on the left side ($i = 1$) and on the right side ($i = 2$) of the Cu foil, and $\mathbf{E}[\cdot]$ denotes the expectation over the measurement noise. Figure 3.3 summarizes the optimization methodology that initially starts by exploring the effects of the process parameters ($\mathbf{x}$) on the quality of both sides. Due to the asymmetric physical conditions on the left side and right side of the Cu foil, the two objectives may be competing, i.e., choosing a process input that increases the quality of graphene deposited on the left side of the Cu foil may result in decreased quality of graphene deposited on the right side. We say that a set of process inputs $\mathbf{x}_1$ dominates a different set of process inputs $\mathbf{x}_2$ if $\mathbf{E}[\mathbf{O_i}(\mathbf{x}_1)] \geq \mathbf{E}[\mathbf{O_i}(\mathbf{x}_2)]$ for $i = 1,2$. In words, $\mathbf{x}_1$ dominates $\mathbf{x}_2$ if $\mathbf{x}_1$ results in higher graphene quality on both sides of the Cu foil. The set of non-dominated process inputs is called the Pareto efficient frontier (PEF) of the two-objective stochastic optimization problem, as shown in Fig. 3.3. For any dominated operating point, there is always an operating point on the Pareto efficient frontier that results in higher quality of graphene on both sides of the Cu foil. In this sense, the PEF defines the optimal operating points of the plasma CVD system for high-quality graphene deposition. The details of the statistical methods are provided in Appendix A.3.

The optimization process methodology starts with performing experiments at different design variables (process parameters) as presented in Fig. 3.3. The results are presented in a Pareto efficient frontier with epistemic uncertainty. If this uncertainty is not acceptable, a new set of

experiment is selected to increase the information and to decrease the I_D/I_G ratio. Data-driven models are developed from these experimental results. The process iterates until convergence initiated by small epistemic uncertainty. As a result, the final Pareto efficiency frontier of the objective (I_D/I_G ratio) is obtained.

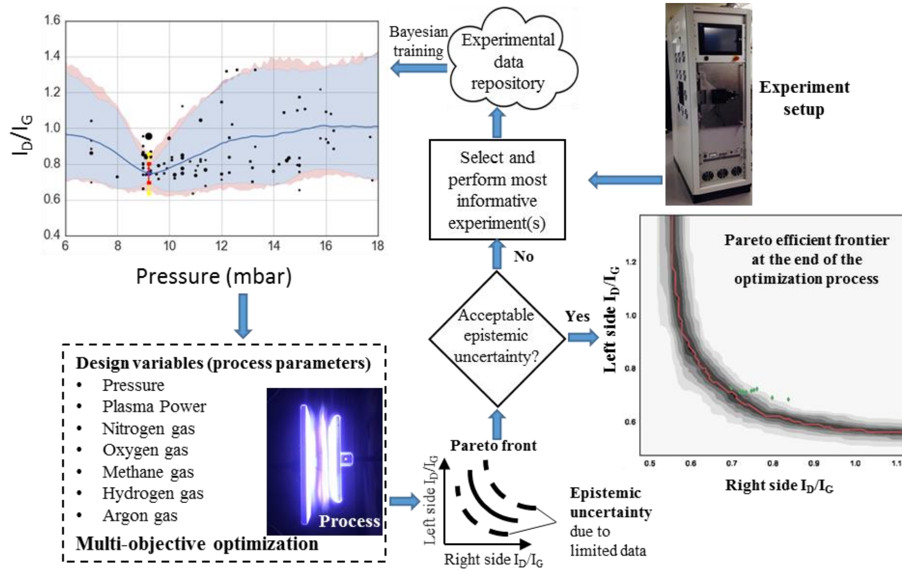

Figure 3.3: Summary of the optimization process methodology used in this chapter.

3.3 Results and Discussion

3.3.1 Graphene Quality Optimization and Characterization

Utilizing the advantages of the roll-to-roll process, multiple experiments were conducted in one set (batch) with negligible influence of experimental sequence on graphene deposition (see Figure A.4 in Appendix A). The total number of experiments in the optimization process is 101, conducted sequentially in 6 sets. After starting with initial sets of random measurements, called Sets 1-3 in Fig. 3.4, the methodology selects the next conditions of the seven process parameters to maximize the quality and information in the PEF. Three more experimental sets were conducted to improve the graphene quality, labeled Sets 4, 5, and 6 in Fig. 3.4. The PEF for Set 6 is included in Fig. 3.3, in which the locations of the optimized conditions are marked with green symbols. The I_D/I_G ratio decreases for Sets 4-6 compared to the initial sets (Sets 1-3). Despite the presence of high-energy ions in the low-frequency rf CCP, the experimental design improves the I_D/I_G ratio from 1.4 to 0.7, as shown in Fig. 3.4.

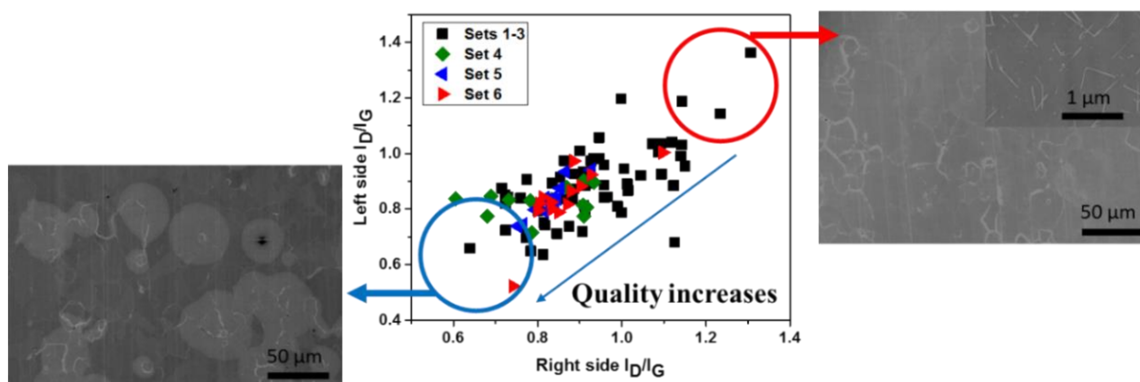

Figure 3.4: Sequential optimization of graphene on both sides of Cu foil. SEM images are shown for representative low and high qualities of graphene.

The optimized process parameters from the above sequential sets are 31% H_2, 25% CH_4, 4% N_2, 1% O_2, and 39% Ar at 9.2 mbar and 750 W. This condition produces the minimum I_D/I_G ratio on both sides as suggested by our model in three different sets of the sequential optimization process. The Raman spectra of graphene on both sides at this condition are shown in Fig. 3.5(a). The I_D/I_G ratio for both sides is 0.7 which remains uniform across the width and length of the substrate as presented in Fig. 3.5(b). The optimized condition produces uniform growth coverage as evident from secondary electron (SE) and backscattering electrons (BSE) SEM images from the same region, as illustrated in Fig. 3.5 (c) and (d). In addition, oxidation tests of the optimized condition and another sample obtained using high plasma power were conducted. The results from the oxidation tests confirm the uniformity of graphene growth and quality, as it acts as a corrosion barrier on copper foil due to the gas impermeability and thermal stability of graphene (Fig. A.5 in Appendix A) [151].

On the other hand, partial coverage of graphene was detected for other samples grown at non-optimal conditions. For instance, a non-uniform I_D/I_G ratio across the width of the substrate is shown in Fig. 3.5(b) with higher values near the edges due to the non-uniform temperature and/or ion flux across the substrate that result in higher I_D/I_G ratio for this sample. Also, since backscattering electrons originate from elastic scattering processes that increase with larger atomic number (Z), the difference between copper with Z=29 and carbon with Z=6 can be detected depending on the contrast of BSE SEM images [144]. Indeed, partial coverage of graphene on copper for a non-optimized condition is observed from the BSE SEM image as evident in Fig. 3.5(e). The image indicates partial coverage of graphene with darker regions compared to brighter regions of copper due to its higher Z.

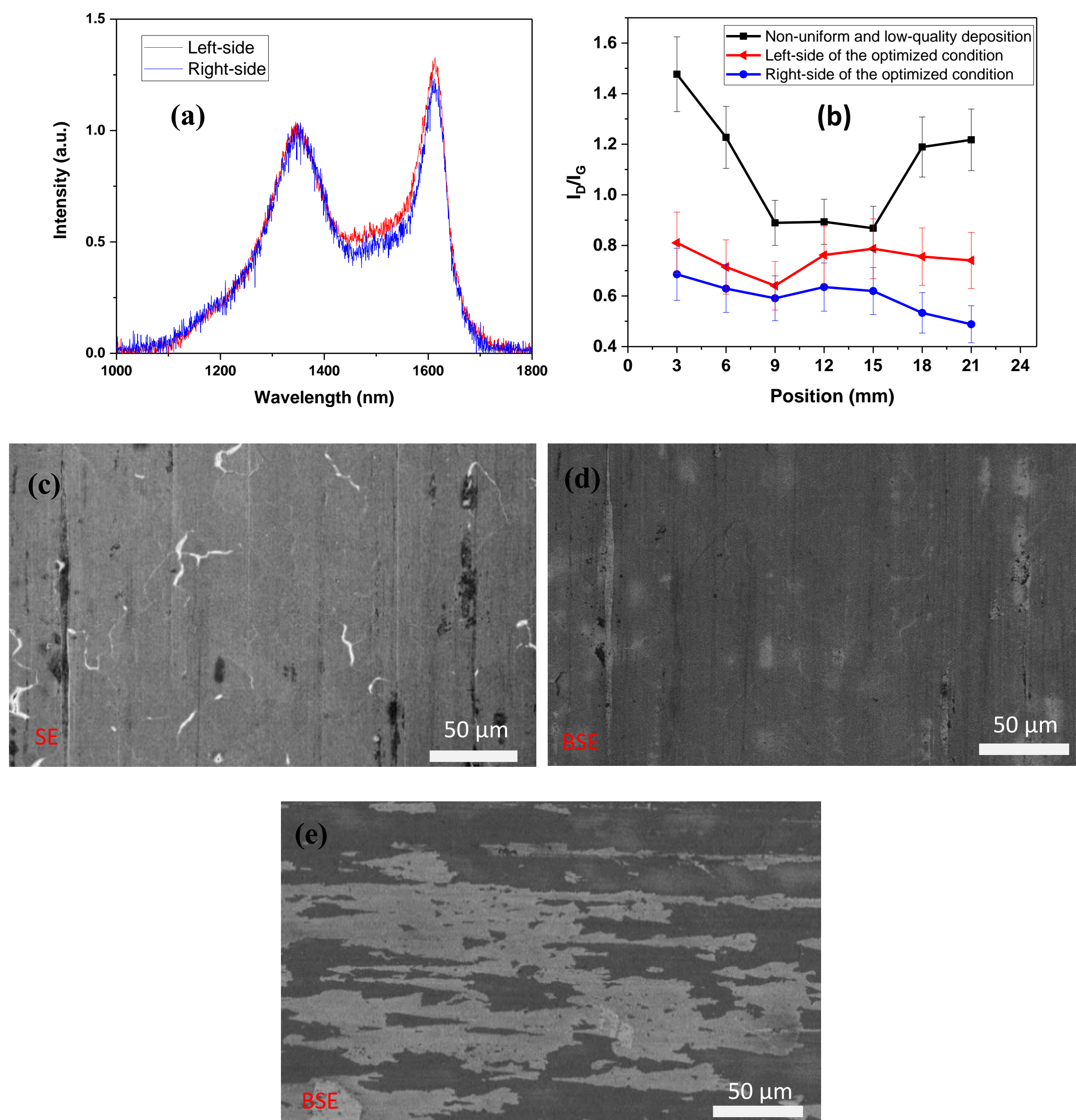

Figure 3.5: (a) Raman spectrum of the optimized condition. (b) Spatial dependence of I_D/I_G representing uniform growth of graphene for the optimized condition, whereas the quality is not uniform for graphene growth at 50% H_2, 21% CH_4, 0% N_2, 0% O_2, 29% Ar at 18.8 mbar and 1250 W. SEM images of graphene on copper obtained from (c) secondary electrons (SE) and (d) backscattering electrons (BSE) of a uniform deposition whereas (e) shows a non-uniform deposition from backscattering electrons (BSE) taken from a non-optimized condition.

The high defect density is a consequence of limitations imposed by the low-frequency CCP discharge. For instance, graphene quality from several samples, including the above optimized condition, remains similar when decreasing the length of the plasma from 20 to about 5 cm using two symmetric small electrodes (Fig. A.6 in Appendix A). Even though the plasma size decreases by 75%, the quality of graphene does not improve due to the severe effects of ion bombardment.

These results suggest that high-energy ions, which exist at this low frequency, have large effects on graphene quality regardless of the plasma size. Keeping the substrate for longer residence time in the plasma was found to enhance the graphitization processes and thus lead to higher I_{2D}/I_G as evident in Fig. 3.2. Similar graphene quality was observed by Terasawa and Saiki [53] with an I_D/I_G area ratio of approximately 0.7 using a higher frequency of 13.56 MHz rf CCP CVD system at 300 W, 1 Pa, 80% H_2 and 20% CH_4. Even though CCP discharges have higher ion energy and larger sheath thickness as plasma frequency decreases [152], [153], the optimization process improved the quality of graphene in our low-frequency plasmas by exploring the process parameter space more efficiently as discussed below.

3.3.2 The Effects of the Plasma Parameters on Graphene Quality

The plasma parameters and their interactions play important roles in optimizing the quality of graphene. For example, Mehedi et al. [139] found that inclusion of interactions among process parameters is important to reach optimum conditions for high-quality graphene. Thus, using statistical design of experiments, the influence of each of the plasma parameter on the graphene quality can be included in the surrogate models. These data-driven models for the two objectives (I_D/I_G ratio of graphene on both sides of Cu foil) are developed and validated with the experimental results. Figure 3.6 shows a comparison between the model and experimental results from Raman spectroscopy at three different positions. Initially, the model in Fig. 3.6(a) deviates from the experiments because of the relatively small number of experiments that intend to cover the seven dimensions (i.e., the process parameters). The data-driven models are improved greatly with increased experiments (Fig. 3.6 (b)), and are then used to derive the importance of each process parameter on graphene quality as discussed below.

From the models, a sensitivity analysis is performed to determine the relative influence of the plasma parameters on the two objectives. The sensitivity factor is derived from length scales that represent the variation of the measured values from the surrogate model values (refer to Appendix A.3 for further details on length scales). The larger the length scale of a process parameter, the less variation of the objective caused by this parameter. Hence, the inverse of the length scales is used to represent the relative sensitivity of the objective to each process condition. Figure 3.7 identifies the relative importance of the process parameters to the quality of graphene on both sides of the Cu foil. The most important input conditions affecting graphene quality on the

right side (in decreasing order of their effect) are pressure, nitrogen mole fraction and oxygen mole fraction. On the other hand, the variables influencing the quality on the left side are oxygen mole fraction, plasma power, and finally pressure and methane mole fraction. These important input parameters affect the plasma properties and consequently the quality of graphene as discussed in the following paragraphs.

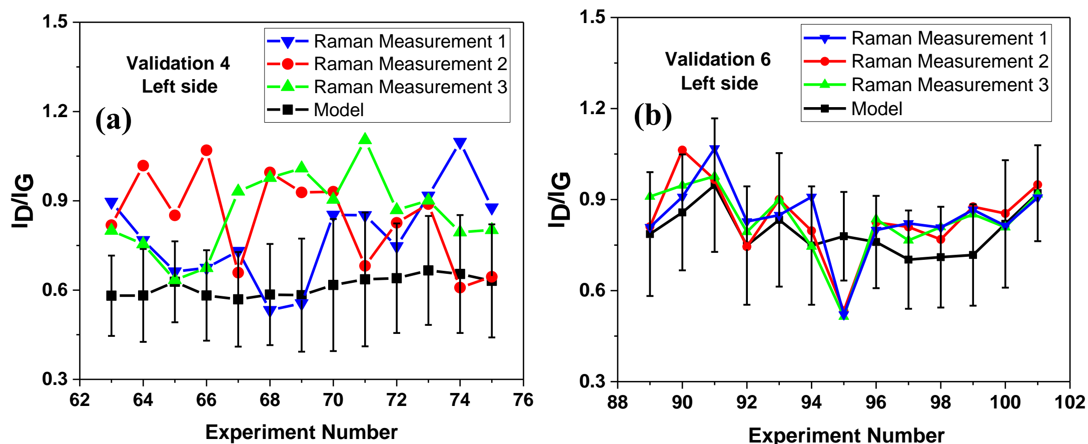

Figure 3.6: Sequential batch runs during the exploration and optimization process. The model results in (b) Validation 6 agree better with the experimental results than the results in (a) Validation 4 due to the increased number of experiments.

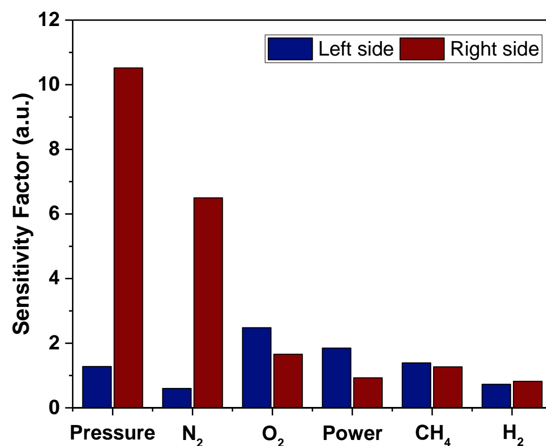

Figure 3.7: The sensitivity analysis of the process inputs that affect the I_D/I_G extracted from the statistical surrogate models.

The pressure in the chamber has the largest influence on the quality of graphene on the right side because the ion bombardment on the substrate is more affected by pressure in low frequency rf plasmas [154]. This is also attributed to the large influence of the pressure on the right electrode sheath that is adjacent to the substrate's right side. With a rise in pressure, the sheath thickness decreases and the I_D/I_G ratio declines due to the absence of direct contact between the

substrate and the sheath, which contains high-energy ions that are accelerated toward the substrate. However, as the pressure further increases, the plasma changes from alpha to gamma mode [155] which is more energetic and thus leads to higher I_D/I_G ratios (Fig. A.7 in Appendix A). Therefore, an optimum pressure exists at which the sheath thickness is small in the alpha mode without any apparent transition to the gamma mode. This optimum pressure value is 9.2 mbar for the condition of 31% H_2, 25% CH_4, 4% N_2, 1% O_2, and 39% Ar at 750 W, as indicated by the response surface in Fig. 3.8(a). The low quality for pressures below 9.2 mbar is due mainly to the large sheath thickness resulting from a lower collision rate and higher mean free path that promote ion bombardment [156]. However, the quality decreases when the pressure increases beyond 9.2 mbar due to the transition to gamma mode, which has higher current density and electron number density [155] that enhance ion flux to the substrate and thus degrade quality.

The second important factor for the right side I_D/I_G ratio is nitrogen mole fraction, which affects the quality as shown in the response surface (Fig. 3.8 (b)). The I_D/I_G ratio decreases with increased nitrogen mole fraction until about 4% when keeping other conditions constant at the optimized condition of 31% H_2, 25% CH_4, 1% O_2, and 39% Ar at 9.2 mbar and 750 W. Adding nitrogen in Ar and H_2 plasmas, which are used as bath gases, results in higher dissipated power in the plasma because of the active vibrational modes of nitrogen gas. Thus, the excitation processes and transfer of energy between electrons and the neutral gas are enhanced with increased N_2 mole fraction. For instance, the OES results suggest higher emission intensities with increased N_2 mole fraction and hence more reactive species present in the plasma to enhance the deposition process. Indeed, the dissociation of methane increases with the addition N_2 to produce HCN species from vibrational excitation reactions as reported for a 13.56 MHz rf plasma [157]. Similarly, the addition of N_2 to a H_2/CH_4 microwave plasma for diamond growth leads to higher production of CH species, indicating enhanced methane decomposition in N_2-containing plasmas [158].

The addition of oxygen is the most important factor for graphene quality on the left side. Figure 3.8(c) shows the response surface of the I_D/I_G ratio as a function of the oxygen concentration at the optimized condition of 31% H_2, 25% CH_4, 4% N_2, and 39% Ar at 9.2 mbar and 750 W. Graphene quality increases when the concentration of oxygen increases till about 4% after which the quality decreases with further increases in oxygen mole fraction [159]. The initial rise in quality (decreased I_D/I_G ratio) could be attributed to the consumption of hydrogen atoms by oxygen, and, thus, a corresponding decrease in graphene etching [40]. Furthermore, oxygen reacts with

amorphous carbon deposited on the Cu surface and results in better graphitization of the deposited carbon film. Previous reports indicate that the presence of oxygen atoms on copper enhances the growth of large graphene domain due to decreased nucleation density and result in higher growth rate [93]. Similar results have been obtained when introducing oxygen in the gas mixture during graphene growth, and show that higher growth rate occurs at an optimum value of oxygen mole fraction [160]. However, further increase in oxygen concentration will degrade graphene quality because of etching as a result of carbon oxidation [161]. In addition, oxygen can bond with the graphene lattice to form oxygen-doped graphene. Also, energetic oxygen atoms can break C-C bonds of the deposited graphene and result in a disordered structure [162]. Therefore, the optimized condition of graphene includes 1% oxygen in the gas mixture to increase graphene domain size and growth rate, without etching or damaging graphene films.

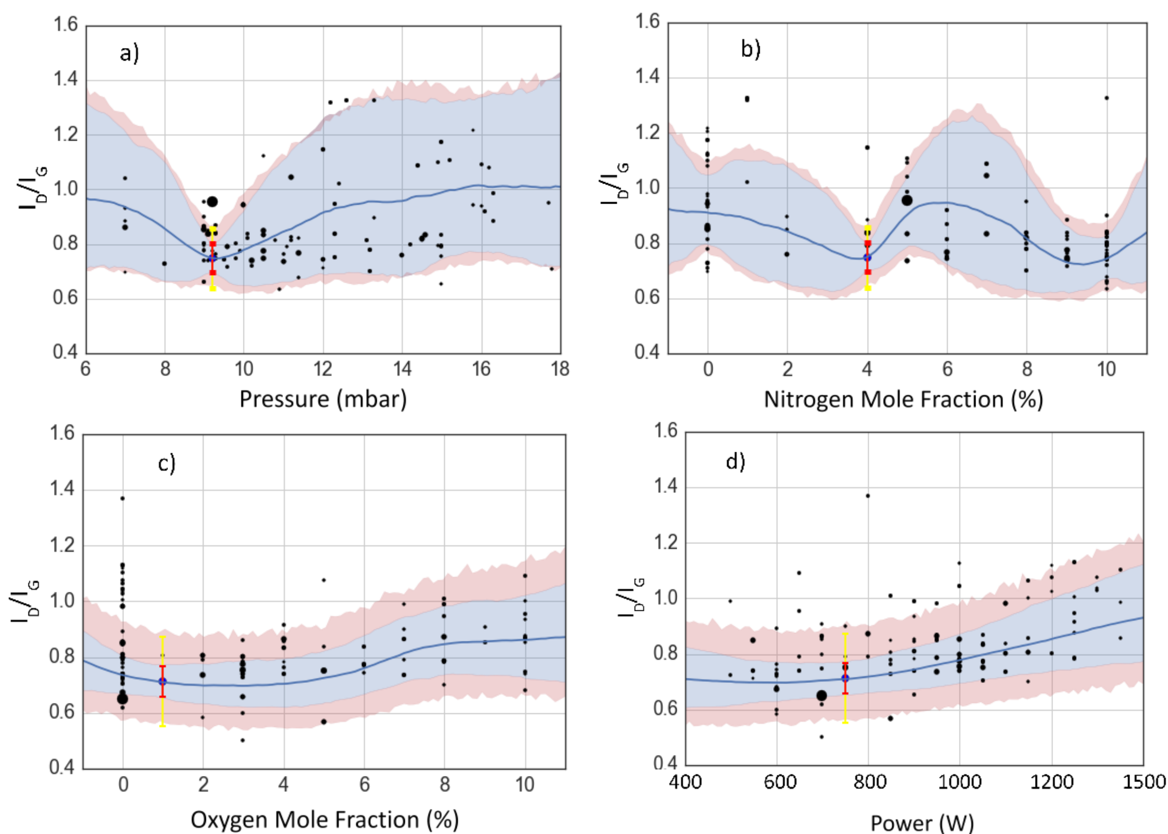

Figure 3.8: I_D/I_G response surfaces as a function of (a) pressure, (b) nitrogen, (c) oxygen and (d) plasma power. The line shows the mean values of the response surface for the predictive model. The shaded uncertainties represent the lack of knowledge (blue) and noise from the experiment (pink). The response surfaces are obtained for fixed conditions of the optimized condition 31% H_2, 25% CH_4, 4% N_2, 1% O_2, and 39% Ar at 9.2 mbar and 750 W, as indicated by the red and yellow arrows.

Figure 3.8(d) presents the response surface of the I_D/I_G ratio as a function of the plasma power at the optimized condition. The quality decreases as power increases because of increased energetic ion concentrations and species fluxes to the substrate that induce defects in the deposited films [46], [52], [63]. The rise in density of excited species with increased power is corroborated by measurements from OES as explained in the next section. On the other hand, the quality decreases at lower plasma power because of the low production of active species and decreased heating of the substrate. Therefore, an average power value at 750 W results in higher quality. The effects of plasma power on graphene growth at higher web speeds are discussed in Section 3.3.4 for two cases: this optimized condition at 750 W, and a higher deposition rate case at 1250 W.

3.3.3 Correlating Results from OES with Graphene Quality and Process Parameters

Figure 3.9 shows an emission spectrum from a probe volume near the substrate material where the most prominent species are present (see Table A.1 in Appendix A). The species emission intensities are correlated to the quality of graphene using a statistical mapping analysis as described in the Supplemental Material (Fig. A.8 in Appendix A). The emission intensities of the species CN, N_2^+, CH, Ar^+, C_2, H_2, H_α, Ar, O, C, and N measured using OES are mapped into a 1D space in order to extract important correlations to graphene quality.

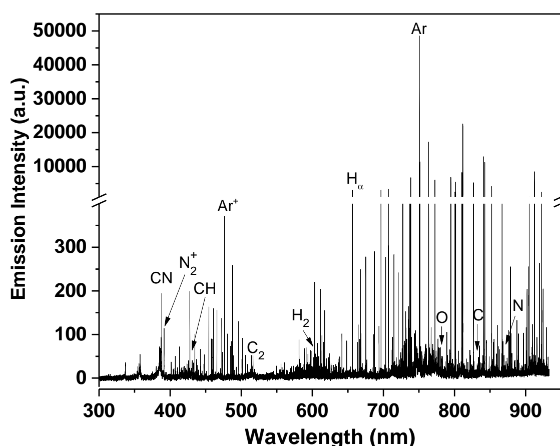

Figure 3.9: A plasma emission spectrum sample measured during the growth process. Important species in the plasma are indicated in the spectrum.

Figure 3.10(a) presents the results of the analysis in which the negative of the importance factor "w_i" indicates a decrease of I_D/I_G ratio, whereas a positive w_i factor indicates an increase in I_D/I_G ratio. The emission of CH is correlated with an increase in graphene quality in agreement with previous theoretical results [142], [143] because the chemical chain -CH is more energetically

favorable on Cu(111) than other carbon clusters [163]. Furthermore, other species that have minor contributions to the increased quality are N, N_2^+, and H_2, as more than 75% of the ranges of their importance factors indicate higher quality (i.e., negative w_i).

On the other hand, increased C_2 and O emission indicates lower graphene quality. Similarly, the importance factors of CN, H_α, C and Ar^+ emission lines lie within the low-quality region in Fig. 3.10(a). The oxygen atoms affect the quality due to their high energy in the plasma, which can break carbon bonds of the graphene deposited on the substrate [164]. Also, ion bombardment by Ar^+ and the etching effects of H_α result in disorder in the carbon films deposited on the Cu substrate, likely resulting in sputtering of C_2 and C species from the surface. Emission from C_2 and C species are higher for samples with thicker carbon films, as evidenced by the corresponding increase in their emission intensities as discussed next. Another possible negative effect of C_2 in graphene quality is the creation of vacancies due to C_2 saturation on the copper substrate [163].

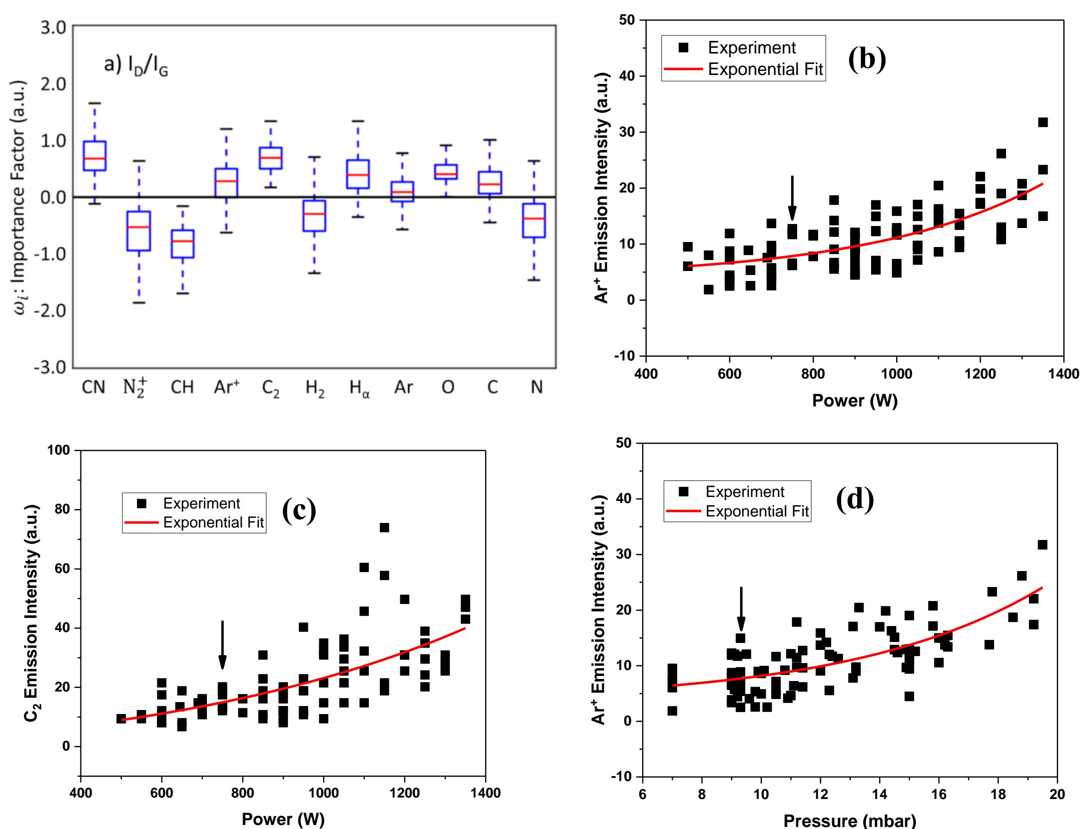

Figure 3.10: (a) The importance of species emission from OES affecting I_D/I_G ratio. The box plots show the median in red between the first and third quartiles. The emission intensities variations of (b) Ar^+ and (c) C_2 with plasma power. (d) The increase of Ar^+ emission intensity with increased gas pressure.

The process inputs for the optimized condition (31% H_2, 25% CH_4, 4% N_2, 1% O_2, and 39% Ar at 9.2 mbar and 750 W) provide a plasma with lower concentrations of C_2, CN, O, Ar^+ and H and thus result in deposition of high-quality graphene. For instance, the emission intensity of Ar^+ increases with power due to higher energy input to the plasma (Fig. 3.10(b)). The increase of Ar^+ concentration can lead to higher defects in the lattice [165] which could result in sputtering of C_2 as suggested by the increase of C_2 emission intensity in Fig. 3.10(c). Therefore, the optimum power of 750 W is high enough to heat the substrate and ionize the gas mixture, but at the same time has lower concentrations of Ar^+ and C_2 (and O and H, which are not shown here). Similar results are observed with the optimum pressure value of 9.2 mbar which, in addition to its important role in determining sheath thickness and plasma type, produces lower Ar^+ emission as shown in Fig. 3.10(d).

The O atom emission intensity is relatively low at the optimized condition of 1% O_2 and increases linearly with increased oxygen mole fraction as shown in Fig. 3.11(a). Higher concentration of oxygen affects the quality of graphene negatively due to etching as discussed above. Furthermore, oxygen consumes carbon species in the plasma which in turn decreases the deposition rate [160]. For example, the emission of C_2 increases with oxygen mole fraction initially, reaches a maximum near 5% O_2 and then decreases with higher oxygen mole fraction (Fig. 3.11(b)), likely due to the consumption of carbon species in the plasma by oxygen to form CO_2 or CO.

Similarly, the optimized condition includes 4% N_2 that produces a low concentration of CN as shown in Fig. 3.11(c). The CN emission intensity rises rapidly for N_2 mole fraction above 4%. From a mapping analysis, CN is considered to contribute negatively to graphene growth due to the consumption of CH by N_2. For instance, the concentration of CN increases more rapidly than CH with increasing pressure and power due to the reaction: $CH + N_2 \rightleftharpoons HCN + N$ [158]. Hence, an optimum amount of 4% N_2 is needed to increase the dissociation of methane through vibrational excitations reactions, without consuming important carbon radicals and ions that contribute to high-quality graphene. The emission intensity of CN has lower values at 9% and 10% N_2 due to variations of other process inputs. These lower values of CN could explain the other local minimum in I_D/I_G ratio at 9% and 10% N_2 in the response surface of Fig. 3.8(b).

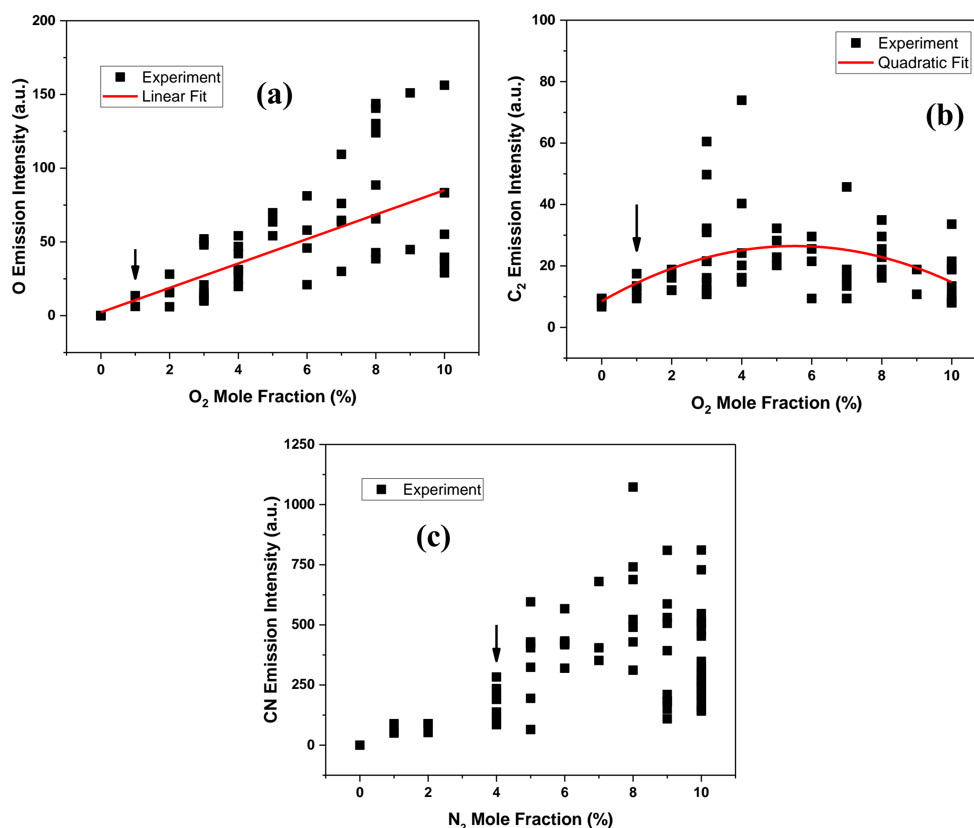

Figure 3.11: The effects of oxygen mole fraction on the emission intensities of (a) O and (b) C_2. (c) The variation of CN emission intensity with N_2 mole fraction.

The variations in the I_D/I_G ratio with CH/O, CH/C_2 and H_2/H emission intensity ratios are presented in Fig. 3.12. These ratios represent the combined effects of species that indicate higher quality (i.e., CH or H_2) to the species that degrade quality (i.e., O, C_2 or H). The quality decreases almost linearly with increasing CH/O (Fig. 3.12 (a)). The wide range of I_D/I_G (i.e., 0.75-1.20) occurs when CH/O is 1.0 or less. However, when the CH/O ratio increases from 1.0 to 4.0, the I_D/I_G ratio decreases linearly from 0.85 to 0.75. Furthermore, Figure 3.12 (b) shows a decreased I_D/I_G ratio with increased CH/C_2, indicating higher quality with higher CH and lower C_2. Finally, the effects of the H_2/H emission ratio on the quality of graphene is presented in Fig. 3.12 (c). The quality of graphene improves with increased H_2/H. The I_D/I_G ratio varies between 0.52 and 1.40 at lower ratios of H_2/H whereas I_D/I_G remains constant at 0.8 as H_2/H increases from 0.025 to 0.06. These emission intensity ratios exhibit higher values at the optimized condition (see Fig A.9 in Appendix A). Thus, these results suggest that higher CH/O, CH/C_2 and H_2/H emission intensity ratios are signatures for high quality and thus can be used for online monitoring for large production of graphene.

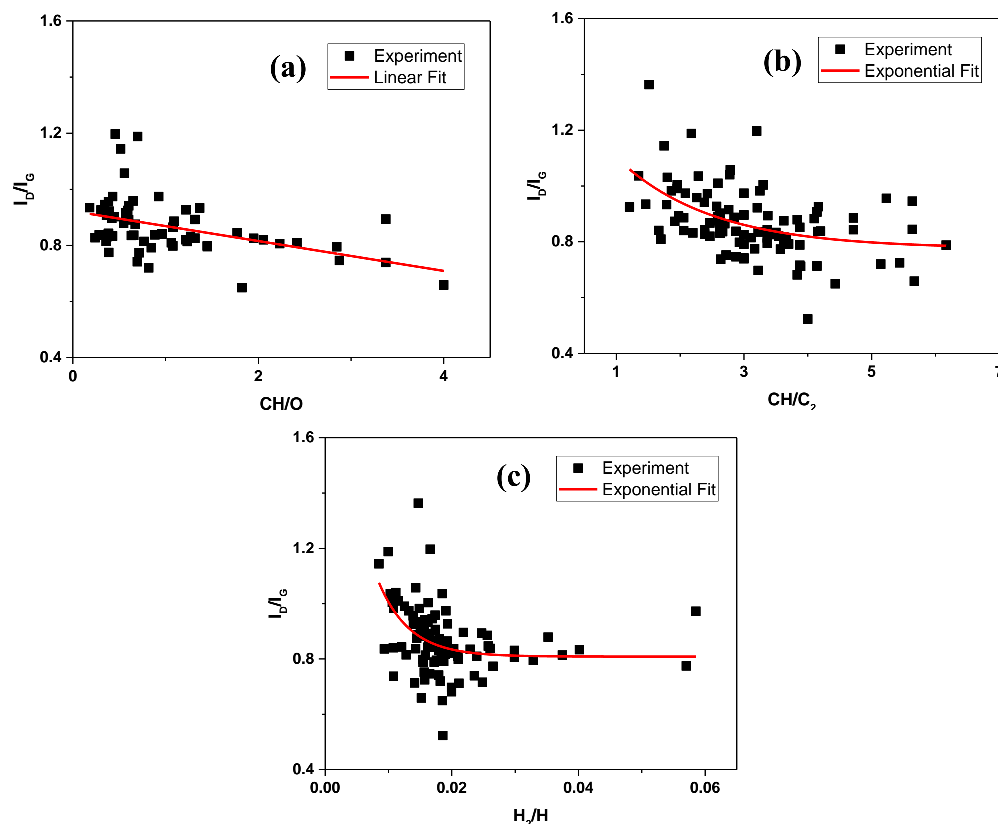

Figure 3.12: (a) The emission intensity ratio effects of (a) CH/O, (b) CH/C_2 and (c) H_2/H on the I_D/I_G ratio.

Correlations between the D-peak position, D-peak full width at half maximum (FWHM), and G-peak FWHM with the OES data were made using the mapping analysis as shown in Fig. 3.13 (a), (b) and (c), respectively. The results from these correlations indicate that emission from O and C_2 is associated with increasing the D-peak position, D-peak FWHM, and G-peak FWHM values. The dependence of D-peak position and the G- and D-peak FWHMs on emission ratios of the important species are presented in Fig. 3.14. The D-peak position decreases exponentially with increased CH/O (Fig. 3.14(a)). At lower CH/O ratio, the position of the D peak ranges from 1360-1372 cm^{-1}, but then decreases to an asymptotic value around 1345 cm^{-1} when the CH/O ratio is higher than 2.0. Such a result agrees with the increase of graphene quality with increased CH/O ratio (Fig. 3.12(a)). Similarly, the effects of the Ar^+/O ratio on the FWHM of the D peak are shown in Fig. 3.14(b). The FWHM of the D peak are 160-200 cm^{-1} when the values of the Ar^+/O ratio are less than or equal to 5. However, the D-peak FWHM decreases to a value around 140 cm^{-1} when the Ar^+/O ratio is higher than 10. Lastly, the FWHM of the G peak decays exponentially with increased CH/O ratio and reaches an asymptotic value of 60 cm^{-1} (Fig. 3.14(c)).

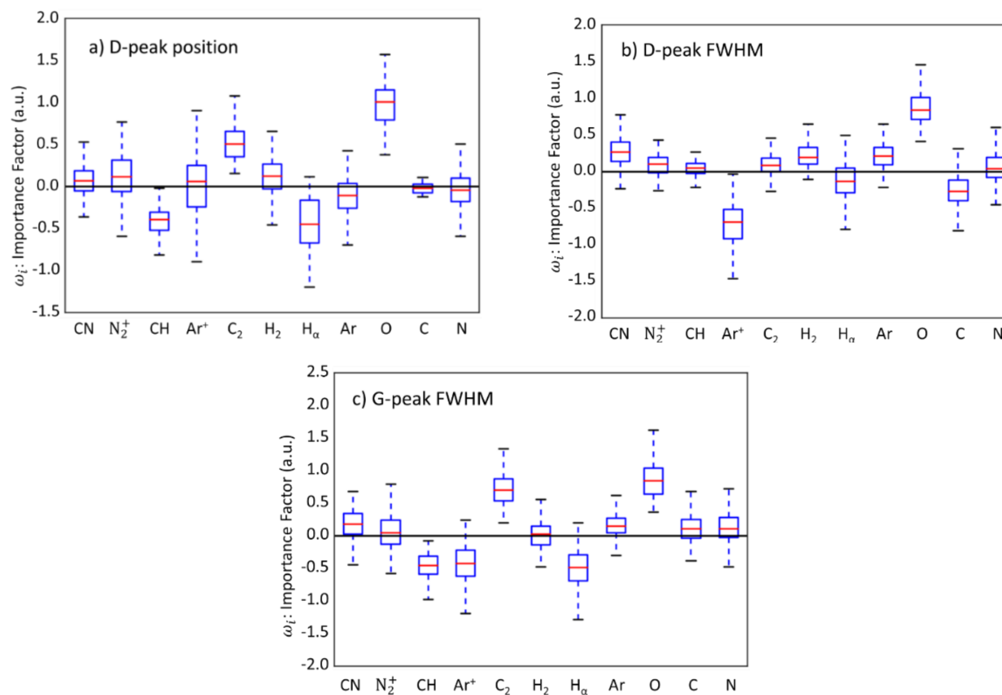

Figure 3.13: The importance of species emission from OES affecting: (a) D-peak position, (b) D-peak FWHM and (c) G-peak FWHM.

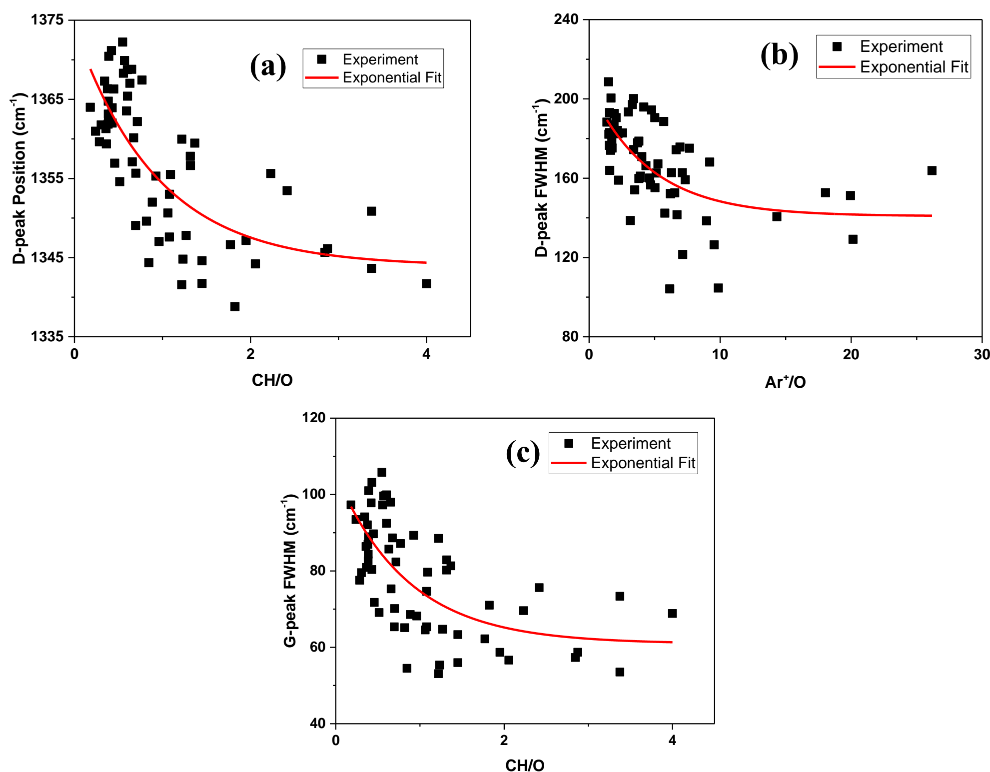

Figure 3.14: (a) The D-peak position decreases when the intensity ratio of CH/O increases. (b) The effects of the Ar^+/O ratio on the FWHM of the D-peak. (c) The exponential decay of the G-peak FWHM with increased CH/O ratio.

Based on the forgoing results, we propose a conceptual model of graphene deposition on copper foil in our system (Fig. 3.15). Considering the left side of the copper foil, the left electrode is powered during a half-cycle from the rf generator. The supplied electric field energizes the electrons in the plasma. Electrons are then accelerated toward the right electrode away from the cathode sheath. Gas molecules react with electrons to produce active radicals, ions and atoms. Intermediate species then reach the copper substrate with CH that favors growth of high-quality graphene. However, energetic species, such as O, Ar^+, or H can break, sputter, or etch the carbon deposited on the copper, respectively. Consequently, C_2 and C species are sputtered from the graphene deposited on the copper substrate. These processes occur during the rf cycle and result in graphene deposition with different thicknesses depending on the web speed as explored in the following section.

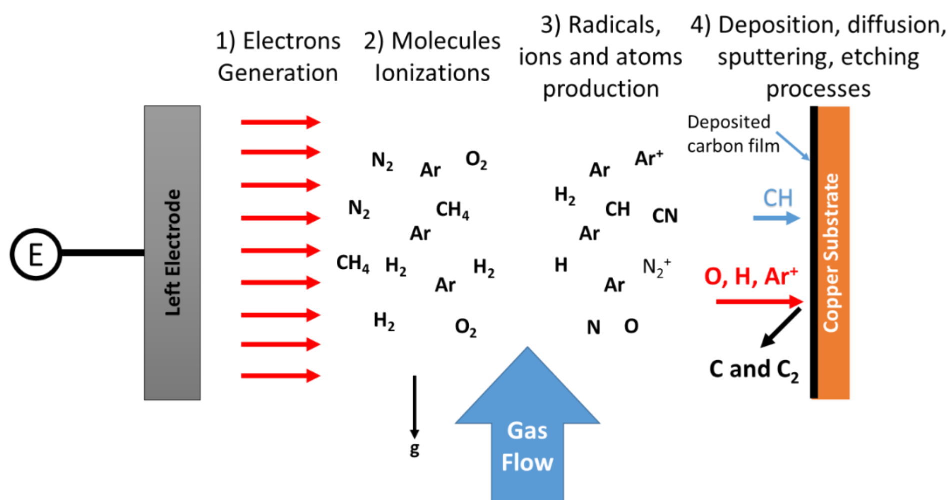

Figure 3.15: Proposed deposition mechanism of graphene on copper substrate during the roll-to-roll plasma CVD process.

3.3.4 Graphene Deposition at Higher Web Speeds

After optimization of graphene at a lower web speed (45 mm/min) in the previous sections, the effect of web speed on graphene deposition was studied for two cases for speeds up to about 959 mm/min (Fig. 3.16). The condition for Case 1 is similar to the optimized condition (31% H_2, 25% CH_4, 4% N_2, 1% O_2, 39% Ar, 9.2 mbar, and 750 W), whereas the condition for Case 2 is 33% H_2, 30% CH_4, 10% N_2, 8% O_2, 19% Ar, 15 mbar, and 1250 W. The quality in the optimized condition (Case 1) decreases with increased web speed (Fig. 3.16(a)). At lower plasma power (750 W), longer residence time is needed to increase the substrate temperature, and supply sufficient

carbon for deposition. The decrease of graphene quality with web speed for Case 1 is consistent with previous reported results, but for a thermal CVD system [16]. However, the I_D/I_G ratios of both sides in Case 2 are independent of web speed because of the high-power plasma (Fig. 3.16 (a)). The high plasma power of Case 2 is sufficient to heat the substrate and produce active carbon species for graphene deposition, even at higher web speed.

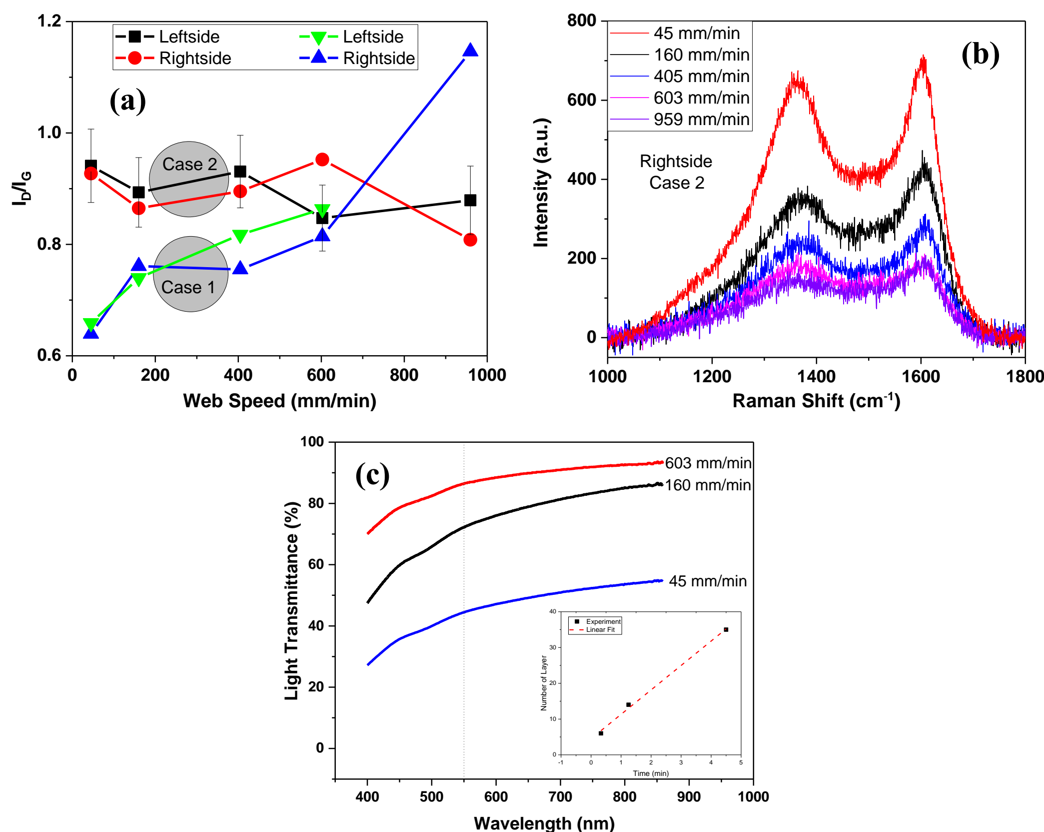

Figure 3.16: (a) The variation of I_D/I_G ratio with web speed. (b) Raman spectra of Case 2 samples at different speeds. (c) Optical transmittance of graphene of Case 2 as a function of web speed, inferring a deposition rate of 7 (±1) layers/min as plotted in the inset.

Figure 3.17 presents SEM images for Case 2 at different speeds compared to a static experiment conducted at a longer residence time of 30 min. The SEM image of the longest residence time shows an area where the carbon film has peeled off, indicating the deposition of thicker carbon layers. We also noticed the appearance of microcracks in the graphene film for Case 2 at speed of 45 mm/min. These negative features could be attributed to the tension during the roll-to-roll process, since the cracks are perpendicular to the direction of rolling [166]. A higher resolution SEM image of the crack region is shown in Fig. 3.17 in which wrinkles and microcracks exist. The tension during the roll-to-roll processing accompanied with heating of the Cu foil could

lead to microcracks due to the different thermal expansion coefficients between the copper substrate and the graphene [138].

On the other hand, copper grains are apparent at high speeds, indicating a lower thickness of the deposited films. Moreover, the presence of the copper grain boundaries for the higher speed sample suggest that the substrate was heated to a temperature sufficient to recrystallize the Cu grains. Furthermore, Raman spectra show a decrease of the D- and G-peak intensities with increased web speed for samples from Case 2 as shown in Fig. 3.16 (b). These results suggest that graphene can be grown at about 1 m/min using plasma as a heat source.

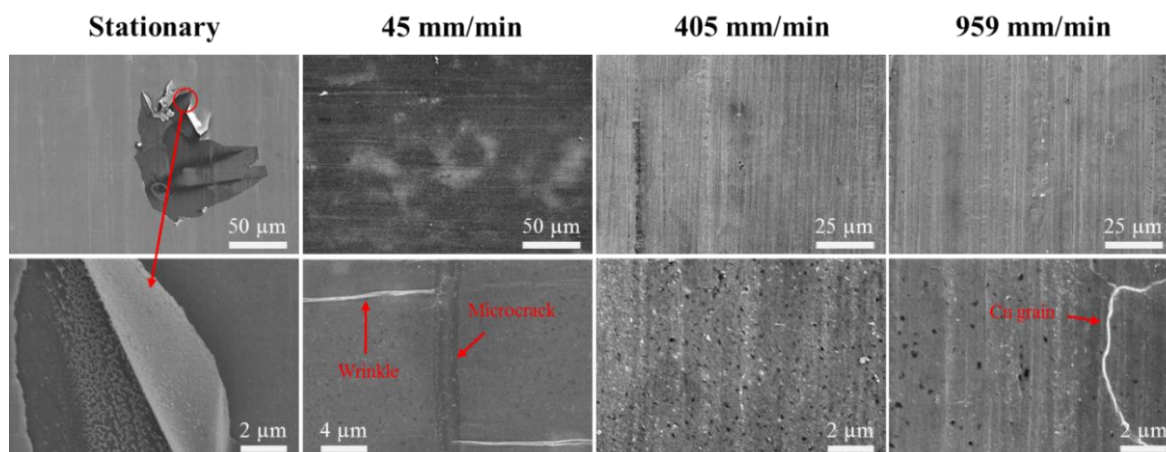

Figure 3.17: SEM images of graphene on copper foil substrate as a function of web speed.

These results reveal a tradeoff between quality and throughput of graphene production for samples prepared at lower plasma power (e.g., Case 1 in this work) or by thermal CVD. For example, the I_D/I_G ratio increases from 0.1 at 25 mm/min to 1.0 at 500 mm/min in thermal CVD as reported by Polsen et al. [16]. The decrease of the quality with increased speed is due to limitations in growth kinetics and graphene nucleation in thermal CVD systems or lower plasma power (and different plasma conditions) as shown for Case 1. However, due to active species in the plasma that accelerate the graphene deposition rate, the plasma CVD produce graphene with similar quality as a function of speed until about 1 m/min for Case 2 (Fig. 3.16).

Graphene deposition in our roll-to-roll plasma CVD system has higher throughput due to a high growth rate of graphene on copper foil. In our system, the estimated growth rate of graphene is 7 (±1) layers/min for Case 2. This rate is estimated from optical transmittance measurements as evident in Fig. 3.16(c) by considering a 2.3% decrease of light transmittance for each layer of graphene [29]. This high growth rate is due to the abundantly active radical species in the plasma.

Similarly, Kato et al. [167] showed that growth rate in plasma CVD is two to three orders of magnitudes higher than thermal CVD. Thus, plasma resources have the advantages of higher throughput for graphene deposition with lower input power compared to thermal CVD, as summarized in Table 3.1. For instance, graphene can be deposited at a rate of 5-500 mm/min for thermal CVD systems whereas this rate can be raised to about 1000 mm/min using plasma CVD as reported here. However, graphene quality from plasma CVD is lower than for thermal CVD systems with negligible values of I_D/I_G compared to I_D/I_G values of 0.5 and 0.7 in plasma CVD systems as reported by Yamada et al. [62] and the results of this work, respectively. Such moderate film quality limits the benefits of graphene production from plasma CVD to applications with less stringent demand of quality, such as oxidation barriers for metals, but not for high quality applications in electronics and photonics [12].

3.3.5 Conclusion

This work takes a statistical approach to scale up graphene production in a custom-built roll-to-roll rf plasma CVD system. Even though the quality of graphene is limited by the plasma in this process, a wealth of information obtained demonstrates the tremendous benefits of combining statistical analysis and *in situ* process monitoring. Based on the developed surrogate models, the quality of graphene is largely influenced by gas pressure, nitrogen, oxygen, and plasma power. Moreover, the results from OES suggest correlations of CH species to low defects, while the presence of Ar^+, C_2, H_α, CN, and O correlate to high defects. This work provides fundamental physical insights for the design and characterization of high-throughput plasma CVD systems for graphene and other 2D materials manufacturing. Further development is needed to obtain higher quality of graphene in plasma systems by minimizing and controlling ion and molecular fluxes to the substrate as discussed in the following chapters.

4. THERMAL AND SPECTROSCOPIC ANALYSIS OF PLASMA ROLL-TO-ROLL DEPOSITION OF GRAPHENE

4.1 Motivation and Background

As described in the previous chapter, large-area deposition of graphene on Cu has been widely used due to the lower cost of Cu, self-limiting graphene growth, and ease of graphene transfer to arbitrary substrates [13]. Because of low carbon solubility in Cu, graphene growth is driven by catalytic reactions that occur at high temperatures (i.e., 900-1000 ℃) [168]. Accordingly, establishing uniform temperature across the Cu substrate is crucial to creating graphene with uniform quality and thickness over the substrate [37]. The substrate temperature is critical for graphene growth kinetics in a R2R setup because the substrate temperature depends significantly on web speed. For example, previous results reported a reduction of graphene quality with increased web speed [16], [23], whereas sufficient heating of the Cu substrate increased the graphene production rate [23], [138]. The lack of detailed understanding of the Cu foil temperature profile during R2R process limits full utilization of R2R CVD systems for large-scale graphene production.

The Cu foil temperature profile in a R2R process can be determined from analysis of a moving plate/web in a fluid medium. The heat transfer and fluid flow of a moving plate in a quiescent fluid medium have been modeled previously using boundary layer theory [169], [170]. However, thermal analysis within the moving plate itself was not included in the studies, since the plate was assumed to be isothermal. Afterwards, the temperature distribution of the moving plate/web was determined either by solving the coupled fluid and plate heat equations [171]–[173], or by using a prescribed heat transfer coefficient and solving the heat diffusion equation in the plate alone [174]–[178]. Consequently, the moving plate temperature was found to depend on web speed, material properties and flow conditions. However, the web temperature was not measured directly in these systems to validate the heat transfer models except for a limited case [179]. In this chapter, Cu foil temperature is measured from blackbody emission to validate the heat transfer model and to infer the convective heat transfer coefficient [180], [181]. Furthermore, the Cu foil temperature distribution is correlated to graphene growth quality on Cu foil during experiments to explore optimal growth conditions in the R2R process.

The purpose of this chapter is to determine Cu foil temperature distribution and how the temperature distribution impacts graphene growth in a R2R plasma CVD process. The heat transfer model includes convection with quiescent flow and plasma gas, radiation exchange with the chamber wall and the plasma electrodes, and conduction and advection associated with the moving foil. Combining the model and experimental results, the effects of the plasma power, web speed, and plasma length on the Cu foil temperature profile are studied during graphene growth. Raman spectroscopy is utilized to assess graphene quality as a function of process parameters to determine the optimum conditions for continuous R2R deposition of graphene. Such thermal analysis can be directly applied to other R2R processes to optimize and control around manufacturing objectives, such as interfacial stresses between the substrate and the deposited film [182], or the drying of wet films on polymers [183].

4.2 Experimental Setup

The R2R plasma CVD system used here is custom-designed to deposit graphene on a variety of flexible substrates. As-received copper substrate (annealed copper 110 from Basic Copper) was placed in the top free-moving winder, passed through the plasma region, and finally collected at the bottom driving winder (Figs. 3.1 and 4.1). After the system was evacuated, a gas mixture of 50:50 H_2:Ar by volume was introduced at 7 mbar to ignite the plasma at a power of 500 W. The pressure was then increased after a warm-up period of 15-20 minutes to 15 mbar, and CH_4 was introduced to the H_2/Ar mixture for graphene growth with flow rates of 150, 610 and 260 standard cubic centimeters per minute (sccm) for Ar, H_2, CH_4, respectively.

Experiments were conducted at plasma powers of 850, 1050, 1250 and 1450 W at a fixed gas pressure of 15 mbar. The power was supplied to two parallel electrodes to generate a capacitively coupled plasma (CCP) as illustrated in Fig. 4.1(a). The graphite electrodes have rectangular shapes with a length of 12.5 cm and a width of 5.0 cm. The electrodes can be rotated to produce a smaller plasma length of 5.0 cm, but a larger width of 12.5 cm. In both cases, the distance between the electrodes is fixed at 4.5 cm, whereas the distance between the right electrode and the foil is fixed at 1.5 cm. Web speed values of 0, 50, 150, 400 and 600 mm/min were assessed during the experiments with a speed uncertainty of 10%.

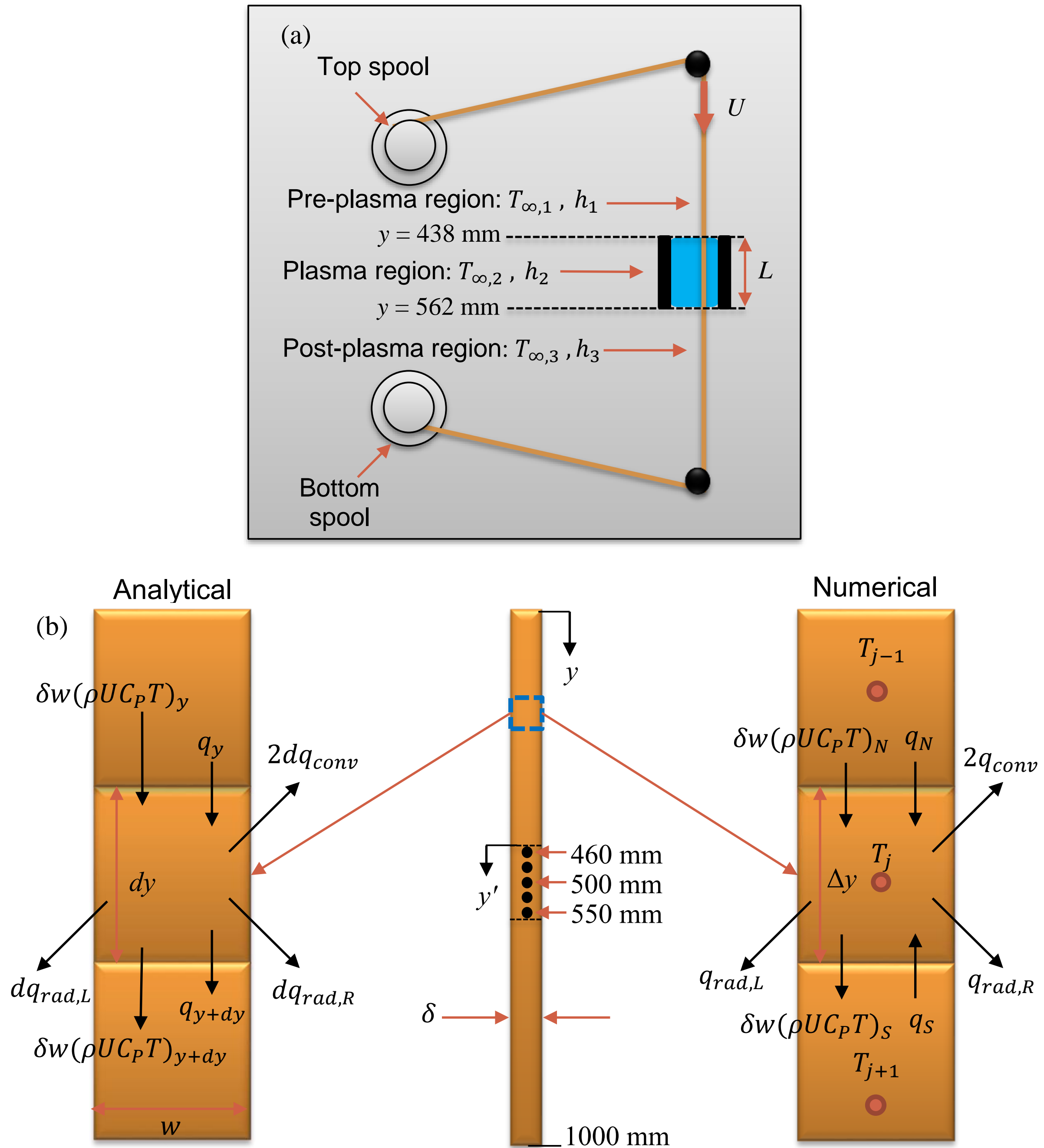

Figure 4.1: (a) Schematic of the roll-to-roll plasma CVD system showing the pre-plasma, plasma, and post-plasma regions during graphene growth. The plasma region starts at $y = 438$ mm ($y' = 0$ mm). (b) The modeling domain of the Cu foil starts from the top spool and ends at the bottom spool after graphene deposition in the plasma region. The positions of the temperature measurements of Cu foil in the plasma region are also indicated.

The temperature of the substrate was measured directly from the Cu foil emission using optical emission spectroscopy [23]. The emission is collected and collimated using 50.8 mm

diameter lenses, focused to a fiber optic held by a fixture that allows motion to a precise location along horizontal and vertical axes using Zaber translation stages. The spatial resolution of the emission is estimated to be approximately 2 mm. The fiber optic transmits the light to a spectrometer calibrated in the range of 650-850 nm using a mercury light source. The emission measurement is controlled by LightField software (from Princeton Instruments) to acquire a high-resolution emission in a broad wavelength range. Equally-spaced spectra, of about 15 nm are individually measured by rotating the grating to cover the whole 650-850 nm range. The discontinuity between each step, which arises from the difference in the grating diffraction efficiency, is corrected by applying an intensity calibration utilizing an intensity-calibration light source. The intensity calibration plays a vital role also in correcting the variation in the grating, the CCD camera efficiencies, and the optical components' transmission to accurately measure the baseline emission from the substrate over the 650-850 nm spectral range.

The emission from the high-temperature Cu substrate in the plasma region can be fitted to Planck's distribution, which depends on temperature (T) and wavelength (λ) as follows:

$$E(\lambda, T) = A + \frac{B}{\lambda^5} \frac{1}{\left[exp\left(\frac{hc}{\lambda k_B T}\right) - 1\right]} \tag{4}$$

where A is the linear offset of the spectrum, and B is a constant that represents Planck's constant (h), the speed of light (c), Cu emissivity and the contribution from the optical emission setup as described in Ref. [184]. Since Cu emissivity is nearly constant in the 650-850 nm wavelength range, the Cu foil is assumed to be a gray surface with an emissivity value of 0.04 [185]. The detector and the grating responses as a function of wavelength are included in the intensity calibration of the spectrometer. The temperature (T) and the constants (A and B) are found from a nonlinear least-squares fitting method using Matlab with an uncertainty in fitted temperature of less than 5%.

4.3 Heat Transfer Model

The Cu foil has a length of 1 meter starting from the top winder spool and ending at the bottom winder spool. From the Eulerian point of view, the Cu foil encounters three regions: pre-plasma, plasma, and post-plasma as illustrated in Fig. 4.1(a). Graphene is only deposited in the plasma region because of the abundant active carbon species interacting with the high-temperature substrate [23]. Gas flow, which is driven by buoyancy, is assumed to be isothermal and uniform

in each of the three regions. The gas temperatures in the pre- and post-plasma regions ($T_{\infty,1}$ and $T_{\infty,3}$, respectively) are assumed to be equal and have lower values than the gas temperature in the plasma region ($T_{\infty,2}$). The heat transfer coefficients in the three regions are derived from fitting the model to the measured Cu foil temperatures as discussed in Section 4.4. In addition, a steady-state flow condition is assumed in the analysis since chamber temperatures reach a steady-state and the Cu foil moves at a constant prescribed web speed. Because of the small substrate thickness and width (76 µm and 25.4 mm, respectively), the Biot number is below 0.01. Therefore, a one-dimensional fin model is developed to solve for the substrate temperature along the foil length using analytical and numerical approaches as explained next.

4.3.1 Analytical Model Derivation

The analytical model treats the three regions (pre-plasma, plasma, and post-plasma) separately, and the final Cu foil temperature distribution is found by combining the three regions with appropriate boundary conditions (Fig. 4.1). To simplify the analysis of the boundary conditions in the analytical model, the coordinate system is shifted to start from the plasma region as marked in Fig. 4.1(b). Applying the heat transfer energy balance in a control volume in the pre-plasma region (Fig. 4.1(b)) results in the following equation:

$$q_y - q_{y+dy} + \delta w(\rho U C_P T)_y - \delta w(\rho U C_P T)_{y+dy} - 2dq_{conv} - dq_{rad,R} - dq_{rad,L} = 0 \quad (5)$$

which represents axial conduction ($q_y - q_{y+dy}$), advection due to the moving foil ($\delta w(\rho U C_P T)_y - \delta w(\rho U C_P T)_{y+dy}$), convection from both sides of the foil to the ambient gas (dq_{conv}), and radiation from the right and left sides of the foil to the chamber wall ($dq_{rad,R}$ and $dq_{rad,L}$, respectively). Here, δ is the substrate thickness, w is the width of the substrate, ρ is the substrate density, U is the web speed, C_P is the specific heat and T is the foil temperature. Expanding each term and rearranging (see Appendix B.1) yields the final simplified differential equation:

$$\frac{d^2\theta_1}{dy^2} - a\frac{d\theta_1}{dy} - m_1\theta_1 = 0 \quad (6)$$

where $\theta_1 = \left(T - T_{\infty,1}\right)$, $a = \frac{\rho U C_p}{k}$ and $m_1 = \frac{2h_1}{\delta k} + \frac{h_{rad,R,1}}{\delta k} + \frac{h_{rad,L,1}}{\delta k}$. To obtain closed solutions, we assume constant material properties by region, as discussed below. Specific heat (C_p) and thermal conductivity (k) values at $T_{\infty,1}$ are taken from Ref. [185]. h_1 is the linearized heat transfer

coefficient in the pre-plasma region, and $h_{rad,R,1}$ and $h_{rad,L,1}$ are the radiative transfer coefficients from the right and left sides of the foil in the pre-plasma region, respectively (see Appendix B.1). The solution of Eq. (6) is:

$$\theta_1(y) = C_1 \exp\left(\frac{1}{2}y\left(\sqrt{a^2+4m_1}+a\right)\right) + C_2 \exp\left(-\frac{1}{2}y\left(\sqrt{a^2+4m_1}-a\right)\right) \quad (7)$$

A similar energy balance analysis in the post-plasma region leads to the same differential equation (Eq. (6)) but with $\theta_3 = \left(T - T_{\infty,3}\right)$ and m_3, instead of θ_1 and m_1, respectively. Also, specific heat (C_p) and thermal conductivity (k) values at a constant temperature of $T_{\infty,3}$ are used. Thus, the general solution of the temperature distribution in the post-plasma region is:

$$\theta_3(y) = C_3 \exp\left(\frac{1}{2}y\left(\sqrt{a^2+4m_3}+a\right)\right) + C_4 \exp\left(-\frac{1}{2}y\left(\sqrt{a^2+4m_3}-a\right)\right) \quad (8)$$

Finally, the energy balance in the plasma region encompasses heating from the plasma constituents and radiation losses to the two electrodes. The heat transfer from the plasma accounts for substrate heating from electrons, neutrals, and ions as well as surface reactions [186]. The heat fluxes depend on electron temperature, electron number density, reaction rates, and gas temperature, which are unknown and challenging to measure with the exception of plasma gas temperature. Nevertheless, plasma processes can be lumped into an effective heat transfer coefficient in the plasma region (h_2), which is used as a fitting parameter between the simulated and measured Cu foil temperatures. The radiation exchange between the Cu foil and the two electrodes, with opposite direction to convection, is derived in Appendix B.2, and the linearized radiative transfer coefficients from Cu foil to the right and left electrodes are included in $h_{rad,R,2}$ and $h_{rad,L,2}$, respectively. Therefore, the final differential equation for temperature in the plasma region is similar to Eq. (6), but with $\theta_2 = \left(T - T_{\infty,2}\right)$ and $m_2 = \frac{2h_2}{\delta k} - \frac{h_{rad,R,2}}{\delta k} - \frac{h_{rad,L,2}}{\delta k}$, instead of θ_1 and m_1, respectively. Similarly, the specific heat (C_p) and thermal conductivity (k) values are obtained at a fixed temperature of $T_{\infty,2}$. Thus, the temperature distribution in the plasma region is:

$$\theta_2(y) = C_5 \exp\left(\frac{1}{2}y\left(\sqrt{a^2+4m_2}+a\right)\right) + C_6 \exp\left(-\frac{1}{2}y\left(\sqrt{a^2+4m_2}-a\right)\right) \quad (9)$$

The above temperature distributions have six constants found by applying boundary conditions:

1) Infinite fin boundary condition: $\theta_1(y' \to -\infty) = 0$, leading to $C_2 = 0$ in Eq. (7).
2) Infinite fin boundary condition: $\theta_3(y' \to \infty) = 0$, leading to $C_3 = 0$ in Eq. (8).
3) Temperature continuity at the interface of the pre-plasma and the plasma regions:

$$\theta_1(y' = 0) + T_{\infty,1} = \theta_2(y' = 0) + T_{\infty,2}$$

4) Heat flux continuity at the interface of the pre-plasma and the plasma regions:

$$k_1 \frac{d\theta_1(y' = 0)}{dy} = k_2 \frac{d\theta_2(y' = 0)}{dy}$$

5) Temperature continuity at the interface of the plasma and the post-plasma regions:

$$\theta_2(y' = L) + T_{\infty,2} = \theta_3(y' = L) + T_{\infty,3}$$

6) Heat flux continuity at the interface of the plasma and the post-plasma regions:

$$k_2 \frac{d\theta_2(y' = L)}{dy} = k_3 \frac{d\theta_3(y' = L)}{dy}$$

where L is the length of the plasma region, and the y-coordinate starts from $y' = y - 0.438$ m (Fig. 4.1(b)). The coordinate transformation simplifies the form of the constants C_1, C_4, C_5, and C_6, which are found by solving the linear equations from boundary conditions 3-6. Final expressions for the constants C_1, C_4, C_5, and C_6 are included in Appendix B.3. The final analytical solution of the Cu foil temperature becomes:

$$T(y') = T_{\infty,1} + C_1\, exp\left(\frac{1}{2} y'\left(\sqrt{a^2 + 4m_1} + a\right)\right) \quad \text{for } -0.438 \leq y' \leq 0 \tag{10}$$

$$T(y') = T_{\infty,2} + C_5\, exp\left(\frac{1}{2} y'\left(\sqrt{a^2 + 4m_2} + a\right)\right) + C_6\, exp\left(-\frac{1}{2} y'\left(\sqrt{a^2 + 4m_2} - a\right)\right) \quad \text{for } 0 \leq y' \leq L$$

$$T(y') = T_{\infty,3} + C_4\, exp\left(-\frac{1}{2} y'\left(\sqrt{a^2 + 4m_3} - a\right)\right) \quad \text{for } L \leq y' \leq 0.562$$

Equation (10) reverts to the infinite fin model when the web speed is set to zero (i.e., $a = 0$) [185].

4.3.2 Numerical Model Derivation

The substrate temperature distribution has also been solved numerically to incorporate non-linearities in the radiation heat transfer and material properties. The energy balance for a control volume of Cu substrate is shown in Fig. 4.1(b) in which conduction (q_N and q_S), advection ($(\delta w \rho U C_P T)_N$ and $(\delta w \rho U C_P T)_S$), convection ($q_{conv}$), and radiation ($q_{rad,R}$ and $q_{rad,L}$) are considered, leading to:

$$q_N + q_S + \delta w(\rho U C_P T)_N = \delta w(\rho U C_P T)_S + 2q_{conv} + q_{rad,R} + q_{rad,L} \tag{11}$$

The heat fluxes from the top and bottom cells (i.e., q_N and q_S, respectively) are assumed to vary linearly over each face of cell *"j"*: $q_N = \frac{kw\delta}{\Delta y}(T_{j-1} - T_j)$ and $q_S = \frac{kw\delta}{\Delta y}(T_{j+1} - T_j)$. In

addition, using the central differencing discretization scheme, the temperatures T_N and T_S of the neighboring cells are given by $T_N = \frac{(T_{j-1}+T_j)}{2}$ and $T_S = \frac{(T_{j+1}+T_j)}{2}$. Also, the convection term is $q_{conv} = h_i w \Delta y (T_j - T_{\infty,i})$ for i=1, 2, and 3, representing the pre-plasma, plasma and post-plasma regions, respectively. The factor of 2 in front of q_{conv} in Eq. (11) accounts for convection from both sides of the foil, which is assumed to be symmetric. Finally, the radiation from the substrate to the two electrodes and to the chamber wall of the right and left sides (i.e., $q_{rad,R}$ and $q_{rad,L}$, respectively) are derived in the Appendix B.4. The final linearized equation is:

$$a_j T_j = a_{j-1} T_{j-1} + a_{j+1} T_{j+1} + b \tag{12}$$

$$a_{j-1} = \frac{k\delta}{\Delta y} + 0.5(\rho U C_p \delta) \quad \text{and} \quad a_{j+1} = \frac{k\delta}{\Delta y} - 0.5(\rho U C_p \delta)$$

$$a_j = 2\frac{k\delta}{\Delta y} + 2h_i \Delta y + 2\frac{4\varepsilon_{Cu} \Delta y \sigma \left(T_j^*\right)^3}{(1-\varepsilon_{Cu})}$$

$$b = 2h_i \Delta y T_{\infty,i} + \frac{\varepsilon_{Cu} \Delta y \left(J_{Cu-R}^* + 3\sigma\left(T_j^*\right)^4\right)}{(1-\varepsilon_{Cu})} + \frac{\varepsilon_{Cu} \Delta y \left(J_{Cu-L}^* + 3\sigma\left(T_j^*\right)^4\right)}{(1-\varepsilon_{Cu})}$$

where the temperatures T_j, T_{j-1}, and T_{j+1} represent the center of the cell, and its top and bottom neighbors' temperatures, respectively (Fig. 4.1(b)). The number of the discretized cells is 10,000 with a cell size of Δy = 1x10^{-4} m. ε_{Cu} and σ are the Cu emissivity and Stefan-Boltzmann constant, respectively. A separate heat transfer coefficient (h_i) and gas temperature $(T_{\infty,i})$ are used for each region (i = 1, 2, and 3) for the pre-plasma, plasma and post-plasma, respectively. An iterative scheme solution is developed to update temperature-dependent properties (i.e., C_p and k), radiosity (J_{Cu-R}^* and J_{Cu-L}^* from the right and left sides of Cu foil, respectively) and temperature from the previous iteration (T_j^*) in Eq. (12). The solution converges when the relative difference between the temperature of the current and previous iterations is less than 10^{-4}.

4.4 Results and Discussion

4.4.1 Determination of Heat Transfer Parameters from Temperatures Measurements

Figure 4.2(a) shows emission spectra from the plasma with and without Cu foil. The emission spectrum without the inclusion of Cu foil exhibits only narrow spectral lines originating from active plasma species (such as Ar, Ar^+, H_2, and H). The plasma emission with the presence of Cu foil has similar narrow spectral lines, but with a broad baseline that represents blackbody

emission from the Cu substrate. In addition, the broad baseline varies considerably along the Cu foil in the plasma region at a plasma power of 1250 W and a web speed of 0 mm/min, as presented in Fig. 4.2(b). The Cu foil has stronger emission near the middle of the plasma region (i.e., 500 mm) compared to the position near the edge of the plasma region (i.e., 460 mm). Fitting spectra to Eq. (4) yields temperatures of 1190 K at 500 mm, and 1140 K at 460 mm as presented in Fig. 4.2(b). At 550 mm, which is near the interface of the plasma and the post-plasma regions, the Cu foil temperature is 1115 K. Hence, the Cu foil temperature reaches a maximum at the plasma centerline, but then decays toward the plasma edges because of heat loss to the regions outside the plasma.

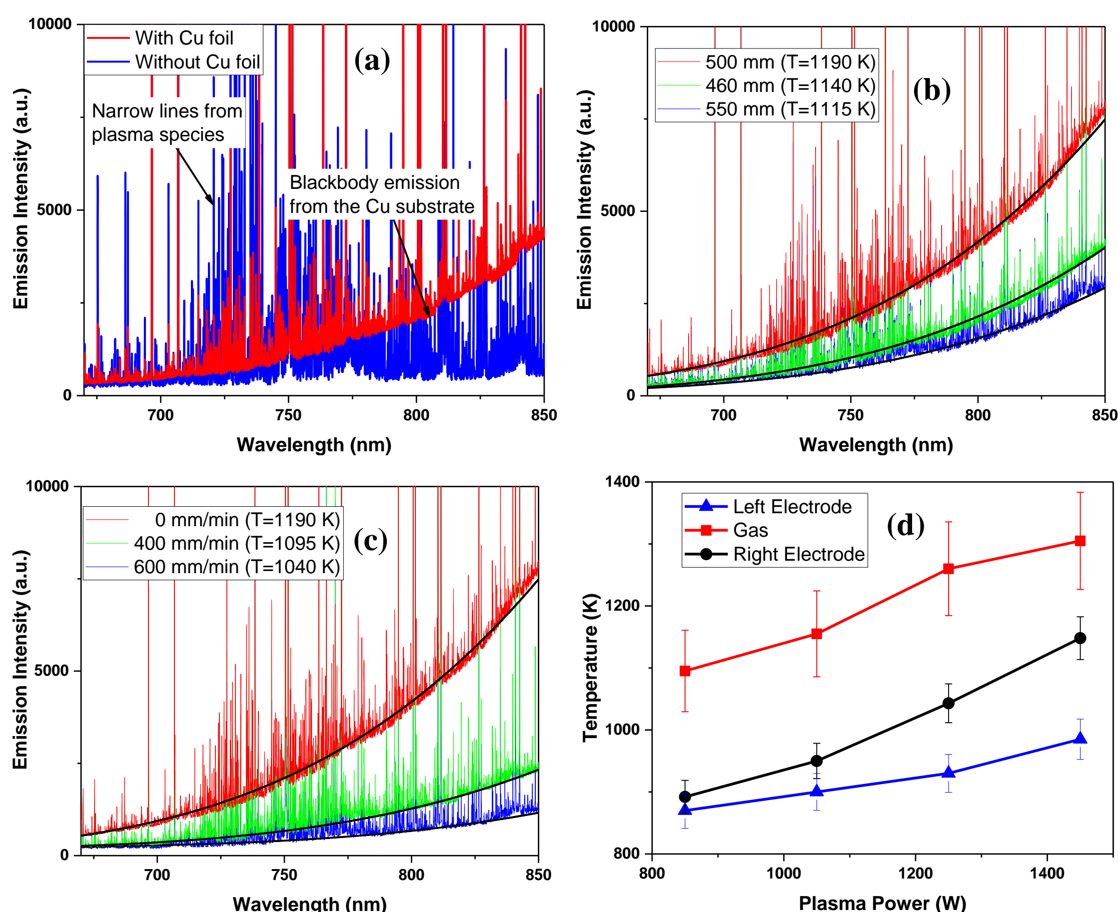

Figure 4.2: (a) Emission spectra from the plasma with and without the Cu substrate, showing the broad baseline with the inclusion of Cu substrate. (b) The variations of Cu substrate emission with vertical positions in the plasma region at a fixed plasma power of 1250 W and a web speed of 0 mm/min. (c) The effects of web speed on Cu foil emission from the same region (500 mm) and at constant plasma power (1250 W). (d) The gas and electrodes measurements as a function of plasma power.

Moreover, the Cu foil blackbody emission decreases with increased web speed due to the cooling effects from the advection term, as shown in Fig. 4.2(c). For example, the peak Cu foil temperature decreases from 1190 K at 0 mm/min, to 1095 K at 400 mm/min and finally to 1040 K at 600 mm/min at a fixed plasma power of 1250 W. Therefore, the precise determination of the Cu foil temperature serves to validate the temperature distribution from the heat transfer model as discussed in the next section.

The electrodes temperatures, which were measured from near-IR emission, increase linearly with plasma power as shown in Fig. 4.2(d). The right electrode, which is closer to the Cu foil, has higher temperatures than the left electrode (Fig. 4.1(a)). Also, the gas temperature in the plasma region ($T_{\infty,2}$) rises with increased plasma power as shown in Fig. 4.2(d). Gas temperature is determined from the rotational temperature of H_2 using the Fulcher band in the range 601-611 nm as reported in Ref. [187]. The rotational temperatures from H_2 are assumed to be in thermal equilibrium with the translational gas temperature in this study and is discussed in Chapter 6. The gas and the electrodes' temperatures remain nearly constant along the length of the plasma, within an uncertainty of less than 10%. The gas temperature was raised to 1160 K for the case of 850 W and 0 mm/min (instead of 1095 K for the remaining web speeds at 850 W) to fit the numerical model to the Cu foil experimental temperature measurements. Lastly, the gas temperatures in the pre- and post-plasma regions ($T_{\infty,1}$ and $T_{\infty,3}$, respectively) are assumed to be similar and equal to the chamber's single-point gas temperature (T_{surr}), measured with a thermocouple. The thermocouple temperature varies linearly with plasma power, and has a value of 313 K at 850 W and 332 K at 1250 W.

After obtaining the Cu foil, electrode, and gas temperatures at different process conditions, the Cu foil temperature distribution can be determined from both analytical and numerical models as presented in Fig. 4.3(a). The web speed and plasma region length in Fig. 4.3(a) are 0 mm/min and 12.5 cm, respectively. Both models have identical temperature profiles when the radiation heat transfer is neglected. The Cu foil temperature is initially equal to the gas temperature ($T_{\infty,1}$) and then increases gradually in the pre-plasma region until it suddenly rises near the plasma region because of heat conduction from the Cu foil in the plasma region. The temperature maximizes at 1255 K in the middle of the plasma region due to a high gas temperature of 1260 K and the reactions of the Cu foil with ions, electrons, and intermediate species. The high-temperature

environment of the plasma allows for sufficient Cu foil heating without the use of supplemental heating commonly used in other R2R systems. After leaving the plasma region, the foil temperature declines steadily in the post-heating region until it reaches the gas temperature ($T_{\infty,3}$).

The maximum Cu foil temperature decreases by approximately 10 and 70 K by including the radiation terms in the analytical and numerical models, respectively (Fig. 4.3(a)). This temperature drop is attributed to heat loss by radiation from the high-temperature substrate to the lower-temperature wall and electrodes [188]. The difference between both models when radiation heat loss is included arises from the simplifications made in the analytical model to linearize the radiation terms in order obtain a closed-form solution of the Cu foil temperature. The larger temperature drop in the numerical model after including the radiation heat transfer is attributed to the higher heat loss by radiation which was derived more rigorously in the numerical model (see B.4 in Appendix B). Therefore, the analytical model including the radiation terms (the "analytical model" in the reminder of this work) is used to qualitatively clarify the trends of the Cu foil temperature with variations in process conditions. On the other hand, the numerical model with the radiation heat transfer (the "numerical model") is used to derive the actual substrate temperature distribution.

The heat transfer coefficients in the three regions (h_1, h_2, and h_3) play crucial roles in determining the Cu foil temperature distribution. Due to the complex fluid flow driven by buoyancy in the plasma, the values of h_1, h_2, and h_3 are derived from fitting the temperature profile from the numerical model to the measured foil temperatures [180]. The Cu foil temperatures measured along the plasma region at 0 mm/min web speed and 1250 W plasma power are shown in Figs. 4.3 (b) and (c). The measured foil temperatures are compared to the temperature profiles from the numerical model with different values of h_1 and h_3, as presented in Fig. 4.3(b). The higher the value of h_1 and h_3, the lower the foil temperatures in the pre- and post-plasma regions, respectively, due to enhanced cooling from the lower temperature gas in these regions. Therefore, the best fit value for h_1 and h_3 is 5 W/m^{2}K, which is kept as a fixed value in this work.

Next, the heat transfer coefficient in the plasma region (h_2) is estimated from fitting the temperature profile from the numerical model to the measured Cu foil temperatures in the plasma at web speed of 0 mm/min and a fixed plasma power of 1250 W, as shown in Fig. 4.3(c). The Cu foil temperature increases with increased h_2, and has best fit value of 64 W/m^{2}K, which is higher than the convective heat transfer coefficients in the other regions due to intense heating from the

active and energetic plasma gas. Hence, h_2 is used as a fitting parameter for the numerical model at different plasma powers, plasma lengths, and web speeds. The error in estimating heat transfer coefficients from this method is approximately 7% [181].

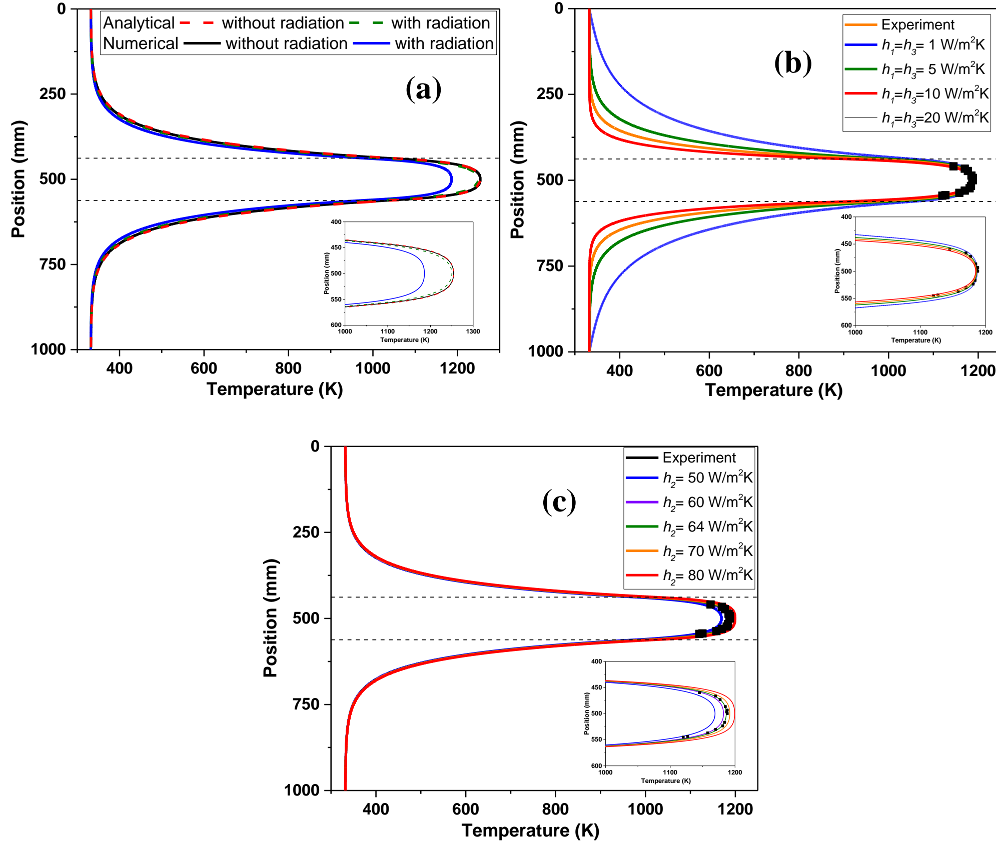

Figure 4.3: (a) Cu foil temperature distributions from the analytical and numerical models with and without the radiation term. The effects of (b) h_1 and h_3, and (c) h_2 on the Cu foil temperature profiles from the numerical model.

4.4.2 Effects of Web Speed and Plasma Power on Cu Foil Temperature Profile

Figure 4.4(a) shows excellent agreement between the fitted numerical model and measurements of the Cu foil temperature at different web speeds at a plasma power of 1250 W. As web speed increases, the temperature profile becomes asymmetric with lower and higher temperatures in the pre- and post-plasma regions, respectively. First, the temperatures in the pre-plasma region decrease with increased web speed due to the higher value of the exponent in Eq. (10) (i.e., $\sqrt{a^2 + 4m_1} + a$) since $a = \frac{\rho U C_p}{k}$, where U is the web speed. As the web speed increases, higher heat is carried downward by the moving foil. Because heat advection has an opposite

direction to the heat conduction by the foil in the pre-plasma region, the Cu foil temperature decreases with increased web speed.

On the other hand, the exponent in the post-plasma region in Eq. (10) (i.e., $\sqrt{a^2 + 4m_3} - a$) decreases with increased web speed, resulting in higher Cu foil temperature. In other words, the Cu foil needs a longer distance to cool to the ambient gas temperature ($T_{\infty,3}$) as web speed increases [179], [188], [189]. For example, the Cu foil temperatures at higher web speeds of 400 and 600 mm/min decline sharply near the bottom spool which is assumed to be at equilibrium with the ambient gas (Fig. 4.4(a)). In the post-plasma region, both heat advection and conduction by the foil occur in the same direction, resulting in a Cu foil temperature rise with increased web speed.

The peak temperature in the plasma region decreases at a rate of 0.12 K/(mm/min) with increased web speed due to the cooling effect provided by the moving foil. Furthermore, this peak temperature shifts downstream as web speed increases at a rate of 0.1 mm/(mm/min) as confirmed by the temperature measurements in the inset of Fig. 4.4(a). Hence, the temperature of the foil suffers from less uniformity in the plasma region with increased web speed. Similar effects of web speed on Cu foil temperature are observed at a lower plasma power of 1050 W as presented in Fig. 4.4(b). However, the Cu foil temperature exhibits lower temperature values because of the reduction in electron number density and electron temperature with decreased plasma power [187], that also decrease the plasma gas temperature ($T_{\infty,2}$) as shown in Fig. 4.2(d).

Figure 4.4(c) illustrates that, at a constant plasma power, h_2 decreases sharply when web speed is raised from 0 to 150 mm/min followed by a gradual decrease with a further increase in web speed. For example, h_2 is 64 W/m^{2}K at 0 mm/min, whereas it is reduced to 35 W/m^{2}K at 600 mm/min under the same plasma power of 1250 W. This reduction in h_2 with increased web speed could be explained from a heat transfer point of view as follows. The fluid flow between the electrodes away from the substrate is generally driven upward by buoyancy. However, since the foil moves downward, the fluid adjacent to the moving foil is inclined to flow downward due to the viscous impact from the foil [189]. Thus, the colder Cu foil is expected to entrain more low-temperature gas near the substrate with increased web speed leading to a minimized h_2. Indeed, the plasma gas temperature measured near the Cu foil region is found to decrease slightly with increased web speed. Furthermore, a recirculation zone of the fluid flow could appear near the foil

leading to a decrease in heat transfer between the fluid and the foil as reported by Choudhury and Jaluria [189].

Furthermore, h_2 takes higher values with increased plasma power at a constant web speed reflecting the enhanced interaction between the plasma gas and the foil (Figure 4.4(c)). Due to the larger temperature difference between the plasma and ambient regions with raised plasma power, the flow velocity is increased leading to higher h_2 with increased plasma power. For example, the plasma gas temperature ($T_{\infty,2}$) increases considerably from 1155 K at 1050 W to 1260 K at 1250 W whereas the ambient gas temperature ($T_{\infty,1}$ and $T_{\infty,3}$) rises slightly from 323 K to 332 K in the same plasma power ranges. Therefore, the flow velocity has higher values at 1250 W than 1050 W because of the greater temperature difference between the plasma and ambient regions at 1250 W leading to greater h_2 with increased plasma power (Fig. 4.4(c)). Results demonstrate the substantial impact web speed has on Cu foil temperature, which in turn affects graphene growth.

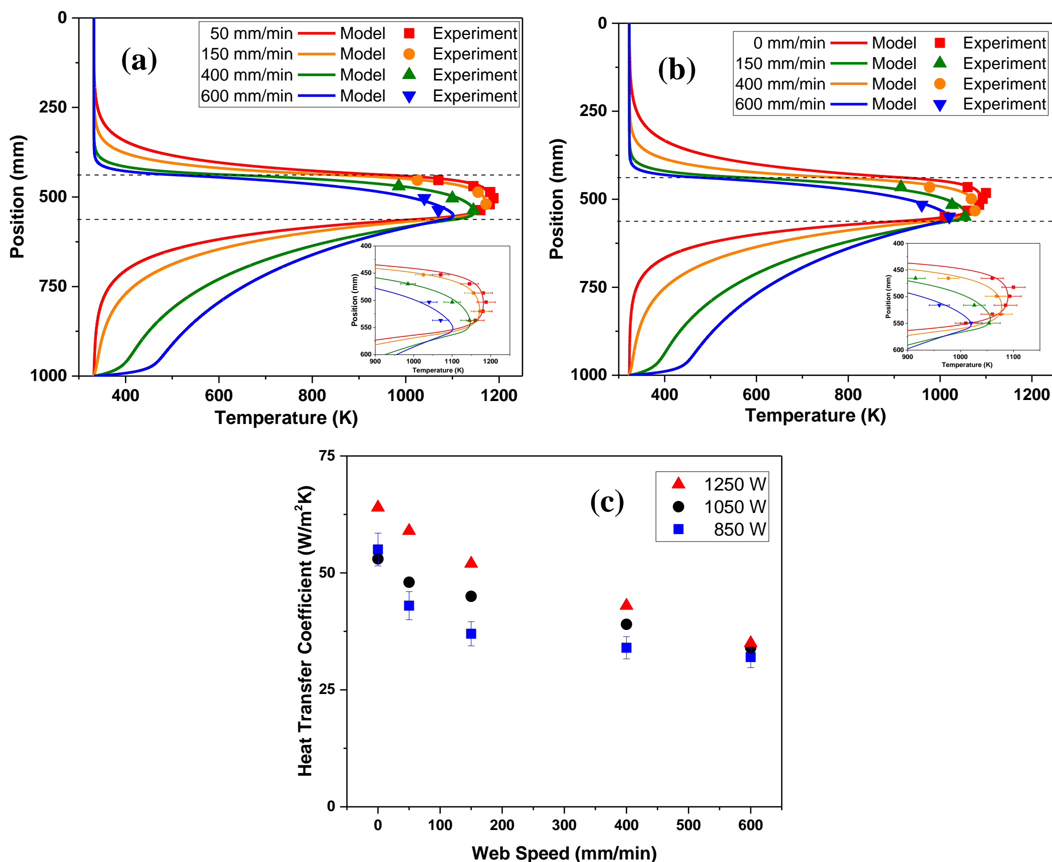

Figure 4.4: The Cu foil temperature distribution from the numerical model compared to the measured Cu foil temperatures in the plasma region at (a) 1250 W and (b) 1050 W at various web speeds. (c) Heat transfer coefficient in the plasma (h_2) as a function of plasma power and web speed.

4.4.3 Effects of Web Speed and Plasma Power on Graphene Growth

Graphene deposition is primarily affected by the Cu foil temperature distribution as a function of plasma power and web speed. Here, Raman spectroscopy is used to quantify the quality of graphene deposited at various process conditions. Graphene has three principal Raman peaks: D at 1350 cm^{-1}, G at 1580 cm^{-1} and 2D at 2700 cm^{-1} as shown in Fig. 4.5(a). The D-peak indicates graphene defect density, whereas the G- and 2D-peak are associated with graphitic lattice structure [145]. Thus, the D and G peak ratio (I_D/I_G), which indicates graphene quality, decreases exponentially with increased web speed, and reaches an asymptotic value at higher web speeds depending on the plasma power, as illustrated in Fig. 4.5(b). The I_D/I_G ratio is higher with increased plasma power because of the enhanced ion bombardment of the Cu foil [23]. For instance, the I_D/I_G ratio decreases from 1.9 at 0 mm/min to 0.8 at 600 mm/min at 1250 W, whereas the I_D/I_G ratio falls from 1.6 to 0.7 in the same web speed range but with a reduced plasma power of 850 W.

The decline of the I_D/I_G ratio with increased web speed is contrary to the results of a R2R thermal CVD system in which the I_D/I_G ratio is raised from 0.1 at 25 mm/min to 1.0 at 500 mm/min [16]. Unlike thermal CVD, graphene grown in plasma CVD is negatively affected by ion bombardment [53]. Also, these results are opposite to the results of Case 1, but almost similar to Case 2 discussed previously in Chapter 3 which indicate the importance of plasma conditions in determining graphene quality as a function of web speed. Thus, lowering the residence time of the Cu foil in the plasma region improves graphene quality in this case. Previous work [165], [190] found that pristine graphene quality decreases with increased ion bombardment dose. The ion dose is defined as $dose = \frac{P}{WU}$ where P is the plasma power, W is the electrode's width, and U is the web speed [191]. Similarly, the I_D/I_G ratio in our work increases with higher ion dose as a consequence of either increasing the power or lowering the web speed (Fig. 4.5(b)).

Moreover, the I_D/I_G ratio reduction with minimized ion dose indicates an increase of the in-plane crystalline size (L_a) following the correlation: $\frac{I_D}{I_G} = \frac{C(\lambda)}{L_a}$ where $C(\lambda) = 2.4\text{x}10^{-10}\lambda^4$, and λ is the laser wavelength excitation in nm [147], [149]. In our setup, graphene growth and defects by ion bombardment compete and occur simultaneously which suggests the enlargement of L_a with increased web speed or decreased plasma power, indicating minimized defects density in the graphene lattice. For example, L_a increased from 11 nm at 0 mm/min to 24 nm at 600 mm/min for a plasma power of 1250 W. Because of the presence of strong ion bombardment in the plasma

could not be eliminated previously to minimize the I_D/I_G ratio, the objective here is to maximize graphene quality in the R2R process by improving the 2D peak.

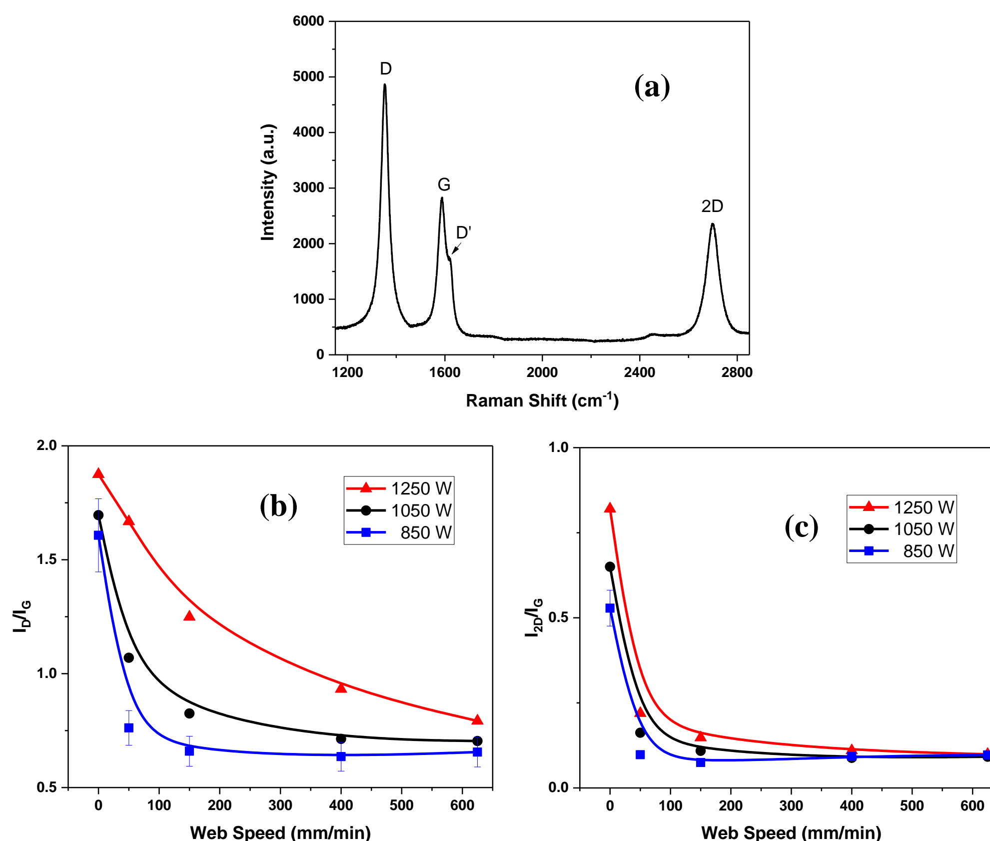

Figure 4.5: (a) A Raman spectrum of graphene at 1250 W and 0 mm/min showing the prominent peaks of graphene. (b) The I_D/I_G peak ratio and (c) The I_{2D}/I_G peak ratio as a function of the web speed at different plasma powers.

The ratio of the 2D and G peaks (I_{2D}/I_G) is correlated to the number of graphene layers, since the 2D peak is sensitive to the electron structure of graphene, which depends on the number of graphene layers [146]. Additionally, the 2D peak is a signature of graphene which was utilized to distinguish graphene from other carbon nanostructures [192]. Figure 4.5(c) shows the decline of the I_{2D}/I_G ratio from 0.8 at 0 mm/min to 0.2 at 50 mm/min at a constant plasma power of 1250 W. After that, the I_{2D}/I_G ratio decreases gradually with increased web speed and reaches an asymptotic value of approximately 0.1. The same trend of the I_{2D}/I_G ratio is observed at the lower plasma powers, but with lower overall I_{2D}/I_G ratio values. Since the number of graphene layers increases with residence time [23], [62], we expected a higher value of the I_{2D}/I_G ratio with increased web speed. However, the opposite is observed in the results of Fig. 4.5(c), suggesting the presence of a weak coupling between graphene layers as commonly found in graphene samples

from CVD systems [20]. Instead, the increase of the I_{2D}/I_G ratio with increased plasma power confirms a direct correlation between the I_{2D}/I_G ratio and the Cu foil substrate temperature [46], [59].

The variation of the I_{2D}/I_G ratio with web speed found here is similar to previous results in a R2R thermal CVD system [16]. The reason for the I_{2D}/I_G ratio decrease is attributed to the decrease of Cu foil temperature due to the advection of the moving film as presented previously in Figs. 4.4 (a) and (b). The decrease in Cu foil residence time in the plasma region with increased web speed could diminish the growth kinetics, especially at lower Cu foil temperatures at which the graphene growth rate minimizes [167]. For example, the I_{2D}/I_G ratio values remain around 0.1 at a reduced plasma power of 850 W with web speeds of 50 mm/min and higher (Fig. 4.5(c)). However, as the plasma power increases, the decay of the I_{2D}/I_G ratio with increased web speed slows because of the raised Cu foil temperature. Thus, the graphitization processes are minimized at a lower substrate temperature and a shorter residence time because of less active C atoms at the Cu surface. As a result, the graphene films grown at high web speeds experience an incomplete formation of the graphene lattice, leading to the deposition of graphene-like films on the Cu foil [193], rather than fully formed graphene layers.

4.4.4 Effects of Plasma Length on Cu Foil Temperature Profile and Graphene Growth

In this section, the plasma length is reduced to approximately 5.0 cm using a smaller slit electrodes (but the width becomes about 12.5 cm) to study the influence of plasma length on Cu foil temperature and graphene growth. The given configuration is referred to as “horizontal”, whereas the setup discussed in the previous sections with plasma length of 12.5 cm and width of 5.0 cm is donated as “vertical”. Due to the reduced plasma length, the temperature distribution of the horizontal configuration has a narrower profile with lower temperature values than the vertical setup, as shown in Fig. 4.6(a). Thus, the difference between the Cu foil temperatures in both configurations becomes larger at positions away from the plasma centerline. For instance, the temperature difference increases from 55 K around 500 mm to 225 K at 530 mm at a plasma power of 1250 W. Therefore, the Cu foil experiences a lesser temperature distribution uniformity in the horizontal configuration because of the shorter plasma slit length.

Figure 4.6(b) presents the Cu foil temperature profile of the horizontal configuration at a plasma power of 1150 W and different web speeds. The Cu foil temperature increases gradually

in the pre-plasma region followed by a temperature rise in the plasma region which lasts for a shorter length until the temperature decays in the post-plasma region. Similar to the vertical configuration, the increase of the web speed reduces the temperature in both the pre-plasma and plasma regions, whereas the temperature in the post-plasma region increases (Fig. 4.6(b)). Remarkably, the position of the peak-temperature in the plasma region is shifted downstream as the web speed increases because of the heat advection of the moving foil, as confirmed by the measurements found in the inset of Fig. 4.6(b). For example, the measured Cu foil temperature near the plasma and the post-plasma interface (i.e., at 530 mm) rises from 955 K at 0 mm/min to 990 K at 150 mm/min because of the heat advection by the moving foil.

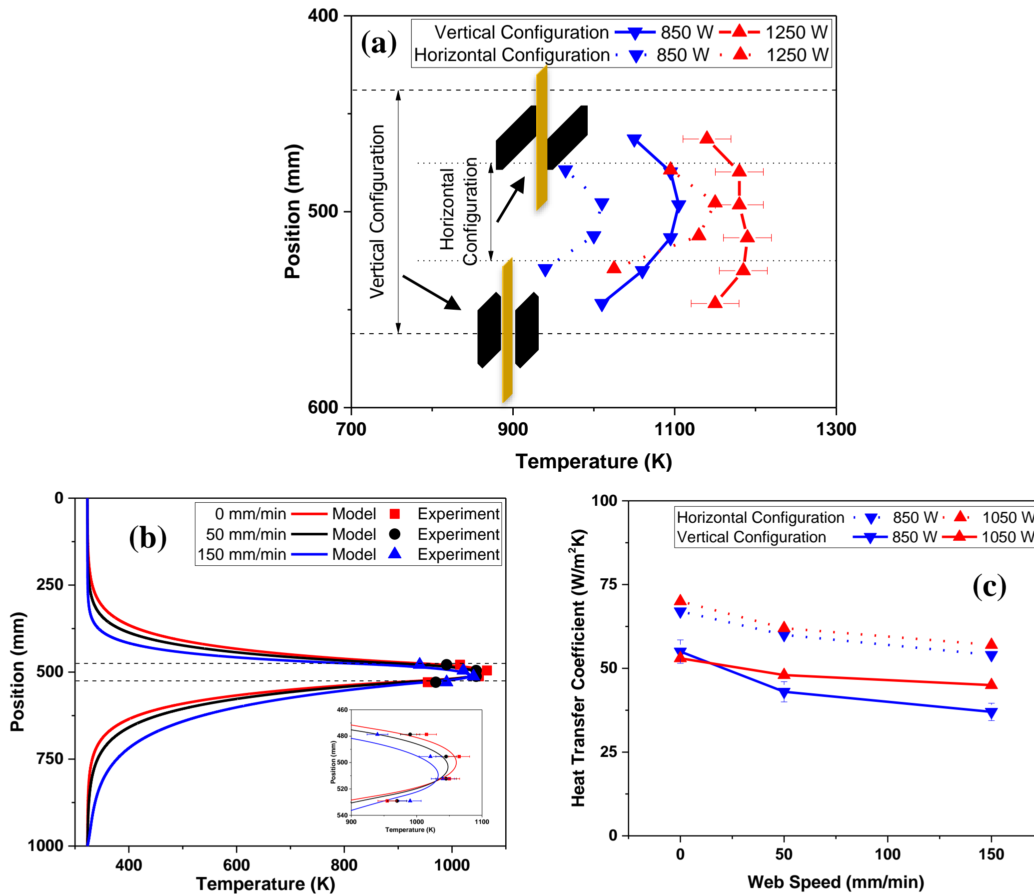

Figure 4.6: (a) Comparison between Cu foil temperature measurements from the vertical and horizontal configurations at various positions in the plasma region. The conditions are 850 and 1250 W at 0 mm/min. (b) Cu foil temperature at 1050 W and various web speeds for the horizontal setup. (c) The heat transfer coefficient in the plasma region (h_2) as a function of web speed and plasma power for the two configurations.

The convective heat transfer coefficients in the pre- and post-plasma regions (h_1 and h_3, respectively) are kept constant at 5 W/m^{2}K in Fig. 4.6(b). On the other hand, the convective heat

transfer coefficient in the plasma region (h_2) is derived by fitting the temperature profile from the numerical model to the experimental temperature measurements (Fig. 4.6(b)). As in the case of the vertical configuration in Fig. 4.4(c), h_2 decreases when either the plasma power is lowered or the web speed is raised as presented in Fig. 4.6(c). However, h_2 in the horizontal configuration has larger values than h_2 in the vertical configuration for all the cases included in Fig. 4.6(c). The enhanced value of h_2 in the horizontal configuration is attributed to the larger electrodes' width of 12.5 cm compared to the lesser width of 5.0 cm for the vertical configuration. Thus, the Cu foil, which has a width of 2.54 cm, is surrounded laterally by a larger volume of plasma gas in the horizontal configuration, which improves plasma gas interactions with the foil. Hence, the recirculation of the fluid flow near the moving foil might be reduced which leads to higher h_2 values in the horizontal configuration [189].

Table 4.1 lists the I_D/I_G and I_{2D}/I_G ratios for graphene grown on the Cu foil in both the horizontal and vertical configurations. The I_D/I_G ratio of both configurations decreases with either increased web speed or reduced plasma power, which is similar to the trend shown in Fig 4.5(b). However, the I_D/I_G ratio in the horizontal configuration exhibits slightly lower values than that of the vertical configuration, as discussed in Chapter 3, because of minimized ion bombardment with a reduced residence time in the plasma [191]. Nevertheless, the I_{2D}/I_G ratio, which has similar trends for both configurations, is higher for the vertical configuration, especially at 1050 W. The increase of the I_{2D}/I_G ratio is due to the higher and more uniform Cu foil temperatures in the vertical configuration, leading to accelerated graphene growth with increased Cu foil temperatures [167].

Table 4.1: Comparison between the I_D/I_G and I_{2D}/I_G ratios of graphene grown by the vertical and horizontal configurations at various plasma powers and web speeds.

Plasma power [W]	**Web speed [mm/min]**	**I_D/I_G ratio (vertical configuration)**	**I_D/I_G ratio (horizontal)**	**I_{2D}/I_G ratio (vertical configuration)**	**I_{2D}/I_G ratio (horizontal configuration)**
850	**0**	1.61	1.54	0.53	0.26
850	**50**	0.76	0.67	0.10	0.10
850	**150**	0.66	0.60	0.07	0.08
1050	**0**	1.70	1.72	0.65	0.43
1050	**50**	1.07	0.95	0.16	0.11
1050	**150**	0.83	0.68	0.12	0.10

Therefore, there is a tradeoff between the I_D/I_G and I_{2D}/I_G ratios for graphene grown in our system due to the different roles of the plasma. In one instance, the substrate is heated to high

temperatures by the plasma, which also supplies active carbon species to enhance graphene growth thus increasing the I_{2D}/I_G ratio and decreasing the I_D/I_G ratio. On the other hand, the plasma also contains ions with high energy (such as H and Ar^+) that degrade graphene quality (e.g., increase the I_D/I_G ratio and decrease the I_{2D}/I_G ratio). Results suggest that a larger plasma length enhances the graphitization processes due to high Cu foil temperatures.

4.4.5 The Optimized Condition for Continuous Graphene Growth on Cu Foil

A high throughput deposition of graphene on Cu foil is attainable provided that the substrate is heated uniformly over an extended length of the plasma region. In other words, Cu foil residence time in the plasma should be increased to improve the I_{2D}/I_G ratio. Therefore, an optimized experiment is carried out with the following modifications: (1) expanding the plasma length to approximately 15 cm by using larger electrodes, (2) raising the plasma power to 1450 W, but (3) reducing the web speed to about 30 mm/min. As a result, the Cu foil temperature using the optimized conditions has a high-temperature, uniform profile in the plasma with values around 1200 K sustained uniformly 10 cm in the plasma region as confirmed by the experimental and numerical model results in Fig. 4.7(a).

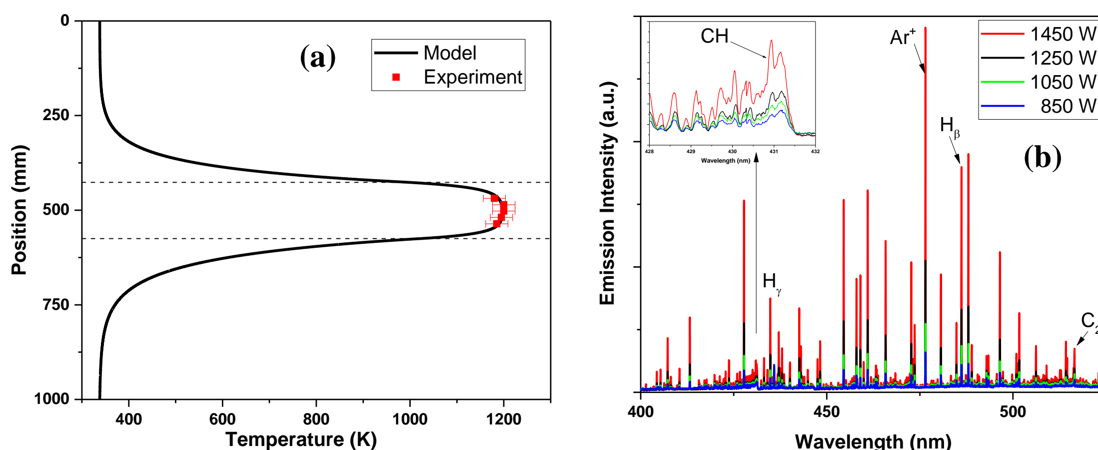

Figure 4.7: (a) Temperature distribution of the Cu foil at the optimized throughput deposition of graphene at 1450 W and 30 mm/min. (b) The emission spectrum of $Ar/H_2/CH_4$ near the foil region in the middle of the plasma (i.e., y=500 mm) as a function of plasma power.

In addition, the increase in plasma power leads to more significant dissociation of the gas mixture because of the higher energy supplied to the system. As a result, the emission intensity of the intermediate species increases with raising plasma power, as shown in Fig. 4.7(b). For instance, the plasma at 1450 W has a higher emission of CH radicals, which enhances graphene quality, as

discussed in Chapter 3, because of the addition of more carbon in the deposition process [23], [167]. Therefore, the elevated concentration of CH radicals combined with the higher substrate temperature at 1450 W aided in consistently depositing higher quality graphene at a web speed of 30 mm/min.

Consequently, the Raman spectrum of graphene for the optimized conditions shows a higher intensity 2D peak with an I_{2D}/I_G ratio value of about 0.7, indicating improved crystallization of carbon atoms on the high-temperature Cu surface (Fig. 4.8(a)). Similar Raman results are obtained across the Cu foil. Furthermore, a uniform graphene film is deposited on a large area of the Cu foil, as presented in the SEM image in Fig. 4.8(b) which shows several wrinkles of graphene across the Cu grains. Therefore, the Cu foil has to be heated to high temperatures for a considerable distance to produce high-quality graphene at faster web speeds.

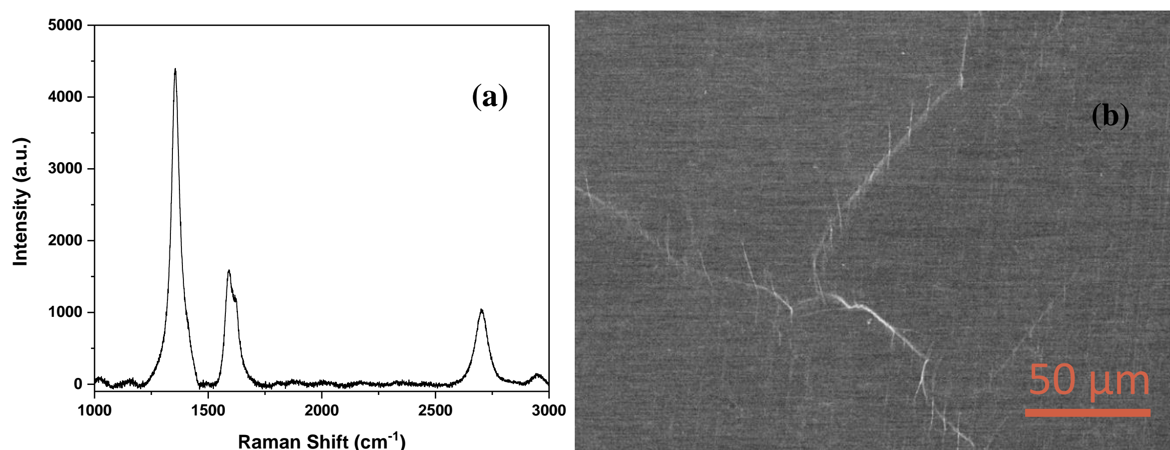

Figure 4.8: (a) Raman spectrum of graphene grown at the optimized condition showing a high peak of the 2D peak. (b) SEM image of graphene on Cu presenting a uniform deposition of graphene of the optimized condition.

Our thermal analysis provides some explanations regarding the differences in reported web speeds from various R2R CVD systems for comparable quality graphene. For example, since the Cu foil was heated for about 40 cm using a direct Joule heating method by Kobayashi et al. [138], graphene was deposited at a web speed of 100 mm/min. On the other hand, a lower web speed of 5 mm/min for graphene deposition was reported by Zhong et al. [17] due to the shorter length of the chamber region in which the Cu foil was heated (about 15 cm). In addition, the Cu foil was heated via a thermal furnace Zhong et al. which is less efficient than the direct Joule heating of Kobayashi et al. Therefore, graphene deposition on Cu foil can be accomplished at higher web speeds provided that the Cu foil is heated uniformly to around 1273 K in a long processing line.

Plasma systems can meet functional specifications with higher efficiency and lower cost than other systems, but ion bombardment should be minimized using dual-frequency capacitively coupled plasmas, or inductively coupled plasmas sources.

4.5 Conclusion

A high throughput production of graphene is the main bottleneck for integration and adoption in existing or future manufacturing facilities. Here, a heat transfer model is developed from first principles to determine the temperature distribution of the copper foil during graphene deposition in a roll-to-roll plasma CVD. The Cu foil temperature is measured by near-IR optical emission spectroscopy at various positions in the plasma region. Temperature measurements aid in validating the fin model at multiple plasma powers, lengths, and web speeds by estimating the convective heat transfer coefficient in the plasma region. The Raman spectroscopy results show that the I_{2D}/I_G ratio declines with increased web speed, particularly at lower plasma powers, limiting the mass production of high-quality graphene. Limitations are due to lessened Cu foil temperature with higher web speed or reduced plasma power and length. Therefore, a high throughput deposition of graphene on Cu foil necessitates a uniform and high-temperature for Cu foil in a long processing line. In our work, the maximum length of the plasma region is limited by the plasma stability at high operating powers. Our thermal analysis reported here aids in providing guidelines for high throughput material processing in various roll-to-roll systems.

5. THE ROLE OF HEAT TRANSFER IN ROLL-TO-ROLL DEPOSITION OF GRAPHENE ON NICKEL FOIL

5.1 Motivation and Background

The limitations of high throughput graphene growth on Cu foil, as explored in the previous chapter, motivate the study of graphene growth on Ni foil as an alternative substrate. Ni has widely been used as a substrate for large-area deposition of graphene: from mono-layer to few-layer and thin graphite. Yu et al. [36] studied the effects of carbon segregation from the Ni substrate and found that the cooling rate played a significant role in producing few-layer graphene on Ni. Reina et al. [35] reported the deposition of few-layer graphene using an atmospheric pressure CVD and also observed the variation of graphene thickness among Ni grains, where graphene nucleates at Ni grain boundaries. Similarly, Kim et al. [14] found that the number of graphene layers differs between Ni grains and depends on Ni film thickness. Moreover, a microwave plasma CVD was used by Kim et al. [41] to deposit graphene on Ni foil at elevated substrate temperatures (e.g., 1023 K). Alternatively, a DC discharge and an inductively coupled plasma were developed by Obraztsov et al. [54] and Cheng et al. [63], respectively, to deposit thin graphite films at low temperatures. Despite a number of previous studies in the area of graphene CVD on Ni, large scale production of graphene on Ni using a roll-to-roll CVD method had not been previously reported.

Graphene growth on a Ni substrate is initiated by the decomposition of methane (CH_4) (or another hydrocarbon source) to intermediate species at temperatures greater than 900 K. Carbon species dissolve in the Ni substrate, forming metastable nickel carbides resulting from the high carbon solubility in Ni (1.3 carbon atomic % at 1273 K) [194]. While cooling, carbon precipitates and segregates on the Ni surface due to the decreased carbon solubility as the substrate temperature cools. As a result, graphene with different qualities and thicknesses can be deposited on Ni, depending on cooling rate. Yu et al. [36] found that a fast cooling rate (20 K/s) produced a thick graphite film, whereas no graphene was grown with a slow cooling rate (0.1 K/s) because carbon atoms could diffuse and evaporate from the Ni surface to the bulk gas. Few-layer graphene was successfully produced at a moderate cooling rate of 10 K/s, demonstrating the efficacy of using the substrate cooling rate to control graphene thickness and quality [36].

Following the work of Yu et al. [36], several studies have investigated cooling rate effects on graphene deposition over a Ni substrate, as summarized in Table 5.1. The previous reports considered categorizing the cooling rates as either slow or fast, or according to an optimum rate between the two. Cooling rates were primarily derived from thermocouple measurements of the substrate holder, and not directly from the substrate [36]. Moreover, the derived cooling rate was assumed to be constant, which is not the case due to the non-linearity of convection and radiation processes with the gas flow and chamber wall. Consequently, cooling rate values associated with the successful growth of few-layer graphene are inconsistent in literature. For example, the optimum cooling rate for high-quality few-layer graphene was found to be 10 K/s [36], whereas this optimum value decreased to 0.07 K/s in another study [195]. Therefore, the lack of a detailed heat transfer analysis of the Ni substrate hinders the potential of utilizing Ni for scalable production of graphene.

Table 5.1: Comparison of process parameters during graphene growth on Ni substrate. CVD: chemical vapor deposition, MPCVD: microwave plasma CVD, PECVD: plasma-enhanced CVD, PLD: pulsed laser deposition, rf CVD: radio-frequency plasma CVD.

Growth Method	**Ni Thickness [μm]**	**Growth Temperature [K]**	**Slow Cooling Rate [K/s]**	**Medium Cooling Rate [K/s]**	**Fast Cooling Rate [K/s]**	**Ref.**
CVD	0.3	1273	-	10.0	-	[14]
CVD	0.3	1123-1273	0.03	0.07	0.1	[195]
CVD	0.3	1273	0.1	-	-	[196]
CVD	5	1173	0.28	-	34.0	[197]
CVD	25	1273	-	3.3	-	[198]
CVD	30	1173	0.3	-	3	[199]
CVD	50	1123-1223	-	10	-	[200]
CVD	500	973-1273	-	2.7	-	[201]
CVD	500	1273	0.1	10.0	20.0	[36]
CVD	1000	1343	0.002	-	NA	[202]
PECVD	0.5	473-1073	0.1	0.3	0.4	[63]
PLD	0.6	1023	0.02	0.8	1.7	[203]
MPCVD	50	723-1023	-	3.0	-	[41]

Here, we focus on the impact of heat transfer on the Ni foil temperature distribution and the relationship to graphene growth on Ni foil in a roll-to-roll plasma CVD system. The heat transfer model is validated with *in situ* temperature measurements. The Ni foil cooling rate is unambiguously derived from basic heat transfer principles, showing that the cooling rate rises with

increasing web speed. Thus, due to the high carbon solubility in Ni substrate, graphene can be deposited at higher web speeds because of enhanced cooling rates. The heat transfer analysis and graphene characterization methods reported here advance the potential of graphene mass production on substrates with high carbon solubility beyond Cu**.**

5.2 Results and Discussion

5.2.1 Roll-to-Roll Deposition of Graphene on Ni Foil

Graphene was deposited on Ni foil during the R2R process with different quality and thickness, depending on the web speed and plasma power, at 15 mbar in an experimental setup similar to the one described in Chapter 4. Figure 5.1 shows the Raman spectra of graphene grown at plasma powers of 850 W and 1050 W at various web speeds. The main Raman peaks of graphene are a D peak at 1350 cm^{-1}, G peak at 1580 cm^{-1}, D′ peak at 1620 cm^{-1}, and 2D peak at 2700 cm^{-1} [145], [192]. The D and D′ peaks occur because of defects in graphene lattice, whereas the G and 2D peaks are signatures of graphitic films. The intensity ratio of the 2D and G peaks (I_{2D}/I_G) for the stationary case at 1050 W is 0.5. However, the I_{2D}/I_G ratio reduces to 0.3 when the plasma power drops to 850 W for the stationary case due decreased Ni foil temperature with reduced plasma power indicating a lower crystallinity of the deposited graphene films [41], [201], [204]. Previous reports show that the I_{2D}/I_G ratio increases with increased substrate temperature indicating improved ordered of the graphitic fragments [204] and decreased number of layers [201].

Furthermore, as the web speed increases to 50 and 150 mm/min, the I_{2D}/I_G ratio of samples grown at 1050 W drops to 0.3 and 0.1, respectively (Fig. 5.1(a)). Similar trends of the I_{2D}/I_G ratio changes with increasing web speed appear at a reduced plasma power of 850 W, as shown in Fig. 5.1(b). For both plasma powers, the 2D peak is weak at a web speed of 150 mm/min because of the lowered foil residence time in the plasma (i.e., 50 s) that minimizes carbon diffusion. In prior work, a lower crystalline-order, thinner graphene was reported with reduced growth time [205]. With increased residence time in the plasma, the deposited graphene crystalline structure is enhanced, and the thickness increases because of the larger concentration of dissolved carbon atoms in Ni [201]. Indeed, the position of the 2D peak, which shifts to lower wavenumbers with decreased graphene thickness [201], shifts from 2704 cm^{-1} for the stationary case, which has a

residence time of 20 min, to 2690 cm^{-1} at 50 mm/min (2.5 min residence time) at a fixed plasma power of 1050 W.

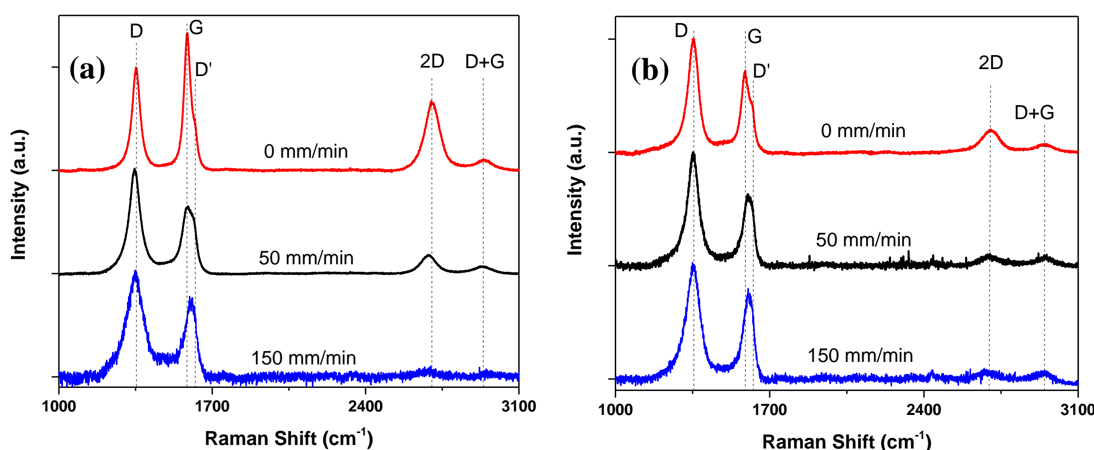

Figure 5.1: Raman spectra of graphene on Ni foil as a function of web speed at (a) 1050 W and (b) 850 W plasma powers.

On the other hand, the I_D/I_G peak ratio, which represents the defect density of graphene, suggests that the deposited graphene is negatively affected by ion bombardment from plasma species such as H and Ar^+ [23]. The I_D/I_G ratio values remain similar at around 1.3 as a function of web speed and plasma power, except for the stationary case at 1050 W, which has a lower value of 0.8 (Fig. 5.1). The decreased I_D/I_G peak ratio for the stationary case at 1050 W (and also for the stationary case at 850 W) could be attributed to defect healing by the higher temperature Ni foil that enhances carbon atom mobility on its surface [206]. The D′ peak is apparently present for these stationary cases, whereas the D′ peak merges with the G peak as the web speed increases (Fig. 5.1). As a result, the G peak position shifts from 1586 cm^{-1} at 0 mm/min to 1602 cm^{-1} at 50 mm/min, and finally to 1606 cm^{-1} at 150 mm/min at a fixed plasma power of 850 W.

Graphene uniformity is presented in the SEM images found in Fig. 5.2, which demonstrate substantial differences in contrast and morphology of deposited film, as a function of web speed at a fixed plasma power of 850 W. The thickness of graphene varies significantly across the Ni surface for the stationary case, as shown in Figs. 5.2 (a) and (b). The darker regions represent thicker carbon films, whereas the lighter regions suggest graphene with a reduced number of layers. This thickness variation within the sample arises from the various orientations in the polycrystalline Ni foil that have distinct carbon perception rates during the substrate cooling period [196], [205], [207].

Conversely, as the web speed increases, the uniformity of graphene is considerably enhanced, as shown in SEM images in Figs. 5.2 (c) and (e), with web speeds of 50 and 150 mm/min, respectively. Furthermore, the contrast between the images in Figs. 5.2 (d) and (f) decreases with higher web speed, indicating reduced graphene thickness. These results can be explained in detail using the Ni foil thermal model in the following subsections.

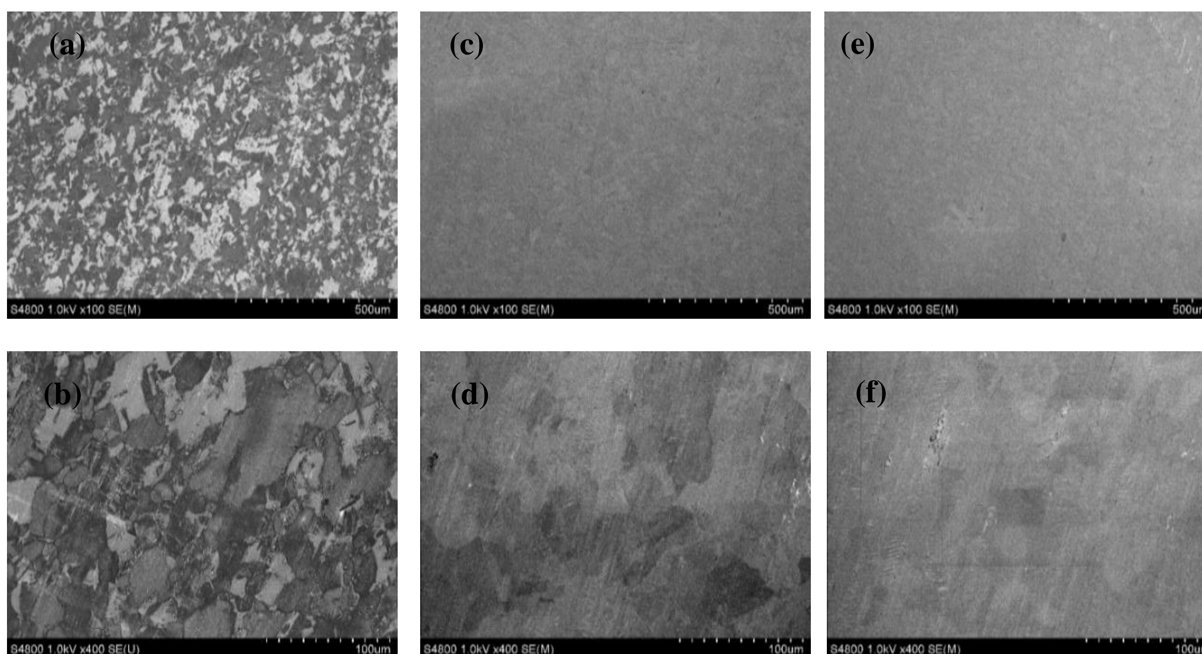

Figure 5.2: SEM images of graphene on Ni foil at a fixed plasma power of 850 W and various web speeds of (a) and (b) 0 mm/min, (c) and (d) 50 mm/min, and (e) and (f) 150 mm/min.

5.2.2 Ni Foil Temperature Distribution during Roll-to-Roll Graphene Growth

The Ni foil temperature in the plasma region is measured through blackbody emission using *in situ* optical emission spectroscopy described in Chapter 4. Figure 5.3(a) shows three emission spectra from Ni foil in the plasma region as a function of plasma power. As the plasma power increases, the emission baseline rises, indicating a higher Ni temperature. As in Chapter 4, the strong baseline spectrum disappears from the plasma emission once the substrate is excluded. Hence, the Ni foil temperatures, inferred from fitting spectra to a Planck's distribution (Eq. (4)), are 990, 1045, and 1065 K at 850, 1050 and 1250 W, respectively. Increasing substrate temperature with increasing plasma power is caused by the higher plasma gas temperature that promotes the substrate heating. Measurements are made at a Ni foil position of y= 490 mm, which is near the centerline of the plasma region.

Ni foil temperature depends primarily on measurement position and web speed, as illustrated in Fig. 5.3(b). At 850 W plasma power and 0 mm/min web speed, the Ni foil temperature decreases slightly from 990 K at the plasma centerline (y = 490 mm) to 965 K at the plasma edge (y = 460 mm). This temperature drop occurs because of heat loss by conduction to the lower temperature Ni foil in the pre-plasma region. In addition, the temperature at y = 460 mm reduces further to 935 K when the Ni foil is moving downward at a web speed of 50 mm/min and at a constant plasma power of 850 W. The heat transfer by advection lowers the Ni temperature, especially near the pre-plasma/plasma interface (y = 460 mm).

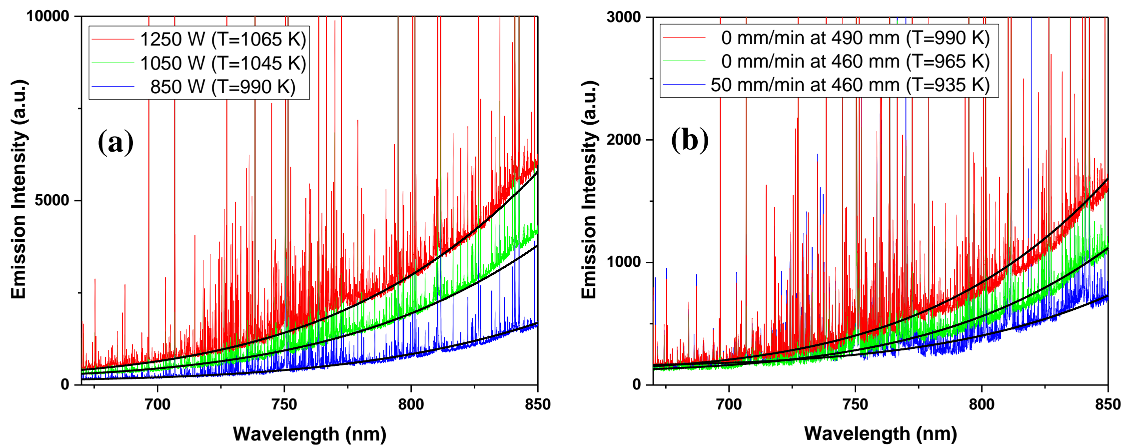

Figure 5.3: (a) Ni emission spectra at 490 mm as a function of plasma power. (b) The variation of Ni emission as a function of position in the plasma region and web speed at 850 W.

Figure 5.4(a) presents a comparison between the Ni foil temperature distribution from the numerical model and experimental results at a plasma power of 850 W and various web speeds. The temperatures from the model agree with the experimental measurements, within a range of uncertainty, shown in the inset of Fig. 5.4(a). In the stationary case (i.e., 0 mm/min), the Ni foil temperature in the plasma region is high due to elevated plasma gas temperature ($T_{\infty,2}$). Also, the Ni foil temperature has a flat profile in the plasma region due to the relatively low thermal conductivity of Ni. However, the Ni foil temperature drops sharply outside the plasma region as the heat is conducted to the low-temperature pre- and post-plasma regions where the Ni foil temperature reaches asymptotic values equal to the gas temperatures in these regions (i.e., $T_{\infty,1}$, $T_{\infty,3}$). Nevertheless, as the web speed increases, the maximum Ni foil temperature in the plasma region decreases with diminished temperature uniformity because of the heat advection of the moving foil.

The effective heat transfer coefficient in the plasma region (h_2) is derived from fitting the model to the measurements, as shown in Fig. 5.4(a). The trends of h_2 from Ni foil experiments in Fig. 5.4(b) are similar to those of Cu foil in the same process conditions, as described in Chapter 4, but with less dependence on plasma power. On the other hand, the decline of h_2 with raised web speed is correlated to the lessened plasma gas interaction with the foil. The foil is moving downward, in the opposite direction from the upward gas flow driven by buoyancy between the two electrodes. Hence, increased web speed could lead to flow recirculation near the moving Ni foil that can decrease the convective heat transfer coefficient [189].

The Ni foil temperature in the pre-plasma region is reduced and the start of the temperature rise is delayed with increased web speed (Fig. 5.4(a)). The changes in temperature profile through web speed can be explained by the increase of the factor $\beta_1 = \sqrt{a^2 + 4m_1} + a$ with higher web speed. The factor β_1 represents the exponent in the analytical solution of the pre-plasma region temperature of Eq. (10) in Chapter 4. As the web speed increases, the parameter a increases the value of β_1 leading to lower foil temperatures in the pre-plasma region. On the other hand, the temperature increases considerably in the post-plasma region with increased web speed, as shown in Fig. 5.4(a). This temperature rise is caused by the decreased value of $\beta_3 = \sqrt{a^2 + 4m_3} - a$ in Eq. (10) with increased web speed. Thus, Ni foil temperature depends primarily on web speed as a result of high heat advection, in contrast to the Cu foil temperature distribution, which depends more strongly on conduction, as discussed next.

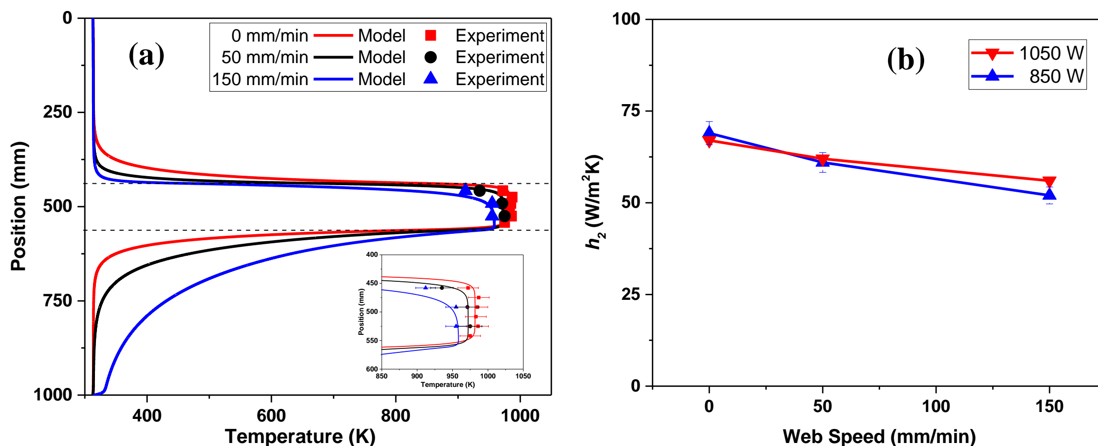

Figure 5.4: (a) Comparison between Ni foil temperature distributions from the model and experimental measurements at 850 W and various web speeds. (b) The heat transfer coefficient in the plasma region (h_2) for Ni foil at different plasma powers and web speeds. The spatial resolution of emission measurements is about 2 mm.

Figure 5.5 compares the temperature distribution of Ni and Cu foils at a plasma power of 1050 W and web speeds of 0, 50 and 150 mm/min. Both the Ni an Cu foils have similar thickness of 76 µm. At the given web speeds, Cu foil has a higher temperature in the plasma region than Ni foil, even though the plasma gas temperature is almost similar for both foils. This temperature difference is related to the higher emissivity of Ni, which is 0.14 for Ni, compared to 0.04 for Cu at 1000 K [185]. Hence, Ni foil experiences higher radiation exchange with the low-temperature chamber wall and electrodes, resulting in a higher heat loss from Ni foil than from Cu foil [188]. If radiation heat transfer is excluded from the model, the difference between the maximum Ni and Cu foil temperatures in the plasma region become negligible within the experimental uncertainty.

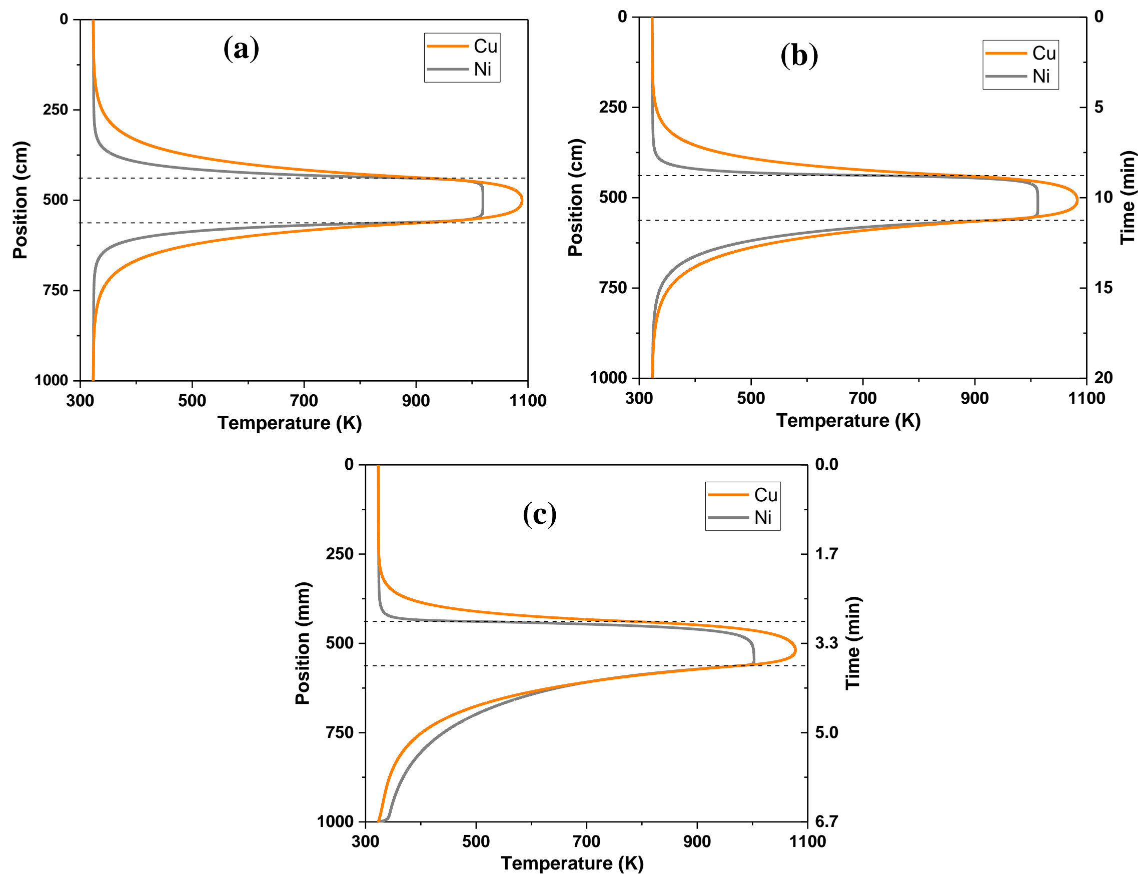

Figure 5.5: Comparison between Ni and Cu foil temperature distributions at 1050 W and web speeds of (a) 0 mm/min, (b) 50 mm/min, and (c) 150 mm/min.

Due to the low thermal conductivity of Ni, the Ni foil temperature remains nearly constant in the plasma region, in contrast to the Cu foil, which shows a strong decaying profile because of its higher thermal conductivity (Fig. 5.5). Similarly, as shown in Fig. 5.5(a), Ni foil conducts less heat to the pre- and post-plasma regions in the stationary case. For Cu, because of its higher thermal

conductivity, the temperature field penetrates to longer distances in the pre- and post-plasma regions at 0 mm/min.

As illustrated in Figs. 5.5 (b) and (c), both Ni and Cu foil temperature profiles evolve as a result of heat advection via foil movement as web speed increases from 0 to 150 mm/min. Ni has a higher Pe number than Cu because of the low thermal diffusivity of Ni, resulting in a larger heat transfer by advection than diffusion processes in Ni foil [185]. The Pe number is defined as $Pe = \frac{LU}{\alpha}$, where $\alpha = \frac{k}{\rho C_p}$ is the thermal diffusivity of the foil, L is the plasma length, and U is the web speed. For example, the Pe number of Ni increases from 6.97 at 50 mm/min to 20.90 at 150 mm/min, whereas the Pe number rises slightly from 1.15 to 3.43 for Cu for the same web speeds. Hence, the temperature distribution of Ni foil changes more significantly than Cu foil with web speed.

Additionally, Ni foil temperature in the pre-plasma region falls with increased web speed more rapidly than for the Cu foil (Fig. 5.5). As a result, the Ni foil temperature profile is less uniform at the beginning of the plasma region, especially at a web speed of 150 mm/min. More significantly, the Ni foil temperature in the post-plasma region decays at a slower rate than that of Cu foil. However, at a web speed of 50 mm/min, Cu foil has a slightly higher temperature than Ni foil in the post-plasma region; at a higher web speed of 150 mm/min, the Ni foil temperature exceeds that of the Cu foil in the post-plasma region (Fig. 5.5(c)).

To explain Ni and Cu foil temperatures variations with web speed, the analytical solution (Eq. (10)) is utilized to study the dependence of the exponents on web speed. Writing the exponents of the pre- and post-plasma regions as $\beta_1 = \sqrt{a^2 + 4m_1} + a$ and $\beta_3 = \sqrt{a^2 + 4m_3} - a$, respectively, the effects of web speed on β_1 and β_3 for both foils are presented in Fig. 5.6. At 0 mm/min, β_1 and β_3 are identical in both regions with values of 75.8 and 37.4 for Ni and Cu, respectively, which correspond to the infinite fin model [185]. However, while β_1 and β_3 rise in the pre-plasma region with increased web speed, they decay in the post-plasma region.

Because of the higher Pe number for Ni, β_1 and β_3 in Ni change more rapidly than for Cu. Hence, with higher web speed, the Ni foil temperature is smaller in the pre-plasma region due to an enlarged β_1. Likewise, with increased web speed, the Ni temperature increases more rapidly in the post-plasma region because of reduced β_3. The difference between β_3 values for Ni and Cu diminishes as the web speed increases, until around 95 mm/min, where the values become identical.

After that, Ni has lower β_3 values than Cu, and, hence, the Ni temperature is higher in the post-plasma region when the web speed is 150 mm/min (Fig. 5.5(c)). As discussed in the next section, alterations of Ni temperature with web speed affect graphene growth quality and thickness.

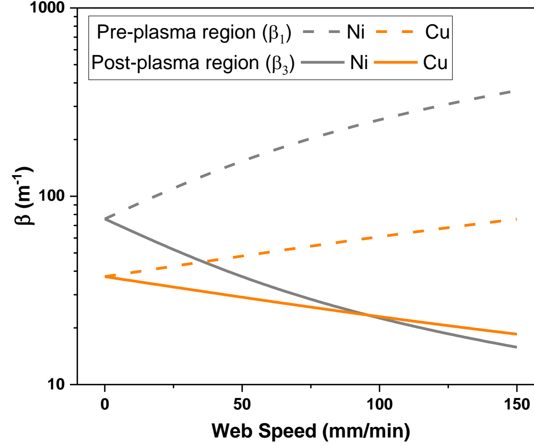

Figure 5.6: The effects of web speed on β_1 and β_3 for Cu and Ni foils.

5.2.3 Correlation between Graphene Growth and Ni Foil Temperature Distribution

The variations of graphene thickness and uniformity as a function of web speed in Fig. 5.2 can be clarified first by estimating the diffusion length of carbon atoms in the Ni substrate during the growth process. The diffusion length (L_D) is defined as:

$$L_D = 2\sqrt{D_T t} \tag{13}$$

where t is the Ni foil residence time in the plasma region: 21.3, 2.5, and 0.8 minutes at 0, 50, and 150 mm/min web speeds, respectively. Also, the carbon diffusivity, D_T, depends on Ni foil temperature, T, as [194], [202], [208]:

$$D_T = D_0 \exp\left(-\frac{E_D}{k_B T}\right) \tag{14}$$

where k_B is Boltzmann's constant (8.617x10^{-5} eV/K), D_0 is 2.4818 cm^2/s, and E_D =1.74 eV representing the entropic pre-factor and the diffusion activation energy, respectively [194], [209]. Figure 5.7 presents carbon diffusion length as a function of web speed at 850 W. At 0 mm/min, the diffusion length is about 38.5 μm, which is almost equal to the half the thickness of Ni foil which is 38.0 μm. Hence, carbon atoms can diffuse freely in the Ni bulk since both sides of the Ni foil are exposed to the plasma. Diffused carbon atoms are expected to segregate and precipitate to the Ni surface during the cooling stage, yielding a thick carbon film, as seen in the corresponding optical image in Fig. 5.7, and the SEM images from Figs. 5.2 (a) and (b).

Because of the decline in both the residence time and foil temperature with increased web speed, the diffusion length drops to 11.9 and 5.9 μm at 50 and 150 mm/min, respectively, (Fig. 5.7). Also, the diffusion length reaches 63% of its maximum at Ni foil positions of 454 and 475 mm for web speeds of 50 and 150 mm/min, respectively, compared to 445 mm for the stationary case (Fig. 5.7). The considerable decline in the diffusion length uniformity is due to reduced Ni foil temperature with increased web speed as shown in Fig. 5.4(a). Therefore, fewer carbon atoms can dissolve deep into the Ni foil as the web speed increases, and explains the lower thickness of graphene in the SEM images at 150 mm/min (Fig. 5.2) and the optical image of graphene on Ni at 150 mm/min (Fig. 5.7). Nevertheless, the higher uniformity of the samples grown at higher web speed indicates the possibility of direct isothermal growth of graphene on Ni. Such growth can occur by surface precipitation of carbon atoms such as CH, C_2 or C. Carbon atoms dissolve near the Ni subsurface to form a Ni-C solid phase solution and deposit graphene at low temperatures [19],[210] or lower deposition durations [198],[207].

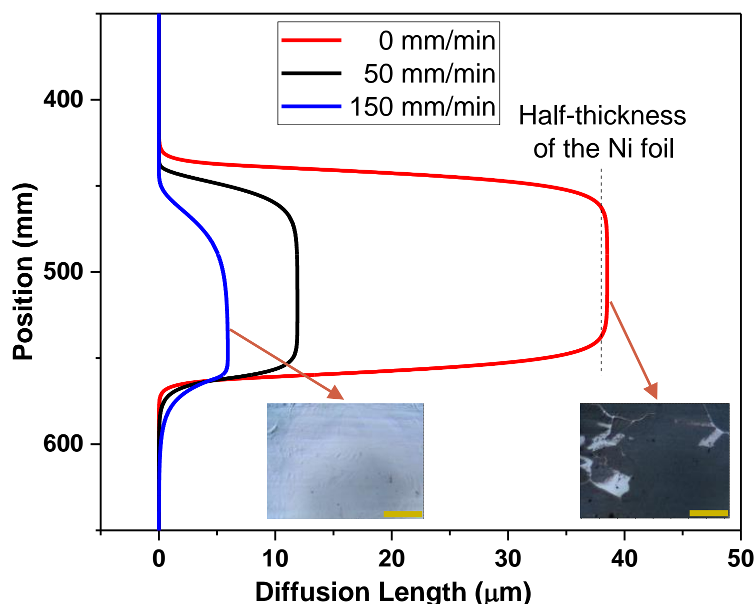

Figure 5.7: Diffusion length of carbon atoms in Ni foil at a plasma power of 850 W and various web speeds. Optical images of graphene on Ni foil at 0 and 150 mm/min are included to demonstrate the deposition of a thick graphite film at 0 mm/min in contrast to a uniform growth of few-layer graphene at 150 mm/min. The scale bars in these optical images are 20 μm.

Second, the cooling rate, which plays a vital role in graphene deposition on Ni, along with the heating rate of Ni foil, are derived by taking the first derivative of the Ni foil temperature distributions using the analytical solution from Eq. (10) from Chapter 4:

$$\frac{dT}{dy} = \frac{1}{2}\left(\sqrt{a^2 + 4m_1} + a\right)C_1 \exp\left(\frac{1}{2}y\left(\sqrt{a^2 + 4m_1} + a\right)\right) \qquad \text{for } -0.438 \le y \le 0 \tag{15}$$

$$\frac{dT}{dy} = \frac{1}{2}\left(\sqrt{a^2 + 4m_2} + a\right)C_5 \exp\left(\frac{1}{2}y\left(\sqrt{a^2 + 4m_2} + a\right)\right)$$

$$- \frac{1}{2}\left(\sqrt{a^2 + 4m_2} - a\right) C_6 \exp\left(-\frac{1}{2}y\left(\sqrt{a^2 + 4m_2} - a\right)\right) \quad \text{for } 0 \le y \le L$$

$$\frac{dT}{dy} = -\frac{1}{2}\left(\sqrt{a^2 + 4m_3} - a\right)C_4 \exp\left(-\frac{1}{2}y\left(\sqrt{a^2 + 4m_3} - a\right)\right) \quad \text{for } L \le y \le 0.562$$

The chain rule is applied to transform the temperature derivatives from the space domain to the time domain as $\frac{dT}{dt} = \frac{dT}{dy}\frac{dy}{dt} = U\frac{dT}{dy}$, where U is the web speed and $\frac{dT}{dy}$ is found from Eq. (15). The heating/cooling rate from the numerical model, found by differentiating the temperature profile, shows results similar to the heating/cooling rates from the analytical solution. Since the web speed for the stationary case is 0 mm/min, the cooling rate due to foil moving is zero and the temperature of the hot foil decreases when the foil moves to the post-plasma region. Instead, a lumped capacitance model (since Bi number is less than 0.1) is developed to find the cooling rate for Ni foil in the stationary case. Considering the heat transfer by radiation, convection, conduction along with the stored energy, the energy balance of Ni foil after leaving the plasma region is:

$$-2h_3A_s\left(T_3 - T_{\infty,3}\right) - 2\varepsilon\sigma A_s\left(T_3^4 - T_{\infty,3}^4\right) - 2\sqrt{h_3pkA_c}\left(T_3 - T_{\infty,3}\right) = \rho\forall C_p\frac{dT}{dt} \tag{16}$$

where p, A_s, $\forall$ are the perimeter, surface area and volume of Ni foil in the plasma region, respectively. Linearizing the radiation term (as in Appendix B.1), and rearranging Eq. (16) leads to: $\frac{d\theta_3}{dt} = -M\theta_3$, where $\theta_3 = T_3 - T_{\infty,3}$, and $M = \frac{2A_sh_3}{\rho\forall C_p} + \frac{2A_sh_{rad,3}}{\rho\forall C_p} + \frac{2\sqrt{h_3pkA_c}}{\rho\forall C_p}$ with $h_{rad,3} = \varepsilon\sigma\left(T^2 + T_{\infty,3}^2\right)\left(T + T_{\infty,3}\right)$. Here, $T_{3,i}$ is the temperature of Ni foil at the interface of the plasma and the post-plasma region. Therefore, the time-dependent Ni foil temperature for the stationary case is:

$$T_3(t) = T_{\infty,3} + \left(T_{3,i} - T_{\infty,3}\right)\exp(-Mt) \tag{17}$$

Figure 5.8(a) presents the heating and cooling rates as a function of plasma power and web speed from the fin model. The heating rate of the foil before entering the plasma is higher than the cooling rate in the post-plasma region. Both rates are non-linear because of Ni foil temperature variations in the three regions due to the convection, radiation, and advection processes. Web speed significantly influences both the heating and cooling rates because of the substantial contribution from the advection term to the temperature distribution profiles (Figs. 5.4 and 5.5). For instance,

at the interface of the pre-plasma and plasma regions (i.e., *y*= 438 mm), the heating rate increases sharply at 50 and 150 mm/min because the foil enters the plasma region rapidly. Similarly, the maximum cooling rates in the post-plasma region rise with increased web speed, with values of 14 and 20 K/s at 50 mm/min and 150 mm/min, respectively at a fixed plasma power of 850 W. On the other hand, the cooling rate at 0 mm/min from the lumped capacitance model has higher values than the cooling rates from the fin model at 50 and 150 mm/min until 19 seconds with a maximum cooling rate of 56 K/s (Fig. 5.8(b)). After that, the cooling rate at 0 mm/min decays slowly until the temperature of Ni foil reaches the gas temperature in the post-plasma region. However, at higher web speeds, the foil requires a longer distance to be cooled to temperatures equal to the post-plasma gas temperature, which explains the sharp rise in the cooling rate near the bottom spool, as shown in Fig. 5.8(b).

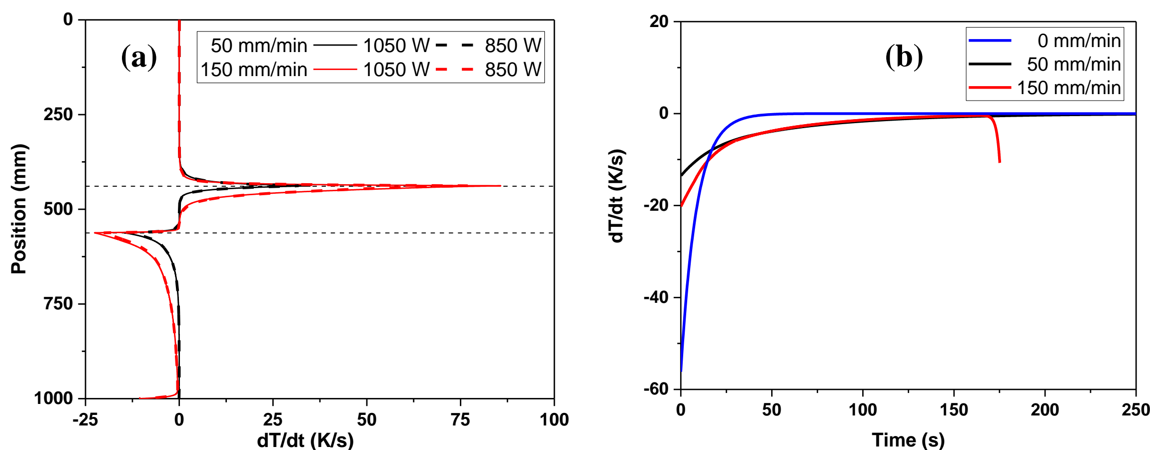

Figure 5.8: (a) Cooling rates of Ni foil during the R2R process at plasma powers of 850 and 1050 W with 50 and 150 mm/min web speeds. (b) Comparison between the cooling rate from the fin model (web speeds of 50 and 150 mm/min) and the lumped capacitance model for the stationary case (i.e., 0 mm/min) at a fixed plasma power of 850 W.

Table 5.2 compares the Raman results of graphene on Cu and Ni foils at the same conditions. As a result of decreased Cu foil temperature, CH_4 catalytic reactions limit the production rate of high-quality graphene as discussed in Chapter 4. For example, the I_{2D}/I_G ratio for graphene on Cu is higher than Ni foil for the stationary cases, whereas Ni has better I_{2D}/I_G ratio at 50 and 150 mm/min as presented in Table 5.2. On the other hand, due to strong plasma ion bombardment, the I_D/I_G ratio of graphene on both foils are large with higher values for Ni than Cu at 50 and 150 mm/min. Nevertheless, graphene growth on Ni excels in the given conditions as evident from higher I_{2D}/I_G ratio for graphene on Ni than Cu as listed in Table 5.2. The improved

I_{2D}/I_G ratio for graphene on Ni is because the growth is driven by diffusion/segregation processes in Ni rather than by surface catalyst reactions on Cu surface. Furthermore, because of the lower diffusion length and higher cooling rate with increased web speed, graphene uniformity on Ni foil is improved at higher web speeds, which allows for a higher throughput deposition of graphene than would be possible on Cu foil.

Table 5.2: Comparison between Raman peak intensity ratios for graphene on Ni foil and Cu foil at various plasma powers and web speeds.

Plasma power [W]	Web speed [mm/min]	I_D/I_G ratio (Ni foil)	I_D/I_G ratio (Cu foil)	I_{2D}/I_G ratio (Ni foil)	I_{2D}/I_G ratio (Cu foil)
850	**0**	1.37	1.61	0.31	0.53
850	**50**	1.56	0.76	0.20	0.10
850	**150**	1.25	0.66	0.12	0.07
1050	**0**	0.74	1.70	0.54	0.65
1050	**50**	1.59	1.07	0.32	0.16
1050	**150**	1.29	0.83	0.16	0.12

5.3 Conclusion

Carbon film can be deposited on Ni foil in a variety of thicknesses, from few-layer graphene to thin graphite film, depending on web speed. To understand and control the quality and thickness of the deposited carbon film, the temperature distribution of Ni foil is determined during a R2R process. Ni foil temperatures from the model and the measurements show a good agreement at various plasma powers and web speeds. Due to the high Pe number of Ni, the temperature distribution is largely affected by web speed. Hence, the cooling rate derived from the model rises with increased web speed or decreased Ni substrate thickness. These findings reveal the importance of using heat transfer analysis to optimize graphene deposition on Ni and other substrates with high carbon solubility in a roll-to-roll process. Even though uniform graphene was successfully deposited on Ni at high web speed, the temperature distribution, which strongly depends on web speed, affects the deposited graphene quality. Hence, in order to further improve the throughput deposition of graphene on Ni, separate temperature-controlled pre- and post-plasma regions should be utilized to regulate the heating and cooling rates of Ni foil due to its high Pe number.

6. THERMAL CHARACTERIZATION OF A CAPACITIVELY COUPLED RADIO-FREQUENCY HYDROGEN PLASMA

6.1 Motivation and Background

Gas temperature plays a crucial role in determining graphene growth rates and quality in plasma CVD systems as discussed in Chapters 4 and 5. These plasmas systems produce a non-equilibrium environment in which the electron temperature (T_e) is higher than the vibrational temperature (T_{vib}) that is higher than the rotational temperature (T_{rot}) (i.e., $T_e \geq T_{vib} \geq T_{rot}$) [105]. Rotational temperatures of excited electron states are quantitatively similar to translational temperatures when rotational energy levels are thermally distributed and exhibit fast rotational transfer [21]. Thus, optical emission spectroscopy (OES) can be a simple and economical method for measuring rotational temperatures of different species and hence gas temperatures in the plasma [101], [102]. However, the rotational temperatures extracted using OES can vary among species because of the non-equilibrium nature of low ionization plasmas [112]. Here, the rotational temperatures of H_2, N_2^+ and CN are measured to estimate the translational gas temperature in capacitively coupled H_2 plasma.

The plasma system in this work is generated through capacitively coupled discharge in H_2 gas mixed with N_2, O_2, and CH_4. Such plasmas have been widely used in industrial processing facilities for etching and deposition of various materials [155]. The characterization of capacitively coupled discharges at moderate pressures has been extensively reported for different gases including H_2 [153], [211]–[213], Ar [214], [215], N_2 [216]–[218], O_2 [219] and CH_4 [220]. In contrast, few prior studies have reported the effects of mixing one or more of these gases with H_2 in order to control the deposition process. Thus, thermal characterization of a H_2 discharge mixed with N_2, O_2, and CH_4 gases is studied here at concentrations similar to the optimized conditions for graphene deposition as described in Chapter 3.

6.2 Experimental System

A capacitively coupled plasma (CCP) is generated at a frequency of 80 kHz between two parallel asymmetric rectangular electrodes, as illustrated in Fig. 6.1 and discussed in previous chapters. A radio frequency (rf) generator, with a maximum input power of 5000 W, is connected

to two ignitor rods that supply power to the electrodes to generate and sustain the plasma. The current is measured with a Pearson Amp Probe (Model 6858) while the voltage is measured with a Tektronix voltage divider (Model 5100). These current and voltage probes are placed over the ignitor that is connected to the larger electrode. The current and voltage waveforms are presented in Fig. 6.2 as a function of set power and pressure. The average dissipated power in the plasma over one period (*T*) is calculated by [221]:

$$P(W) = \frac{1}{T}\int_0^T V(t).I(t)dt \tag{18}$$

where $V(t)$ and $I(t)$ are the measured time-dependent voltage and current, respectively.

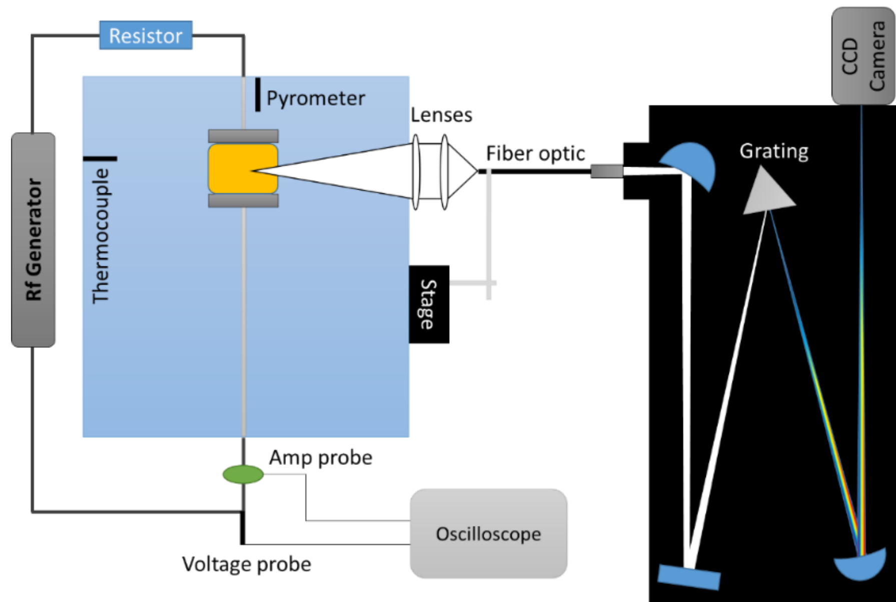

Figure 6.1: The experimental setup showing the capacitively coupled plasma system generated between the two rectangular electrodes. The current and voltage waveforms are measured using Amp and voltage probes, respectively. The optical emission spectroscopy (OES) setup consists of lenses that collect and direct the light to a fiber optic which is connected to the entrance of the spectrometer. The light is finally detected by a CCD camera.

The emission spectra of H_2, N_2^+, and CN are collected and collimated using two lenses with diameters of 50.8 mm. The light obtained from the plasma is focused on a fiber optic mounted in a Zaber translational stage that is controlled using Labview software to allow for spatial emission measurements between the two electrodes. The fiber optic directs the light to the entrance slit of the spectrometer. The spectrometer (Princeton Instruments, Acton SP-2756) has a focal length of 750 mm, and an 1800 G/mm grating blazed at 500 nm. The diffracted light is detected by an unintensified CCD camera (Princeton Instruments, PIXIS 256E). The spectrometer was

calibrated using a Hg light source, and the instrument broadening function is found from a Gaussian fit of a Hg line at 404 nm that results in a full width at half maximum (FWHM) of 0.029 nm.

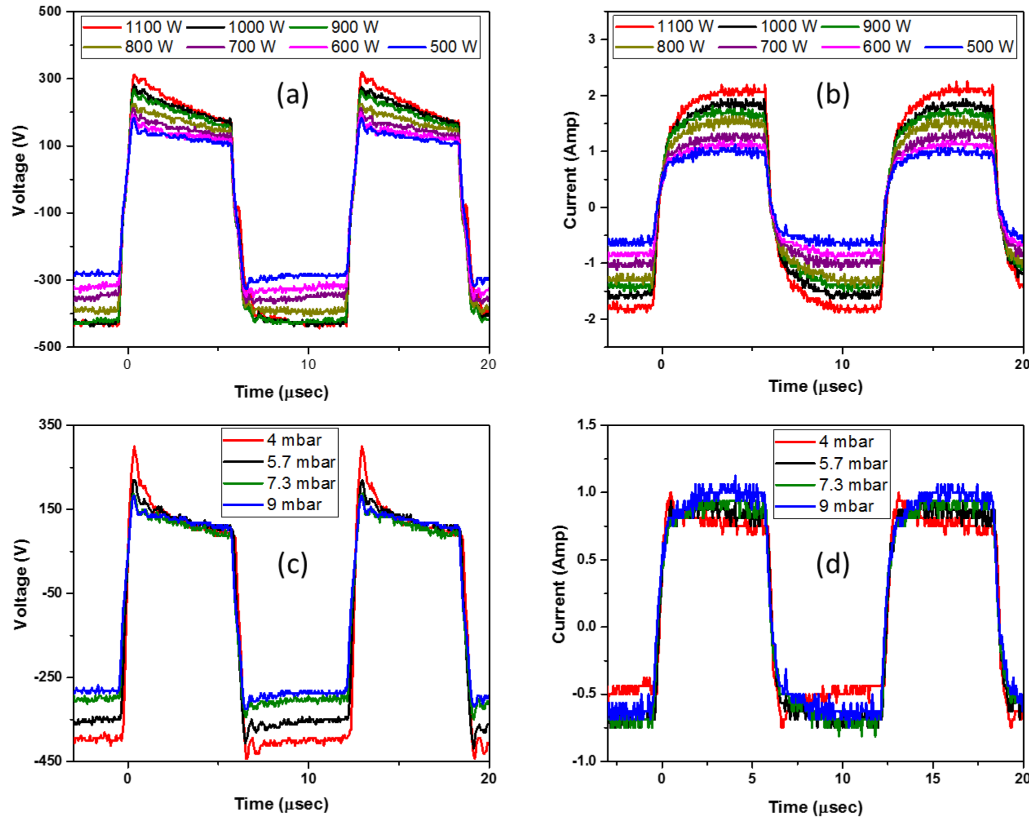

Figure 6.2: The current and the voltage waveforms of 95%/5% H_2/N_2 plasma as a function of pressure and set power. (a) and (b) represent the voltage and current traces, respectively, at 9 mbar as a function of set power. (c) and (d) show the voltage and current traces, respectively, at 500 W set power as a function of pressure.

The Q-branch of the $(d^3\Pi_u(0) \rightarrow a^3\Sigma_g^+(0))$ transition is used to obtain the rotational temperature of the H_2 excited state $(d^3\Pi_u)$ using a Boltzmann plot [109], [187]. Figure 6.3 shows H_2 emission in which five lines are used as presented in the inset of Fig. 6.3. The given H_2 band is free from perturbations when compared to other H_2 bands. Also, the rotational temperatures of N_2^+(B-X) and CN (B-X) are measured for comparison to the rotational temperature of H_2. The rotational temperature of CN (B-X) is found from the spectral fit of the (0,0) vibrational transition [222] using Lifbase software [223], as illustrated in Fig. 6.4(a). Similarly, the rotational temperature of N_2^+(B-X) is derived from the best fit of the (0,0) vibrational transition with a band head at 391.4 nm (Fig. 6.4(b)).

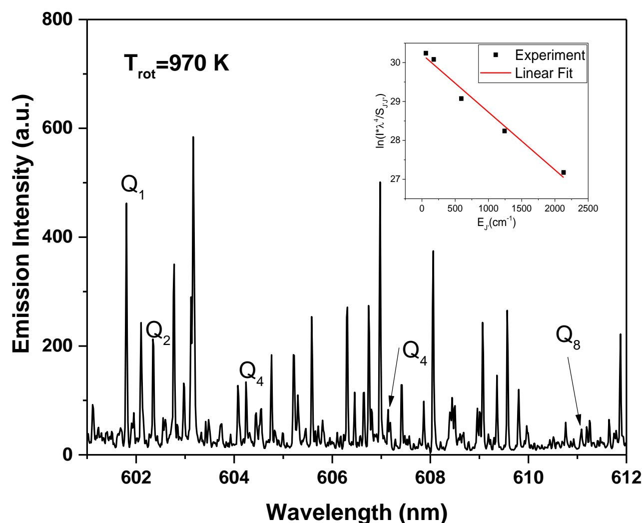

Figure 6.3: The emission spectrum of H_2 at 2.25 mm from the left electrode. The Q-branch lines used to determine the rotational temperature are indicated by arrows in the plot of the spectrum. The Boltzmann plot used to determine the rotational temperature is shown as an inset. The plasma condition is 95% H_2/5% N_2 at 9 mbar and 1100 W set power.

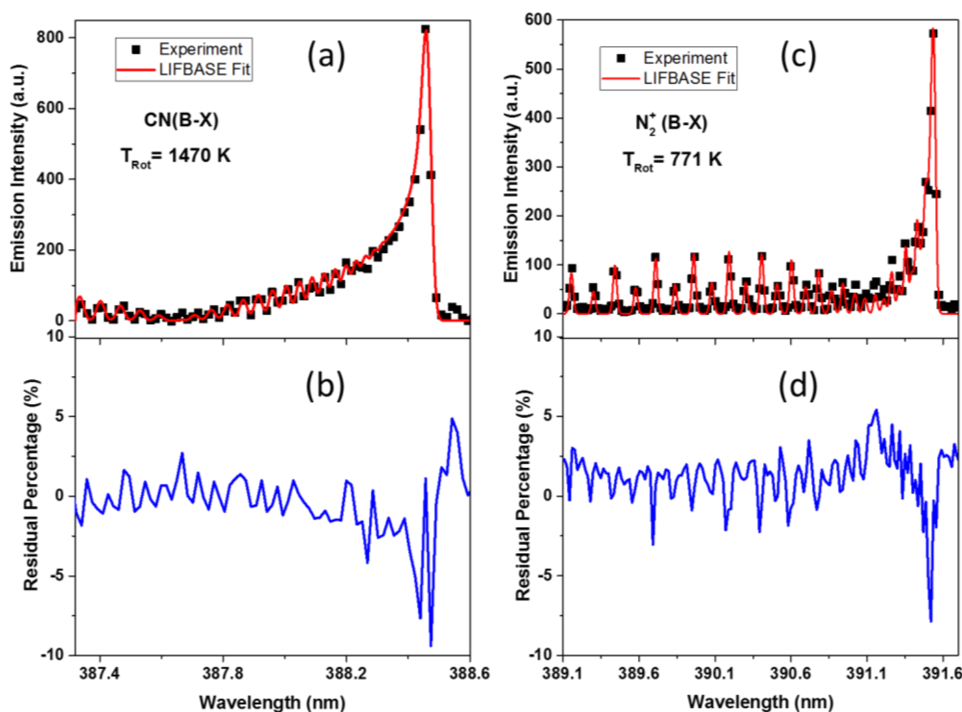

Figure 6.4: (a) The measured emission spectra of CN and its fit using LIFbase. (b) The residual of the difference the experimental and theoretical spectra of CN divided by the corresponding peak intensity. (c) Comparison between the measured and the synthetic emission spectra of N_2^+. (d) The residual of the difference the experimental and theoretical spectra of N_2^+ divided by the corresponding peak intensity. The plasma condition is 95% H_2/5% N_2 at 9 mbar and 1100 W set power.

6.3 Results and Discussion

Experimental measurements of the power dissipation, spatial optical emission, and the rotational temperatures are presented first as functions of input set plasma power and gas pressure with a gas mixture of 95% H_2 and 5% N_2. Then, we present the variations of dissipated power, spatial optical emission, and rotational temperatures with the addition of the nitrogen (N_2), oxygen (O_2) and methane (CH_4) mole fraction (X%) into (95-X)% H_2 and 5% N_2 plasmas at a constant plasma set power of 1000 W and a fixed pressure of 9 mbar. These ranges of inputs are selected to study the plasma in conditions commonly used for graphene deposition as discussed in Chapter 3. Finally, the differences between the rotational temperatures of N_2^+, CN, and H_2 are described in detail to determine accurate values of translation gas temperatures in this work.

6.3.1 Effects of Set Power and Gas Pressure on Power Dissipation and Rotational Temperatures

The power dissipated in the 95%/5% H_2/N_2 plasma at 9 mbar increases linearly from 134 W to 510 W when the set power increases from 500 W to 1100 W (Fig. 6.5(a)). The increase in dissipated power with the set power leads to higher energy absorbed by the plasma and, thus, an increase in electron temperature and number density [153], [187], [211]. Therefore, the spatial emission intensity of the plasma increases because of higher ionization (Fig. 6.6(a)). Similarly, the sheath of the right electrode, estimated from the spatial emission profile, increases from approximately 1.5 cm to 2.2 cm with increased power from 500 to 1100 W. The spatial emission shows two distinct peaks near the right electrode that grow with increased plasma power as reported previously for H_2 plasma at 13.56 MHz [224]. These peaks correspond to the formation of a double layer that is commonly found in capacitively coupled H_2 plasmas [224], [225]. The peak far from the electrode (Peak 2) is related to electron acceleration during sheath expansion, whereas the peak closer to the electrode (Peak 1) occurs due to the field reversal [226].

The percentage of the power dissipation increases from 27% at 500 W to 46% at 1100 W due to the rise of the voltage drop because of sheath expansion [227]. For instance, the root mean square (RMS) value of the supplied voltage rises from 219 V at 500 W to 320 V at 900 W (Fig. 6.6(b)). The voltage remains constant in the range from 900-1100 W, which could be attributed to the confinement of the sheath between the electrodes at the given power values as evident in Fig 6.6(a). On the other hand, the RMS current displays a nearly linear relationship with set power

(Fig 6.6(b)). The increases in current and/or voltage lead to higher dissipated power in the plasma as expressed in Eq. (18). The same trend of increasing dissipated power fraction with voltage has been observed at higher frequencies in a capacitively coupled H_2 plasma at 0.3 Torr [153].

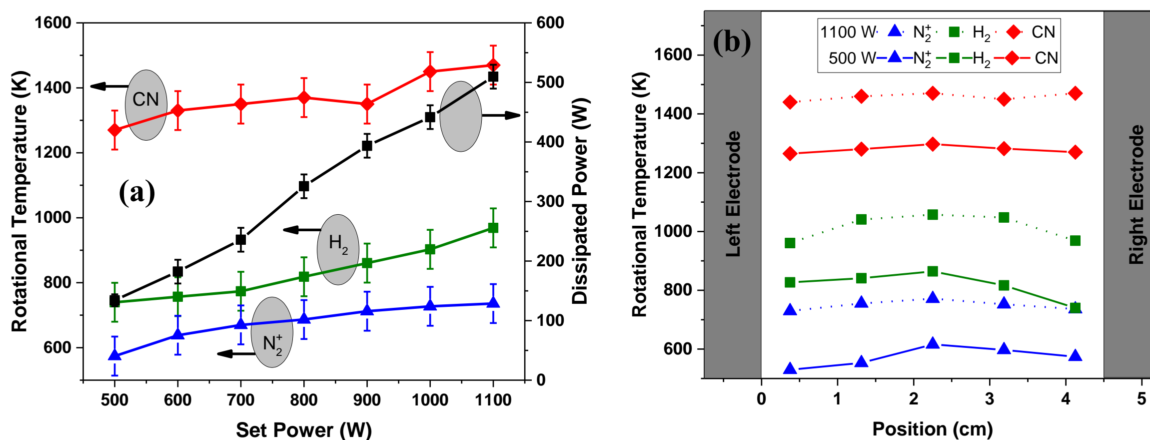

Figure 6.5: (a) The rotational temperatures of N_2^+, CN and H_2 as a function of plasma power. The plasma composition is 95%/5% H_2/N_2. These temperatures are measured at a position of 4 cm from the left electrode. (b) Spatial measurements of the rotational temperature at set powers of 500 and 1100 W.

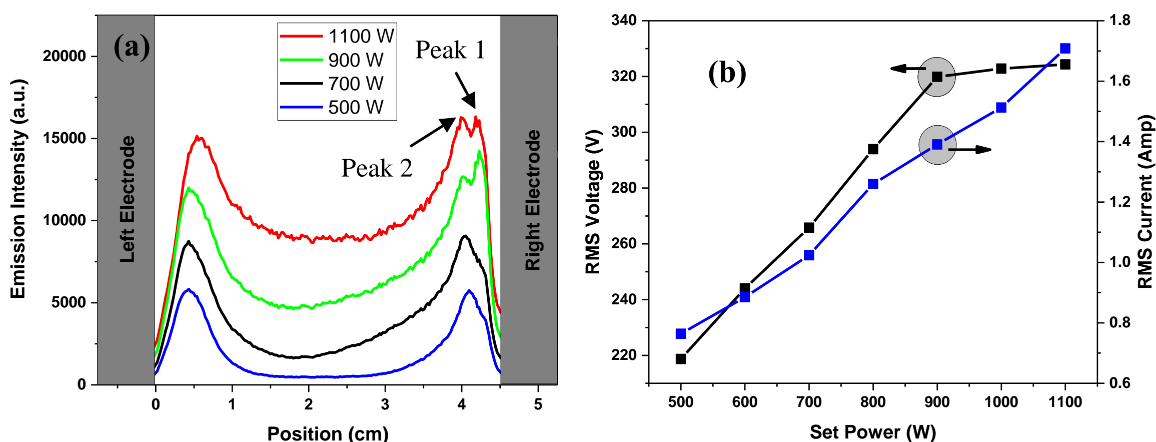

Figure 6.6: (a) Spatial emission of the plasma and (b) The root-mean-square (RMS) of the voltage and current as a function of plasma power. The plasma condition is 95% H_2/5% N_2 at 9 mbar.

Consequently, the rotational temperatures of H_2, N_2^+, and CN increase with increasing power (Fig. 6.5). A higher plasma power results in higher electron temperature and density, which lead to a higher power density and thus an increase in rotational temperatures. When the set power increases from 500 to 1100 K, the rotational temperature of N_2^+ increases from 571 to 738 K, the H_2 rotational temperature rises from 743 to 968 K, and the rotational temperature of CN increases from 1273 to 1468 K. These rotational temperatures have parabolic-like profiles between the

electrodes similar to the distribution of electron number density of H_2 plasma [153]. The maximum temperature occurs at the center of the gap where the electron number density is also highest. The differences between rotational temperatures for the three species and the determination of an accurate translational gas temperature from the OES measurements are discussed later in this chapter.

The dissipated power in the 95%/5% H_2/N_2 plasma at 500 W increases initially with pressure, but then decreases, with a maximum dissipated power near 5.67 mbar (or 4.25 Torr) as shown in Fig. 6.7. Previously, the dissipated power in H_2 plasma was shown to maximize at 3 Torr (or 4 mbar) for a 13.56 MHz H_2 plasma [153], which is in agreement with our work since the maximum power shifts to higher pressures with decreasing plasma frequency. This dependence of dissipated power on pressure is attributed to the increase of both the electric field and the electron number density in the sheath with increased pressure for values less than 3 Torr. However, the electric field in the sheath decreases with a further increase in pressure [153]. Similarly, our measurements show that the current supplied to the plasma increases slightly when raising pressure from 4 to 5.67 mbar but then remains nearly constant at higher pressures (Fig. 6.8(b)).

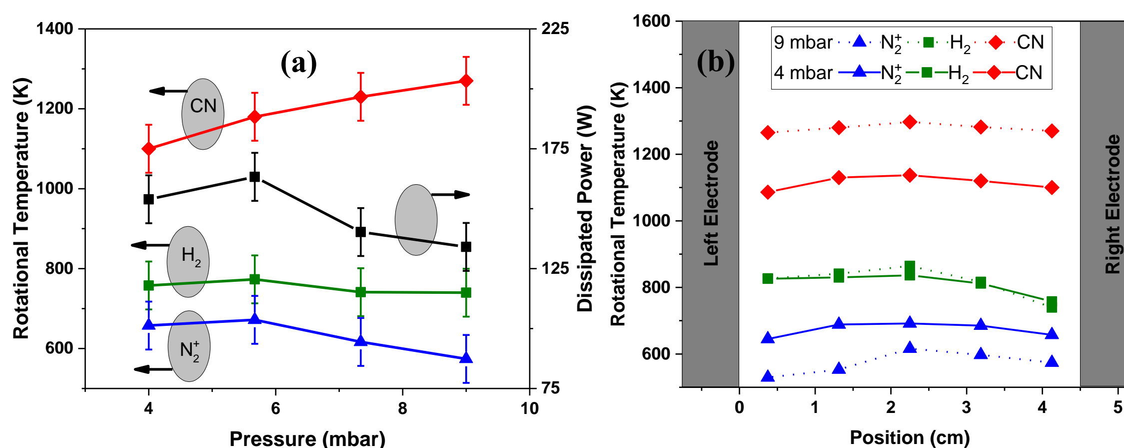

Figure 6.7: (a) The rotational temperatures of N_2^+, CN and H_2 as a function of pressure. These temperatures are measured at a position of 4 cm from the left electrode. (b) Spatial measurements of the rotational temperature at 4 and 9 mbar. The plasma condition is 95% H_2/5% N_2 at 9 mbar and a set power of 500 W.

Interestingly, the emission of Peak 1 in the spatial emission profile in Fig. 6.8(a) increases first with pressure until 5.67 mbar after which it disappeares or merges with Peak 2, in agreement with the findings in Refs. [224], [225]. The emission intensity decreases as pressure increases due to lower electron temperature. Thus, the RMS value of the voltage drops from 300 to 220 V when

the pressure increases from 4 to 9 mbar at 500 W (Fig. 6.8(b)). The drop of voltage with increased pressure is accompanied by a decrease of the sheath thickness when the pressure rises from 4 to 9 mbar, as shown in Fig. 6.8(a). The overall effect is a maximum dissipated power near 5.67 mbar, and hence, the rotational temperatures of H_2, N_2^+ exhibit similar dependence on pressure, as shown in Fig. 6.7. The H_2 rotational temperatures remain at values around 750 K with increased pressure from 4 to 9 mbar. However, the rotational temperature of N_2^+ decreases from 660 to 575 K, whereas the CN rotational temperature rises from 1100 to 1270 K in the same pressure range.

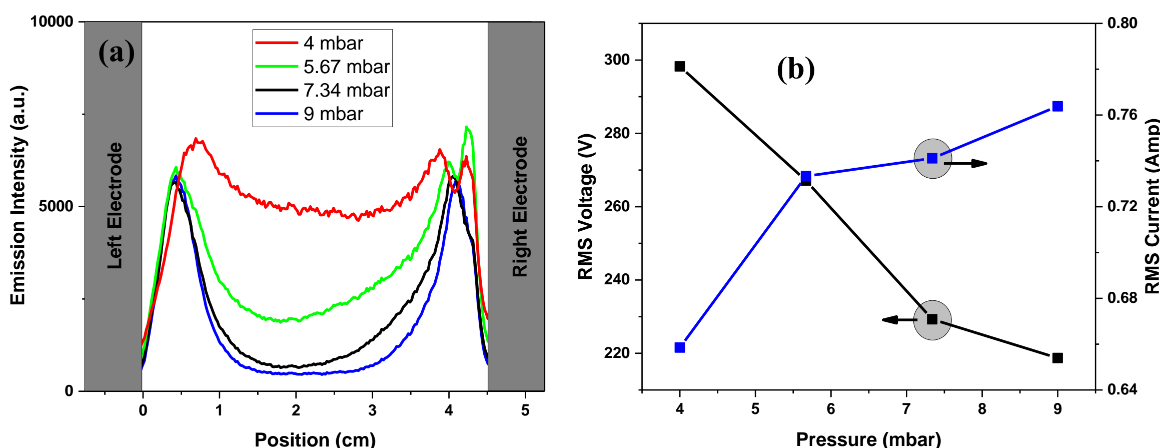

Figure 6.8: (a) Spatial emission of the plasma as a function of pressure. (b) The root-mean-square (RMS) of the voltage and current as a function of pressure. The plasma condition is 95% H_2/5% N_2 at 9 mbar and a set power of 500 W.

6.3.2 Effects of Nitrogen, Oxygen, and Methane Addition on Power Dissipation and Rotational Temperatures

The addition of nitrogen (N_2), oxygen (O_2), or methane (CH_4) to the H_2 plasma at 9 mbar and 1000 W affects the H_2 plasma properties. For instance, the spatial emission intensity between the electrodes increases with increased N_2 mole fraction at constant pressure and power (Fig. 6.9(a)). However, because of the electronegativity of O_2 and CH_4 gases, the emission intensity decreases with increased O_2 or CH_4 mole fraction as shown in Figs. 6.9 (b) and (c), respectively. These results indicate the difference in ionization and excitation processes with the addition N_2, O_2, or CH_4 to H_2 plasma. Indeed, the evolution of the two emission peaks near the right electrode (especially Peak 1) with the addition of these gases indicates a change in the ionization processes [224]–[226]. Peak 2 remains similar with the addition of these gases. However, the intensity of Peak 1 increases with N_2 mole fraction, decreases with CH_4 mole fraction, and increases initially at 3 and 5% O_2 but then decreases at higher oxygen mole fraction.

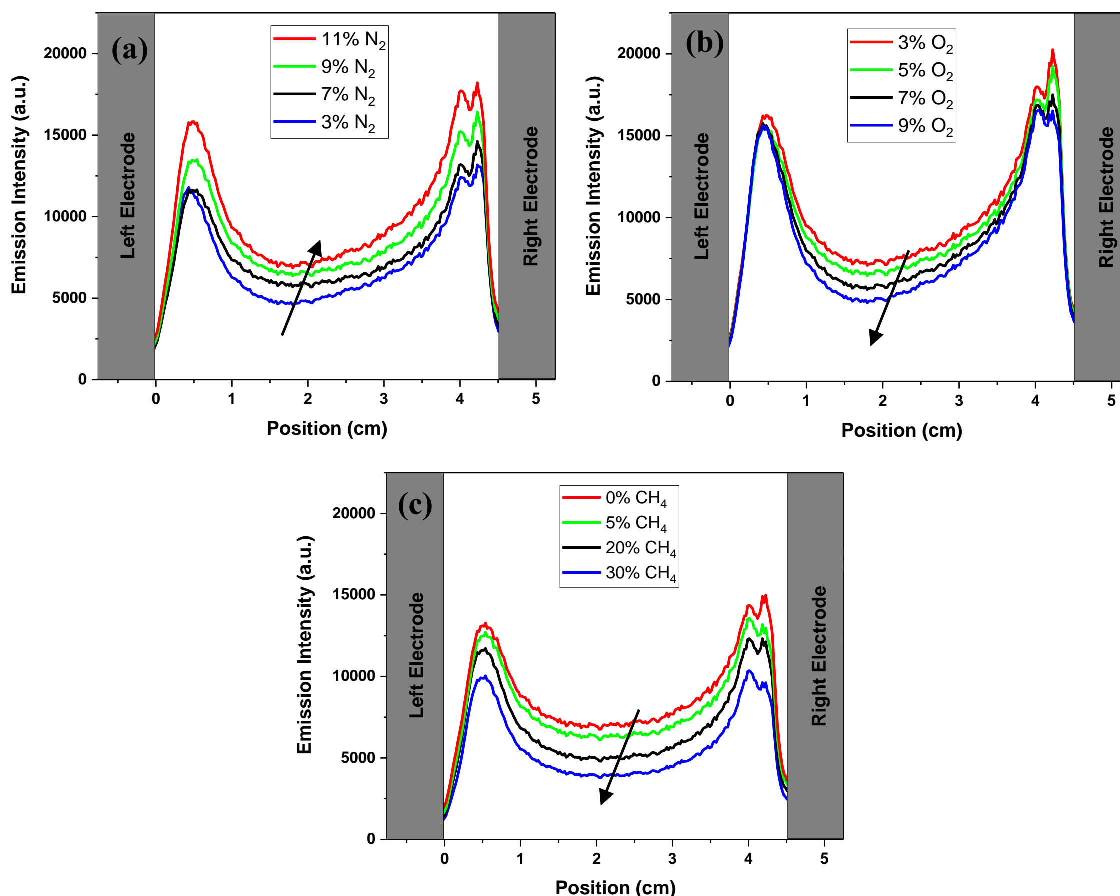

Figure 6.9: The variations of spatial plasma emission with (a) N_2 mole fraction, (a) O_2 mole fraction, and (a) CH_4 mole fraction at a set power of 1000 W and 9 mbar.

Figure 6.10 reveals a slight increase of dissipated power with increased N_2 mole fraction. Consequently, the H_2 rotational temperature increases from 877 to 994 K as N_2 mole fraction increases from 3% to 9%. Similarly, the rotational temperature of N_2^+ increases from 752 K at 3% N_2 and 97% H_2, to 915 K at 9% N_2 and 91% H_2 (Fig 6.10). The increase of the temperature with increased N_2 mole fraction is due to enhanced collisional frequencies, in agreement with a previous report in a microwave plasma [97]. On the other hand, the rotational temperature of CN changes little with the addition of N_2, with temperature values of 1400 K at 3% N_2 and 1450 K at 9% N_2 (Fig 6.10).

The power dissipation rises sharply (by 68 W) with the addition of only 3% O_2 to the 92%/ 5% H_2/N_2 plasma but then remains approximately constant beginning around 500 W (Fig. 6.11). This higher dissipated power increase can be related to compensating for the electron number density decrease due to electron attachment processes of O_2 [219]. Thus, the rotational temperature

of N_2^+ increases strongly from 727 K at 0% O_2 (95%H_2/5% N_2 plasma) to 900 K at 3% O_2 (and 92%H_2/5% N_2), which later becomes equal to the H_2 rotational temperature. Both remain nearly constant (around 900 K) as oxygen mole fraction further increases (Fig. 6.11). However, the CN rotational temperature stays at a relatively stable value near 1450 K as a function of O_2 mole fraction.

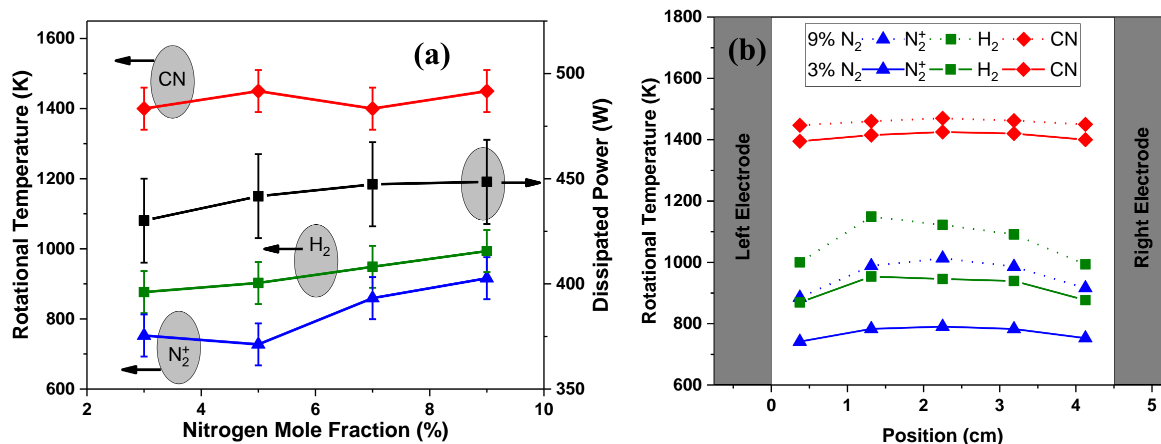

Figure 6.10: (a) The rotational temperatures of N_2^+, CN and H_2 as a function of nitrogen mole fraction at 9 mbar and a set power of 1000 W. Temperatures are measured at a position of 4 cm from the left electrode. (b) The spatial dependence of the rotational temperatures at 97%/3% H_2/N_2 (3%N_2) and 91%/9% H_2/N_2 (3%N_2).

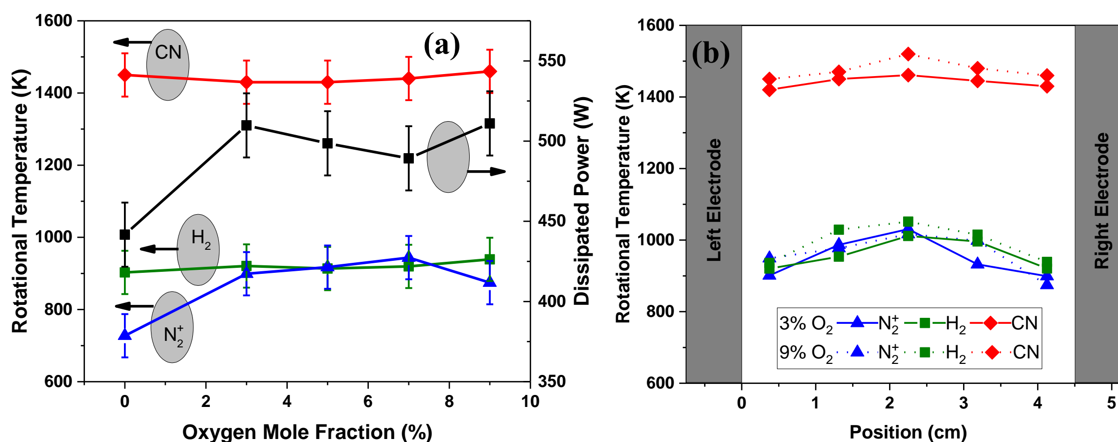

Figure 6.11: (a) The rotational temperatures of N_2^+, CN and H_2 as a function of oxygen mole fraction at a set power of 1000 W and 9 mbar. The temperatures are measured at a position of 4 cm from the left electrode. (b) The spatial dependence of the rotational temperatures at 92%/5%/ 3% H_2/N_2/O_2 (3% O_2) and 86%/5%/9% H_2/N_2/O_2 (9% O_2).

The addition of CH_4 raises the dissipated power from 442 W to 540 W with an increase of CH_4 mole fraction from 0% CH_4 in 95%/5% H_2/N_2 plasma to 20% CH_4 in 75%/5% H_2/N_2 plasma (Fig. 6.12(a)). However, the dissipated power then decreases slightly for 25% CH_4 in 70%/5%

H_2/N_2 plasma and 30% CH_4 in 65%/5% H_2/N_2 plasma. The addition of CH_4 to H_2 in a microwave plasma in prior work increased the electron number density but decreased the electron number density, indicating a change in energy exchange between electrons and neutrals [228]. Similarly, gas temperature rises with the addition of methane in a H_2 microwave plasma [97]. Thus, with increased methane mole fraction from 0% to 30%, the N_2^+ rotational temperature increases from 727 to 974 K whereas the temperature of H_2 remains stable around 870 K (Fig. 6.12). Both species have similar temperatures at 5% and 10% CH_4 in agreement with the previous results for the addition of N_2 and O_2. The difference between the H_2 and N_2^+ rotational temperatures remains similar with changes in H_2 mole fraction (e.g., an increase of CH_4 mole fraction). Finally, the rotational temperature of CN declines from 1450 to about 1330 K when methane mole fraction increases from 0 to 15%, but then CN temperature increases to 1550 K at 30% CH_4. The initial decrease in the CN temperature with the addition of CH_4 could be related to the production mechanism of CN, as discussed in the next section.

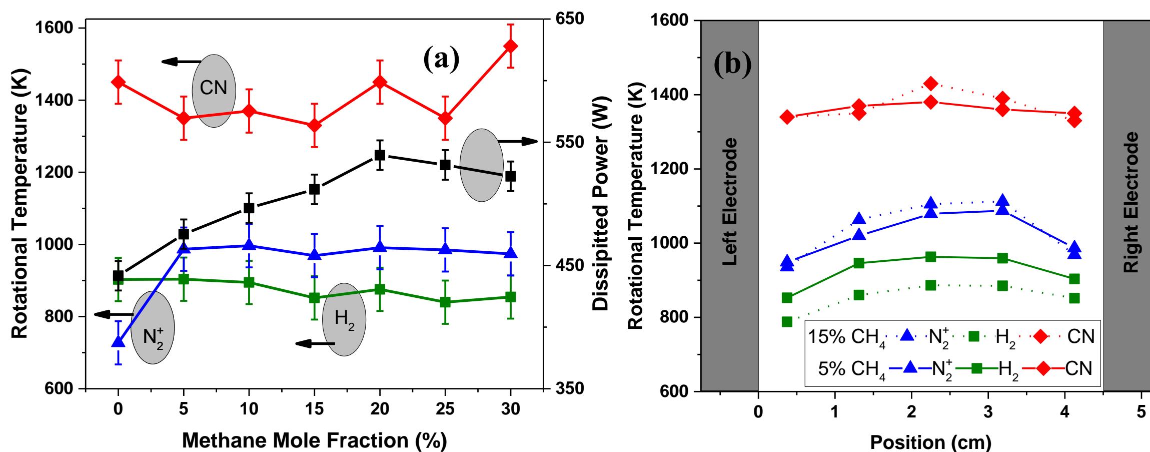

Figure 6.12: The rotational temperatures of N_2^+, CN and H_2 as a function of methane mole fraction. The plasma set power and pressure are kept constant at 1000 W and 9 mbar, respectively. The temperatures are measured at a position of 4 cm from the left electrode. (b) The spatial dependence of the rotational temperatures at 90%/5%/5% $H_2/N_2/CH_4$ (5% CH_4) and 80%/5%/15% $H_2/N_2/CH_4$ (15% CH_4).

6.3.3 Differences among H_2, N_2^+ and CN Rotational Temperatures

The differences in rotational temperatures of H_2, N_2^+, and CN are due to the non-equilibrium nature of the plasma [112]. These measurements are obtained from emission spectra that reflect the upper electronic states of the corresponding species. The CN temperatures have higher values than those from N_2^+ and H_2 because of the production mechanism of CN from the

graphite electrodes in N_2-containing plasmas without CH_4 (or other gas-phase carbon sources). Similar observations have been reported previously in a N_2 glow discharge [229] as well as plasmas containing N_2 [230], [231]. Kutasi et al. [229] suggested that the CN was produced from sputtering of CN due to the surface reactions of N atoms (at ground state 'S' or metastable states 'P or D') with a graphite surface ($C_{surface}$):

$$C_{surface} + N(S) \rightarrow CN(X) \quad \text{(R4)}$$

$$C_{surface} + N(P) \rightarrow CN(B) \quad \text{(R5)}$$

$$C_{surface} + N(D) \rightarrow CN(X, A) \quad \text{(R6)}$$

Because the surface reactions of CN are exothermic, part of the energy is absorbed by CN rotational lines to yield high rotational temperatures. Indeed, the CN temperature decreases from 1450 to 1350 K with the addition of 5% CH_4 and then gradually decreases to 1330 K at 15% CH_4. This initial decrease of the CN rotational temperatures in the presence of CH_4 is because of the alternative source of carbon production from the gas-phase reactions in the presence of methane. On the other hand, the increase of CN temperature at 20% CH_4 is likely related to the higher dissipated power with increased methane mole fraction. Therefore, the CN rotational temperature is far from equilibrium with the translational gas temperature and does not represent the gas temperature in the system.

The rotational temperatures of H_2 have values lower than CN but higher than N_2^+ temperatures. Nevertheless, the H_2 rotational temperatures become similar to the rotational temperature of N_2^+ with the addition of N_2, O_2, and low to moderate concentrations of CH_4. With further increases in methane mole fraction, however, the H_2 temperature becomes lower than that of N_2^+ as shown above. Previous reports indicate that the translational gas temperature of low-pressure plasmas (5 Pa [111] and 133 Pa [232]) is twice the rotational temperature determined from the upper state of the H_2 Fulcher band. In this low-pressure limit, the rotational distribution of the H_2 Fulcher upper state, which is populated by direct electron excitation, is an image of its lower state [21],[111]. A correction factor of 2 is applied to account for the difference between the rotational constants of the lower and upper states, which are 60.809 and 30.364 cm^{-1}, respectively. Conversely, both the rotational and gas temperatures become equal in the high-pressure limit when the excited states are populated by electron excitation and the rotational relaxation time is higher than the radiative lifetime of the upper state ($d^3\Pi_u$), which is approximately 25 nsec [21]. At

intermediate pressures, on the other hand, the relaxation time is 18 nsec at 9 mbar [232]. Since both rates are comparable, partial thermalization of the excited state occurs, leading to an incomplete equilibrium between rotational and gas temperatures. Therefore, the deviation of the rotational temperature of H_2 from the other species in this study is related the partial equilibrium of the upper state of the H_2 Fulcher band, as shown in Figs. 6.5 and 6.7. Nevertheless, the thermalization processes might be enhanced with addition of other molecular gases (such as N_2, O_2, and CH_4) that enhance collision rates, as presented in Figs. 6.10-6.12. In general, the rotational temperature derived from the H_2 Fulcher band has a weaker dependence on the plasma parameters, as reported previously [233].

The rotational temperature of N_2^+ is more sensitive to the plasma conditions and produces lower values than CN and H_2 (except with the addition of N_2, O_2, and CH_4 as discussed above). The upper state ($N_2^+(B)$) is excited by direct electron excitations of either $N_2(X)$ or $N_2^+(X)$ depending on the electron temperature [21]:

$$N_2(X) + e^- \rightarrow N_2^+(B) + 2e^- \quad \text{(R7)}$$

$$N_2^+(X) + e^- \rightarrow N_2^+(B) + e^- \quad \text{(R8)}$$

If thermalization is not fully completed in the excited state, then its rotational distribution is a map of those of the ground states that have similar rotational constant values (2.00 cm^{-1}, 1.93 cm^{-1} and 2.08 cm^{-1} for $N_2(X)$ or N_2^+ (X) and $N_2^+(B)$, respectively) [21]. Therefore, the N_2^+ rotational temperatures are reasonably representative of the gas temperatures in the conditions studied above.

6.4 Conclusion

Three measurements, namely the power dissipation, rotational temperatures of various species, and plasma emission, have been combined to study a capacitively coupled H_2 plasma at 80 kHz at different conditions relevant to graphene growth. The power dissipated in the plasma is found to be substantially less than the set power, and its percentage depends on the process conditions. The dissipated power increases with higher set power, the addition of N_2, O_2, and CH_4 mole fractions, whereas it decreases for gas pressures higher than 5.67 mbar. The rotational temperatures from $H_2(d^3\Pi_u \rightarrow a^3\Sigma_g^+)$, N_2^+(B-X) and CN(B-X) are measured using optical emission spectroscopy (OES). The effects of variations in plasma power and gas pressure, and the addition of nitrogen (N_2), oxygen (O_2), and methane (CH_4) gases on the rotational temperatures have been quantified.

The rotational temperature of N_2^+ represents the translational gas temperature in our system. Both the N_2^+ and H_2 rotational temperatures have similar values with the addition of N_2, O_2, and CH_4, whereas the CN rotational temperature is found to be higher due to a production mechanism from graphite electrodes. Furthermore, the plasma emission intensity between the electrodes increases with the set power and the addition of N_2, whereas the intensity decreases with pressure and the addition of O_2 and CH_4. The emission results reveal a double-layer formation near the smaller electrode that also depends on process conditions. These experimental results aid in understanding and controlling the plasma environment for graphene deposition in a roll-to-roll fashion.

7. EXPERIMENTAL ANALYSIS OF AN 80 KHZ CAPACITIVELY COUPLED ARGON PLASMA

7.1 Motivation and Background

Capacitively coupled plasmas (CCPs) operate in two different modes: alpha and gamma, depending on gas mixture, pressure, discharge gap and plasma power [155], [216]. The current density is low in the alpha-mode (α-mode) which is sustained by a volume ionization processes in the plasma bulk during sheath oscillations, "i.e., the wave-riding mechanism" [234]. The α-mode's sheath in the electrode vicinity is non-conductive, and, thus, the current flows in the sheath as displacement current to match the conduction current in the plasma bulk and close the electrical circuit. As the current (or power) is raised to a critical value, the sheath breaks down and the plasma transitions to a gamma mode (γ-mode) which is sustained by secondary electron emission processes from the electrode surface due to strong ion bombardment [234]. The transition from alpha to gamma modes (α-to-γ transition) is identified by the contraction of the plasma size and the drastic change of the current-voltage characteristics curve at high gas pressures [155].

The low-frequency CCPs exist mostly in the γ-mode, as reported previously for a N_2 plasma at 40 kHz and 0.15 Torr [217], and an Ar plasma at 10 kHz and 0.38 Torr [235], since the displacement current is low in low-frequency plasmas [236]. The displacement current (I_{dis}) exhibits a linear dependence on the sheath capacitance (C_s) and the plasma frequency (ω) written as $I_{dis} = C_s \frac{dV}{dt}$, assuming a sinusoidal voltage waveform of $V = V_o \cos(\omega t)$ where V and t are the voltage and time, respectively [236]. Thus, the existence of alpha discharge is limited to high-frequency plasmas, and the operation boundary of alpha discharge can be extended by increasing the plasma frequency at moderate pressures [216], [237] and atmospheric pressures [238], [239].

The prior results in Chapter 3 show that graphene deposition on Cu foil is of a better quality when the plasma exists in an alpha-like mode, or hybrid, mode [23]. Alpha discharges are more favorable for industrial applications due to their higher plasma uniformity and stability at lower current densities [240], [241]. Therefore, two methods have been attempted to expand the operational space of the α-mode. One method is to increase the plasma frequency to intensify the displacement current [216], [237]–[239], while the other is to apply a dielectric coating to the electrodes to delay the secondary electron emission processes [242]. However, applying a coating

to the electrodes can lead to contamination from sputtering the coating, which degrades the thin-film quality, whereas increasing plasma frequency could add cost and complexity to the rf system while also decreasing ion energy at high plasma frequencies [243], [244]. Here, we show that, when using a square waveform voltage, Ar plasma can operate in an alpha-like mode at 80 kHz leading to a uniform and stable plasma for high-quality graphene production.

In this chapter, an 80 kHz Ar CCP is studied experimentally at different gas pressures and plasma set powers to examine the existence of an alpha-like mode at low-frequencies. The experimental setups for the electrical and spectroscopy measurements are detailed in Section 7.2. Section 7.3 presents the results from the electrical and optical experiments, and the spatial spectra from optical emission spectroscopy (OES). The results of this work show the possibility of sustaining an alpha-like discharge at low frequencies that can be directly and economically transformed to useful plasma sources for several applications in the semiconductor industry.

7.2 Experimental Setup

The plasma experimental setup is similar to the previous chapters and explained here briefly for clarity. Figure 7.1 shows a schematic of the experiment setup including the plasma generated between two electrodes, the current and voltage probes and the iCCD camera for plasma imaging. At the beginning of the experiment, the chamber is brought to vacuum (less than 0.01 mbar). Then, argon gas (Ar) is introduced into the chamber until a pressure of 7 mbar is achieved, at which point the plasma is initially ignited at a plasma set power of 500 W. The gas pressure, which is monitored using 10 and 100 mbar pressure gauges, is then set at 5.5, 9.5 and 13.8 mbar, with corresponding Ar gas flow rates of 90, 220, and 400 standard cubic centimeters per minute (sccm), respectively.

The frequency of the plasma is fixed at 80 kHz, and the plasma set power is varied from 300 to 900, 1100 and 1300 W for gas pressure values of 5.5, 9.5 and 13.8 mbar, respectively. The outputs from the rf generator are connected to ignitor rods attached to symmetrical graphite electrodes with length of 12.5 cm. The voltage supplied to the electrodes is measured with a Tektronix voltage divider (Model 5100), and the current is measured with a Pearson Current Probe (Model 6858). Probes are fixed in the ignitor rod to directly measure the current and voltage supplied to the plasma [215]. The current and voltage waveforms are measured simultaneously through an Agilent Technologies oscilloscope (Model DSO5014A, 100 MHz, and 2 GSa/s). Three

measurements of current and voltage waveforms are acquired at each condition, and their averages are used in the analysis with an experimental error of less than 10% in the current and voltage values.

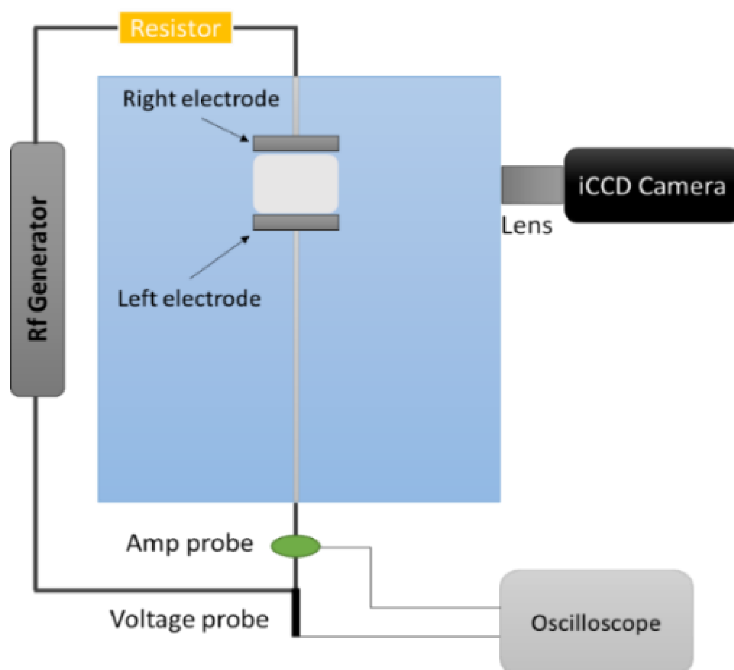

Figure 7.1: The experimental setup of the capacitively coupled plasma at 80 kHz. The current and the voltage probes are placed on the ignitor connected to the graphite electrode. Emission of the plasma in the range of 300-800 nm is measured using an iCCD camera. Also, optical emission spectroscopy (OES) is used to detect the emission spectrum between the electrodes.

Figure 7.2 shows the voltage and current waveforms at 13.8 mbar and powers of 300 and 900 W. The current and voltage are in-phase, which is a characteristic of low-frequency discharges [235], [245]. Both the current and voltage have a square waveform shape that becomes slightly distorted at 900 W due to the higher discharge capacitance with increased plasma set power [215]. In addition, the time-averaged emission from the plasma is measured using an iCCD camera (Princeton Instruments PI-MAX 4 iCCD) over the wavelength range 300-800 nm. For direct and qualitative analysis of the plasma luminosity at different conditions, the plasma emission profile is extracted using Lightfield software (from Princeton Instruments). The plasma emission spectrum is also measured spatially between the two electrodes using optical emission spectroscopy (OES) in the spectral range of 400-870 nm, as discussed in the previous chapters.

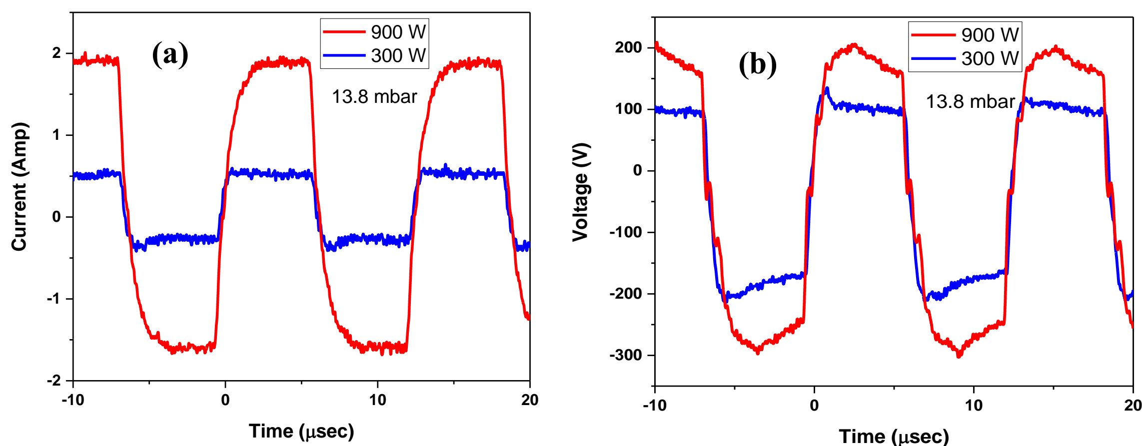

Figure 7.2: (a) Voltage and (b) current waveforms of Ar plasma measured at 13.8 mbar with plasma set powers of 300 and 900 W.

7.3 Results and Discussion

7.3.1 Electrical and Spectroscopy Characterizations

The root mean square (RMS) current and voltage increase monotonically with the plasma set power at 9.5 and 13.8 mbar, as presented in Fig. 7.3(a). The current exhibits strong dependence on the plasma set power, with negligible effects from the gas pressure [215], [246]. For example, the RMS current rises from 0.44 to 2.26 Amp, with increased plasma set power from 300 to 1300 W at a fixed gas pressure of 13.8 mbar. Similarly, the RMS voltage depends on the plasma set power, with voltage values of 147 V and 244 V at plasma set powers of 300 and 1300 W, respectively, at a constant gas pressure of 13.8 mbar. In addition, the RMS voltage decreases remarkably with increased gas pressure, especially at higher plasma set powers, since the sheath thickness decreases with raised gas pressure. Hence, a higher RMS voltage is needed to sustain plasma with a thicker sheath where the voltage drops [215].

The dissipated power, derived from Eq. (18) in Chapter 6, improves with increased RMS current (or plasma set power), as shown in Fig. 7.3(b). At a constant set power, the dissipated power is marginally higher at lower pressures because of higher voltages (Fig. 7.3(a)). The correlation between the current and the dissipated power is nearly quadratic at low frequency, particularly at lower currents and higher pressures. Hence, the power is dissipated mostly in the sheath by the ions that bombard the electrode surfaces [214], [215], [247]. Furthermore, the dissipated power at 13.8 mbar increases from 54 to 520 W with an increase in the current (or

plasma set power) from 0.44 Amp (or 300 W) to 2.26 Amp (or 1300 W). Correspondingly, the ratio of the dissipated power to the set power rises from 18% at 300 set power to 40% at 1300 set power due to the rise in the number of collisions between electrons, ions, and atoms at a high plasma input power [248].

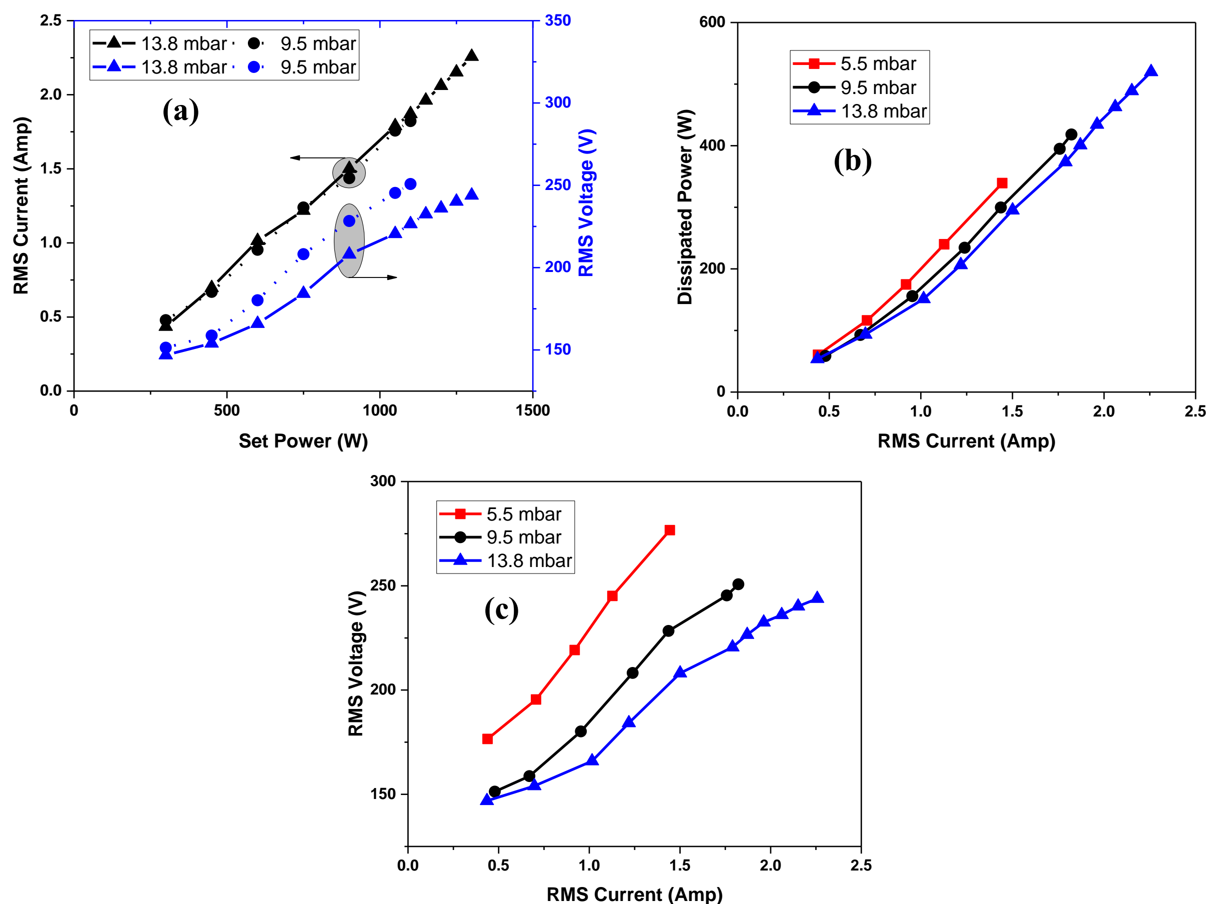

Figure 7.3: (a) The RMS values of voltage and current at 9.5 and 13.8 mbar as a function of plasma set power. (b) The dissipated power in the plasma as a function of measured current at 5.5, 9.5 and 13.8 mbar. (c) The current and voltage characteristics at 5.5, 9.5 and 13.8 mbar.

The current and voltage characteristic curve is presented in Fig 7.3(c), which is derived from the results of Fig. 7.3(a). At a constant gas pressure, the current and voltage have a linear correlation which is a common characteristic of Ar plasma at high frequencies [215]. However, the slope of the voltage-current curve changes as a function of current, particularly for the plasma at 13.8 mbar (Fig. 7.3(c)). For instance, the slope of the 13.8 mbar plasma is small at currents below 1.0 Amp, then increases in the range of 1.0-1.5 Amp, but finally minimizes for current values greater than 1.5 Amp.

The time-averaged emission profiles of the plasma at various pressures and set powers are presented in Fig. 7.4. The intensity profiles include the total spectra from all species emitting in the wavelength range of 300-800 nm. At lower and moderate pressures (5.5 mbar and 9.5 mbar) the plasma exhibits two peaks near the electrodes with negligible intensity at the middle of the discharge region, as illustrated by the plasma images in the inset of Fig. 7.4(b). A similar behavior of the emission profile is observed at 13.8 mbar but at lower plasma set powers (i.e., 300-600 W) (Fig. 7.4(c)). The emission profiles for such cases indicate an alpha-like mode, as reported previously [155], [249]. However, a substantial emission appears in the middle of the discharge for the 13.8 mbar plasma when increasing the set power over 750 W (the inset of Fig. 7.4(c)). This sharp increase in plasma luminosity demonstrates a change in the ionization processes when the power is raised to 750 W and higher. Such plasma emission alterations and the corresponding voltage-current characteristic results of Fig. 7.3(c) indicate the existence of alpha-like and gamma modes in low-frequency square-waveform plasma.

Capacitively coupled plasmas exist mostly in the γ-mode at low frequencies due to low displacement current [217]. α-discharge is sustained when the displacement current in the non-conducting sheath is high and equal to the conduction current in the plasma bulk. The displacement current has a linear-dependence on the plasma frequency and the sheath capacitance in a sinusoidal voltage waveform. However, alpha-like discharge can be sustained at low frequency using the square wave voltage because of the higher frequency components in the square waveform. Thus, Fast Fourier Transform (FFT) analysis was made for the voltage waveforms to reveal the primary frequency's components. The 80-kHz square waveform contains strong high harmonics of the real part of the FFT up to the 9th harmonic at 720 kHz, as shown in Fig. 7.5(a). Similar high-frequency components were obtained from the current waveform. The odd harmonics (ω_3, ω_5, ω_7, ω_9, ω_{11}) have higher values than the even harmonics, due to the time variation of the sheath capacitances within the rf field at a frequency of 2ω [246], [249]. Thus, the existence of high frequencies strengthens the displacement current in the sheath. Furthermore, the time derivative of the voltage at 13.8 mbar and 300 W shows sharp peaks when the voltage changes its polarity, which is equivalent to a sinusoidal waveform with a frequency of 720 kHz (Fig. 7.5(b)).

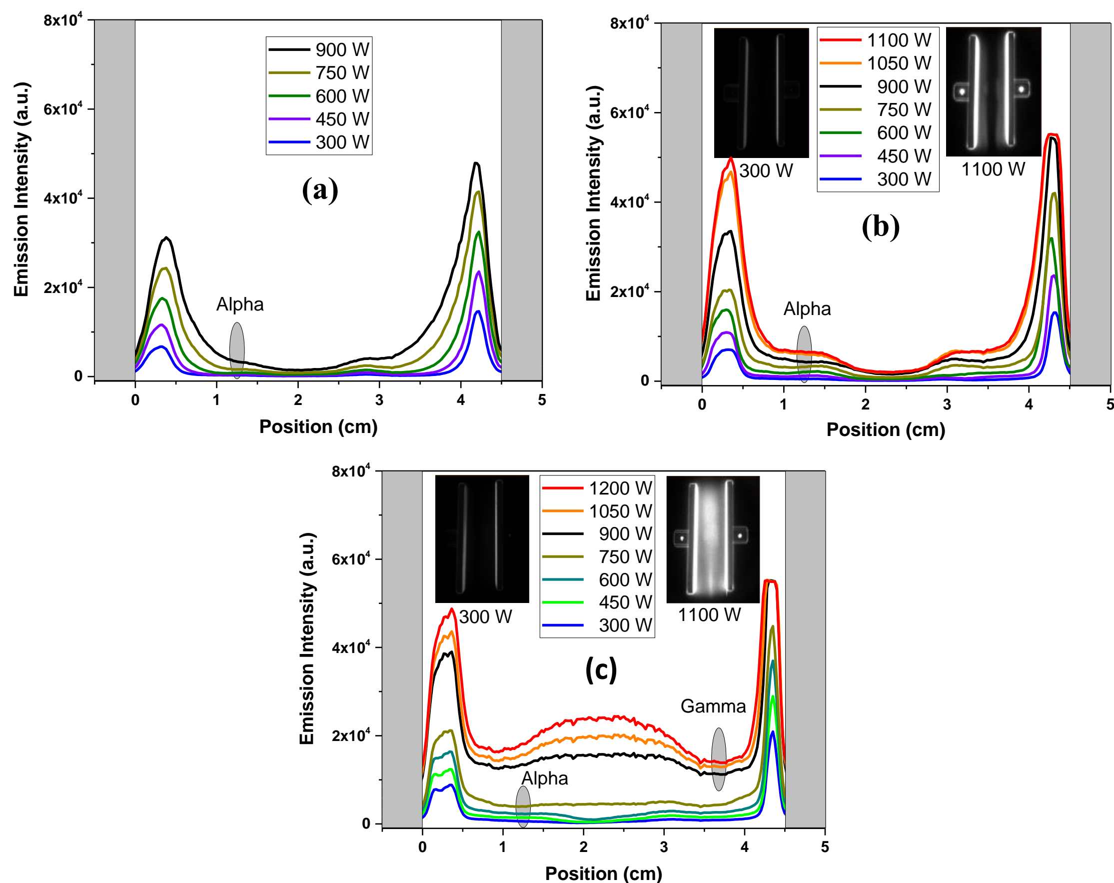

Figure 7.4: Spatial profiles of plasma emission showing the differences between plasma luminosity in alpha and gamma modes at (a) 5.5 mbar, (b) 9.5 mbar and (c) 13.8 mbar as a function of plasma set power. Plasma images from the iCCD camera are shown at 9.5, and 13.8 mbar are shown in the inset of (b) and (c) respectively, at plasma set powers of 300 and 1100 W. The intensity scale for these images is 0 to 25,000 counts.

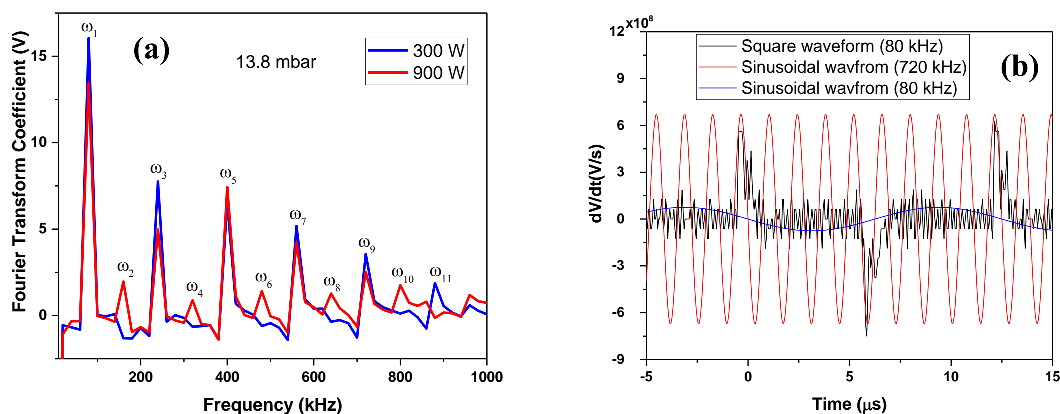

Figure 7.5: (a) Fourier transform coefficients of the voltage waveform at 13.8 mbar and different plasma powers. (b) The time-derivative of the voltage square waveform compared to sinusoidal waveforms at 80 kHz and 720 kHz with identical RMS and offset voltages at 13.8 mbar pressure and 300 W set power.

7.3.2 Comparison between Species Emission from OES

The plasma emission in the 400-870 nm spectral range is measured between the electrodes using OES. Figure 7.6 presents a comparison between the spectra of 9.5 and 13.8 mbar as a function of set power near the gap center (around 2.6 cm from the left electrode). At 9.5 mbar, only Ar and Ar^+ lines exist with higher emission intensity as the plasma set power is increased from 600 W to 900 W due to enhanced electron number density with raised plasma power (Fig. 7.6 (a)). Also, the emission spectrum at 13.8 mbar and 600 W has similar features to the 9.5 mbar spectra (Fig. 7.6(b)). The three spectra exist in the hybrid mode, as shown previously in Fig. 7.4.

However, when the plasma set power is raised to 900 W at 13.8 mbar, the plasma transits to the gamma mode associated with a high-intensity emission spectrum, as presented in Fig. 7.6(b). The spectrum exhibits strong emission from carbon-based species and hydrogen lines in the 400-600 nm spectral region, as presented in Fig. 7.6(b). The non-Ar species are expected to originate from graphite electrodes, since only Ar gas is supplied to the chamber. At higher set power and gas pressure (13.8 mbar), the secondary electron emission processes are enhanced due to the intensified ion bombardment [234], which lead to graphite electrodes sputtering and eventually the production of carbon based species and hydrogen.

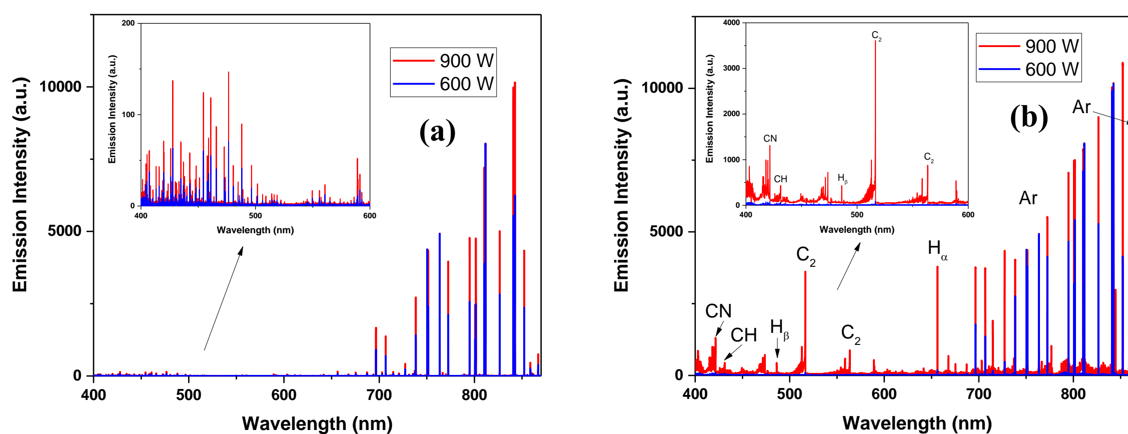

Figure 7.6: Plasma emission spectra measured near the discharge gap center (around 2.6 cm from the left electrode) at (a) 9.5 mbar and (b) 13.8 mbar as a function of plasma set power.

Figure 7.7 presents the spatial distribution of emission intensities for Ar, Ar^+, C_2 and H_β as a function of plasma set power and gas pressure. The Ar line emission intensity has two peaks near the electrodes associated with high electron temperatures. The emission of Ar is negligible in the middle of the discharge gap in the hybrid mode, whereas a strong Ar emission intensity is present in the discharge center indicating a gamma plasma. However, the Ar^+ emission intensity has only

two peaks near the electrodes with zero emission intensity at the middle of the discharge for all the cases (Fig. 7.7(b)). Also, Ar^+ emission intensity increases with raised plasma set power with an insignificant dependence on pressure. The Ar^+ emission profile suggests that ions exist mainly near the electrodes' sheath due to their lower electron number density.

The emission spectra also reveal the presence of non-Ar species, such as C_2 and H_β, predominantly in the gamma discharge, as illustrated in Fig. 7.7 (c) and (d), respectively. The C_2 emission intensity has only minor peaks near each electrode in the hybrid mode. However, a significant amount of C_2 occurs with a bell-shaped profile for the gamma mode at 13.8 mbar and 900 W. Secondary electrons are emitted from the graphite electrodes due to ion bombardment, and accelerated toward the plasma bulk. The ionization processes are responsible for sustaining the gamma-mode at high plasma powers [234], [237]. Electrode sputtering also occurs as a result of ion bombardment processes leading to the production C atoms which recombine in the plasma bulk to for a more stable intermediate C_2 and other carbon-based species at the center of the discharge.

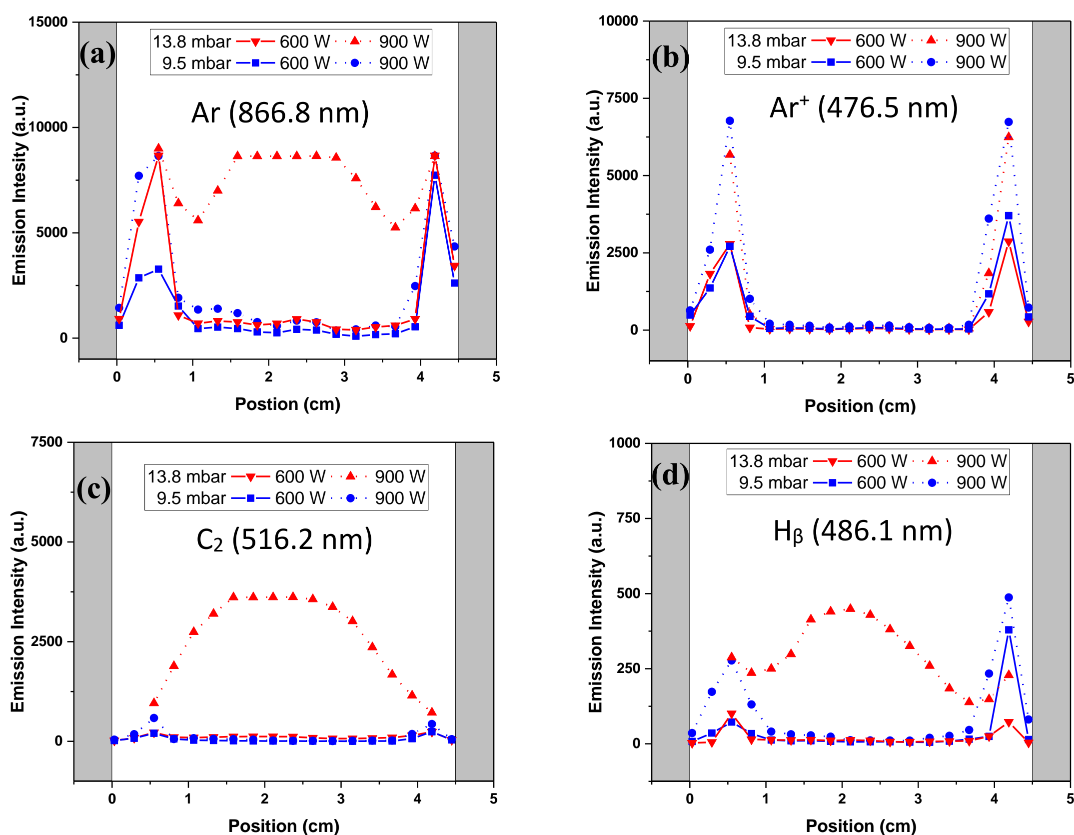

Figure 7.7: Spatial emission intensity profiles of (a) Ar at 866.8 nm, (b) Ar^+ at 476.5 nm, (c) C_2 at 516.2 nm and (d) H_β at 486.1 nm.

In addition, a modest contribution from H atoms is observed in the plasma emission with two peaks near the electrodes and higher intensity at lower pressure (Fig. 7.7(d)). Furthermore, the H_β emission disappears at the middle of the discharge in the hybrid mode, whereas a strong emission intensity profile arises in the gamma mode. The presence of H emission in Ar plasma might be due to the presence of H_2 gas adsorbed in the graphite electrodes during graphene growth from previous experiments. Due to the existence of non-Ar plasma species in the gamma mode, plasma properties, such as electron temperature and electron number density, are expected to change. The effects of decreasing plasma set power below the transition critical value are experimentally investigated next to determine if non-Ar plasma species prevent the reverse transition to the hybrid mode.

7.3.3 Plasma Hysteresis during the Transition from Gamma to Hybrid Mode

The plasma returns to the hybrid mode from the gamma mode when the set power is lower than 750 W (Fig. 7.8(a)) [216]. However, the transition from gamma to hybrid mode is shifted to a lower power than the shift from hybrid to gamma because of active secondary electron emission ionization processes in the gamma mode [220]. Consequently, the difference in the emission intensity near the transition point (i.e., 750 W) is higher at 13.8 mbar than at 9.5 mbar (Fig. 7.8(b)).

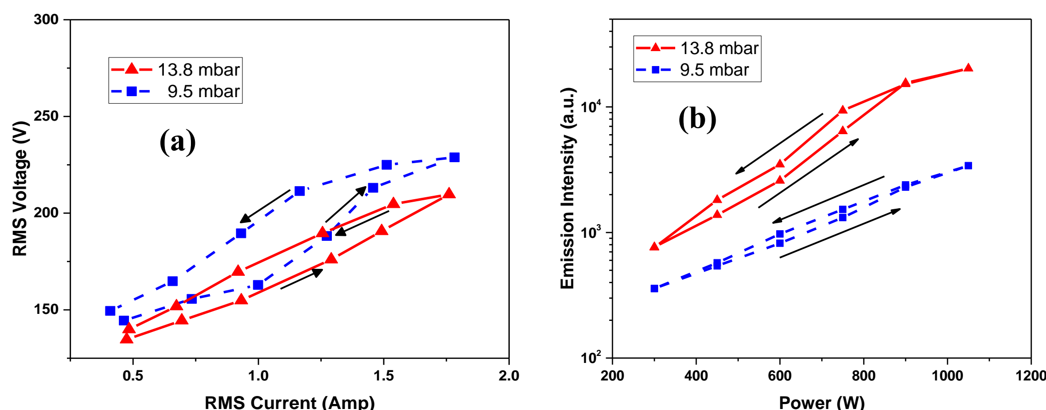

Figure 7.8: (a) The RMS current and voltage curve at 9.5 and 13.8 mbar as a function of increasing/decreasing plasma set power. (b) The emission intensity at the middle of the discharge at 9.5 and 13.8 mbar as a function of increasing/decreasing plasma set power.

The voltages measured during plasma power decrease from gamma to hybrid modes are slightly higher than initial values, whereas the current remains unchanged within measurement uncertainty. Such hysteresis was detected previously [250]–[252]; which arises when electrons reach a higher number density at an increased power and requires a higher voltage input to sustain

the plasma. For instance, the peak emission intensity intensities at the middle of the discharge, extracted from the emission profile as in Fig. 7.4, are higher when decreasing in power, as shown in Fig. 7.8(b). Thus, the existence of active ionization processes initiated by previous higher power conditions results in higher electron number density, which dissipates more plasma power to sustain the plasma [220].

7.4 Conclusion

Our work demonstrates the existence of the hybrid and gamma modes in a capacitively coupled argon plasma at 80 kHz frequency sustained by a square waveform voltage. Fourier transform analysis of the voltage shows the presence of high-frequency components with values up to 720 kHz. Such high-frequency components promote the displacement current values. The gamma mode also contributes to alpha plasma due to energetic ion bombardment in the low-frequency plasma. At 5.5 and 9.5 mbar, only the hybrid discharge exists. Although initially the plasma exists in the hybrid mode at 13.8 mbar, it then transits to gamma plasma when the plasma set power is higher than 750 W. Thus, a significant emission occurs at the middle of the discharge, with considerable contribution from non-Ar species such as C_2, CH and H. The plasma transits back to the hybrid mode when the plasma set power decreases below 750 W. The current and voltage curve and plasma emission intensity experience a hysteresis while the plasma set power is ramping down from a higher value. These results aid in understanding the plasma properties of Ar plasma to derive useful observations that can be correlated to the plasma behavior during graphene growth.

8. DIRECT LARGE-SCALE DEPOSITION OF THIN GRAPHITE FILM ON CU FOIL

Recent developments in semiconductor electronic devices have created enormous challenges surrounding intensified power dissipation and heat generation in ever decreasing device sizes [253]–[256]. In order to increase system reliability and performance, various thermal spreaders, in the form of interface materials, have been developed [255]. Of such materials, graphene has been recognized as an efficient heat spreading material owing to a high thermal conductivity of 2000-4000 W/mK for suspended single-layer graphene in the temperature range of 300-350 K [4], [257], [258], and 600 W/mK near room temperature for graphene on a SiO_2 substrate [259]. Single-layer and/or few-layer graphene have been applied to enhance the thermal management of Cu interconnects [260], Cu nanowires [261], and Cu films [262]. For example, the thermal conductivity of few-layer graphene coated Cu nanowires is improved by about 50% with decreased temperature rise due to Joule heating, and eventually leads to increased current breakdown [261]. Similarly, single-layer and few-layer graphene films deposited over both sides of a 9 μm thick Cu foil enhance the thermal conductivity of the foil by about 20% near room temperature [262].

However, the thermal conductance of thin graphene films (i.e., single-layer and few-layer) is restricted by the infinitesimal thickness of the film compared to the device or the substrate [255]. For instance, the improvement of a graphene-Cu-graphene structure was attributed to Cu grain growth during annealing assisted by the presence of graphene films [262]. Therefore, multilayer graphene and/or thin graphite films on Cu substrate have shown higher thermal conductivity improvement with enhanced current breakdown [260]. For instance, the current density breakdown and the temperature breakdown are significantly enhanced for graphite-coated Cu interconnects, and the current density breakdown increases with increased graphite thickness in the Cu interconnect [263]. Similarly, current density breakdown for graphite-coated Cu interconnect is enhanced by 5.2% through minimizing the heat dissipation and electromigration [264].

A direct method to grow graphite on Cu substrate is required to avoid the transfer process and minimize the structural defects that could degrade graphite quality [264]. The growth of thin graphite on a Cu substrate is challenging using conventional thermal CVD processes due to the self-limiting surface-activated deposition process [13]. Also, graphite deposited on a Ni substrate,

which has high carbon solubility, is not uniform due to anisotropic carbon segregation and precipitation during cooling [14], [201]. Alternatively, a thin graphite film of thickness up to 45 nm was deposited on Cu foil using a plasma CVD process [263]. Also, a laser-assisted CVD process was reported for 20 nm graphite deposition on Cu interconnect [264]. Since previous studies reported batch-based CVD processes, our experiments extend the existing scope of graphite deposition methods to describe a scalable custom-built roll-to-roll plasma CVD system for graphite deposition on Cu foil for thermal management in electronic devices such as Cu interconnects [264] and GaN transistors [265].

A thin graphite film is deposited on both sides of Cu foil in a roll-to-roll CVD system operated by an 80 kHz capacitively coupled rf plasma generated between two parallel rectangular graphite electrodes. The plasma is operated at 15 mbar with a 1250 W set power using 33% H_2, 30% CH_4, 10% N_2, 8% O_2, 19% Ar gas mixture which has been found critical in the successful graphite deposition. The given plasma condition was discovered during the statistical design of experiments in Chapter 3 denoted as Case 2 in Figs. 3.16 and 3.17. The plasma emission is monitored by OES to determine qualitative species concentration.

Here, a full characterization of the deposited graphite film is carried out including Raman spectroscopy, which is a non-intrusive technique to estimate the quality of the deposited film. A laser excitation wavelength of 532 nm with a 100x objective lens was used to measure the Raman spectrum of the film. Also, the graphite film was analyzed using a scanning electron microscopy (SEM) (Hitachi Corp., s-4800) by measuring secondary electrons to check the film uniformity. Furthermore, a Titan Environmental Transmission Electron Microscope (TEM) was used to structurally analyze the graphite film after sample preparation using focused ion beam (FIB) technique. Finally, the film composition was studied by X-ray photoelectron spectroscopy (XPS) with a Kratos Ultra DLD spectrometer and Al Kα radiation ($h\nu$ = 1486.58 eV).

8.1 Results and Discussion

Figure 8.1(a) presents the uniformity of the thin graphite film from the SEM across a wide region of the Cu foil. Due to the considerable thickness of the graphite film, the Cu grains could not be observed in this sample. The thickness of the thin graphite film is about 26 nm as determined from the TEM image of Fig. 8.1(b) which shows the bottom Cu foil and the top platinum (Pt) layer

which is deposited to protect the thin graphite film during sample preparation in the FIB technique. The interlayer distance is estimated to be approximately 0.45 nm which is higher than the common distance of 0.34 for graphitic layers, and thus suggesting the deposition of a turbostatic graphite film with reduced interactions between the graphene layers. The layers are aligned perpendicular to the Cu foil with ordered structure indicating the layer-by-layer deposition. A 20-40 nm thick amorphous-like layer appeared between the thin graphite and Cu substrate in few regions due to the Cu foil roughness (Fig. 8.1(c)). However, the thickness and structure of the graphite film remains uniform throughout the region.

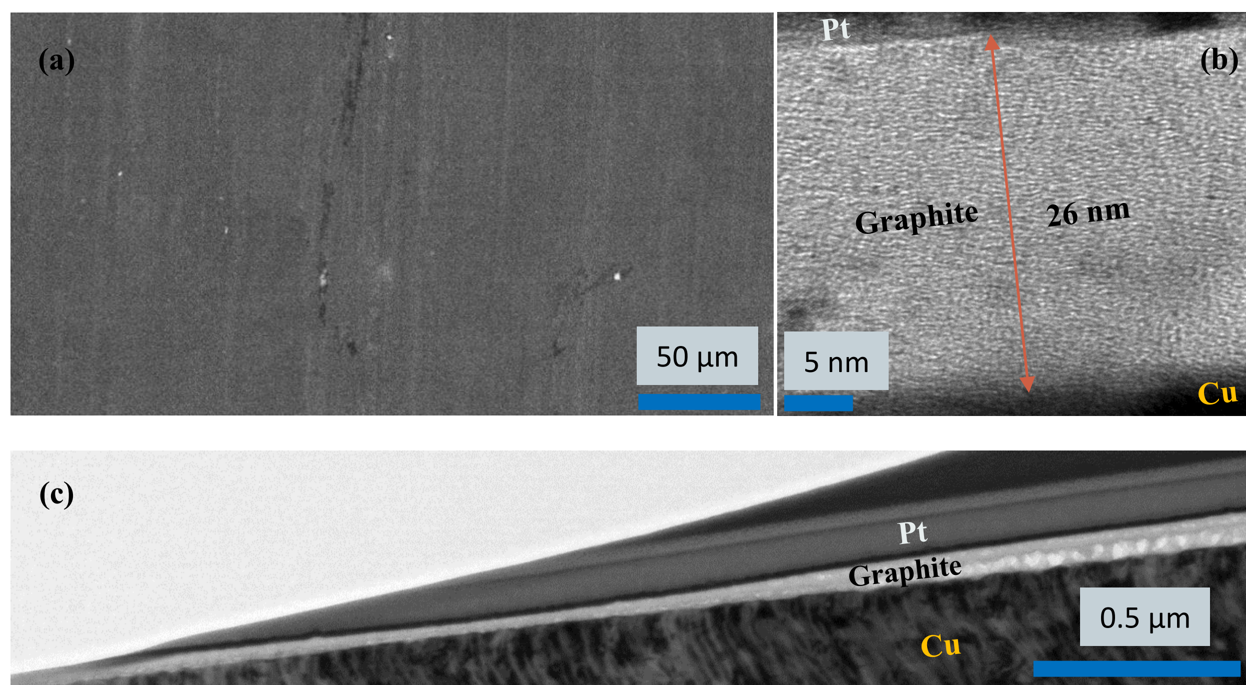

Figure 8.1: (a) SEM image of the uniform graphite film on Cu foil. (b) TEM image of the thin graphite film between Cu foil and Pt protective layer. The thickness of the graphite film is about 26 nm. (c) The graphite film remains uniform except for some regions (toward the right of the sample) where large voids are observed between the graphite film and Cu foil.

Figure 8.2(a) presents the Raman spectra of the carbon films synthesized at different plasma compositions. The main Raman peaks of graphene and graphite films are G at 1580 cm^{-1}, and 2D at 2700 cm^{-1}, whereas the D peak at 1350 cm^{-1} and D′ peak at 1620 cm^{-1} appear due to defects. The peaks' intensity and position vary considerably among the samples from the three plasma compositions due the sensitivity of Raman spectra to carbon film quality and electronic structure [145], [192]. The I_D/I_G intensity ratio, which measures the defects density, has values of 1.83, 1.16 and 0.87 at conditions 35%Ar/35%H_2/30%CH_4 (Ar-H_2-CH_4), 30%Ar/30%H_2/30%CH_4/10%N_2

($Ar-H_2-CH_4-N_2$), and 19%Ar/33%H_2/30%CH_4/10%N_2/8%O_2 ($Ar-H_2-CH_4-N_2-O_2$), respectively. The corresponding in-plane crystalline lengths (L_a) [147], [149] are 10.51, 16.57, and 22.10 nm indicating improved graphene quality with the addition of N_2 and O_2 gases. On the other hand, the I_{2D}/I_G intensity ratio decreases from 0.26 ($Ar-H_2-CH_4$) to 0.07 ($Ar-H_2-CH_4-N_2$) and 0.05 ($Ar-H_2-CH_4-N_2-O_2$) reflecting the influence of N_2 [266] and O_2 [162] containing plasmas in modifying graphene electronic structure. Furthermore, the G-peak and D-peak positions shifts from 1596 cm^{-1} and 1353 cm^{-1} for the $Ar-H_2-CH_4$ plasma sample to 1605 cm^{-1} and 1360 cm^{-1} with N_2 gas addition. The shift of both peaks with the addition of N_2 is due to the tension in the graphene lattice initiated from the possible C-N bonds [267]. However, the peak positions shift back to 1598 cm^{-1} and 1347 cm^{-1} with the addition of O_2 gases to the $Ar-H_2-CH_4-N_2$ plasma (Fig, 8.2(a)).

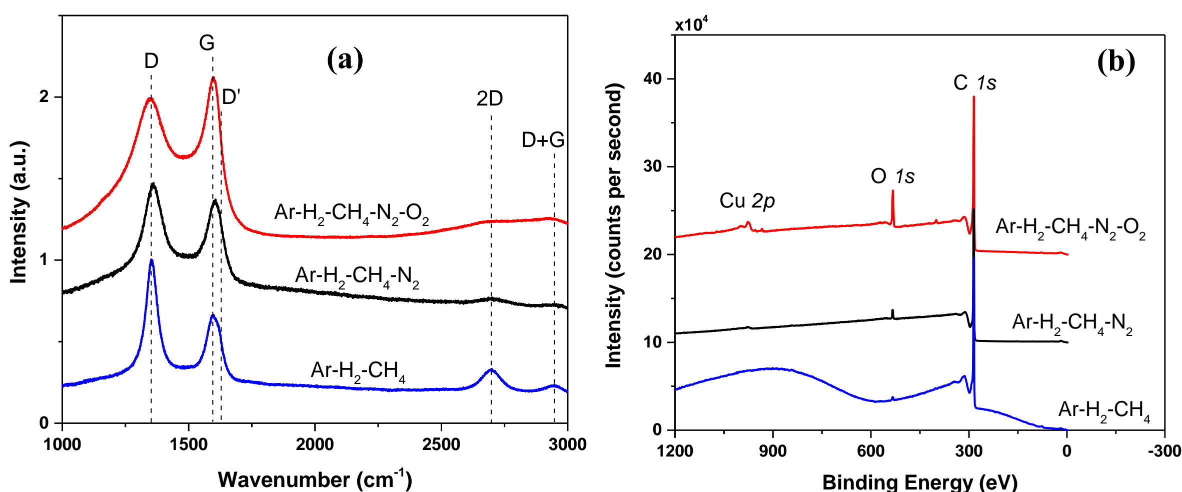

Figure 8.2: (a) Raman and (b) XPS spectra of the deposited carbon film at different plasma conditions of $Ar-H_2-CH_4$, $Ar-H_2-CH_4-N_2$, and $Ar-H_2-CH_4-N_2-O_2$. The plasma set power and gas pressure remain constant at 1250 W and 15 mbar, respectively.

The XPS measurements agree with the Raman findings and suggest that the carbon film from $Ar-H_2-CH_4$ plasma has a low-crystalline structure, as suggested by the hump in the 600-1200 eV region observed in Fig. 8.2(b). However, the additions of N_2 and O_2 gases to the plasma enhance the film crystallinity due to the increased plasma reactivity and the chemical growth kinetics. The XPS spectra show small oxygen contents near 530 eV for the samples from $Ar-H_2-CH_4$, $Ar-H_2-CH_4-N_2$ plasma conditions due to ambient exposure, whereas the oxygen peak increases substantially for the $Ar-H_2-CH_4-N_2-O_2$ sample. Furthermore, the C *1s* peak near 285 eV indicates the binding energy for graphitic content, with small contribution from the Cu surface due to the thick graphite sample of about 26 nm.

OES was used to measure plasma emission during carbon deposition for the three gas compositions. The plasma emission increases significantly with the addition of N_2 gas to the Ar-H_2-CH_4 plasma as presented in Fig. 8.3(a). N_2 has higher vibrational levels that lead to increased power dissipation in the plasma with enhanced energy transfer between plasma species. The emission spectrum remains almost similar with the addition of O_2 gas to the Ar-H_2-CH_4-N_2 plasma.

The emission intensity of several species normalized to the emission intensity of Ar line at 703 nm are presented in Fig. 8.3(b) to provide qualitative comparison between the three spectra. The positions of these species are listed in Table A.1 in Appendix A. The emission intensities of H_2 varies slightly with the addition of N_2 and O_2 gases to Ar-H_2-CH_4 plasma (Fig. 8.3(b)). However, the emission intensities of C_2, H_β, Ar^+ and CH decrease with the addition of N_2 to Ar-H_2-CH_4 plasma, whereas their emission intensities increase in the Ar-H_2-CH_4-N_2-O_2 plasma. Also, strong emission is observed for N_2, CN and N_2^+ with the addition of N_2 and O_2 to Ar-H_2-CH_4 plasma. The enhancement of C_2, H_β, Ar^+ and CH emission intensities could lead to the increase of the graphite film deposition rate. Similarly, the addition of oxygen enhances the deposition rate by minimizing graphene nucleation density [93], [160]. Finally, the spectrum of Ar-H_2-CH_4-N_2-O_2 plasma shows strong emission of C_2 band near 516-519 nm which could indicate the enhancement of the production of carbon species in the plasma that enhances the deposition rate (inset of Fig. 8.3(b)).

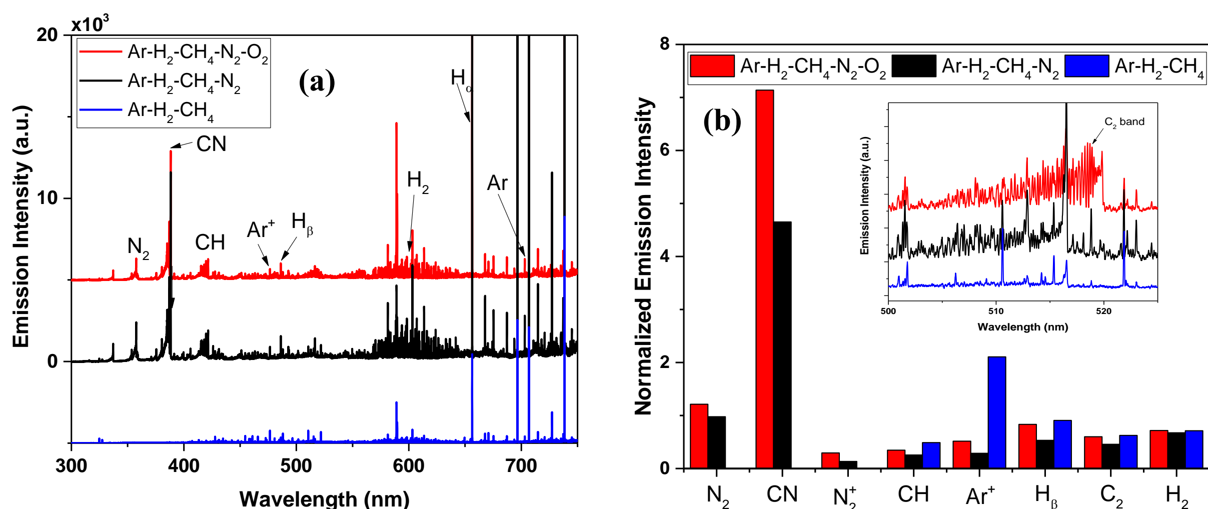

Figure 8.3: (a) Optical emission spectra of Ar-H_2-CH_4, Ar-H_2-CH_4-N_2 and Ar-H_2-CH_4-N_2-O_2 plasmas. (b) Comparison between the species emission intensities as a function of plasma compositions at 1250 W and 15 mbar. The emission intensity is normalized by Ar emission line at 703 nm. The inset shows a zoom-in to the spectra near 516 nm which shows strong C_2 band emission from Ar-H_2-CH_4-N_2-O_2 plasma.

8.2 Conclusion

Large scale deposition of graphite on Cu foil was demonstrated using a roll-to-roll plasma CVD system. Plasma condition is determined to be critical in the successful growth of about 26 nm graphite on Cu foil. The deposition process takes advantages of the fast growth of graphene layers accelerated by active carbon and other plasma species toward the substrate. The addition of N_2 and O_2 are crucial to increase plasma reactivity and promote chemical kinetics to favor graphite film synthesis, as revealed via OES. In addition, XPS and Raman spectra suggest better quality and crystalline structures with the addition of N_2 and O_2 that are expected to etch amorphous carbon to yield an increased quantity of organized sp^2 carbons.

9. CONCLUSIONS

A roll-to-roll plasma CVD process has been statistically, thermally, spectroscopically, and electrically assessed to scale up graphene production. Our work is meant to pave the way for using plasma sources for graphene and other nanomaterial mass production. A common challenge in current research in nanoscale materials production is the process repeatability, where carbons, in the case of graphene, need to be arranged perfectly in a honeycomb structure to form high-quality graphene with exceptional properties. In the present study, statistical design of experiment was applied to quantify the uncertainty of graphene quality with the goal of quality optimization using a reduced number of experiments. The developed algorithms were used to discover surrogate models representing graphene quality from both sides of the Cu foil, as a function of the process parameters: plasma set power, gas pressure, and gas constituents of H_2, CH_4, N_2, O_2, and Ar. Sensitivity analysis of the models reveals that gas pressure, nitrogen and oxygen gases, and plasma power are the main factors influencing graphene quality. The influence of the graphene quality factor is due to significant roles in specifying plasma types: hybrid or gamma, controlling the ion bombardment, and graphene deposition rate.

Even though capacitively coupled low-frequency plasmas have high ion energy that severely bombards the substrate, the implemented statistical technique found optimal operation conditions with a moderate quality of graphene. If the discussed methods were applied to a high-frequency microwave plasma, graphene quality would be significantly improved. Such a hypothesis, which was preliminarily tested in a microwave plasma CVD system, suggests the importance of designing and developing plasma sources with lower ion energy by using high-frequency plasma or generating plasma in an electrodeless configuration. The objective of process optimization is to minimize the energy absorbed by ions from electrons and the electric field to reduce ion bombardment on the substrate and eventually improve overall graphene quality.

In situ optical emission spectroscopy (OES) was applied to correlate species emission to graphene quality with the aim of developing a diagnostic tool to monitor and control graphene deposition. Using a statistical mapping analysis, the OES results found that CH emission is correlated to high-quality graphene, whereas O and H atoms, the Ar^+ ion, and C_2 and CN radicals emission are correlated to low quality. Emission intensities ratios of CH/C_2, CH/O, and H_2/H can

be used to on-line monitor graphene production in the roll-to-roll process. Such *in situ* sensors can significantly help in providing quality control inspection without the need to interrupt production and perform detailed material characterizations. Also, the OES results in formulating a conceptual graphene growth mechanism that starts by decomposing CH_4 to CH, which is more thermodynamically stable and kinetically favorable on a Cu substrate than other CH_4 decomposition species. Upon the successful recombination of CH on a Cu surface to form graphene, energetic Ar^+ ions, O atoms, and H atoms bombard the surface and sputter carbon atoms from the formed C-C bonds. Therefore, an optimum condition for graphene growth on Cu foil was determined with a low concentration of O_2 and N_2 gases at moderate pressures of 9.2 mbar and moderate plasma set power values of 750 W.

The optimized condition described above is reached when Cu foil is rolled with a web speed of around 45 mm/min. However, as the web speed increases, graphene quality decreases with a loss in deposition uniformity, which is in agreement with previous roll-to-roll thermal CVD processes. Thus, due to the significant influence Cu foil temperature on the growth process, a thermal characterization of the Cu substrate was made to improve high-quality graphene throughput. A detailed heat transfer analysis was made to find the Cu foil temperature distribution during the roll-to-roll process. The modeled temperature distribution was validated with a near-IR temperature sensor that measured the Cu foil temperature in the plasma region at various plasma set powers and web speeds. To increase graphene crystallization quality, an optimum condition was defined by the heat transfer model. The optimum condition was reached by raising the plasma power, lowering the web speed and increasing the plasma region length. Our heat transfer analysis demonstrates that the production rate of graphene on Cu foil is limited by sufficient heating for high-quality graphene growth. Therefore, high throughput graphene deposition on Cu foil is amenable, provided that (1) plasma length is enlarged to increase the residence time and the Cu foil temperature and (2) plasma set power is raised to provide adequate substrate heating and sufficient methane ionization to allow active intermediate carbon species to accelerate the growth process.

The web speed limitation imposed on Cu foil graphene deposition is primarily due to the growth mechanism driven by temperature-dependent catalytic Cu surface reactions in response to low carbon solubility in Cu. Thus, graphene production rates can be improved using a substrate with high-carbon solubility, such as Ni foil which also has a superior hydrocarbon decomposition

reactivity with a greater lattice match with graphene. So, the roll-to-roll graphene deposition on Ni was successfully attempted at different plasma powers and web speeds. Graphene uniformity and thickness depend primarily on web speed, whereas the influence of plasma power is negligible. To interpret results, the Ni foil temperature distribution was determined at various conditions and validated by temperature measurements from the *in situ* near-IR sensor. Because of low thermal diffusivity, Ni temperature depends significantly on web speed leading to a decreased temperature in the pre-plasma and plasma regions, whereas the Ni foil temperature increases in the post-plasma region. Thus, the diffusion length scale of carbon atoms in Ni during the growth process decreases with increased web speed and leads to a reduced amount of carbons precipitated in Ni foil. However, after growth, the Ni foil cooling rate increases with increased web speed. Since graphene growth is driven by carbon segregation from Ni after the growth process, higher web speed is desirable, provided that sufficient carbon atoms have diffused in Ni. Therefore, graphene deposition on Ni foil has a greater potential for high throughput than Cu foil once controlled-temperature pre- and post-plasma regions are developed for better adjustment of the heating and cooling rates of Ni foil.

The main advantages of using plasma sources for large-scale graphene are the supply of active carbon intermediate species from electron excitation reactions and the self-heating of the substrate without the need of a supplemental heating source. Such low-pressure, low-ionization plasmas exist in a non-equilibrium status, where the electron temperature is higher than the translational gas temperature. Hence, determining the gas temperature of given plasmas is crucial because of the significant role it plays in graphene growth reaction rates and uniformity, as discussed above. Therefore, N_2^+(B-X), CN(B-X), and $H_2(d^3\Pi_u \rightarrow a^3\Sigma_g^+)$ rotational temperatures are measured by OES to determine accurate translational gas temperatures in the plasma at conditions similar to graphene growth. We assess the effects of plasma set power and gas pressure as well as the addition of N_2, O_2 and CH_4 gases on gas temperature and power dissipation in H_2 plasma. Plasma set power is the main factor that determines the actual power dissipated in the plasma. The ratio of the dissipated power to the set power increases from 26% to 47% as the set input power increases from 500 W to 1100 W at 9 mbar. For a given set power, the dissipated power initially increases with rising pressure, reaches a maximum around 5.67 mbar, and then decreases at higher pressures. In addition, for a given set power and a gas pressure, the dissipated power increases with the addition of N_2, O_2, and CH_4 gases, which play a critical role in graphene

synthesis. Results show that rotational temperatures of N_2^+, CN, and H_2 increase as the dissipated power increases and as the plasma process parameters are varied with different values, due to the non-equilibrium nature of the plasma. Consequently, the rotational temperature of N_2^+, and H_2 to some extent, are most accurate in representing the translational gas temperature.

To further understand plasma properties and their effects on graphene growth, Ar plasma was experimentally analyzed at different plasma set powers and gas pressures. At pressures less than 10 mbar (i.e., 5.5 and 9.5 mbar), the plasma exists in a hybrid mode with contributions from both alpha and gamma ionization processes. However, at a higher pressure of 13.8 mbar, the plasma exists in the hybrid mode initially and then transits to gamma mode as the plasma set power increases (above 750 W set power). The observed plasma mode transition is due to enhanced secondary electron emission originating from ion bombardment of the electrodes. Results explain why gas pressure is the most significant process parameter for high-quality graphene growth in the hybrid mode, as explored in Chapter 3.

The voltage square waveform plays a significant role in sustaining the hybrid mode by enhancing the displacement current. Results show the possibility of sustaining the hybrid mode at low plasma frequency using a tailored waveform. The hybrid mode has better plasma uniformity and lower ion bombardment, which results in better graphene quality than the gamma mode. Results demonstrate the possibility of controlling the plasma properties by engineering the supplied voltage waveform, which could open a wide range of applications demanding a uniform alpha discharge.

The comprehensive techniques applied to characterize the roll-to-roll plasma CVD process in this work provide a framework for efficiently manufacturing graphene by revealing critical physical and chemical processes in the plasma system. For example, the addition of N_2 and O_2 was found to be important to successfully deposit a 26 nm thick graphite film on Cu foil. Thus, plasma R2R process is a feasible technique to mass produce graphene and other nanostructures. However, a detailed plasma design and engineering including the plasma source, plasma frequency, and operating conditions is mandatory to mass produce high-quality graphene. The interactions between the plasma and the substrate play significant roles in defining the growth rate and the materials quality. Thus, developing physical models supported with statistical models significantly improve the understanding and control of deposition process to enable large-scale production of graphene.

Also, the temperature of the pre- and post-plasma regions should be separately controlled to increase the R2R system flexibility and capability for high throughput. Both Ni foil and Cu foil remain the most attractive candidates for high-throughput deposition of graphene once the plasma deposition region is enlarged to allow a uniform high-temperature environment with longer residence time. The deposited graphene can be transferred from Ni foil and Cu foil to any arbitrary substrates by implementing existing roll-to-roll transfer process methods. Future work can focus on developing a R2R scheme for low-temperature deposition to allow graphene direct integration into devices and substrates with low melting temperatures. Finally, attention should be taken to reduce the issues of graphene microcracks originating from tension in the R2R process.

REFERENCES

[1] K. S. Novoselov *et al.*, “Two-dimensional gas of massless Dirac fermions in graphene,” *Nature*, vol. 438, no. 7065, pp. 197–200, Nov. 2005.

[2] K. S. Novoselov *et al.*, “Two-dimensional atomic crystals,” *Proc. Natl. Acad. Sci. U. S. A.*, vol. 102, no. 30, pp. 10451–3, Jul. 2005.

[3] A. S. Mayorov *et al.*, “Micrometer-scale ballistic transport in encapsulated graphene at room temperature,” *Nano Lett.*, vol. 11, no. 6, pp. 2396–2399, Jun. 2011.

[4] A. A. Balandin, “Thermal properties of graphene and nanostructured carbon materials,” *Nature Materials*, vol. 10, no. 8. pp. 569–581, 2011.

[5] C. Lee, X. Wei, J. W. Kysar, and J. Hone, “Measurement of the elastic properties and intrinsic strength of monolayer graphene,” *Science*, vol. 321, no. 5887, pp. 385–8, Jul. 2008.

[6] J. S. Bunch *et al.*, “Impermeable atomic membranes from graphene sheets,” *Nano Lett.*, vol. 8, no. 8, pp. 2458–2462, Aug. 2008.

[7] S. Bae *et al.*, “Roll-to-roll production of 30-inch graphene films for transparent electrodes,” *Nat. Nanotechnol.*, vol. 5, no. 8, pp. 574–578, Aug. 2010.

[8] F. Xia, T. Mueller, Y. M. Lin, A. Valdes-Garcia, and P. Avouris, “Ultrafast graphene photodetector,” *Nat. Nanotechnol.*, vol. 4, no. 12, pp. 839–843, Dec. 2009.

[9] N. T. Kirkland, T. Schiller, N. Medhekar, and N. Birbilis, “Exploring graphene as a corrosion protection barrier,” *Corrosion Science*, vol. 56. pp. 1–4, Mar-2012.

[10] G. Xiong, C. Meng, R. G. Reifenberger, P. P. Irazoqui, and T. S. Fisher, “Graphitic petal electrodes for all-solid-state flexible supercapacitors,” *Adv. Energy Mater.*, vol. 4, no. 3, p. 1300515, Feb. 2014.

[11] J. C. Claussen *et al.*, “Nanostructuring platinum nanoparticles on multilayered graphene petal nanosheets for electrochemical biosensing,” *Adv. Funct. Mater.*, vol. 22, no. 16, pp. 3399–3405, Aug. 2012.

[12] K. S. Novoselov *et al.*, “A roadmap for graphene,” *Nature*, vol. 490, no. 7419, pp. 192–200, Oct. 2012.

[13] X. Li *et al.*, “Large-area synthesis of high-quality and uniform graphene films on copper foils,” *Science*, vol. 324, no. 5932, pp. 1312–1314, Jun. 2009.

[14] K. S. Kim *et al.*, “Large-scale pattern growth of graphene films for stretchable transparent electrodes,” *Nature*, vol. 457, no. 7230, pp. 706–710, Feb. 2009.

[15] T. Hesjedal, “Continuous roll-to-roll growth of graphene films by chemical vapor deposition,” *Appl. Phys. Lett.*, vol. 98, no. 13, p. 133106, Mar. 2011.

[16] E. S. Polsen, D. Q. McNerny, B. Viswanath, S. W. Pattinson, and A. John Hart, “High-speed roll-to-roll manufacturing of graphene using a concentric tube CVD reactor,” *Sci. Rep.*, vol. 5, no. 1, p. 10257, 2015.

[17] G. Zhong *et al.*, “Growth of continuous graphene by open roll-to-roll chemical vapor deposition,” *Appl. Phys. Lett.*, vol. 109, no. 19, p. 193103, Nov. 2016.

[18] I. Levchenko, K. Ostrikov, J. Zheng, X. Li, M. Keidar, and K. B. K. Teo, “Scalable graphene production: perspectives and challenges of plasma applications,” *Nanoscale*, vol. 8, no. 20, pp. 10511–10527, 2016.

[19] R. S. Weatherup, B. Dlubak, and S. Hofmann, “Kinetic control of catalytic CVD for high-quality graphene at low temperatures,” *ACS Nano*, vol. 6, no. 11, pp. 9996–10003, Nov. 2012.

[20] A. Kumar, A. A. Voevodin, D. Zemlyanov, D. N. Zakharov, and T. S. Fisher, “Rapid synthesis of few-layer graphene over Cu foil,” *Carbon N. Y.*, vol. 50, no. 4, pp. 1546–1553, Apr. 2012.

[21] P. J. Bruggeman, N. Sadeghi, D. C. Schram, and V. Linss, “Gas temperature determination from rotational lines in non-equilibrium plasmas: a review,” *Plasma Sources Sci. Technol.*, vol. 23, no. 2, p. 23001, Apr. 2014.

[22] M. A. Alrefae, N. R. Glavin, A. A. Voevodin, and T. S. Fisher, “Plasma Chemical and Physical Vapour Deposition Methods and Diagnostics for 2D Materials,” in *2D Inorganic Materials beyond Graphene*, R. CNR and W. UV, Eds. 2017, pp. 275–315.

[23] M. A. Alrefae, A. Kumar, P. Pandita, A. Candadai, I. Bilionis, and T. S. Fisher, “Process optimization of graphene growth in a roll-to-roll plasma CVD system,” *AIP Adv.*, vol. 7, no. 11, p. 115102, Nov. 2017.

[24] A. K. Geim and K. S. Novoselov, “The rise of graphene,” *Nat. Mater.*, vol. 6, no. 3, pp. 183–191, Mar. 2007.

[25] P. R. Wallace, “The band theory of graphite,” *Phys. Rev.*, vol. 71, no. 9, pp. 622–634, May 1947.

[26] K. S. Novoselov *et al.*, “Electric field effect in atomically thin carbon films.,” *Science*, vol. 306, no. 5696, pp. 666–669, Oct. 2004.

[27] J.-C. Charlier, P. C. Eklund, J. Zhu, and A. C. Ferrari, “Electron and Phonon Properties of Graphene: Their Relationship with Carbon Nanotubes,” in *Topics in Applied Physics*, 2007, pp. 673–709.

[28] A. A. Balandin, “Thermal Properties of Graphene, Carbon Nanotubes and Nanostructured Carbon Materials,” *Nat. Mater.*, vol. 10, pp. 569–581, 2011.

[29] R. R. Nair *et al.*, “Fine Structure Constant Defines Visual Transparency of Graphene,” *Science (80-.).*, vol. 320, no. 5881, pp. 1308–1308, Jun. 2008.

[30] A. K. Geim, “Graphene: Status and Prospects,” *Science (80-.).*, vol. 324, no. 5934, pp. 1530–1534, Jun. 2009.

[31] E. P. Randviir, D. A. C. Brownson, and C. E. Banks, “A decade of graphene research: production, applications and outlook,” *Mater. Today*, vol. 17, no. 9, pp. 426–432, 2014.

[32] Y. Hernandez *et al.*, “High-yield production of graphene by liquid-phase exfoliation of graphite,” *Nat. Nanotechnol.*, vol. 3, no. 9, pp. 563–568, 2008.

[33] K. R. Paton *et al.*, “Scalable production of large quantities of defect-free few-layer graphene by shear exfoliation in liquids,” *Nat. Mater.*, vol. 13, no. 6, pp. 624–630, 2014.

[34] C. Berger *et al.*, “Ultrathin epitaxial graphite: 2D electron gas properties and a route toward graphene-based nanoelectronics,” *J. Phys. Chem. B*, vol. 108, no. 52, pp. 19912–19916, 2004.

[35] A. Reina *et al.*, “Large Area, Few-Layer Graphene Films on Arbitrary Substrates by Chemical Vapor Deposition,” *Nano Lett.*, vol. 9, no. 1, pp. 30–35, Jan. 2009.

[36] Q. Yu, J. Lian, S. Siriponglert, H. Li, Y. P. Chen, and S. S. Pei, “Graphene segregated on Ni surfaces and transferred to insulators,” *Appl. Phys. Lett.*, vol. 93, no. 11, p. 113103, Sep. 2008.

[37] S. Bhaviripudi, X. Jia, M. S. Dresselhaus, and J. Kong, “Role of kinetic factors in chemical vapor deposition synthesis of uniform large area graphene using copper catalyst,” *Nano Lett.*, vol. 10, no. 10, pp. 4128–4133, Oct. 2010.

[38] X. Li, W. Cai, L. Colombo, and R. S. Ruoff, “Evolution of graphene growth on Ni and Cu by carbon isotope labeling.,” *Nano Lett.*, vol. 9, no. 12, pp. 4268–72, Dec. 2009.

[39] I. Vlassiouk *et al.*, "Role of hydrogen in chemical vapor deposition growth of large single-crystal graphene," *ACS Nano*, vol. 5, no. 7, pp. 6069–6076, Jul. 2011.

[40] L. Gan and Z. Luo, "Turning off hydrogen to realize seeded growth of subcentimeter single-crystal graphene grains on copper," *ACS Nano*, vol. 7, no. 10, pp. 9480–9488, Oct. 2013.

[41] Y. Kim *et al.*, "Low-temperature synthesis of graphene on nickel foil by microwave plasma chemical vapor deposition," *Appl. Phys. Lett.*, vol. 98, no. 26, p. 263106, Jun. 2011.

[42] H. Conrads and M. Schmidt, "Plasma generation and plasma sources," *Plasma Sources Sci. Technol.*, vol. 9, no. 4, pp. 441–454, Nov. 2000.

[43] A. Bogaerts, E. Neyts, R. Gijbels, and J. van der Mullen, "Gas discharge plasmas and their applications," *Spectrochim. Acta Part B At. Spectrosc.*, vol. 57, no. 4, pp. 609–658, Apr. 2002.

[44] Z. Bo, Y. Yang, J. Chen, K. Yu, J. Yan, and K. Cen, "Plasma-enhanced chemical vapor deposition synthesis of vertically oriented graphene nanosheets," *Nanoscale*, vol. 5, no. 12, p. 5180, Jun. 2013.

[45] M. A. Lieberman and A. J. Lichtenberg, *Principles of Plasma Discharges and Materials Processing*. Hoboken, NJ, USA: John Wiley & Sons, Inc., 2005.

[46] Y. S. Kim *et al.*, "Methane as an effective hydrogen source for single-layer graphene synthesis on Cu foil by plasma enhanced chemical vapor deposition," *Nanoscale*, vol. 5, no. 3, p. 1221, Feb. 2013.

[47] D. Wei, Y. Lu, C. Han, T. Niu, W. Chen, and A. T. S. Wee, "Critical crystal growth of graphene on dielectric substrates at low temperature for electronic devices," *Angew. Chemie - Int. Ed.*, vol. 52, no. 52, pp. 14121–14126, Dec. 2013.

[48] N. Woehrl, O. Ochedowski, S. Gottlieb, K. Shibasaki, and S. Schulz, "Plasma-enhanced chemical vapor deposition of graphene on copper substrates," *AIP Adv.*, vol. 4, no. 4, p. 47128, Apr. 2014.

[49] D. A. Boyd *et al.*, "Single-step deposition of high-mobility graphene at reduced temperatures," *Nat. Commun.*, vol. 6, no. 1, p. 6620, Jan. 2015.

[50] C. S. Lee *et al.*, "Dual graphene films growth process based on plasma-assisted chemical vapor deposition," in *Proc. SPIE 7761, Carbon Nanotubes, Graphene, and Associated Devices III, 77610P*, 2010, vol. 7761, p. 77610P.

[51] J. L. Qi, W. T. Zheng, X. H. Zheng, X. Wang, and H. W. Tian, "Relatively low temperature synthesis of graphene by radio frequency plasma enhanced chemical vapor deposition," *Appl. Surf. Sci.*, vol. 257, no. 15, pp. 6531–6534, May 2011.

[52] L. Van Nang and E.-T. Kim, "Controllable Synthesis of High-Quality Graphene Using Inductively-Coupled Plasma Chemical Vapor Deposition," *J. Electrochem. Soc.*, vol. 159, no. 4, p. K93, Jan. 2012.

[53] T. Terasawa and K. Saiki, "Growth of graphene on Cu by plasma enhanced chemical vapor deposition," *Carbon N. Y.*, vol. 50, no. 3, pp. 869–874, 2012.

[54] A. N. Obraztsov, E. A. Obraztsova, A. V. Tyurnina, and A. A. Zolotukhin, "Chemical vapor deposition of thin graphite films of nanometer thickness," *Carbon N. Y.*, vol. 45, no. 10, pp. 2017–2021, Sep. 2007.

[55] H. K. Jeong, J. D. C. Edward, G. H. Yong, and L. Choong Hun, "Synthesis of Few-layer Graphene on a Ni Substrate by Using DC Plasma Enhanced Chemical Vapor Deposition (PE-CVD)," *J. Korean Phys. Soc.*, vol. 58, no. 1, p. 53, Jan. 2011.

[56] C. S. Lee *et al.*, "Synthesis of conducting transparent few-layer graphene directly on glass at 450°C," *Nanotechnology*, vol. 23, no. 26, p. 265603, Jul. 2012.

[57] L. Zhang, Z. Shi, Y. Wang, R. Yang, D. Shi, and G. Zhang, "Catalyst-free growth of nanographene films on various substrates," *Nano Res.*, vol. 4, no. 3, pp. 315–321, Dec. 2010.

[58] S. Wang *et al.*, "A growth mechanism for graphene deposited on polycrystalline Co film by plasma enhanced chemical vapor deposition," *New J. Chem.*, vol. 37, no. 5, p. 1616, 2013.

[59] L. Van Nang and E.-T. Kim, "Low-temperature synthesis of graphene on Fe2O3 using inductively coupled plasma chemical vapor deposition," *Mater. Lett.*, vol. 92, pp. 437–439, Feb. 2013.

[60] K.-J. Peng *et al.*, "Hydrogen-free PECVD growth of few-layer graphene on an ultra-thin nickel film at the threshold dissolution temperature," *J. Mater. Chem. C*, vol. 1, no. 24, p. 3862, May 2013.

[61] J. Kim, M. Ishihara, Y. Koga, K. Tsugawa, M. Hasegawa, and S. Iijima, "Low-temperature synthesis of large-area graphene-based transparent conductive films using surface wave plasma chemical vapor deposition," *Appl. Phys. Lett.*, vol. 98, no. 9, p. 91502, 2011.

[62] T. Yamada, M. Ishihara, J. Kim, M. Hasegawa, and S. Iijima, “A roll-to-roll microwave plasma chemical vapor deposition process for the production of 294mm width graphene films at low temperature,” *Carbon N. Y.*, vol. 50, no. 7, pp. 2615–2619, Jun. 2012.

[63] L. Cheng *et al.*, “Low temperature synthesis of graphite on Ni films using inductively coupled plasma enhanced CVD,” *J. Mater. Chem. C*, vol. 3, no. 20, pp. 5192–5198, May 2015.

[64] S. Chugh, R. Mehta, N. Lu, F. D. Dios, M. J. Kim, and Z. Chen, “Comparison of graphene growth on arbitrary non-catalytic substrates using low-temperature PECVD,” *Carbon N. Y.*, vol. 93, pp. 393–399, Nov. 2015.

[65] S. Chen *et al.*, “Hydrogen-free synthesis of graphene–graphitic films directly on Si substrate by plasma enhanced chemical vapor deposition,” *J. Mater. Sci. Mater. Electron.*, vol. 26, no. 3, pp. 1485–1493, Dec. 2014.

[66] Y. Ando, X. Zhao, and M. Ohkohchi, “Production of petal-like graphite sheets by hydrogen arc discharge,” *Carbon N. Y.*, vol. 35, no. 1, pp. 153–158, 1997.

[67] D. Banerjee, S. Mukherjee, and K. K. Chattopadhyay, “Synthesis of amorphous carbon nanowalls by DC-PECVD on different substrates and study of its field emission properties,” *Appl. Surf. Sci.*, vol. 257, no. 8, pp. 3717–3722, Feb. 2011.

[68] K. V Mironovich *et al.*, “Tailoring of the carbon nanowall microstructure by sharp variation of plasma radical composition,” *Phys. Chem. Chem. Phys.*, vol. 16, no. 46, pp. 25621–25627, Dec. 2014.

[69] M. Hiramatsu, K. Shiji, H. Amano, and M. Hori, “Fabrication of vertically aligned carbon nanowalls using capacitively coupled plasma-enhanced chemical vapor deposition assisted by hydrogen radical injection,” *Appl. Phys. Lett.*, vol. 84, no. 23, p. 4708, 2004.

[70] J. Wang, M. Zhu, R. A. Outlaw, X. Zhao, D. M. Manos, and B. C. Holloway, “Synthesis of carbon nanosheets by inductively coupled radio-frequency plasma enhanced chemical vapor deposition,” *Carbon N. Y.*, vol. 42, no. 14, pp. 2867–2872, Jan. 2004.

[71] J. Zhao, M. Shaygan, J. Eckert, M. Meyyappan, and M. H. Rümmeli, “A Growth Mechanism for Free-Standing Vertical Graphene,” *Nano Lett.*, vol. 14, no. 6, pp. 3064–3071, Jun. 2014.

[72] K. Davami *et al.*, “Synthesis and characterization of carbon nanowalls on different substrates by radio frequency plasma enhanced chemical vapor deposition,” *Carbon N. Y.*, vol. 72, pp. 372–380, Jun. 2014.

[73] M. Cai, R. A. Outlaw, R. A. Quinlan, D. Premathilake, S. M. Butler, and J. R. Miller, “Fast Response, vertically oriented graphene nanosheet electric double layer capacitors synthesized from C2H2,” *ACS Nano*, vol. 8, no. 6, pp. 5873–82, Jun. 2014.

[74] M. V Jacob *et al.*, “Catalyst-Free Plasma Enhanced Growth of Graphene from Sustainable Sources.,” *Nano Lett.*, vol. 15, no. 9, pp. 5702–8, Sep. 2015.

[75] K. Davami, M. Shaygan, and I. Bargatin, “Fabrication of vertical graphene-based nanocomposite thin films,” *J. Mater. Res.*, vol. 30, no. 5, pp. 617–625, Feb. 2015.

[76] Y. Wu, P. Qiao, T. Chong, and Z. Shen, “Carbon nanowalls grown by microwave plasma enhanced chemical vapor deposition,” vol. 14, no. 1, pp. 64–67, Jan. 2002.

[77] A. Malesevic *et al.*, “Synthesis of few-layer graphene via microwave plasma-enhanced chemical vapour deposition,” *Nanotechnology*, vol. 19, no. 30, p. 305604, Jul. 2008.

[78] R. Vitchev *et al.*, “Initial stages of few-layer graphene growth by microwave plasma-enhanced chemical vapour deposition,” *Nanotechnology*, vol. 21, no. 9, p. 95602, Mar. 2010.

[79] T. Bhuvana *et al.*, “Contiguous petal-like carbon nanosheet outgrowths from graphite fibers by plasma CVD.,” *ACS Appl. Mater. Interfaces*, vol. 2, no. 3, pp. 644–8, Mar. 2010.

[80] R. H. Gerzeski, A. Sprague, J. Hu, and T. S. Fisher, “Growth of contiguous graphite fins from thermally conductive graphite fibers,” *Carbon N. Y.*, vol. 69, pp. 424–436, Apr. 2014.

[81] G. Xiong, K. P. S. S. Hembram, D. N. Zakharov, R. G. Reifenberger, and T. S. Fisher, “Controlled thin graphitic petal growth on oxidized silicon,” *Diam. Relat. Mater.*, vol. 27–28, pp. 1–9, Jul. 2012.

[82] K. Ostrikov, E. C. Neyts, and M. Meyyappan, “Plasma nanoscience: from nano-solids in plasmas to nano-plasmas in solids,” *Adv. Phys.*, vol. 62, no. 2, pp. 113–224, Apr. 2013.

[83] Y. A. Mankelevich, M. N. R. Ashfold, and J. Ma, “Plasma-chemical processes in microwave plasma-enhanced chemical vapor deposition reactors operating with C/H/Ar gas mixtures,” *J. Appl. Phys.*, vol. 104, no. 11, p. 113304, 2008.

[84] G. Lombardi, K. Hassouni, G.-D. Stancu, L. Mechold, J. Röpcke, and A. Gicquel, “Modeling of microwave discharges of H2 admixed with CH4 for diamond deposition,” *J. Appl. Phys.*, vol. 98, no. 5, p. 53303, 2005.

[85] I. B. Denysenko, B. S. Xu, J. D. Long, P. P. Rutkevych, N. A. Azarenkov, and K. Ostrikov, "Inductively coupled Ar/CH4/H2 plasmas for low-temperature deposition of ordered carbon nanostructures," *J. Appl. Phys.*, vol. 95, no. 5, p. 2713, 2004.

[86] D. K. Davies, L. E. Kline, and W. E. Bies, "Measurements of swarm parameters and derived electron collision cross sections in methane," *J. Appl. Phys.*, vol. 65, no. 9, p. 3311, 1989.

[87] T. Nakano, H. Toyoda, and H. Sugai, "Electron-impact dissociation of methane into CH3 and CH2 radicals II. Absolute cross sections," *Japanese J. Appl. Physics, Part 1 Regul. Pap. Short Notes Rev. Pap.*, vol. 30, no. 11 A, pp. 2912–2915, 1991.

[88] F. Paschen, "On sparking over in air, hydrogen, carbon dioxide under the potentials corresponding to various pressures," *Wied. Ann.*, vol. 37, no. 5. pp. 69–96.

[89] Z. Bo, K. Yu, G. Lu, P. Wang, S. Mao, and J. Chen, "Understanding growth of carbon nanowalls at atmospheric pressure using normal glow discharge plasma-enhanced chemical vapor deposition," *Carbon N. Y.*, vol. 49, no. 6, pp. 1849–1858, May 2011.

[90] A. Yoshimura, H. Yoshimura, S. C. Shin, K. Kobayashi, M. Tanimura, and M. Tachibana, "Atomic force microscopy and Raman spectroscopy study of the early stages of carbon nanowall growth by dc plasma-enhanced chemical vapor deposition," *Carbon N. Y.*, vol. 50, no. 8, pp. 2698–2702, Jul. 2012.

[91] R. Koch, D. Hu, and A. K. Das, "Compressive stress in polycrystalline Volmer-Weber films," *Phys. Rev. Lett.*, vol. 94, no. 14, p. 146101, Apr. 2005.

[92] X. Song *et al.*, "Direct versatile PECVD growth of graphene nanowalls on multiple substrates," *Mater. Lett.*, vol. 137, pp. 25–28, Dec. 2014.

[93] Y. Hao *et al.*, "The role of surface oxygen in the growth of large single-crystal graphene on copper," *Science (80-.).*, vol. 342, no. 6159, pp. 720–723, 2013.

[94] J. Qi, L. Zhang, J. Cao, W. Zheng, X. Wang, and J. Feng, "Synthesis of graphene on a Ni film by radio-frequency plasma-enhanced chemical vapor deposition," *Chinese Sci. Bull.*, vol. 57, no. 23, pp. 3040–3044, Apr. 2012.

[95] M. Zhu *et al.*, "A mechanism for carbon nanosheet formation," *Carbon N. Y.*, vol. 45, no. 11, pp. 2229–2234, Oct. 2007.

[96] A. D. Tuesta, A. Bhuiyan, R. P. Lucht, and T. S. Fisher, "H2 Mole Fraction Measurements in a Microwave Plasma Using Coherent Anti-Stokes Raman Scattering Spectroscopy," *J. Micro Nano-Manufacturing*, vol. 4, no. 1, p. 11005, Dec. 2015.

[97] A. D. Tuesta, A. Bhuiyan, R. P. Lucht, and T. S. Fisher, “Laser Diagnostics of Plasma in Synthesis of Graphene-Based Materials,” *J. Micro Nano-Manufacturing*, vol. 2, no. 3, Jul. 2014.

[98] H. J. Park *et al.*, “Direct synthesis of multi-layer graphene film on various substrates by microwave plasma at low temperature,” *Thin Solid Films*, vol. 587, pp. 8–13, Jul. 2015.

[99] M. C. McMaster, W. L. Hsu, M. E. Coltrin, D. S. Dandy, and C. Fox, “Dependence of the gas composition in a microwave plasma-assisted diamond chemical vapor deposition reactor on the inlet carbon source: CH4 versus C2H2,” *Diam. Relat. Mater.*, vol. 4, no. 7, pp. 1000–1008, May 1995.

[100] J. Luque, W. Juchmann, and J. B. Jeffries, “Absolute concentration measurements of CH radicals in a diamond-depositing dc-arcjet reactor,” *Appl. Opt.*, vol. 36, no. 15, p. 3261, May 1997.

[101] W. R. Harshbarger, R. A. Porter, and P. Norton, “Optical detector to monitor plasma etching,” *J. Electron. Mater.*, vol. 7, no. 3, pp. 429–440, May 1978.

[102] J. W. Coburn and M. Chen, “Optical emission spectroscopy of reactive plasmas: A method for correlating emission intensities to reactive particle density,” *J. Appl. Phys.*, vol. 51, no. 6, p. 3134, 1980.

[103] C. J. Mogab, A. C. Adams, and D. L. Flamm, “Plasma etching of Si and SiO2—The effect of oxygen additions to CF4 plasmas,” *J. Appl. Phys.*, vol. 49, no. 7, p. 3796, 1978.

[104] N. M. Laurendeau, *Statistical thermodynamics: fundamentals and applications*. Cambridge University Press, 2005.

[105] N. Britun, M. Gaillard, A. Ricard, Y. M. Kim, K. S. Kim, and J. G. Han, “Determination of the vibrational, rotational and electron temperatures in N2 and Ar–N2 rf discharge,” *J. Phys. D. Appl. Phys.*, vol. 40, no. 4, pp. 1022–1029, Feb. 2007.

[106] D. L. Crintea, U. Czarnetzki, S. Iordanova, I. Koleva, and D. Luggenhölscher, “Plasma diagnostics by optical emission spectroscopy on argon and comparison with Thomson scattering,” *J. Phys. D. Appl. Phys.*, vol. 42, no. 4, p. 45208, Feb. 2009.

[107] A. Gicquel, M. Chenevier, K. Hassouni, A. Tserepi, and M. Dubus, “Validation of actinometry for estimating relative hydrogen atom densities and electron energy evolution in plasma assisted diamond deposition reactors,” *J. Appl. Phys.*, vol. 83, no. 12, pp. 7504–7521, 1998.

[108] C. O. Laux, T. G. Spence, C. H. Kruger, and R. N. Zare, "Optical diagnostics of atmospheric pressure air plasmas," *Plasma Sources Sci. Technol.*, vol. 12, no. 2, pp. 125–138, May 2003.

[109] R. K. Garg, T. N. Anderson, R. P. Lucht, T. S. Fisher, and J. P. Gore, "Gas temperature measurements in a microwave plasma by optical emission spectroscopy under single-wall carbon nanotube growth conditions," *J. Phys. D. Appl. Phys.*, vol. 41, no. 9, p. 95206, May 2008.

[110] T.-L. Zhao *et al.*, "Determination of vibrational and rotational temperatures in a gliding arc discharge by using overlapped molecular emission spectra," *J. Phys. D. Appl. Phys.*, vol. 46, no. 34, p. 345201, Aug. 2013.

[111] Z. Qing, D. K. Otorbaev, G. J. H. Brussaard, M. C. M. van de Sanden, and D. C. Schram, "Diagnostics of the magnetized low-pressure hydrogen plasma jet: Molecular regime," *J. Appl. Phys.*, vol. 80, no. 3, p. 1312, 1996.

[112] B. A. Cruden, M. V. V. S. Rao, S. P. Sharma, and M. Meyyappan, "Neutral gas temperature estimates in an inductively coupled CF4 plasma by fitting diatomic emission spectra," *J. Appl. Phys.*, vol. 91, no. 11, p. 8955, 2002.

[113] H. N. Chu *et al.*, "Measurements of the gas kinetic temperature in a CH4-H2 discharge during the growth of diamond," *Phys. Rev. A*, vol. 44, no. 6, pp. 3796–3803, Sep. 1991.

[114] J. Luque, M. Kraus, A. Wokaun, K. Haffner, U. Kogelschatz, and B. Eliasson, "Gas temperature measurement in CH4/CO2 dielectric-barrier discharges by optical emission spectroscopy," *J. Appl. Phys.*, vol. 93, no. 8, p. 4432, 2003.

[115] S. W. Reeve, "Plasma diagnostics of a direct-current arcjet diamond reactor. II. Optical emission spectroscopy," *J. Vac. Sci. Technol. A Vacuum, Surfaces, Film.*, vol. 13, no. 2, p. 359, Mar. 1995.

[116] S. Y. Moon and W. Choe, "A comparative study of rotational temperatures using diatomic OH, O2 and N2 + molecular spectra emitted from atmospheric plasmas," in *Spectrochimica Acta - Part B Atomic Spectroscopy*, 2003, vol. 58, no. 2, pp. 249–257.

[117] J. Ma, M. N. R. Ashfold, and Y. A. Mankelevich, "Validating optical emission spectroscopy as a diagnostic of microwave activated CH4 /Ar/ H2 plasmas used for diamond chemical vapor deposition," *J. Appl. Phys.*, vol. 105, no. 4, p. 43302, 2009.

[118] B. Marcus, M. Mermoux, F. Vinet, A. Campargue, and M. Chenevier, “Relationship between emission spectroscopy and structural properties of diamond films synthesized by plasma-assisted chemical vapor deposition,” *Surf. Coatings Technol.*, vol. 47, no. 1–3, pp. 608–617, Aug. 1991.

[119] T. Lang, J. Stiegler, Y. von Kaenel, and E. Blank, “Optical emission diagnostics and film growth during microwave-plasma-assisted diamond CVD,” *Diam. Relat. Mater.*, vol. 5, no. 10, pp. 1171–1184, Aug. 1996.

[120] M. A. Elliott, P. W. May, J. Petherbridge, S. M. Leeds, M. N. R. Ashfold, and W. N. Wang, “Optical emission spectroscopic studies of microwave enhanced diamond CVD using CH4/CO2 plasmas,” *Diam. Relat. Mater.*, vol. 9, no. 3–6, pp. 311–316, Apr. 2000.

[121] T. Vandevelde, M. Nesladek, C. Quaeyhaegens, and L. Stals, “Optical emission spectroscopy of the plasma during CVD diamond growth with nitrogen addition,” *Thin Solid Films*, vol. 290–291, pp. 143–147, Dec. 1996.

[122] J. C. Richley, M. W. Kelly, M. N. R. Ashfold, and Y. A. Mankelevich, “Optical emission from microwave activated C/H/O gas mixtures for diamond chemical vapor deposition,” *J. Phys. Chem. A*, vol. 116, no. 38, pp. 9447–9458, Sep. 2012.

[123] A. N. Obraztsov, A. A. Zolotukhin, A. O. Ustinov, A. P. Volkov, Y. Svirko, and K. Jefimovs, “DC discharge plasma studies for nanostructured carbon CVD,” *Diam. Relat. Mater.*, vol. 12, no. 3–7, pp. 917–920, Mar. 2003.

[124] K. W. Hemawan and R. J. Hemley, “Optical emission diagnostics of plasmas in chemical vapor deposition of single-crystal diamond,” *J. Vac. Sci. Technol. A Vacuum, Surfaces, Film.*, vol. 33, no. 6, p. 61302, Nov. 2015.

[125] E. Sandoz-Rosado *et al.*, “Vertical graphene by plasma-enhanced chemical vapor deposition: Correlation of plasma conditions and growth characteristics,” *J. Mater. Res.*, vol. 29, no. 3, pp. 417–425, Oct. 2013.

[126] Y. Ma, H. Jang, S. J. Kim, C. Pang, and H. Chae, “Copper-Assisted Direct Growth of Vertical Graphene Nanosheets on Glass Substrates by Low-Temperature Plasma-Enhanced Chemical Vapour Deposition Process.,” *Nanoscale Res. Lett.*, vol. 10, no. 1, p. 1019, Dec. 2015.

[127] S. Vizireanu, S. D. Stoica, C. Luculescu, L. C. Nistor, B. Mitu, and G. Dinescu, "Plasma techniques for nanostructured carbon materials synthesis. A case study: carbon nanowall growth by low pressure expanding RF plasma," *Plasma Sources Sci. Technol.*, vol. 19, no. 3, p. 34016, Jun. 2010.

[128] S. Mori, T. Ueno, and M. Suzuki, "Synthesis of carbon nanowalls by plasma-enhanced chemical vapor deposition in a CO/H2 microwave discharge system," *Diam. Relat. Mater.*, vol. 20, no. 8, pp. 1129–1132, Aug. 2011.

[129] M. Zhu, J. Wang, R. A. Outlaw, K. Hou, D. M. Manos, and B. C. Holloway, "Synthesis of carbon nanosheets and carbon nanotubes by radio frequency plasma enhanced chemical vapor deposition," *Diam. Relat. Mater.*, vol. 16, no. 2, pp. 196–201, Feb. 2007.

[130] Y. Ma, D. Kim, H. Jang, S. M. Cho, and H. Chae, "Characterization of Low Temperature Graphene Synthesis in Inductively Coupled Plasma Chemical Vapor Deposition Process with Optical Emission Spectroscopy," *J. Nanosci. Nanotechnol.*, vol. 14, no. 12, pp. 9065–9072, Dec. 2014.

[131] J. D. Morse, "Nanofabrication Technologies for Roll-to-Roll Processing. In: Workshop on Nanofabrication Technologies for Roll-to-Roll Processing," pp. 1–32, 2011.

[132] F. C. Krebs, T. Tromholt, and M. Jørgensen, "Upscaling of polymer solar cell fabrication using full roll-to-roll processing," *Nanoscale*, vol. 2, no. 6, p. 873, Jun. 2010.

[133] K. Hwang *et al.*, "Toward large scale roll-to-roll production of fully printed perovskite solar cells," *Adv. Mater.*, vol. 27, no. 7, pp. 1241–1247, Feb. 2015.

[134] R. R. Søndergaard, M. Hösel, and F. C. Krebs, "Roll-to-Roll fabrication of large area functional organic materials," *Journal of Polymer Science, Part B: Polymer Physics*, vol. 51, no. 1. pp. 16–34, Jan-2013.

[135] C.-Y. Chang and M.-H. Tsai, "Development of a continuous roll-to-roll processing system for mass production of plastic optical film," *J. Micromechanics Microengineering*, vol. 25, no. 12, p. 125014, Dec. 2015.

[136] S. H. Ahn and L. J. Guo, "High-speed roll-to-roll nanoimprint lithography on flexible plastic substrates," *Adv. Mater.*, vol. 20, no. 11, pp. 2044–2049, Jun. 2008.

[137] I. Vlassiouk *et al.*, "Large scale atmospheric pressure chemical vapor deposition of graphene," *Carbon N. Y.*, vol. 54, pp. 58–67, 2013.

[138] T. Kobayashi *et al.*, “Production of a 100-m-long high-quality graphene transparent conductive film by roll-to-roll chemical vapor deposition and transfer process,” *Appl. Phys. Lett.*, vol. 102, no. 2, p. 23112, 2013.

[139] H.-A. Mehedi *et al.*, “Synthesis of graphene by cobalt-catalyzed decomposition of methane in plasma-enhanced CVD: Optimization of experimental parameters with Taguchi method,” *J. Appl. Phys.*, vol. 120, no. 6, p. 65304, 2016.

[140] S. Santangelo *et al.*, “Taguchi optimized synthesis of graphene films by copper catalyzed ethanol decomposition,” *Diam. Relat. Mater.*, vol. 41, pp. 73–78, 2014.

[141] Á. Kukovecz, D. Méhn, E. Nemes-Nagy, R. Szabó, and I. Kiricsi, “Optimization of CCVD synthesis conditions for single-wall carbon nanotubes by statistical design of experiments (DoE),” *Carbon N. Y.*, vol. 43, no. 14, pp. 2842–2849, 2005.

[142] H. Shu *et al.*, “What are the active carbon species during graphene chemical vapor deposition growth?,” *Nanoscale*, vol. 7, no. 5, pp. 1627–1634, 2015.

[143] W. Zhang, P. Wu, Z. Li, and J. Yang, “First-Principles Thermodynamics of Graphene Growth on Cu Surfaces,” *J. Phys. Chem. C*, vol. 115, no. 36, pp. 17782–17787, Sep. 2011.

[144] J. Kim, F. Kim, and J. Huang, “Seeing graphene-based sheets,” *Mater. Today*, vol. 13, no. 3, pp. 28–38, Mar. 2010.

[145] L. M. Malard, M. A. Pimenta, G. Dresselhaus, and M. S. Dresselhaus, “Raman spectroscopy in graphene,” *Physics Reports*, vol. 473, no. 5–6. pp. 51–87, Apr-2009.

[146] A. C. Ferrari *et al.*, “Raman spectrum of graphene and graphene layers,” *Phys. Rev. Lett.*, vol. 97, no. 18, p. 187401, Oct. 2006.

[147] F. Tuinstra and J. L. Koenig, “Raman Spectrum of Graphite,” *J. Chem. Phys.*, vol. 53, no. 3, pp. 1126–1130, Aug. 1970.

[148] K. Sato *et al.*, “D-band Raman intensity of graphitic materials as a function of laser energy and crystallite size,” *Chem. Phys. Lett.*, vol. 427, no. 1–3, pp. 117–121, 2006.

[149] L. G. Caṇado *et al.*, “General equation for the determination of the crystallite size La of nanographite by Raman spectroscopy,” *Appl. Phys. Lett.*, vol. 88, no. 16, p. 163106, Apr. 2006.

[150] P. Pandita, I. Bilionis, J. Panchal, B. P. Gautham, A. Joshi, and P. Zagade, “Stochastic Multi-objective Optimization on a Budget: Application to multi-pass wire drawing with quantified uncertainties,” *arXiv:1706.01665*, Jun. 2017.

[151] C. Jia *et al.*, “Direct Optical Characterization of Graphene Growth and Domains on Growth Substrates,” *Sci. Rep.*, vol. 2, pp. 1–6, Oct. 2012.

[152] A. Perret, P. Chabert, J. Jolly, and J.-P. Booth, “Ion energy uniformity in high-frequency capacitive discharges,” *Appl. Phys. Lett.*, vol. 86, no. 2, p. 21501, Jan. 2005.

[153] A. Salabas, L. Marques, J. Jolly, G. Gousset, and L. L. Alves, “Systematic characterization of low-pressure capacitively coupled hydrogen discharges,” *J. Appl. Phys.*, vol. 95, no. 9, pp. 4605–4620, May 2004.

[154] Y. Catherine and P. Couderc, “Electrical characteristics and growth kinetics in discharges used for plasma deposition of amorphous carbon,” *Thin Solid Films*, vol. 144, no. 2, pp. 265–280, Nov. 1986.

[155] Y. P. Raizer, M. N. Shneider, and N. A. Yatsenko, *Radio-frequency capacitive discharges*. Boca Raton: CRC Press LLC, 1995.

[156] N. Mutsukura, K. Kobayashi, and Y. MacHi, “Plasma sheath thickness in radio-frequency discharges,” *J. Appl. Phys.*, vol. 68, no. 6, pp. 2657–2660, Sep. 1990.

[157] S. Y. Savinov, H. Lee, H. K. Song, and B. K. Na, “The Effect of Vibrational Excitation of Molecules on Plasmachemical Reactions Involving Methane and Nitrogen,” *Plasma Chem. Plasma Process.*, vol. 23, no. 1, pp. 159–173, 2003.

[158] B. S. Truscott, M. W. Kelly, K. J. Potter, M. N. R. Ashfold, and Y. A. Mankelevich, “Microwave Plasma-Activated Chemical Vapor Deposition of Nitrogen-Doped Diamond. II: CH4/N2/H2 Plasmas,” *J. Phys. Chem. A*, vol. 120, no. 43, pp. 8537–8549, 2016.

[159] A. J. Strudwick *et al.*, “Chemical vapor deposition of high quality graphene films from carbon dioxide atmospheres,” *ACS Nano*, vol. 9, no. 1, pp. 31–42, Jan. 2015.

[160] T. Terasawa and K. Saiki, “Effect of vapor-phase oxygen on chemical vapor deposition growth of graphene,” *Appl. Phys. Express*, vol. 8, no. 3, p. 35101, Mar. 2015.

[161] E. Starodub, N. C. Bartelt, and K. F. McCarty, “Oxidation of Graphene on Metals,” *J. Phys. Chem. C*, vol. 114, no. 11, pp. 5134–5140, Mar. 2010.

[162] A. Nourbakhsh *et al.*, “Bandgap opening in oxygen plasma-treated graphene,” *Nanotechnology*, vol. 21, no. 43, p. 435203, Oct. 2010.

[163] T. Niu, M. Zhou, J. Zhang, Y. Feng, and W. Chen, “Growth intermediates for CVD graphene on Cu(111): Carbon clusters and defective graphene,” *J. Am. Chem. Soc.*, vol. 135, no. 22, pp. 8409–8414, Jun. 2013.

[164] J. M. Grace and L. J. Gerenser, "Plasma Treatment of Polymers," *J. Dispers. Sci. Technol.*, vol. 24, no. 3–4, pp. 305–341, Jan. 2003.

[165] M. M. Lucchese *et al.*, "Quantifying ion-induced defects and Raman relaxation length in graphene," *Carbon N. Y.*, vol. 48, no. 5, pp. 1592–1597, Apr. 2010.

[166] S. R. Na, X. Wang, R. D. Piner, R. Huang, C. G. Willson, and K. M. Liechti, "Cracking of Polycrystalline Graphene on Copper under Tension," *ACS Nano*, vol. 10, no. 10, pp. 9616–9625, Oct. 2016.

[167] R. Kato, S. Minami, Y. Koga, and M. Hasegawa, "High growth rate chemical vapor deposition of graphene under low pressure by RF plasma assistance," *Carbon N. Y.*, vol. 96, pp. 1008–1013, 2016.

[168] C. Mattevi, H. Kim, and M. Chhowalla, "A review of chemical vapour deposition of graphene on copper," *J. Mater. Chem.*, vol. 21, no. 10, pp. 3324–3334, Feb. 2011.

[169] B. C. Sakiadis, "Boundary layer behavior on continuous solid surfaces: I. Boundary layer equations for two dimensional and axisymmetric flow," *AIChE J.*, vol. 7, no. 1, pp. 26–28, Mar. 1961.

[170] F. K. Tsou, E. M. Sparrow, and R. J. Goldstein, "Flow and heat transfer in the boundary layer on a continuous moving surface," *Int. J. Heat Mass Transf.*, vol. 10, no. 2, pp. 219–235, Feb. 1967.

[171] S. L. Lee and J. S. Tsai, "Cooling of a continuous moving sheet of finite thickness in the presence of natural convection," *Int. J. Heat Mass Transf.*, vol. 33, no. 3, pp. 457–464, Mar. 1990.

[172] M. V. Karwe and Y. Jaluria, "Thermal Transport From a Heated Moving Surface," *J. Heat Transfer*, vol. 108, no. 4, p. 728, Nov. 1986.

[173] M.-I. Char, C.-K. Chen, and J. W. Cleaver, "Conjugate forced convection heat transfer from a continuous, moving flat sheet," *Int. J. Heat Fluid Flow*, vol. 11, no. 3, pp. 257–261, Sep. 1990.

[174] G. Comini, S. Savino, N. Magriotis, and S. Muratori, "Thermal modeling of vacuum web coating," *Appl. Therm. Eng.*, vol. 27, no. 2–3, pp. 611–618, Feb. 2007.

[175] E. O. Cobos Torres and P. R. Pagilla, "Temperature Distribution in Moving Webs Heated by Radiation Panels: Model Development and Experimental Validation," *J. Dyn. Syst. Meas. Control*, vol. 139, no. 5, p. 51003, Mar. 2017.

[176] A. Aziz and R. J. Lopez, “Convection-radiation from a continuously moving, variable thermal conductivity sheet or rod undergoing thermal processing,” *Int. J. Therm. Sci.*, vol. 50, no. 8, pp. 1523–1531, Aug. 2011.

[177] M. V. Karwe and Y. Jaluria, “Numerical Simulation of Thermal Transport Associated With a Continuously Moving Flat Sheet in Materials Processing,” *J. Heat Transfer*, vol. 113, no. 3, p. 612, Aug. 1991.

[178] S. Roy Choudhury and Y. Jaluria, “Analytical solution for the transient temperature distribution in a moving rod or plate of finite length with surface heat transfer,” *Int. J. Heat Mass Transf.*, vol. 37, no. 8, pp. 1193–1205, May 1994.

[179] B. H. Kang, J. Yoo, and Y. Jaluria, “Experimental Study of the Convective Cooling of a Heated Continuously Moving Material,” *J. Heat Transfer*, vol. 116, no. 1, p. 199, Feb. 1994.

[180] G. M. Carlomagno and G. Cardone, “Infrared thermography for convective heat transfer measurements,” *Exp. Fluids*, vol. 49, no. 6, pp. 1187–1218, Dec. 2010.

[181] H. Ay, J. Jang, and J.-N. Yeh, “Local heat transfer measurements of plate finned-tube heat exchangers by infrared thermography,” *Int. J. Heat Mass Transf.*, vol. 45, no. 20, pp. 4069–4078, Sep. 2002.

[182] Y. Huang, J. Chen, Z. Yin, and Y. Xiong, “Roll-to-roll processing of flexible heterogeneous electronics with low interfacial residual stress,” *IEEE Trans. Components, Packag. Manuf. Technol.*, vol. 1, no. 9, pp. 1368–1377, Sep. 2011.

[183] R. Søndergaard, M. Hösel, D. Angmo, T. T. Larsen-Olsen, and F. C. Krebs, “Roll-to-roll fabrication of polymer solar cells,” *Mater. Today*, vol. 15, no. 1, pp. 36–49, 2012.

[184] J. Luque, W. Juchmann, E. A. Brinkman, and J. B. Jeffries, “Excited state density distributions of H, C, C2, and CH by spatially resolved optical emission in a diamond depositing dc-arcjet reactor,” *J. Vac. Sci. Technol. A Vacuum, Surfaces, Film.*, vol. 16, no. 2, pp. 397–408, Mar. 1998.

[185] T. L. Bergman, A. S. Lavine, F. P. Incropera, and D. P. Dewitt, *Fundamentals of heat and mass transfer*. Wiley, 2002.

[186] S. Nunomura, M. Kondo, and H. Akatsuka, “Gas temperature and surface heating in plasma enhanced chemical-vapour-deposition,” *Plasma Sources Sci. Technol.*, vol. 15, no. 4, p. 783, Nov. 2006.

[187] G. Shivkumar, S. S. Tholeti, M. A. Alrefae, T. S. Fisher, and A. A. Alexeenko, “Analysis of hydrogen plasma in a microwave plasma chemical vapor deposition reactor,” *J. Appl. Phys.*, vol. 119, no. 11, p. 113301, 2016.

[188] M. V. Karwe and Y. Jaluria, “Fluid Flow and Mixed Convection Transport From a Moving Plate in Rolling and Extrusion Processes,” *J. Heat Transfer*, vol. 110, no. 3, p. 655, Aug. 1988.

[189] S. R. Choudhury and Y. Jaluria, “Forced convective heat transfer from a Continuously loving Heated Cylindrical Rod in materials processing,” *J. Heat Transfer*, vol. 116, no. 3, pp. 724–734, Aug. 1994.

[190] L. G. Cançado *et al.*, “Quantifying defects in graphene via Raman spectroscopy at different excitation energies,” *Nano Lett.*, vol. 11, no. 8, pp. 3190–3196, Aug. 2011.

[191] J. M. Grace, H. K. Zhuang, L. J. Gerenser, and D. R. Freeman, “Time-resolved investigation of the surface chemical modification of poly(ethylene naphthalate) by nitrogen plasma treatment,” *J. Vac. Sci. Technol. A Vacuum, Surfaces, Film.*, vol. 21, no. 1, pp. 37–46, Jan. 2003.

[192] A. C. Ferrari and D. M. Basko, “Raman spectroscopy as a versatile tool for studying the properties of graphene,” *Nature Nanotechnology*, vol. 8, no. 4. pp. 235–246, 2013.

[193] J. Sun, N. Lindvall, M. T. Cole, K. B. K. Teo, and A. Yurgens, “Large-area uniform graphene-like thin films grown by chemical vapor deposition directly on silicon nitride,” *Appl. Phys. Lett.*, vol. 98, no. 25, pp. 10–13, 2011.

[194] J. J. Lander, H. E. Kern, and A. L. Beach, “Solubility and diffusion coefficient of carbon in nickel: Reaction rates of nickel-carbon alloys with barium oxide,” *J. Appl. Phys.*, vol. 23, no. 12, pp. 1305–1309, Dec. 1952.

[195] B.-J. Lee, H.-Y. Yu, and G.-H. Jeong, “Controlled Synthesis of Monolayer Graphene Toward Transparent Flexible Conductive Film Application,” *Nanoscale Res. Lett.*, vol. 5, no. 11, pp. 1768–1773, Nov. 2010.

[196] H. J. Park, J. Meyer, S. Roth, and V. Skákalová, “Growth and properties of few-layer graphene prepared by chemical vapor deposition,” *Carbon N. Y.*, vol. 48, no. 4, pp. 1088–1094, Apr. 2010.

[197] Y. Miyata, K. Kamon, K. Ohashi, R. Kitaura, M. Yoshimura, and H. Shinohara, “A simple alcohol-chemical vapor deposition synthesis of single-layer graphenes using flash cooling,” *Appl. Phys. Lett.*, vol. 96, no. 26, p. 263105, Jun. 2010.

[198] L. Huang *et al.*, “Synthesis of high-quality graphene films on nickel foils by rapid thermal chemical vapor deposition,” *Carbon N. Y.*, vol. 50, no. 2, pp. 551–556, Feb. 2012.

[199] Z.-Y. Juang *et al.*, “Graphene synthesis by chemical vapor deposition and transfer by a roll-to-roll process,” *Carbon N. Y.*, vol. 48, no. 11, pp. 3169–3174, Sep. 2010.

[200] W. Cai, Y. Zhu, X. Li, R. D. Piner, and R. S. Ruoff, “Large area few-layer graphene/graphite films as transparent thin conducting electrodes,” *Appl. Phys. Lett.*, vol. 95, no. 12, p. 123115, Sep. 2009.

[201] S. J. Chae *et al.*, “Synthesis of Large-Area Graphene Layers on Poly-Nickel Substrate by Chemical Vapor Deposition: Wrinkle Formation,” *Adv. Mater.*, vol. 21, no. 22, pp. 2328–2333, Jun. 2009.

[202] M. R. Anisur, P. Chakraborty Banerjee, C. D. Easton, and R. K. Singh Raman, “Controlling hydrogen environment and cooling during CVD graphene growth on nickel for improved corrosion resistance,” *Carbon N. Y.*, vol. 127, pp. 131–140, Feb. 2018.

[203] A. T. T. Koh, Y. M. Foong, and D. H. C. Chua, “Cooling rate and energy dependence of pulsed laser fabricated graphene on nickel at reduced temperature,” *Appl. Phys. Lett.*, vol. 97, no. 11, p. 114102, Sep. 2010.

[204] G. Gutierrez *et al.*, “Multi-layer graphene obtained by high temperature carbon implantation into nickel films,” *Carbon N. Y.*, vol. 66, pp. 1–10, Jan. 2014.

[205] J. Kozlova, A. Niilisk, H. Alles, and V. Sammelselg, “Discontinuity and misorientation of graphene grown on nickel foil: Effect of the substrate crystallographic orientation,” *Carbon N. Y.*, vol. 94, pp. 160–173, Nov. 2015.

[206] E. C. Neyts, A. C. T. van Duin, and A. Bogaerts, “Formation of single layer graphene on nickel under far-from-equilibrium high flux conditions,” *Nanoscale*, vol. 5, no. 16, p. 7250, Jul. 2013.

[207] R. S. Weatherup *et al.*, “On the mechanisms of Ni-catalysed graphene chemical vapour deposition,” *ChemPhysChem*, vol. 13, no. 10, pp. 2544–2549, Jul. 2012.

[208] L. Baraton *et al.*, “On the mechanisms of precipitation of graphene on nickel thin films,” *EPL*, vol. 96, no. 4, p. 46003, Nov. 2011.

[209] Q. Hu *et al.*, "Large-scale nanometer-thickness graphite films synthesized on polycrystalline Ni foils by two-stage chemical vapor deposition process," *Carbon N. Y.*, vol. 113, pp. 309–317, Mar. 2017.

[210] A. A. Puretzky *et al.*, "Real-time optical diagnostics of graphene growth induced by pulsed chemical vapor deposition," *Nanoscale*, vol. 5, no. 14, p. 6507, Jul. 2013.

[211] S. Nunomura and M. Kondo, "Characterization of high-pressure capacitively coupled hydrogen plasmas," *J. Appl. Phys.*, vol. 102, no. 9, p. 93306, Nov. 2007.

[212] E. Abdel-Fattah and O. F. Farag, "Alpha to gamma mode transition in hydrogen capacitive radio-frequency discharge," *Can. J. Phys.*, vol. 91, no. 12, pp. 1062–1067, Dec. 2013.

[213] E. Amanatides and D. Mataras, "Frequency variation under constant power conditions in hydrogen radio frequency discharges," *J. Appl. Phys.*, vol. 89, no. 3, pp. 1556–1566, 2001.

[214] C. Beneking, "Power dissipation in capacitively coupled rf discharges," *J. Appl. Phys.*, vol. 68, no. 9, pp. 4461–4473, Nov. 1990.

[215] V. A. Godyak, R. B. Piejak, and B. M. Alexandrovich, "Electrical Characteristics of Parallel-Plate RF Discharges in Argon," *IEEE Trans. Plasma Sci.*, vol. 19, no. 4, pp. 660–676, 1991.

[216] P. Vidaud, S. M. A. Durrani, and D. R. Hall, "Alpha and gamma RF capacitance discharges in N2 at intermediate pressures," *J. Phys. D. Appl. Phys.*, vol. 21, no. 1, p. 57, Jan. 1988.

[217] S. Conti *et al.*, "Experimental and numerical investigation of a capacitively coupled low-radio frequency nitrogen plasma," *Exp. Therm. Fluid Sci.*, vol. 24, no. 3–4, pp. 79–91, May 2001.

[218] L. L. Alves *et al.*, "Capacitively coupled radio-frequency discharges in nitrogen at low pressures," *Plasma Sources Sci. Technol.*, vol. 21, no. 4, p. 45008, Aug. 2012.

[219] S. Kechkar, P. Swift, S. Kelly, S. Kumar, S. Daniels, and M. Turner, "Investigation of the electron kinetics in O2 capacitively coupled plasma with the use of a Langmuir probe," *Plasma Sources Sci. Technol.*, vol. 26, no. 6, p. 65009, May 2017.

[220] I. V. Schweigert, "Different modes of a capacitively coupled radio-frequency discharge in methane," *Phys. Rev. Lett.*, vol. 92, no. 15, pp. 155001–1, Apr. 2004.

[221] S. Hofmann, A. F. H. van Gessel, T. Verreycken, and P. Bruggeman, "Power dissipation, gas temperatures and electron densities of cold atmospheric pressure helium and argon RF plasma jets," *Plasma Sources Sci. Technol.*, vol. 20, no. 6, p. 65010, Dec. 2011.

[222] S. Y. Moon, D. B. Kim, B. Gweon, and W. Choe, "Temperature measurement of an atmospheric pressure arc discharge plasma jet using the diatomic CN (B2Σ+-X2Σ+, violet system) molecular spectra," *J. Appl. Phys.*, vol. 105, no. 5, p. 53307, Mar. 2009.

[223] J. Luque and D. R. Crosley, "LIFBASE Software Spectroscopy Tool: Database and Spectral Simulation Program (Version 1.9), SRI International, Report MP 99-009." 1999.

[224] O. Leroy, P. Stratil, J. Perrin, J. Jolly, and P. Belenguer, "Spatiotemporal analysis of the double layer formation in hydrogen radio frequency discharges," *J. Phys. D. Appl. Phys.*, vol. 28, no. 3, pp. 500–507, Mar. 1995.

[225] N. Mutsukura, K. Kobayashi, and Y. Machi, "Monitoring of radio-frequency glow-discharge plasma," *J. Appl. Phys.*, vol. 66, no. 10, pp. 4688–4695, Nov. 1989.

[226] C. M. O. Mahony, R. Al Wazzan, and W. G. Graham, "Sheath dynamics observed in a 13.56 MHz-driven plasma," *Appl. Phys. Lett.*, vol. 71, no. 5, pp. 608–610, Jun. 1997.

[227] U. Czarnetzki, D. Luggenhölscher, and H. F. Döbele, "Space and time resolved electric field measurements in helium and hydrogen RF-discharges," *Plasma Sources Sci. Technol.*, vol. 8, no. 2, p. 230, May 1999.

[228] S. Prasanna, A. Michau, C. Rond, K. Hassouni, and A. Gicquel, "Self-consistent simulation studies on effect of methane concentration on microwave assisted H2/CH4 plasma at low pressure," *Plasma Sources Sci. Technol.*, vol. 26, no. 9, p. 97001, Aug. 2017.

[229] K. Kutasi, Z. Donkó, M. Mohai, L. Nemes, and G. Marosi, "Formation of CNx layers in a nitrogen glow discharge with graphite electrodes," *Vacuum*, vol. 68, no. 4, pp. 311–319, 2002.

[230] C. Vivien, J. Hermann, A. Perrone, and C. Boulmer-Leborgne, "A study of molecule formation during laser ablation of graphite in low-pressure ammonia," *J. Phys. D. Appl. Phys.*, vol. 32, no. 4, pp. 518–528, May 1999.

[231] H. Riascos, G. Zambrano, and P. Prieto, "Spectroscopic analysis of a pulsed-laser deposition system for fullerene-like Cnx film production," *Plasma Chem. Plasma Process.*, vol. 26, no. 3, pp. 277–291, Jun. 2006.

[232] L. Tomasini, A. Rousseau, G. Gousset, and P. Leprince, "Spectroscopic temperature measurements in a microwave discharge," *J. Phys. D. Appl. Phys.*, vol. 29, no. 4, pp. 1006–1013, Apr. 1996.

[233] A. N. Goyette, W. B. Jameson, L. W. Anderson, and J. E. Lawler, “An experimental comparison of rotational temperature and gas kinetic temperature in a H2 discharge,” *J. Phys. D. Appl. Phys.*, vol. 29, no. 5, pp. 1197–1201, May 1996.

[234] P. Belenguer and J. P. Boeuf, “Transition between different regimes of rf glow discharges,” *Phys. Rev. A*, vol. 41, no. 8, pp. 4447–4459, Apr. 1990.

[235] T. L. Ni, B. Ke, X. D. Zhu, F. Arefi-Khonsari, and J. Pulpytel, “Probe diagnostics and numerical simulations of a low pressure argon slender plasma excited by a low frequency discharge,” *Plasma Sources Sci. Technol.*, vol. 17, no. 4, p. 45006, Nov. 2008.

[236] P. M. Vallinga and F. J. de Hoog, “Sheath properties of RF plasmas in a parallel-plate etch reactor; the low-frequency regime (ω<ωi),” *J. Phys. D. Appl. Phys.*, vol. 22, no. 7, pp. 925–932, Jul. 1989.

[237] V. A. Godyak and A. S. Khanneh, “Ion Bombardment Secondary Electron Maintenance of Steady RF Discharge,” *IEEE Trans. Plasma Sci.*, vol. 14, no. 2, pp. 112–123, Apr. 1986.

[238] S. Y. Moon, D. B. Kim, B. Gweon, and W. Choe, “Driving frequency effects on the characteristics of atmospheric pressure capacitive helium discharge,” *Appl. Phys. Lett.*, vol. 93, no. 22, p. 221506, Dec. 2008.

[239] Y.-T. Zhang and S.-Y. Cui, “Frequency effects on the electron density and α-γ mode transition in atmospheric radio frequency discharges,” *Phys. Plasmas*, vol. 18, no. 8, p. 83509, Aug. 2011.

[240] P. Chabert and N. Braithwaite, *Physics of Radio-Frequency Plasmas*. Cambridge: Cambridge University Press, 2011.

[241] M. Napari *et al.*, “The α and γ plasma modes in plasma-enhanced atomic layer deposition with O2-N2 capacitive discharges,” *J. Phys. D. Appl. Phys.*, vol. 50, no. 9, p. 95201, Mar. 2017.

[242] J. J. Shi, D. W. Liu, and M. G. Kong, “Plasma stability control using dielectric barriers in radio-frequency atmospheric pressure glow discharges,” *Appl. Phys. Lett.*, vol. 89, no. 8, pp. 2006–2008, 2006.

[243] R. H. Bruce, “Ion response to plasma excitation frequency,” *J. Appl. Phys.*, vol. 52, no. 12, pp. 7064–7066, Dec. 1981.

[244] K. Köhler, D. E. Horne, and J. W. Coburn, "Frequency dependence of ion bombardment of grounded surfaces in rf argon glow discharges in a planar system," *J. Appl. Phys.*, vol. 58, no. 9, pp. 3350–3355, Nov. 1985.

[245] S. Kakuta, T. Makabe, and F. Tochikubo, "Frequency dependence on the structure of radio frequency glow discharges in Ar," *J. Appl. Phys.*, vol. 74, no. 8, pp. 4907–4914, Oct. 1993.

[246] P. Bletzinger and M. J. Flemming, "Impedance characteristics of an rf parallel plate discharge and the validity of a simple circuit model," *J. Appl. Phys.*, vol. 62, no. 12, pp. 4688–4695, Dec. 1987.

[247] S. J. You, H. C. Kim, C. W. Chung, H. Y. Chang, and J. K. Lee, "Mode transition for power dissipation induced by driving frequency in capacitively coupled plasma," *J. Appl. Phys.*, vol. 94, no. 12, pp. 7422–7426, 2003.

[248] P. Belenguer, P. Guillot, and L. Therese, "Electrical characterization of radiofrequency glow discharge used for optical emission spectroscopy," *Surf. Interface Anal.*, vol. 35, no. 7, pp. 604–610, Jul. 2003.

[249] C. Bohm and J. Perrin, "Spatially resolved optical emission and electrical properties of SiH4 RF discharges at 13.56 MHz in a symmetric parallel-plate configuration," *J. Phys. D. Appl. Phys.*, vol. 24, no. 6, pp. 865–881, Jun. 1991.

[250] S. Y. Moon, J. K. Rhee, D. B. Kim, and W. Choe, "α, γ, and normal, abnormal glow discharge modes in radio-frequency capacitively coupled discharges at atmospheric pressure," *Phys. Plasmas*, vol. 13, no. 3, p. 33502, Mar. 2006.

[251] J. J. Shi, X. T. Deng, R. Hall, J. D. Punnett, and M. G. Kong, "Three modes in a radio frequency atmospheric pressure glow discharge," *J. Appl. Phys.*, vol. 94, no. 10, pp. 6303–6310, Nov. 2003.

[252] S. Y. Moon, J. K. Rhee, D. B. Kim, B. M. Gweon, and W. Choe, "Capacitive discharge mode transition in moderate and atmospheric pressure," *Curr. Appl. Phys.*, vol. 9, no. 1, pp. 274–277, Jan. 2009.

[253] E. Pop, S. Sinha, and K. E. Goodson, "Heat generation and transport in nanometer-scale transistors," *Proc. IEEE*, vol. 94, no. 8, pp. 1587–1601, Aug. 2006.

[254] P. K. Schelling, L. Shi, and K. E. Goodson, "Managing heat for electronics," *Materials Today*, vol. 8, no. 6. pp. 30–35, Jun-2005.

[255] A. L. Moore and L. Shi, "Emerging challenges and materials for thermal management of electronics," *Mater. Today*, vol. 17, no. 4, pp. 163–174, May 2014.

[256] W. Haensch *et al.*, "Silicon CMOS devices beyond scaling," *IBM J. Res. Dev.*, vol. 50, no. 4.5, pp. 339–361, Jul. 2006.

[257] S. Chen *et al.*, "Raman measurements of thermal transport in suspended monolayer graphene of variable sizes in vacuum and gaseous environments," *ACS Nano*, vol. 5, no. 1, pp. 321–328, Jan. 2011.

[258] S. Chen *et al.*, "Thermal conductivity of isotopically modified graphene," *Nat. Mater.*, vol. 11, no. 3, pp. 203–207, Mar. 2012.

[259] J. H. Seol *et al.*, "Two-dimensional phonon transport in supported graphene," *Science (80-.).*, vol. 328, no. 5975, pp. 213–216, Apr. 2010.

[260] C. G. Kang *et al.*, "Effects of multi-layer graphene capping on Cu interconnects," *Nanotechnology*, vol. 24, no. 11, p. 115707, 2013.

[261] R. Mehta, S. Chugh, and Z. Chen, "Enhanced electrical and thermal conduction in graphene-encapsulated copper nanowires," *Nano Lett.*, vol. 15, no. 3, pp. 2024–2030, Mar. 2015.

[262] P. Goli, H. Ning, X. Li, C. Y. Lu, K. S. Novoselov, and A. A. Balandin, "Thermal properties of graphene-copper-graphene heterogeneous films," *Nano Lett.*, vol. 14, no. 3, pp. 1497–1503, Mar. 2014.

[263] C. H. Yeh *et al.*, "Scalable graphite/copper bishell composite for high-performance interconnects," *ACS Nano*, vol. 8, no. 1, pp. 275–282, Jan. 2014.

[264] C. Cho *et al.*, "Pulsed KrF laser-assisted direct deposition of graphitic capping layer for Cu interconnect," *Carbon N. Y.*, vol. 123, pp. 307–310, Oct. 2017.

[265] Z. Yan, G. Liu, J. M. Khan, and A. A. Balandin, "Graphene quilts for thermal management of high-power GaN transistors," *Nat. Commun.*, vol. 3, no. 1, p. 827, Jan. 2012.

[266] A. Kumar *et al.*, "Nitrogen-doped graphene by microwave plasma chemical vapor deposition," in *Thin Solid Films*, 2013, vol. 528, pp. 269–273.

[267] B. Guo, Q. Liu, E. Chen, H. Zhu, L. Fang, and J. R. Gong, "Controllable N-doping of graphene," *Nano Lett.*, vol. 10, no. 12, pp. 4975–4980, Dec. 2010.

[268] J. Sacks, W. J. Welch, T. J. Mitchell, H. P. Wynn, and J. Welch, "Design and Analysis of Computer Experiments," *Stat. Sci.*, vol. 4, no. 4, pp. 409–423, 2013.

[269] C. E. Rasmussen and C. Williams, *Gaussian Processes for Machine Learning*. MIT Press, 2006.

[270] J.-X. Pan and K.-T. Fang, "Maximum Likelihood Estimation," Springer New York, 2002, pp. 77–158.

[271] M. Binois, D. Ginsbourger, and O. Roustant, "Quantifying uncertainty on Pareto fronts with Gaussian process conditional simulations," *European Journal of Operational Research*, vol. 243, no. 2, pp. 386–394, 2014.

[272] A. Kramida, Y. Ralchenko, J. Reader, and NIST ASD Team, "NIST Atomic Spectra Database (version 5.4)," *National Institute of Standards and Technology, Gaithersburg, MD.*, 2016. [Online]. Available: https://physics.nist.gov/asd. [Accessed: 01-Sep-2017].

[273] C. V. V Prasad and P. F. Bernath, "Fourier transform spectroscopy of the Swan (d3pig - a3piu) system of the jet-cooled C2 molecule," *Astrophys. J.*, vol. 426, no. 2, pp. 812–821, May 1994.

[274] D. R. Farley, D. P. Stotler, D. P. Lundberg, and S. A. Cohen, "Modeling of hydrogen ground state rotational and vibrational temperatures in kinetic plasmas," *J. Quant. Spectrosc. Radiat. Transf.*, vol. 112, no. 5, pp. 800–819, Mar. 2011.

[275] M. F. Modest, *Radiative heat transfer*. San Diego: Academic Press (Elsevier Science), 2003.

APPENDIX A. PROCESS OPTIMIZATION OF GRAPHENE GROWTH IN A ROLL-TO-ROLL PLASMA CVD SYSTEM

Appendix A originates from the published manuscript [23] which is reused with permission form AIP Advances, Vol. #7, Article ID #11, (2017); used in accordance with the Creative Commons Attribution (CC BY) license.
[23] M. A. Alrefae, A. Kumar, P. Pandita, A. Candadai, I. Bilionis, and T. S. Fisher, “Process optimization of graphene growth in a roll-to-roll plasma CVD system,” *AIP Adv.*, vol. 7, no. 11, p. 115102, Nov. 2017.
The statistical models implemented in this work and described in Sections A.3 and A.8 have been developed by Piyush Pandita and Ilias Bilionis. The work is published in Ref. [23] and is reused with permission as listed above.

A.1 Plasma Stability Conditions

Figure A.1 shows images of plasma emission in which the pressure/power coupling affects the stability of the plasma. Lower power results in lifted plasmas for both alpha and gamma modes. These images correspond to plasma emission integrated over the range 200-800 nm measured using an iCCD camera (Princeton Instruments PI-MAX 4 iCCD).

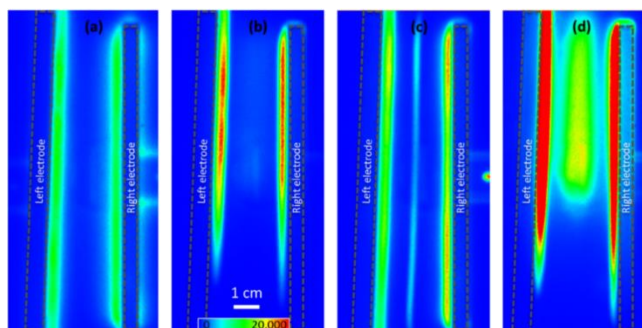

Figure A.1: Images of the plasma emission at different plasma conditions showing: a) stable alpha plasma at 30% H_2, 20% CH_4, 10% N_2, 10% O_2, 30% Ar, 7 mbar and 800 W, b) unstable alpha plasma at 0% H_2, 20% CH_4, 0% N_2, 10% O_2, 70% Ar, 15 mbar and 850 W, c) stable gamma plasma at 40% H_2, 20% CH_4, 0% N_2, 0% O_2, 40% Ar, 16 mbar and 1250 W, and d) unstable gamma plasma at 0% H_2, 0% CH_4, 10% N_2, 0% O_2, 90% Ar, 14 mbar and 750 W.

A.2 Raman Spectroscopy Analysis

The copper substrate has a Raman signal in the range of 1000-1800 cm^{-1}. We measured several spectra of bare copper foil, and the average of these spectra was used in the background subtraction process as shown in Fig. A.2. The raw Raman spectrum of graphene on copper foil is subtracted by the average signal of copper (Fig. A.2). The subtracted signal is used in the analysis after fitting the D- and G- peaks with Gaussian functions.

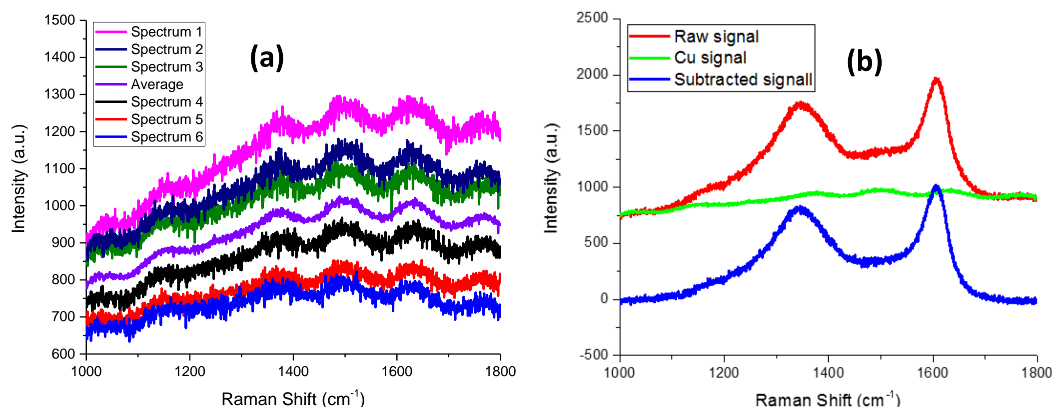

Figure A.2: (a) Raman spectra of the copper-only background without graphene growth. The average baseline of the copper background signal is subtracted from the Raman spectrum of graphene on copper foil as shown in (b). The condition of graphene growth is 20% H_2, 27% CH_4, 10% N_2, 3% O_2, 40% Ar, 9.3 mbar and 850 W.

Figure A.3 shows that the Raman spectrum of graphene transferred to Si/SiO_2 substrate is similar to the Raman spectrum measured directly from copper foil after background substation. The Raman spectrum from Fig. A.2 is used for this comparison. The spectra are then fitted to find the intensities, FWHM and positions of the G- and D-peaks.

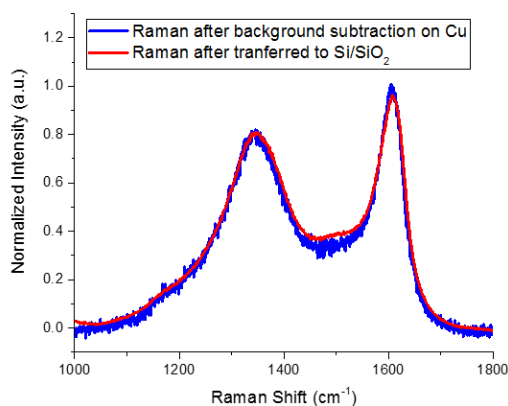

Figure A.3: Raman spectra of graphene after transfer to a Si/SiO_2 substrate. The condition of graphene growth is similar to Figure A.2: 20% H_2, 27% CH_4, 10% N_2, 3% O_2, 40% Ar, 9.3 mbar and 850 W.

A.3 Description of the Statistical Methods

To acquire a reasonable experimental data set for suggesting further optimized experiments, a sampling technique called Latin hypercube was used. The ranges of the inputs are given in Table II in the main paper. Experiments were then conducted at the conditions selected by the above method that serve as the data set for surrogate modeling.

A.3.1 Gaussian Process Regression

The motivation behind meta modeling stems from seminal work in the field of computer simulation design [268]. Due to incomplete knowledge about the physical system, we aim to approximate the objectives mathematically by developing data-driven models. Gaussian Process regression (GPR) [269] is ubiquitously used to construct probabilistic representations of unknown objectives. A GPR is fully specified by a mean function (taken to be zero here) and a covariance function that allows us to incorporate characteristics of the unknown objectives, such as smoothness and continuity, by estimating certain parameters (called hyper-parameters) of the covariance function. We use the Matern32 covariance function for this purpose [269]. The hyper-parameters include the following: a) length scales (l) which represent the influence of each input variable on the output, b) a signal strength (s^2) which represents the scale of magnitude of the objective, and c) a noise variance (σ^2) which estimates the noise in the observations. The parameters of the covariance, called hyper-parameters, are determined by using the standard technique of maximum likelihood estimation [270].

A.3.2 Information Acquisition Function (IAF)

The probabilistic nature of the GPRs allows us to quantify the uncertainty around the objectives mainly due to a finite number of measurements contaminated with noise. This allows us to mathematically quantify the plausible information contained in a hypothetical experiment. The IAF weighs the improvement, over the hyper-volume dominated by the Pareto efficient frontier (PEF), that is carried by a hypothetical experiment. We denote the hypothetical experiment by y, and the PEF by $\widetilde{P^e}$. We define the improvement over the hyper-volume dominated by the PEF as follows: $\mathrm{IHV} = \mu(\widetilde{\mathbf{P^e}} \cup \mathbf{y}) - \mu(\widetilde{\mathbf{P^e}})$. Since the hypothetical observation is characterized by a probabilistic model, we work with the expected IHV (EIHV) $\mathrm{EIHV} = \int_{-\infty}^{\infty} \mathrm{IHV}\, \mathrm{P}(\mathbf{y})\mathbf{dy}$, where $P(\boldsymbol{y})$ represents the GPRs. For this work, we use a reformulated definition of the EIHV, known as the EEIHV [150], which focuses on extending the EIHV to problems with noisy measurements.

A.3.3 Epistemic Uncertainty and its Visualization

The PEF and its uncertainty are characterized by leveraging the methodology given in Binois et. al. [271]. The PEF is simply the lower left boundary of the attainment set in the minimization problem, as shown in Fig. 3 in the main paper. Framing the problem in this way, our

prediction of the PEF will be the boundary of the Vorob'ev expectation of the random attainment set. The uncertainty about this prediction will be captured by the Vorob'ev deviation of the random attainment set. We represent the uncertainty in our estimation of the Pareto frontier by plotting contours of the probability of achieving a particular region in the objective space.

A.3.4 Suggesting Multiple Experiments

After starting with an initial set of noisy measurements called 'Sets 1-3' in Fig. 4 in the main paper, the methodology selects the experimental condition that maximizes the information acquisition function (IAF). However, it is infeasible in this problem to conduct just one experiment in one batch; therefore, the methodology suggests multiple experiments in one set (batch) which is an addendum of our work. This is done by adding to the data set/initial measurements a sample from the modeled response surface (GPRs) of the outputs corresponding to the experimental condition selected. This augmented set is used to run the BGO algorithm to suggest another condition, and the process iterates until the required number of conditions for a batch of experiments to be conducted are obtained. This methodology is cost-effective in our roll-to-roll system as several experiments can be completed in one batch without ending the experiment and removing the samples.

A.3.5 The Sequential Experimental Design Algorithm using BGO.

Given: Measurement data: $(\mathbf{Y}, \mathbf{X})$; Constructed surrogate model: $\mathrm{P}(\mathrm{y}|\mathbf{x}, \boldsymbol{\theta})$; Desired number of suggested experiments in one batch: T, the virtual measurement set : $(\breve{\mathbf{Y}}, \breve{\mathbf{X}}) = (\mathbf{Y}, \mathbf{X})$.

1. $\mathrm{t} \leftarrow 1$.
2. Find the design/condition $\mathbf{x}_t^*$: $\mathbf{x}_t^* = \arg\min \mathrm{EEIHV}$.
3. Obtain a GPR realization from $\mathrm{P}(\mathbf{y}|\mathbf{x}, \boldsymbol{\theta})$ corresponding to $\mathbf{x}_t^*$, denoted by $\mathbf{y}(\mathbf{x}_t^*)$.
4. Augment the virtual measurement set: $(\breve{\mathbf{Y}}, \breve{\mathbf{X}}) = (\breve{\mathbf{Y}} \cup \mathbf{y}(\mathbf{x}_t^*), \breve{\mathbf{X}} \cup \mathbf{x}_t^*)$
5. $\mathrm{t} \leftarrow \mathrm{t} + 1$. GOTO step 2.
6. If t = T Conduct experiments at the set of experiments $\breve{\mathbf{X}}_{\mathrm{n+1:T}}$ and measure $\mathbf{Y}_{\mathrm{n+1:T}}$
   Augment the original data set: $(\mathbf{Y}, \mathbf{X}) = (\mathbf{Y} \cup \mathbf{Y}_{\mathrm{n+1:T}}, \mathbf{X} \cup \breve{\mathbf{X}}_{\mathrm{n+1:T}})$
7. Continue for another batch of suggested experiments.

The effects of experimental order in one set had little effect on the process parameters (gas flow rates, and temperatures measured by a thermocouple and a pyrometer) when a sufficient warm-up period (e.g., approximately 15-20 minutes) was allowed. Thus, the Raman results from

similar experiments, one at the beginning of the batch and at the end, fall within experimental uncertainties (I_D/I_G ratio of both sides). Two identical experiments were made: one at the beginning of Set 5 and the other at the end. Figure A.4 shows the Raman results of both experiments showing similar results. Furthermore, the pyrometer and the gas temperatures are similar for both experiments even though the experiments between the two had different temperatures values.

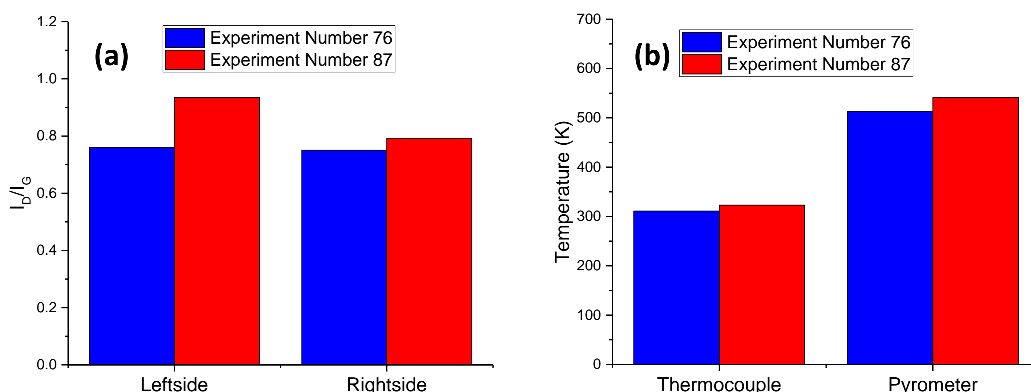

Figure A.4: (a) The I_D/I_G ratio of graphene on the left and right sides of the copper foil for experiment numbers 76 and 87. (b) The thermocouple and the pyrometer temperatures of both experiments. The conditions were the same: 31% H_2, 25% CH_4, 4% N_2, 1% O_2, 39% Ar, 9.2 mbar and 750 W.

A.4 Uniformity of Graphene Growth

Graphene-coated copper foil is protected from oxidation due to the high gas impermeability and thermal stability of graphene [151]. Hence, there is no color change in the graphene-coated copper when subjected to mild thermal annealing, indicating uniformity of graphene deposition over a large area measured by optical microscope at a magnification of 100x as shown in Fig. A.5 (a), (c) and (d). On the other hand, extensive color change occurs when a bare copper foil is subjected to the oxidation test due to the formation of copper oxides on its surface (Fig. A.5 (b)). Also, a greater degree of color change is observed in the graphene sample grown at higher speed (959 mm/min), due to a lower number of graphene layers deposited at this high speed as compared to the growth speed of 45 mm/min. Quantifying results from this oxidation test method is under development for future work to aid in characterization graphene produced in large scale production facilities.

A.5 Effects of Plasma Length on Graphene Quality

The length of the plasma slit was decreased to 5 cm from 20 cm to study the effects of ion bombardment on graphene quality. The residence time of the substrate in this reduced plasma

length configuration is 1.1 min at a speed of 45 mm/min. Figure A.6 presents the I_D/I_G ratios from four experiments and shows that quality remains similar regardless of the decreased plasma frontal area. Hence, ion bombardment in a low-frequency capacitively coupled plasma has strong effects of on graphene quality.

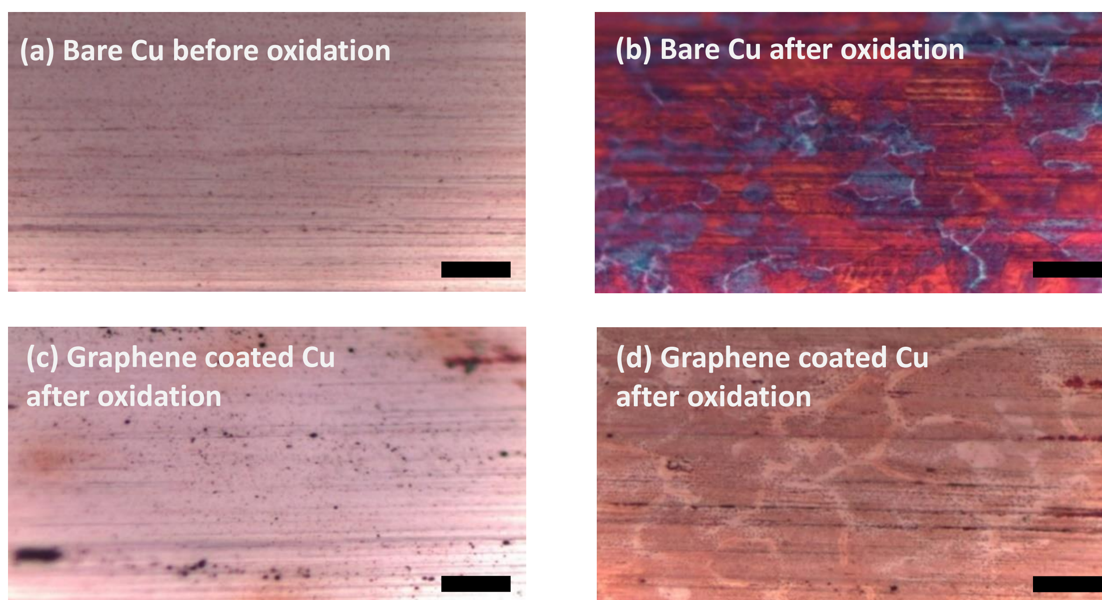

Figure A.5: Optical images of (a) bare copper foil before oxidation test, (b) bare copper foil after oxidation test, (c) and (d) graphene on copper foil after oxidation. The growth condition for graphene on copper foil in (c) and (d) is similar to Case 2 in the main paper (33% H_2, 30% CH_4, 10% N_2, 8% O_2, 19% Ar, 15 mbar, and 1250 W) at web speeds of 45 and 959 mm/min, respectively. The scale bar is 10 µm.

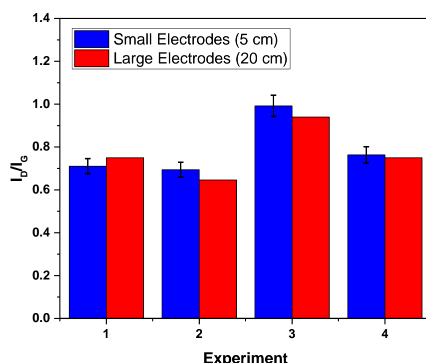

Figure A.6: The effects of decreasing plasma length using small and large electrodes with plasma lengths of 5 and 20 cm, respectively. The length of the plasma has minimum influence of graphene quality due to large impact of ion bombardment in the plasma. The conditions for the experiments are: 1) 39% H_2, 20% CH_4, 10% N_2, 7% O_2, and 24% Ar at 10.5 mbar and 750 W, 2) 31% H_2, 25% CH_4, 4% N_2, 1% O_2, and 39% Ar at 9.2 mbar and 750 W, 3) 33% H_2, 30% CH_4, 10% N_2, 8% O_2, and 19% Ar at 15.0 mbar and 1,250 W, 4) 10% H_2, 19% CH_4, 10% N_2, 6% O_2, and 55% Ar at 10.6 mbar and 700 W.

A.6 Effects of Pressure on Plasma Sheath and the Transition from Alpha to Gamma Modes

The effects of the gas pressure on the plasma type is shown in Fig. A.7. At lower pressure, the sheath for the right electrode is larger and could touch the right side face of the copper foil resulting in lower quality due to strong ion bombardment. As the pressure increases, the sheath thickness decreases (as seen in the images at 13.6 and 15.2 mbar). Further increase of pressure changes the plasma type to a gamma mode where the current density is high. This mode exhibits strong emission intensity in the middle of the gap between the two electrodes (compare the images of the plasma at 15.2 and 15.4 mbar).

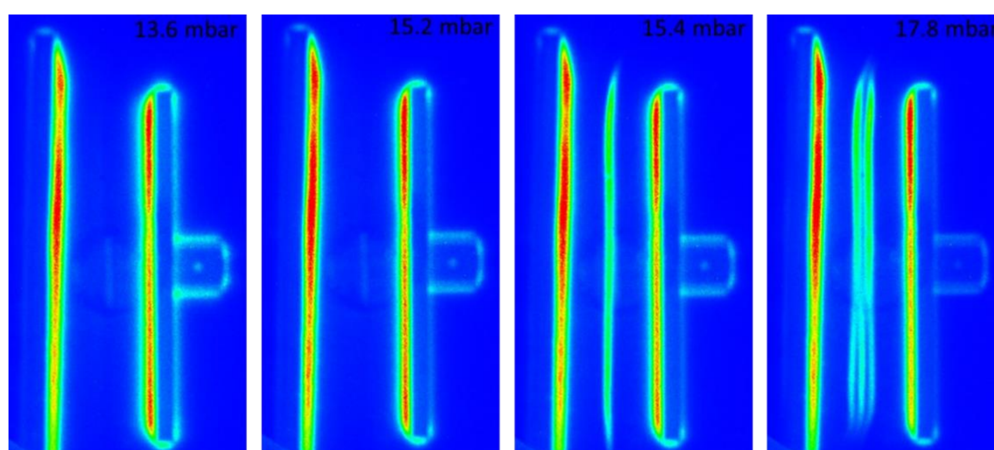

Figure A.7: Plasma emission images showing the effect of pressure on the plasma type. The transition occurs near 15.4 mbar. The other plasma conditions are the same: 70% H_2, 25% CH_4, 5% O_2 at 1000 W. The scale of the emission is from 10 to 5,535 counts.

A.7 Optical Emission Spectroscopy

The spectroscopic details of the emission lines are summarized in Table A.1.

Table A.1: The species emission lines used in this work.

Species [ref]	**CN** [223]	**N_2^+** [223]	**CH** [223]	**Ar^+** [272]	**C_2** [273]	**H_2** [274]	**H_α** [272]	**Ar** [272]	**O** [272]	**C** [272]	**N** [272]
Wavelength (nm)	388.3	391.4	431.2	476.5	516.0	601.8	656.3	750.4	777.2	833.5	868.0
Transition	B-X	B-X	A-X	$^2P^o$-^2P	$d^3\Pi_g - a^3\Pi$	$d^3\Pi - a^3\Sigma$	3-2	$^2[^1/_2]$-$^2[^1/_2]^o$	^5P - $^5S^o$	^1S-$^1P^o$	$^4D^o$-^4P

A.8 Mapping between the OES and Raman Results

We use a vector w as follows: $z = w^T * x$ where x is the emission intensity matrix, and z is a variable that maps the I_D/I_G. The variable z can be expressed as a 3rd order polynomial as: $\left(\frac{I_D}{I_G}\right) = b_o + b_1 z + b_2 z^2 + b_3 z^3$, where the coefficients are fitted using a hierarchical Bayes model assuming Gaussian noise as shown in Fig. A.8.

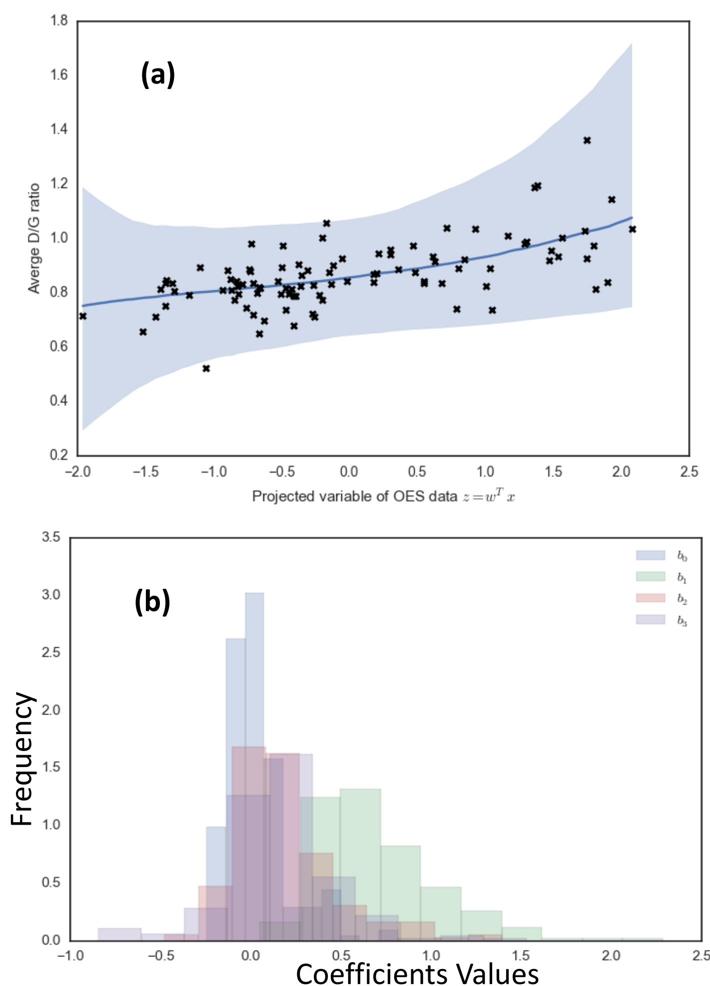

Figure A.8: (a) I_D/I_G ratio of graphene on copper foil as a function of the projected variables, *z*. The line describes the model, while the shaded area shows the uncertainty of the model. (b) The coefficients of the variable *z* which are chosen based on a hierarchical Bayes model assuming Gaussian noise.

A.9 Correlations between OES Species Emission Ratios and Process Parameters

The emission intensity ratios (CH/O, CH/C_2 and H_2/H) have higher values at the optimized condition (31% H_2, 25% CH_4, 4% N_2, 1% O_2, and 39% Ar at 9.2 mbar and 750 W) as shown in Fig. A.9. For example, CH/C_2 and H_2/H have higher values near 9.2 mbar as shown in Fig. A.9(a)

and (b). Similarly, CH/C_2 decreases with increased plasma power and has higher value around 750 W (Fig. A.9(c)). Also, the CH/O ratio decreases with increased O_2 mole fraction and maximizes at 1% O_2 (Fig. A.9(d)). Finally, the CH/O peaks in 4% N_2 due to higher dissociation of methane and lower CN as shown in (Fig. A.9(e)).

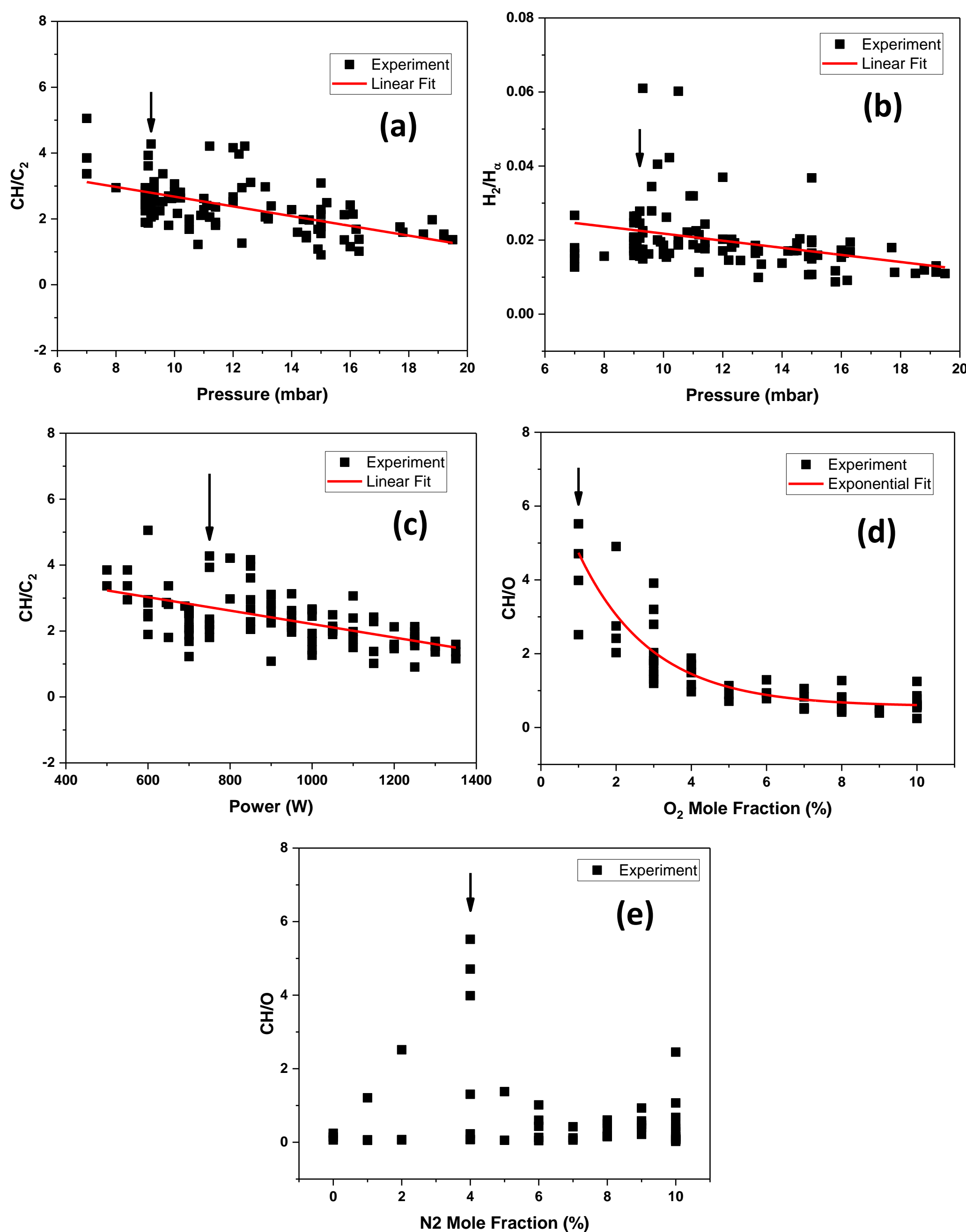

Figure A.9: The optimized condition (31% H_2, 25% CH_4, 4% N_2, 1% O_2, and 39% Ar at 9.2 mbar and 750 W) produces higher values of CH/O, CH/C_2 and H_2/H. The effects of pressure on (a) CH/C_2, and (b) H_2/H. (c) CH/C_2 decreases linearly with plasma power. The variations of CH/O as a function of (d) O_2 mole fraction and (e) N_2 mole fraction.

APPENDIX B. FIN MODEL DERIVATION

B.1 Derivation Details of the Analytical Model

Applying the Taylor expansion for heat conduction and advection terms in Eq. (5):

$$q_y - q_{y+dy} = q_y - \left(q_y + \frac{dq_y}{dy}dy\right) = -\frac{dq_y}{dy}dy \quad \text{(B1)}$$

$$\delta w(\rho U C_P T)_y - \delta w(\rho U C_P T)_{y+dy} = \delta w \rho U C_P T_y - \delta w \rho U (C_P T_y + \frac{dC_P T}{dy}dy) =$$
$$-\delta w \rho U C_P dy \frac{dT}{dy} \quad \text{(B2)}$$

Applying the Fourier's law for the conduction in Eq. (B1):

$$-\frac{dq_y}{dy}dy = -dy\left(\frac{d}{dy}(-\delta wk\frac{dT}{dy})\right) = \delta wkdy\frac{d^2T}{dy^2} \quad \text{(B3)}$$

Expanding the convective and radiative terms in Eq. (5) as follow:

$$dq_{conv} = wh_1(T - T_{\infty,1})dy \quad \text{(B4)}$$

$$dq_{rad,R} = dyw\varepsilon\sigma(T^4 - T_{surr}^4) = dyw\varepsilon\sigma(T^2 + T_{surr}^2)(T + T_{surr})(T - T_{surr}) =$$
$$wh_{rad,1}(T - T_{surr})dy \quad \text{(B5)}$$

where $T_{\infty,1}$ is the gas temperature, h_1 is the convective heat transfer coefficient and $h_{rad,R,1}$ is the linearized radiative heat transfer coefficient written as $h_{rad,1} = \varepsilon_{Cu}\sigma(T^2 + T_{surr}^2)(T + T_{surr})$. The temperature of the chamber wall (T_{surr}) is assumed to be equal to the gas temperature in the pre-plasma region ($T_{\infty,1}$). Finally, ε_{Cu} and σ are the emissivity of the Cu foil and the Stefan-Boltzmann constant, respectively. So, the final form of the differential equation becomes:

$$\delta wkdy\frac{d^2T}{dy^2} - \delta w\rho U C_p dy\frac{dT}{dy} - 2dywh_1(T - T_{\infty,1}) - 2\,dywh_{rad,1}(T - T_{surr}) = 0 \quad \text{(B6)}$$

Dividing Eq. (B6) by $\delta wkdy$ yields the simplified differential equation which is written in Eq. (6):

$$\frac{d^2T}{dy^2} - \frac{\rho U C_p}{k}\frac{dT}{dy} - \frac{2h_1}{\delta k}(T - T_{\infty,1}) - \frac{2h_{rad,1}}{\delta k}(T - T_{surr}) = 0 \quad \text{(B7)}$$

B.2 Derivation of Radiation Exchange between Cu Foil and the Electrodes in the Analytical Model

Radiation from Cu foil to both electrodes is linearized to simplify the differential heat equation in the plasma region. The linearized radiation heat transfer coefficient from Cu foil to the right electrode, for example, is determined by employing the radiation resistance network [185]:

$$dq_{rad,RE} = \frac{wdy\, \sigma(T^2+T_{RE}^2)(T+T_{RE})}{\frac{1-\varepsilon_{Cu}}{\varepsilon_{Cu}}+\frac{1-\varepsilon_E}{\varepsilon_E}\frac{dy}{L}+\frac{1}{F_{Cu-RE}}}(T-T_{RE}) \quad \text{(B8)}$$

where T_{RE} is the electrode temperature (Fig. 4.2(d)). The view factor F_{Cu-RE} and the emissivity of copper and graphite (ε_{Cu} and ε_E respectively) are obtained from Ref. [185]. We can write the linearized radiative heat transfer coefficient due to the radiation exchange between Cu foil and the right electrode as:

$$h_{rad,RE} = \frac{\sigma(T^2+T_{RE}^2)(T+T_{RE})}{\frac{1-\varepsilon_{Cu}}{\varepsilon_{Cu}}+\frac{1-\varepsilon_E}{\varepsilon_E}\frac{dy}{L}+\frac{1}{F_{Cu-RE}}} \quad \text{(B9)}$$

The denominator represents the copper surface resistance, the electrode surface resistance, and the space resistance, respectively. A similar formula is written for radiation transfer between substrate and the other electrode to simplify the differential equation in the plasma region and lead to the temperature distribution solution in the plasma region (i.e., Eq. (8)).

B.3 The Constants Expressions in the Analytical Solution

The constants (C_1, C_4, C_5, C_6) in the analytical solution expressed in Eq. (10) have the forms:

$$C_1 = (k_3k_2r_4r_5T_{\infty,3} - k_3k_2r_4r_5T_{\infty,2} + k_3k_2r_4r_6T_{\infty,3} - k_3k_2r_4r_6T_{\infty,2} - e_5k_2^2r_5r_6T_{\infty,1} + e_6k_2^2r_5r_6T_{\infty,1} + e_5k_2^2r_5r_6T_{\infty,2} - e_6k_2^2r_5r_6T_{\infty,2} - e_5k_3k_2r_4r_6T_{\infty,1} - e_6k_3k_2r_4r_5T_{\infty,1} + e_5k_3k_2r_4r_6T_{\infty,2} + e_6k_3k_2r_4r_5T_{\infty,2})/(e_5k_2^2r_5r_6 - e_6k_2^2r_5r_6 + e_5k_1k_3r_1r_4 - e_6k_1k_3r_1r_4 + e_5k_1k_2r_1r_5 + e_6k_1k_2r_1r_6 + e_5k_3k_2r_4r_6 + e_6k_3k_2r_4r_5)$$

$$C_4 = -(e_5k_2^2r_5r_6T_{\infty,3} - e_5k_2^2r_5r_6T_{\infty,2} - e_6k_2^2r_5r_6T_{\infty,3} + e_6k_2^2r_5r_6T_{\infty,2} + e_5k_1k_2r_1r_5T_{\infty,3} - e_5k_1k_2r_1r_5T_{\infty,2} + e_6k_1k_2r_1r_6T_{\infty,3} - e_6k_1k_2r_1r_6T_{\infty,2} - e_5e_6k_1k_2r_1r_5T_{\infty,1} - e_5e_6k_1k_2r_1r_6T_{\infty,1} + e_5e_6k_1k_2r_1r_5T_{\infty,2} + e_5e_6k_1k_2r_1r_6T_{\infty,2})/(e_4(e_5k_2^2r_5r_6 - e_6k_2^2r_5r_6 + e_5k_1k_3r_1r_4 - e_6k_1k_3r_1r_4 + e_5k_1k_2r_1r_5 + e_6k_1k_2r_1r_6 + e_5k_3k_2r_4r_6 + e_6k_3k_2r_4r_5))$$

$$C_5 = (k_1k_3r_1r_4T_{\infty,3} - k_1k_3r_1r_4T_{\infty,2} + k_3k_2r_4r_6T_{\infty,3} - k_3k_2r_4r_6T_{\infty,2} - e_6k_1k_3r_1r_4T_{\infty,1} + e_6k_1k_2r_1r_6T_{\infty,1} + e_6k_1k_3r_1r_4T_{\infty,2} - e_6k_1k_2r_1r_6T_{\infty,2})/(e_5k_2^2r_5r_6 - e_6k_2^2r_5r_6 + e_5k_1k_3r_1r_4 - e_6k_1k_3r_1r_4 + e_5k_1k_2r_1r_5 + e_6k_1k_2r_1r_6 + e_5k_3k_2r_4r_6 + e_6k_3k_2r_4r_5)$$

$$C_6 = -(k_1k_3r_1r_4T_{\infty,3} - k_1k_3r_1r_4T_{\infty,2} - k_3k_2r_4r_5T_{\infty,3} + k_3k_2r_4r_5T_{\infty,2} - e_5k_1k_3r_1r_4T_{\infty,1} - k_1k_2r_1r_5 + e_5k_1k_3r_1r_4T_{\infty,2} + e_5k_1k_2r_1r_5T_{\infty,2})/(e_5k_2^2r_5r_6 - e_6k_2^2r_5r_6 + e_5k_1k_3r_1r_4 - e_6k_1k_3r_1r_4 + e_5k_1k_2r_1r_5 + e_6k_1k_2r_1r_6 + e_5k_3k_2r_4r_6 + e_6k_3k_2r_4r_5)$$

where: $r_1 = \sqrt{a^2 + 4m_1} + a$, $r_4 = \sqrt{a^2 + 4m_3} - a$, $r_5 = \sqrt{a^2 + 4m_2} + a$, $r_6 = \sqrt{a^2 + 4m_2} - a$, $e_5 = \exp\left(\frac{r_5 L}{2}\right)$ and $6 = \exp\left(-\frac{6L}{2}\right)$. k_1, k_1, and k_3 represent Cu foil thermal conductivity in the pre-plasma, plasma, and post-plasma regions, respectively. Also, $T_{\infty,1}, T_{\infty,2}$, and $T_{\infty,3}$ are the gas temperature in the pre-plasma, plasma, and post-plasma regions, respectively.

B.4 Derivation of the Radiation Term in the Numerical Model

Radiation from Cu foil to the right electrode and the chamber wall ($q_{rad,R}$), is written in terms of the space resistance as:

$$q_{rad,R} = \frac{E_{b,Cu} - J_{Cu-R}}{\frac{1-\varepsilon_{Cu}}{\varepsilon_{Cu}\Delta yw}} \quad \text{(B10)}$$

Here, $E_{b,Cu} = \sigma T_j^4$, and the radiosity J_{Cu-R} is obtained from the previous iteration (i.e., J_{Cu}^*). Thus, the radiation term of Eq. (B10) is written as:

$$q_{rad,R} = \frac{\sigma T_j^4 - J_{Cu-R}}{\frac{1-\varepsilon_{Cu}}{\varepsilon_{Cu}\Delta yw}} = \frac{\varepsilon_{Cu}\Delta yw(\sigma T_j^4 - J_{Cu-R}^*)}{1-\varepsilon_{Cu}} = \frac{\varepsilon_{Cu}\Delta yw\sigma T_j^4}{1-\varepsilon_{Cu}} - \frac{\varepsilon_{Cu}\Delta yw J_{Cu-R}^*}{1-\varepsilon_{Cu}} \quad \text{(B11)}$$

The first term in the right hand side of Eq. (B11) is linearized as follow:

$$\frac{\varepsilon_{Cu}\Delta yw\sigma T_j^4}{1-\varepsilon_{Cu}} = \frac{\varepsilon_{Cu}\Delta yw\sigma\left(T_j^*\right)^4}{1-\varepsilon_{Cu}} + \left(4\frac{\varepsilon_{Cu}\Delta yw\sigma\left(T_j^*\right)^3}{1-\varepsilon_{Cu}}\left(T_j - T_j^*\right)\right) = 4\frac{\varepsilon_{Cu}\Delta yw\sigma\left(T_j^*\right)^3}{1-\varepsilon_{Cu}}T_j - 3\frac{\varepsilon_{Cu}\Delta yw\sigma(T_j^*)^4}{1-\varepsilon_{Cu}} \quad \text{(B12)}$$

where T_j^* is the temperature of cell "j" from the previous iteration. Therefore, the radiation term can be written as:

$$q_{rad,R} = \frac{4\varepsilon_{Cu}\Delta yw\sigma\left(T_j^*\right)^3}{1-\varepsilon_{Cu}}T_j - \frac{\varepsilon_{Cu}\Delta yw\left(J_{Cu-R}^* + 3\sigma\left(T_j^*\right)^4\right)}{1-\varepsilon_{Cu}} \quad \text{(B13)}$$

We find J_{Cu-R}^* by writing the radiation resistance network using the radiosity of the right side of Cu foil to the right side electrode (J_{RE}) and the radiosity of the chamber wall ($J_{Wall} = \varepsilon_{Wall}\sigma T_W^4$):

$$\frac{E_{b,Cu} - J_{Cu-R}}{\frac{1-\varepsilon_{Cu}}{\varepsilon_{Cu}A_{Cu}}} = \frac{J_{Cu-R} - J_{RE}}{\frac{1}{A_{Cu}F_{Cu-RE}}} + \frac{J_{Cu-R} - J_{Wall}}{\frac{1}{A_{Cu}F_{Cu-Wall}}} \quad \text{(B14)}$$

The view factor (F_{Cu-RE}) is determined using the differential planar element to a finite parallel rectangle adopted from Ref. [275]. Using the summation rule, we find $F_{Cu-Wall} = 1 - F_{Cu-RE}$. Therefore, the radiosity is found from the previous iteration value as:

$$a_{Cu}J_{Cu-R}^* = a_{Cu-RE}J_{Cu-RE}^* + a_{Cu-Wall}J_{Cu-Wall}^* + \frac{\varepsilon_{Cu}\Delta yw}{1-\varepsilon_{Cu}}\sigma\left((T_j^*)^4\right) \quad \text{(B15)}$$

$$a_{Cu} = a_{Cu-RE} + a_{Cu-Wall} + \frac{\varepsilon_{Cu}\Delta yw}{1-\varepsilon_{Cu}},\ a_{Cu-RE} = \Delta yw F_{Cu-RE}, \text{ and } a_{Cu-Wall} = \Delta yw F_{Cu-Wall}$$

Similar derivations can be obtained from the radiation from the substrate to the left electrode which result in similar equations.

VITA

Majed A. Alrefae was born in Saudi Arabia where he received his Bachelor degree from King Fahad University of Petroleum and Minerals (KFUPM) in 2008. He worked in SABIC, a petrochemicals company, between 2008 and 2011. In 2011, he started his academic career by joining Yanbu Industrial College as a lecturer in Mechanical Engineering Department. Shortly afterward, he started his Master degree at King Abdullah University of Science and Technology (KAUST) and obtained the MS degree in 2013. Majed then began his PhD study at Purdue University, West Lafayette in 2014, and joined the Nanoscale Transport Research Group led by Prof. Timothy S. Fisher in Birck Nanotechnology Center. Majed's research involves the characterizations of a scalable roll-to-roll plasma chemical vapor deposition system to mass produce graphene on various flexible substrates. Upon graduation, Majed will resume his academic career work in Yanbu Industrial College, and he is looking forward to building a research group focusing on scalable manufacturing of nanostructure materials utilizing plasma sources.

PUBLICATIONS

1. **M A Alrefae**, A Kumar, P Pandita, A Candadai, I Bilionis, T S Fisher, "Process Optimization of Graphene Growth in a Roll-to-roll Plasma CVD System", *AIP Advances,* 7 (11), 115102, 2017.
2. **M A Alrefae**, N R Glavin, A A Voevodin, and T S Fisher, "Plasma Chemical and Physical Vapour Deposition Methods and Diagnostics for 2D Materials," in *2D Inorganic Materials beyond Graphene*, R CNR and W UV, Eds. 2017, pp. 275–315.
3. A Kundu, **M A Alrefae**, T S Fisher, "Magnetothermoelectric Effects in Graphene and their Dependence on Scatterer Concentration, Magnetic Field, and Band Gap," *Journal of Applied Physics,* 121, 12, 125113, 2017.
4. G Shivkumar, SS Tholeti, **M A Alrefae**, T S Fisher, A A Alexeenko, "Analysis of Hydrogen Plasma in a Microwave Plasma Chemical Vapor Deposition Reactor," *Journal of Applied Physics,* 119 (11), 113301, 2016.

The following manuscripts have been accepted for publications:

1. **M A Alrefae**, and T S Fisher, "Thermal Analysis and Optimization of Graphene Deposition in a Roll-to-roll Plasma CVD Process," accepted in *the 16th International Heat Transfer Conference,* China, August 2018.
2. K R Saviers, **M A Alrefae**, and T S Fisher, " Roll-to-roll production of graphitic petals on carbon fiber tow," accepted in *Advanced Engineering Materials*.
3. A A Candadai, A Kumar, **M A Alrefae**, D Zemlyanov, and T S Fisher, "Rapid colorimetric analysis of graphene on copper," accepted in *Corrosion Science*.

The following manuscript has been submitted to a conference:

1. **M A Alrefae**, A Kumar, D Zemlyanov, T S Fisher, "Scaling up graphene-like carbon film: Insights into the deposition process in a roll-to-roll rf plasma CVD system," submitted to *The International Conference on Metallurgical Coatings and Thin Films (ICMCTF)*, San Diego, CA, April 2018.